Evolution and Dynamical Signatures of Massive Black Hole Binaries in Merging Star Clusters, Galactic Nuclei and Circumbinary Discs

Lazaros Souvaitzis

München 2025

Evolution and Dynamical Signatures of Massive Black Hole Binaries in Merging Star Clusters, Galactic Nuclei and Circumbinary Discs

Lazaros Souvaitzis

Dissertation
an der Fakultät für Physik
der Ludwig–Maximilians–Universität
München

vorgelegt von
Lazaros Souvaitzis
aus Thessaloniki, Greece

München, den 29.10.2025

Erstgutachter: Prof. Dr. Simon D.M. White
Zweitgutachter: Prof. Dr. Klaus Dolag
Tag der mündlichen Prüfung: 10.12.2025

Dedicated to my parents.

Contents

List of Figures

List of Tables

Zusammenfassung

Massive Schwarze-Loch-Binärsysteme mit Massen im Bereich von $10^3 - 10^9\,\mathrm{M}_\odot$ können in einer Vielzahl astrophysikalischer Umgebungen entstehen und stellen eine natürliche Konsequenz der hierarchischen Strukturbildung im Rahmen des ΛCDM-Paradigmas dar. Auf galaktischen Skalen führen Verschmelzungen massereicher Galaxien zur Annäherung ihrer zentralen supermassereichen Schwarzen Löcher (SMBHs), die infolgedessen SMBH-Binärsysteme bilden, deren Entwicklung durch dynamische Wechselwirkungen innerhalb des Fusionsprodukts bestimmt wird. Auf kleineren Skalen können einfallende, dichte Sternhaufen, die jeweils ein intermediäres Schwarzes Loch (IMBH) beherbergen, diese Objekte in galaktische Zentren transportieren, wo sie SMBH–IMBH-Binärsysteme bilden. Ebenso können Verschmelzungen von Sternhaufen zur Paarbildung zweier IMBHs führen, wodurch IMBH-Binärsysteme in Haufenumgebungen entstehen. Sobald ein massives Schwarze-Loch-Binärsystem auf sub-parsec-Skalen gebunden ist, kann das Vorhandensein einer zirkumbinären Akkretionsscheibe effizient Drehimpuls entziehen und das System entweder in Richtung einer Verschmelzung treiben oder – abhängig vom Zusammenspiel zwischen Gasdynamik und Binäreigenschaften – seine Entwicklung abbremsen. Obwohl bereits zahlreiche Kandidaten massiver Schwarze-Loch-Binärsysteme in diesen Umgebungen identifiziert wurden, basiert nur eine geringe Zahl auf belastbaren Beobachtungsnachweisen. Dies unterstreicht die Bedeutung präziser theoretischer und numerischer Modellierung, um ihre Entstehungspfade und evolutiven Endzustände zu verstehen.

Im ersten Teil dieser Arbeit präsentiere ich eine Reihe direkter N-Körper-Simulationen mit dem Bifrost-Code, in denen die Verschmelzung von Sternhaufen mit unterschiedlichen Anzahlen an IMBHs untersucht wird. Der Fokus liegt auf deren Einfluss auf den Resthaufen sowie auf die umgebenden Stern- und kompakten Objektpopulationen. Ziel der Studie ist es, die unterschiedlichen Evolutionspfade des Haufens – ohne IMBH, mit einem einzelnen IMBH oder mit zwei IMBHs – zu unterscheiden und mögliche beobachtbare oder dynamische Signaturen ihrer Anwesenheit zu identifizieren. Wenn beide Ursprungshaufen IMBHs enthalten, bildet sich ein hartes IMBH-Binärsystem, das eine signifikante Zahl von Sternen mit Geschwindigkeiten von bis zu $\gtrsim 300, \mathrm{km}, \mathrm{s}^{-1}$ ausstößt. Im Gegensatz dazu verlieren Systeme mit höchstens einem IMBH deutlich weniger Sterne, und ihre Ausstoßgeschwindigkeitsverteilungen unterscheiden sich sowohl qualitativ als auch quantitativ – ein charakteristisches dynamisches Kennzeichen für ein zentrales IMBH-Binärsystem in Sternhaufen.

Im zweiten Teil dieser Arbeit präsentiere ich eine Serie von 300 direkten N-Körper-

Simulationen mit dem MSTAR-Code, in denen die Dynamik massereicher Schwarzer Löcher (MBHs) untersucht wird, die entweder um ein einzelnes oder um ein binäres SMBH-System kreisen. Motivation hierfür ist die Erwartung, dass geringfügige Galaxienverschmelzungen solche Systeme erzeugen können. Diese Studie adressiert die Notwendigkeit konsistenter Definitionen der Bahnexzentrizität unter Einbeziehung allgemeiner relativistischer Effekte und implementiert einen adaptiven Zeitschrittalgorithmus, um inspiralförmige Bahnen, die durch Gravitationswellenemission angetrieben werden, präzise aufzulösen. Das Hauptziel besteht darin, zwischen direkten Plunges (DPs) und schweren Intermediate-Mass-Ratio Inspirals (IMRIs) zu unterscheiden und gleichzeitig den Einfluss von Einzel- gegenüber Binär-SMBH-Konfigurationen sowie die Rolle der räumlichen Ausdehnung (Kompaktheit) der umgebenden MBH-Population zu bewerten. Unsere Ergebnisse zeigen, dass das Vorhandensein eines sekundären SMBHs die Verschmelzungsrate zwischen MBHs und dem primären SMBH deutlich erhöht, wobei die Mehrheit dieser Ereignisse als hoch exzentrische Plunges auftritt. Obwohl diese Ereignisse in das LISA-Frequenzband eintreten, dürfte ihre rasche Entwicklung aufgrund eines geringen Signal-zu-Rausch-Verhältnisses eine Detektion erschweren.

Im dritten Teil dieser Arbeit untersuche ich die Bahnentwicklung geneigter massereicher Schwarze-Loch-Binärsysteme, die in zirkumbinären Akkretionsscheiben eingebettet sind, sowie deren Einfluss auf die umgebende Scheibenstruktur. Zu diesem Zweck führe ich eine Reihe hochaufgelöster, dreidimensionaler hydrodynamischer Simulationen mit dem Arepo-Code durch, in denen sowohl kreisförmige als auch exzentrische Binärsysteme bei unterschiedlichen Scheiben–Binär-Neigungswinkeln betrachtet werden. Die vollständig dreidimensionale Behandlung – in früheren zweidimensionalen Studien häufig vernachlässigt – offenbart signifikante Modifikationen in der Bahnentwicklung der Binärsysteme, da akkretion- und gravitationsgetriebene Drehmomente effizient Drehimpuls aus dem Binärsystem extrahieren und innerhalb der Scheibe umverteilen. Für ausreichend große Fehlstellungen entwickelt sich das System schließlich in eine retrograde Konfiguration, was eine charakteristische dynamische Signatur gasgetriebener Entwicklung darstellt, die insbesondere für exzentrische LISA-Quellen von Relevanz ist.

Insgesamt unterstreichen die Ergebnisse dieser Arbeit die Bedeutung einer präzisen Modellierung massereicher Schwarze-Loch-Binärsysteme in verschiedenen astrophysikalischen Umgebungen. Jedes der vorgestellten Projekte trägt zu einem tieferen Verständnis ihrer dynamischen Entwicklung, ihres Endzustands und der charakteristischen Signaturen bei, die sie in ihrer Umgebung hinterlassen. Solche Bemühungen sind entscheidend für die Interpretation gegenwärtiger und zukünftiger Beobachtungen – insbesondere im Rahmen von Pulsar-Timing-Arrays (PTAs), die den Gravitationswellenhintergrund im Nanohertz-Bereich untersuchen, sowie der Laser Interferometer Space Antenna (LISA), die einzelne Verschmelzungen im Millihertz-Bereich detektieren wird.

Abstract

Massive black hole binaries with masses ranging $10^3 - 10^9$ $M_\odot$, can arise in a variety of astrophysical environments as a natural consequence of hierarchical structure formation (according to ΛCDM paradigm) . On galactic scales, mergers between massive galaxies bring together their central supermassive black holes (SMBHs), forming SMBH binaries that evolve through dynamical interactions within the merger remnant. On smaller scales, infalling dense star clusters hosting intermediate-mass black holes (IMBHs) can deposit these objects into galactic centers, where they form SMBH–IMBH binaries. Similarly, mergers between star clusters may lead to the pairing of IMBHs, producing IMBH binaries in cluster environments. Finally, once a massive black hole binary is bound on sub-parsec scales, the presence of a circumbinary accretion disc can efficiently extract angular momentum, either driving the system toward coalescence or stalling its evolution depending on the interplay between gas dynamics and binary properties. Although numerous massive black hole binary candidates have been identified across these environments, only a few are supported by robust observational evidence, underscoring the importance of accurate theoretical and numerical modeling to unravel their formation pathways and evolutionary outcomes.

In the first part of this thesis, I present a suite of direct N-body simulations (`BIFROST` code) of merging star clusters with varying numbers of IMBHs, focusing on their influence on the remnant cluster and the surrounding stellar and compact object populations. The aim of the study is to disentangle the cluster's evolutionary pathways in the absence of IMBHs, with a single IMBH, or with two IMBHs, and to identify potential observational and dynamical signatures of their presence. When both progenitor clusters host IMBHs, a hard IMBH binary is formed which drives the ejection of a significant number of stars, with velocities reaching $\gtrsim 300\,\mathrm{km\,s^{-1}}$. In contrast, remnants containing at most one IMBH lose far fewer stars, and their ejection velocity distributions differ both qualitatively and quantitatively, providing a distinctive dynamical signature of a central IMBH binary in star clusters.

In the second part of this thesis, I present a set of 300 direct N-body simulations (`MSTAR` code) of massive black holes (MBHs) orbiting either single or binary SMBHs, motivated by the expectation that minor galaxy mergers can generate such systems. This study addresses the need for consistent definitions of orbital eccentricity when incorporating general relativistic effects and implements an adaptive timestep algorithm to accurately resolve inspiral trajectories driven by gravitational-wave emission. The primary objective

is to distinguish between the formation of direct plunges (DPs) and heavy intermediate-mass-ratio inspirals (IMRIs), while assessing the influence of single versus binary SMBH configurations and the impact of the spatial extent (compactness) of the surrounding MBH population. Our results show that the presence of a secondary SMBH markedly enhances the merger rate between MBHs and the primary SMBH, with the majority occurring as highly eccentric plunges; although these events enter the LISA band, their rapid evolution likely renders them undetectable due to low signal-to-noise ratios.

In the third part of this thesis, I examine the orbital evolution of inclined massive black hole binaries embedded in circumbinary accretion discs and their impact on the surrounding disc structure. To this end, I perform a suite of high-resolution three-dimensional hydrodynamical simulations with the `AREPO` code, exploring both circular and eccentric binaries while varying the disc–binary inclination angle. The fully three-dimensional treatment—often neglected in previous two-dimensional studies—reveals significant modifications to the binary's orbital evolution, as accretion- and gravity-driven torques efficiently extract angular momentum from the binary and redistribute it within the disc. Moreover, for sufficiently large misalignments, the system evolves toward a retrograde configuration, providing a distinct dynamical signature of gas-driven evolution that is particularly relevant for eccentric LISA sources.

Overall, the findings of this thesis underscore the importance of accurate modeling of massive black hole binaries across diverse astrophysical environments, with each project serving as a step toward a deeper understanding of their dynamical evolution, eventual fate, and the environmental signatures they imprint. Such efforts are crucial for interpreting current and future observations, particularly with pulsar timing arrays (PTAs) probing the nanohertz gravitational-wave background and the Laser Interferometer Space Antenna (LISA) targeting individual mergers in the millihertz band.

Chapter 1

Formation and Evolutionary Pathways of Massive Black Hole Binaries

The discovery of quasars in the 1960s as powerful extragalactic sources (Schmidt, 1963) and the recognition that their immense luminosities are powered by accretion onto supermassive black holes (SMBHs) (Robinson et al., 1965; Lynden-Bell, 1999) established the modern view that SMBHs reside at the centers of most massive galaxies Kormendy & Richstone (1995). Soon after, it was realized that the formation and mergers of SMBHs would produce gravitational-wave (GW) bursts detectable at Earth (Thorne & Braginskii, 1976). Building on this, Begelman et al. (1980) outlined the key astrophysical mechanisms driving the pairing and evolution of SMBHs in galactic nuclei, and suggested observational signatures of massive black hole binaries (MBHBs), including core light deficits, disturbed jet morphologies, emission line shifts, and photometric variability (see also Komberg, 1968). While the formation of MBHBs during galaxy mergers seems inevitable, coalescence requires that the separation between binary components first drop by a few orders of magnitude, due presumably to interaction of the binary with stars and gas in a galactic nucleus (Merritt & Milosavljević, 2005). In the decades since, theoretical work has framed this in terms of the *final parsec problem* (Milosavljević & Merritt, 2003; Merritt & Milosavljević, 2005; Colpi, 2014), namely the uncertainty over whether MBH pairs can be efficiently driven to coalescence within a Hubble time. Despite progress in identifying plausible mechanisms for orbital hardening, the processes that actually operate in galactic nuclei remain poorly constrained. This challenge mirrors the ongoing debate over the formation channels of stellar-mass black hole binaries observed through gravitational waves (GWs) (e.g., Zevin et al., 2021), where theory allows for multiple possibilities but their relative importance in nature is unclear. Addressing this "supermassive merger problem" (D'Orazio & Charisi, 2023) requires not only observational efforts to identify binaries across evolutionary stages, but also accurate and robust theoretical and numerical modeling to connect candidate signatures with their underlying astrophysical processes. In this introductory chapter, I focus on the different stages of the formation and multi-scale evolutionary pathways of MBHBs,

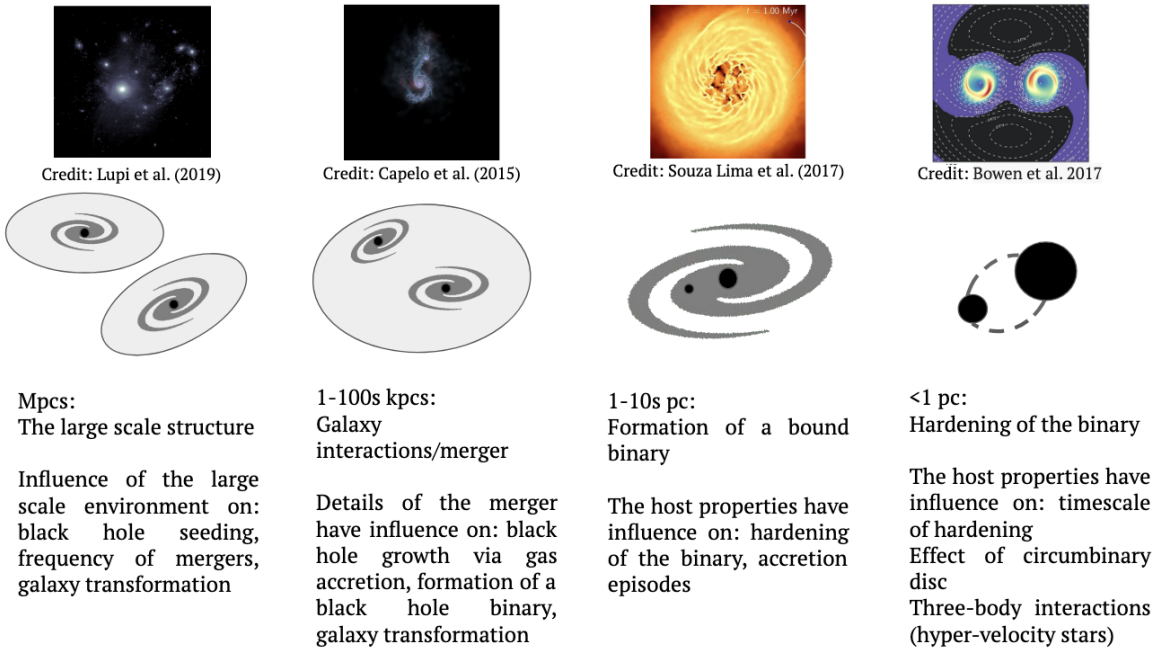

Figure 1.1: Overview of the different evolutionary phases of MBH binaries. Figure credit: Amaro-Seoane et al. (2023).

from kpc scales of merging galaxies down to the final coalescence stage driven by GW emission. MBHB evolution can be divided in three major phases: the dynamical friction stage (Section 1.1; kpc scales), during which MBHs and their host systems sink toward the center of the merger remnant while losing orbital energy and angular momentum until they become gravitationally bound as a binary; the binary hardening stage (Section 1.2; pc scales), where the binary evolution is primarily driven by interactions with surrounding stars and/or gas; and finally the relativistic stage (Section 1.5; mpc scales), when the dynamics are governed by gravitational wave (GW) emission.

1.1 Pairing Massive Black Holes via Galaxy Mergers and Dynamical Friction

Observational evidence supports the idea that most galaxies host MBHs in their centre (Kormendy & Ho, 2013) with additional evidence suggesting that at least some have hosted them since the earliest stages of structure formation (Bañados et al., 2014; Wu et al., 2015; Bañados et al., 2017). At the same time the hierarchical structure formation suggests that massive galaxies grow via repeated mergers of smaller ones (Ostriker & Hausman, 1977; White, 1980; Lacey & Cole, 1993; Fakhouri et al., 2010; O'Leary et al., 2020) , which leads

to the conclusion that a number of MBHBs have formed across cosmic time and their coalescence could be detectable by future GW facilities like LISA (Amaro-Seoane et al., 2023).

The initial evolutionary stage of MBHBs is the pairing phase at kiloparsec scales, where they are expected to reside for the majority of their lifetime. When a massive perturber, such as an MBH of mass $M_\bullet$, moves through a background medium of collisionless particles (e.g., stars or dark matter) with individual masses $m_\star \ll M_\bullet$, perturbs their trajectories. This interaction generates a trailing overdensity, or *wake* whose gravitational pull exerts a force opposite to the perturber's motion, effectively causing its deceleration. This drag force is the so-called dynamical friction (DF) (Chandrasekhar, 1943). Given an infinite homogeneous medium of density ρ and an isotropic background with Maxwellian velocity distribution and dispersion σ the force the perturber feels is then (Chandrasekhar, 1943):

$$\frac{d\mathbf{v}_M}{dt} = -16\pi^2(\ln\Lambda)G^2 m(M+m)\frac{\mathbf{v}_M}{v_M^3}\int_0^{v_M} v^2 f(v)dv \tag{1.1}$$

where $\mathbf{v}_M$ is the perturber's velocity w.r.t. the surrounding background $\left(v_M = |\mathbf{v}_M|\right)$, $\ln\Lambda \sim 10$ is the Coulomb logarithm[1] and $f(v)$ depends on the velocity distribution of the system. Let's now assume an MBH on a circular orbit with radius r in a stellar background with $\rho \propto \sigma^2 r^{-2}$ (singular isothermal sphere) . The orbital decay time-scale is then given by (Binney & Tremaine, 2008)

$$\tau_{\rm DF} \approx \frac{8{\rm Gyr}}{\ln\Lambda}\left(\frac{r}{\rm kpc}\right)^2 \frac{\sigma}{200\ {\rm km/s}}\frac{10^7{\rm M}_\odot}{M_\bullet}. \tag{1.2}$$

For an MBH of $M_\bullet = 10^6{\rm M}_\odot$ at a distance of $r = 1$kpc from a galaxy with $\sigma = 100$km/s the time-scale at which DF acts to sink the MBH is $\tau_{\rm DF} = 4$Gyr , illustrating the efficiency of the process. In the early stage of galactic mergers, one might replace $M_\bullet$ with the mass of the remnant's core embedding the MBH, which results in even shorter timescales (Yu & Tremaine, 2002).

Two MBHs M_1 and M_2 will form a binary when they reach a relative separation given by (Dotti et al., 2012)

$$a_{\rm b} \sim \frac{GM_{\rm b}}{2\sigma^2} \sim 0.2 M_{\rm b}\sigma_{100}^{-2}{\rm pc}, \tag{1.3}$$

where $M_{\rm b} = M_1 + M_2$. Observations show that MBH masses at galaxy centers correlate with their host via the $M_\bullet - \sigma$ relation (Ferrarese & Merritt, 2000; Gebhardt et al., 2000). Following this relation (e.g., Gültekin et al., 2009; Graham et al., 2011, and references therein) as shown in Fig. 1.2, equation (1.3) implies $a_{\rm b} \sim 0.5 M_{\rm b}^{1/2}$pc.

[1]The Coulomb factor Λ is defined as the ratio between the maximum and minimum effective impact parameters for encounters between background stars and the perturber (Merritt, 2013). In practice, Λ is often approximated using global system properties—for instance, as the ratio of the galaxy mass to the MBH mass, or alternatively the MBH mass to the mass of individual stars, with the former being more suitable for systems containing both stars and dark matter.

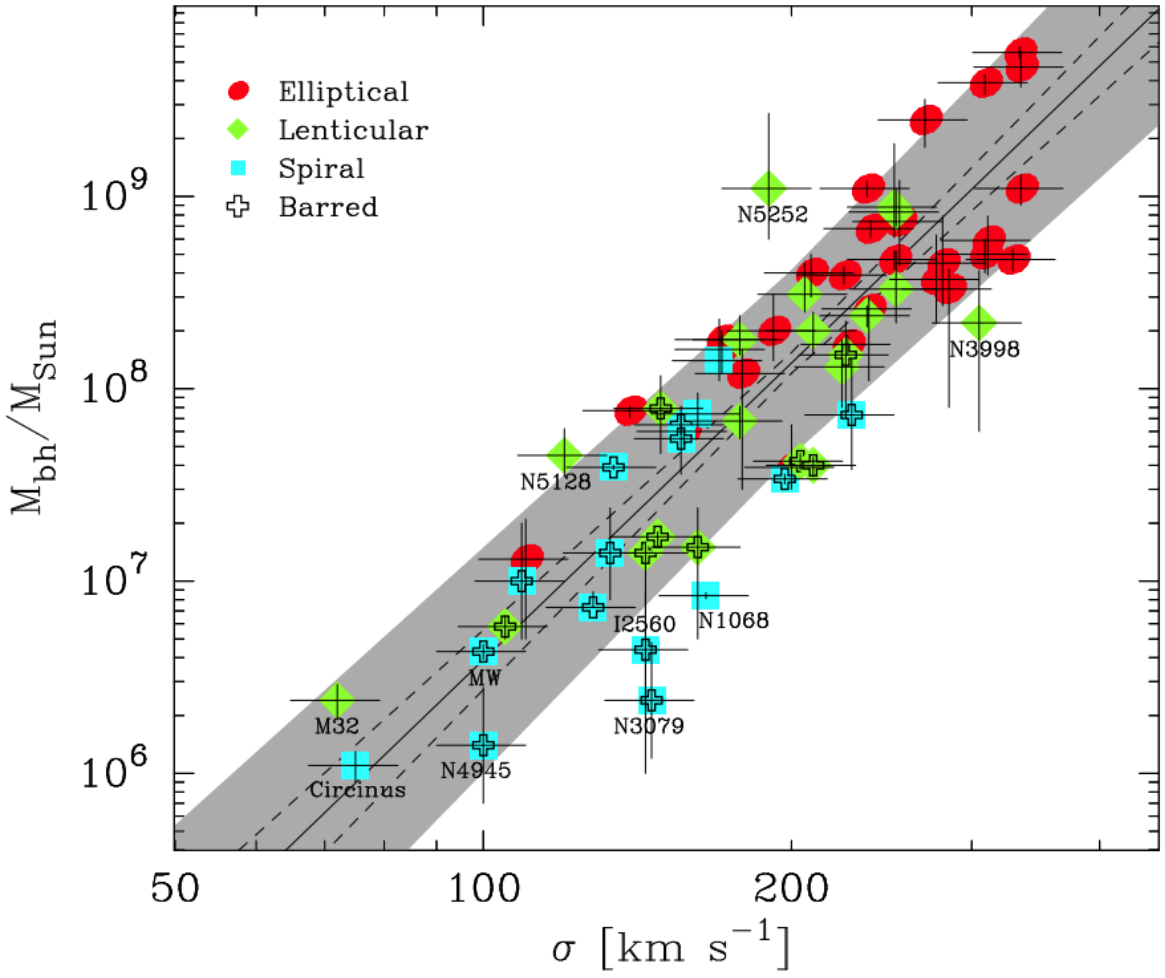

Figure 1.2: The $M_\bullet - \sigma$ relation for 64 galaxies with reliable SMBH masses (see Graham et al., 2011). The solid line shows the regression of $\log M_\bullet$ on $\log \sigma$ (with 10% uncertainty in σ); dashed lines mark the 1σ bounds, and the shaded region indicates the additional 0.43 dex scatter.

The efficiency of MBHB formation depends on the mass ratio of the merging galaxies. In major mergers with comparable masses, the binary forms rapidly, whereas in minor mergers the satellite galaxy is tidally disrupted during the interaction, leaving its central MBH wandering in the outskirts of the primary galaxy (e.g., Governato et al., 1994). When the mass enclosed within the binary orbit becomes comparable to that of the secondary MBH, DF becomes inefficient, and other mechanisms are needed to further shrink the binary (Section 1.2). For equal-mass binaries, this critical separation approximately corresponds to the point where the binary becomes effectively bound. In contrast, for binaries in which the secondary is much less massive than the primary, DF continues to drive orbital decay even below the binding separation. In this regime, a limitation of Eq. (1.1) arises because it only accounts for stars moving slower than the secondary MBH (Chandrasekhar, 1943).

Antonini & Merritt (2011) showed that for an inner density profile $\rho \propto r^{-\gamma}$, the standard Chandrasekhar formula performs reasonably well if $\gamma > 1$, but fails for shallow profiles ($\gamma \sim 0.6$), where faster-moving stars dominate DF. As a result, conventional theory would predict stalling, whereas the secondary can still inspiral, albeit more slowly (Dosopoulou & Antonini, 2017).

Accurately resolving this process in simulations requires stellar and dark matter particle masses much smaller than that of the sinking MBH, as well as properly capturing close encounters with minimal or no force softening (Pfister et al., 2019). Since such resolution is generally unattainable in cosmological simulations, dynamical friction is instead modelled through subgrid prescriptions, often based on Eq. (1.1), which account for unresolved particle deflections. These approaches have been shown to significantly improve the fidelity of MBH orbital evolution in simulations (Tremmel et al., 2015; Ma et al., 2023; Genina et al., 2024; Damiano et al., 2025).

1.1.1 Dark Matter Profile

The isothermal sphere used to derive Eq. (1.2) is only a simplification, as real galaxies exhibit significantly more complex structural profiles. For example, the inner density profile of dark matter (DM) halos is often modeled with a Navarro–Frenk–White (NFW) profile $\rho \propto r^{-\gamma}$, $\gamma = 1$ though observations suggest shallower cores in low-mass dwarf galaxies (Oh et al., 2015). Such cores may arise from baryonic feedback (Governato et al., 2010) or from alternative DM models, e.g. self-interacting or fuzzy DM (Hui et al., 2017). Numerical simulations show that shallow inner profiles ($\gamma \lesssim 0.6$) can stall MBH pairs at tens of parsecs, preventing coalescence (Tamfal et al., 2018), while self-interacting DM halos may further suppress dynamical friction and produce wandering MBHs at kiloparsec separations (Di Cintio et al., 2017). Since many dwarf galaxies are inferred to host cored DM distributions (Moore, 1994; Contenta et al., 2018; Leung et al., 2019), the rate of MBH mergers observable by LISA offers a potential probe of the central density structure of DM halos and, ultimately, the microphysics of DM.

1.1.2 Gas Dynamical Friction

In addition to stars and dark matter, gas can significantly affect MBH orbital decay, particularly in high-redshift galaxies where gas fractions are large (Tacconi et al., 2018; Decarli et al., 2020). Gas-driven dynamical friction is generally stronger than stellar friction in the transonic regime (Ostriker, 1999), but its efficiency depends sensitively on the density, thermodynamics, and morphology of the gaseous medium. Semi-analytic models suggest that in gas-poor systems with prominent stellar bulges, stellar friction dominates (Li et al., 2020), while simulations reveal contrasting outcomes: some find negligible gas contribution (Pfister et al., 2017), whereas others show rapid MBH sinking in gas-rich mergers due to efficient gas inflows (Chapon et al., 2013). These discrepancies highlight the importance of galaxy structure and merger conditions, and point to the need for further investigation of gaseous environments in shaping the formation and detection of MBH binaries.

1.2 The Orbital Decay of Massive Black Hole Binaries

The sphere around an MBH of mass $M_\bullet$ where its presence dominates the motion of stars and gas in the system is called *sphere of influence*. The radius of this sphere r_h is then given by (Merritt, 2013)

$$r_\mathrm{h} = \frac{GM_\bullet}{\sigma^2}, \tag{1.4}$$

where σ is the velocity of the surrounding stellar or gaseous background. As dynamical friction causes the orbits of MBHs to decay, the two objects eventually enter their mutual sphere of influence, leading to the formation of a bound MBH binary (Begelman et al., 1980; Milosavljević & Merritt, 2001). The subsequent evolution of the system is governed by a variety of mechanisms whose efficiency depends strongly on the surrounding galactic environment, implying that each binary may follow a distinct evolutionary pathway. On kiloparsec scales, the further shrinking of the binary separation is generally attributed to two broad classes of processes: those operating in predominantly stellar systems and those sustained by significant reservoirs of gas. This division is not absolute, as both stellar- and gas-driven hardening can act simultaneously, even though most studies focus on one regime at a time (Kelley et al., 2017a; Bortolas et al., 2021). In what follows, I highlight the main physical ingredients of these mechanisms, expected to inhabit environments containing both stars and gas.

1.2.1 Stellar Hardening

Once two MBHs form a bound binary, dynamical friction rapidly loses efficiency at subparsec scales, where the surrounding mass is insufficient to produce a substantial backreaction to the perturbation induced by the system. In stellar-dominated galactic nuclei, the primary mechanism driving further orbital decay becomes three-body interactions between individual stars and the binary (Mikkola & Valtonen, 1992; Quinlan, 1996; Sesana et al., 2006). Initially, dynamical friction and stellar encounters act together, causing a rapid orbital decay, but the process soon transitions into a slower, nearly constant hardening phase. This occurs at the so-called hard binary separation, a_h , defined by the relation (Merritt & Milosavljević, 2005)

$$a_h \equiv \frac{G\mu}{4\sigma^2}, \tag{1.5}$$

where $\mu = (M_1 M_2)/(M_1 + M_2)$ is the reduced mass of the binary and σ the velocity dispersion of the surrounding stellar population. Physically, this marks the point at which the orbital velocity of the MBHB exceeds the characteristic stellar speed, effectively decoupling the binary from the background. As a consequence of repeated three-body interactions, stars are ejected from the galactic nucleus at high velocities, lowering the stellar density within several influence radii (Ebisuzaki et al., 1991; Volonteri et al., 2003; Khan

et al., 2012). This depletion in turn reduces the frequency of subsequent stellar encounters, further slowing the binary's evolution.

1.2.2 The Final-parsec Problem

As soon as the MBH binary becomes hard, the rate at which it shrinks is governed by

$$\frac{d}{dt}\left(\frac{1}{a_{\rm b}}\right) = \frac{G\rho}{\sigma}H, \tag{1.6}$$

where ρ is the density of the stellar background, σ is the velocity dispersion, $a_{\rm b}$ is the binary semi-major axis and H is the hardening rate (a numerical coefficient with typical values of $H \approx 15-20$) which is weakly coupled to the properties of the binary (Mikkola & Valtonen, 1992; Quinlan, 1996; Sesana et al., 2006; Ogiya et al., 2020). For a fixed ρ and σ background, Eq. (1.6) suggests that the shrinking rate would be constant. In reality however, while the binary shrinks, its orbital energy

$$E = -\frac{GM_1M_2}{2a_{\rm b}}, \tag{1.7}$$

is transferred to the surrounding stellar background, either via DF (Begelman et al., 1980; Varisco et al., 2021) or through three-body encounters (Hills 1991). In the latter case, stars are ejected from the nucleus (see also Souvaitzis et al., 2025b, for an application of this process in merging star clusters), carrying away energy and angular momentum, which progressively lowers the stellar density around the MBHB. This mechanism, commonly referred to as *core scouring*, is thought to play a central role in the origin of the shallow cores observed in luminous galaxies (e.g. Rantala et al. 2018).

Equation (1.6) remains valid as long as the MBHB loss cone—the region of phase space containing stars with sufficiently low angular momentum to interact with the binary (see Section 1.2.3) —remains populated. However, during the early stages of the hardening phase, the loss cone is typically depleted within a timescale of a typical stellar orbital period, and continued MBHB shrinking relies critically on mechanisms capable of replenishing it. In principle, two-body relaxation (Yu & Tremaine, 2003) can restore stars to the loss cone, but in the case of typical galactic nuclei with approximately spherical potentials, the corresponding timescale exceeds the Hubble time (Binney & Tremaine, 2008), though it may be short enough in dwarf galaxies hosting low-mass MBHs. This limitation has led to the suggestion that MBHBs may stall at parsec scales, a scenario known as the *final parsec problem*, supported by both theoretical arguments (Begelman et al., 1980) and numerical studies (Makino & Funato, 2004; Berczik et al., 2005).

1.2.3 Loss Cone Dynamics

In galactic nuclei, the loss cone denotes the region of orbital phase space where objects have sufficiently low angular momentum that their pericentre lies within a critical radius

of the central SMBH. For stars, this critical distance is the tidal disruption radius (Hills, 1975a),

$$r_{\rm t} \simeq R_\star \left(\frac{M_\bullet}{m_\star}\right)^{1/3}, \tag{1.8}$$

where $M_\bullet$ is the SMBH mass, and $(m_\star, R_\star)$ are the stellar mass and radius. For compact objects such as stellar-mass or intermediate-mass black holes, disruption does not occur; instead, the relevant boundary is the capture radius, usually approximated by a few Schwarzschild radii (e.g., Merritt et al., 2011; Merritt, 2013; Brem et al., 2014; Hamers et al., 2014),

$$r_{\rm c} \simeq \mathcal{O}(4-10)R_{\rm s}, \quad R_{\rm s} = \frac{2GM_{\rm o}}{c^2}, \tag{1.9}$$

depending on orbital inclination, spin, and relativistic corrections. Orbits that cross $r_{\rm t}$ or $r_{\rm c}$ are effectively lost to the system, resulting in either tidal disruption events (TDEs) or direct plunges/captures. The loss-cone radius $r_{\rm lc}$ is then defined as the larger of $r_{\rm t}$ or $r_{\rm c}$ for a given type of object. An orbit grazing the sphere at $r = r_{\rm lc}$ has angular momentum (Merritt, 2013),

$$L_{\rm lc}^2(E) = 2r_{\rm lc}^2\left[E - \Phi\left(r_{\rm lc}\right)\right] \approx 2GM_\bullet r_{\rm lc}, \tag{1.10}$$

assuming $|E| \ll GM_\bullet/r_{\rm lc}$, i.e., that the star is on an orbit with semi-major axis much greater than $r_{\rm lc}$. Orbits with $L \leq L_{\rm lc}$ are called loss-cone orbits and their phase space ensemble has been named as *loss cone*. The loss cone may also be understood geometrically as the set of velocity vectors, at a distance r from the SMBH, that correspond to orbits with pericentres inside $r_{\rm lc}$ Fig.1.3. In this picture, the star's velocity vector must fall within a cone of half-opening angle $\theta_{\rm lc}$, which is approximately given by

$$\begin{aligned} \theta_{\rm lc} &\approx \left(r_{\rm lc}/r\right)^{1/2}, \quad && r \lesssim r_{\rm h} \\ &\approx \left(r_{\rm lc}r_{\rm h}/r^2\right)^{1/2}, && r \gtrsim r_{\rm h} \end{aligned} \tag{1.11}$$

where $r_{\rm h}$ is the SMBH influence radius given in Eq. (1.4). An alternative definition of the influence radius, applicable to spherical mass distributions, is the radius at which the stellar mass enclosed within a sphere around the SMBH becomes comparable to the hole's mass $M_\bullet$ (Merritt, 2013)

$$M_\star(r < r_{\rm m}) = 2M_\bullet. \tag{1.12}$$

The long-term evolution of binary SMBHs depends critically on the supply of stars into their loss cone—the region of phase space defined by orbits with sufficiently low angular momentum to interact with the binary (Begelman et al., 1980). In spherical galaxies, this reservoir is rapidly depleted on a dynamical timescale, after which replenishment relies solely on two-body relaxation (Milosavljević & Merritt, 2001; Milosavljević & Merritt,

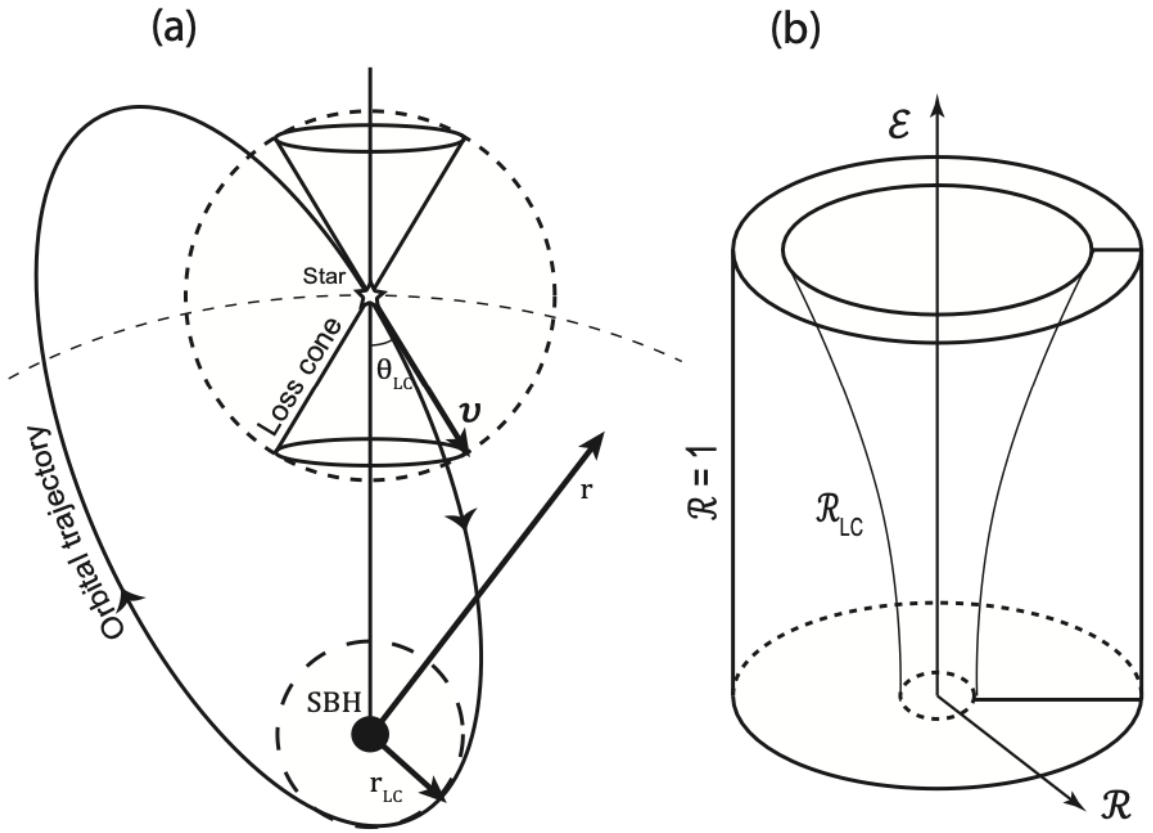

Figure 1.3: Two representations of the loss cone. a) Orbits with velocity vectors that fall within the cone $\theta \leq \theta_{\rm lc}$ will pass within the capture/disruption sphere at $r = r_{\rm lc}$. b) The loss cone in energy-angular-momentum space consists of orbits with $L \leq L_{\rm lc}$. In the E-L space, $\mathcal{E} \equiv -E$ and $\mathcal{R} \equiv L^2/L_c(E)^2$, where $\mathcal{R} = 0$ corresponds to radial orbits and $\mathcal{R} = 1$ to circular ones. Figure credit by Merritt (2013).

2003). Two-body (non-resonant, NR) relaxation arises from uncorrelated, close gravitational encounters. It affects both the energy and angular momentum of stars. This leads to the change of orbital elements on a timescale given by (Rauch & Tremaine, 1996; Hopman & Alexander, 2006),

$$t_{\rm NR} \approx \frac{M_\bullet^2}{m^2 N} P, \tag{1.13}$$

where m is the mass of test star-particle, P its orbital period around the SMBH with semi-major axis a and N the number of stars inside a. Since relaxation operates on timescales much longer than the Hubble time for most galaxies, binaries in spherical systems are effectively in the empty loss-cone regime. This behavior is evident in N-body simulations, where the binary hardening rate scales with N due to the relaxation time

$\propto N/\log N$ (Makino & Funato, 2004; Berczik et al., 2005; Merritt et al., 2007). Collisional processes therefore play only a minor role in real galaxies and are insufficient on their own to drive SMBH binaries to coalescence.

In contrast, non-spherical systems allow for collisionless loss-cone refilling. Torques from axisymmetric or triaxial potentials induce angular momentum diffusion on timescales far shorter than collisional relaxation (Merritt, 2013), enabling stars to reach low-L orbits. Axisymmetric nuclei admit *saucer* orbits, which can attain small pericentres, while triaxial nuclei support *pyramid* orbits that are truly centrophilic and eventually pass arbitrarily close to the SMBH binary (Merritt & Vasiliev, 2010). Even if the fraction of saucer orbits is small, the abundance of pyramid orbits in triaxial systems suggests that collisionless mechanisms can efficiently sustain the loss cone, allowing binaries to overcome stalling and progress to coalescence (Norman & Silk, 1983; Merritt & Poon, 2004).

There is no final-parsec problem

Over the past decades, it has become clear that the so-called final parsec problem arises only in perfectly spherical, idealized galaxies, where stellar orbits conserve all angular momentum components and the loss cone cannot be efficiently refilled. In more realistic triaxial systems, however, torques from the asymmetric potential break angular momentum conservation, allowing stars to diffuse into the loss cone collisionlessly (Yu & Tremaine, 2002; Merritt & Poon, 2004; Merritt & Vasiliev, 2010). Numerical simulations confirmed that MBHBs in triaxial nuclei—naturally produced in galaxy mergers—can coalesce rapidly through stellar interactions alone (Berczik et al., 2005; Khan et al., 2012; Preto et al., 2011).

Subsequent work generalized these results to a broad range of binary mass ratios, density profiles, and merger orbits, showing that binaries in realistic merger remnants efficiently reach the GW-driven regime without stalling (Khan et al., 2012; Vasiliev et al., 2015; Sesana & Khan, 2015; Khan et al., 2016; Gualandris et al., 2017; Bortolas et al., 2017). The consensus is that stellar hardening alone suffices to drive coalescence, although the precise timescale depends on the details of the stellar density distribution and the binary's eccentricity evolution.

1.3 Hardening in Gas-rich Environments

Following the MBHB formation from kpc down to pc scales discussion from the above, I now focus on their orbital evolution in gas-rich nuclei. A first gas-related effect, relevant even at small separations, concerns accretion onto the MBHs. In the limiting case where the inflowing material has negligible angular momentum, the accretion proceeds in a purely radial fashion, resembling Bondi–Hoyle–Lyttleton accretion (hereafter Bondi Hoyle & Lyttleton, 1939; Bondi & Hoyle, 1944; Bondi, 1952). Accretion of this type onto binaries has been investigated in a number of studies (Farris et al., 2010; Giacomazzo et al., 2012; Kelly et al., 2017; Antoni et al., 2019; Comerford et al., 2019). These works generally find that the inspiral timescale induced by the wakes generated in the gas remains of the same

order as the standard Bondi drag timescale for a single compact object, differing only by a factor of a few within the explored parameter ranges.

On galactic scales, however, gas is expected to carry substantial angular momentum, typically far exceeding that associated with the innermost stable circular orbit (ISCO) of the MBHs. For gas to flow from kpc to sub-pc scales, significant angular momentum transport must occur. Since some residual angular momentum is likely to persist at small radii, the natural outcome is the formation of a circumbinary disc around the MBHB, analogous to an accretion disc in the case of a single SMBH.

1.3.1 Circumbinary Discs

The properties and long-term evolution of circumbinary discs around MBHBs remain an active area of research, as large-scale simulations capable of simultaneously resolving galactic inflows and the small-scale structure of the disc are still limited (but see Souza Lima et al., 2020). To overcome this, a number of idealized studies have investigated circumbinary disc formation and dynamics by modelling the impact of gas clouds onto MBHBs (Goicovic et al., 2015, 2017, 2018; Maureira-Fredes et al., 2018), demonstrating that disc properties are highly sensitive to the angular momentum and dynamics of the infalling gas. At sufficiently small separations, the binary exerts strong gravitational torques on the surrounding material, opening either an annular gap or a central cavity depending on the mass ratio (MacFadyen & Milosavljević, 2008; D'Orazio et al., 2016). Early studies suggested that such cavities would halt accretion, but more recent high-resolution simulations have shown that gas continues to stream through the cavity edges, sustaining accretion onto the MBHs in a variable and asymmetric fashion (Farris et al., 2014; D'Orazio et al., 2016; Souza Lima et al., 2020).

Once the disc mass enclosed within the binary orbit becomes negligible compared to the MBHB mass, the system enters a regime where the disc is gravitationally stable and drives binary hardening on a timescale comparable to the viscous timescale, analogous to Type II migration in planetary systems (Ward, 1997; Goodman, 2003; Gold et al., 2014). The viscous timescale is defined as the characteristic time for disc material to drift radially under the action of viscous stresses (Frank et al., 2002),

$$t_\nu \sim \frac{r}{|v_r|} \simeq \frac{2}{3}\frac{r^2}{\nu}, \tag{1.14}$$

where ν is the effective kinematic viscosity. Using the α-prescription, $\nu = \alpha c_\mathrm{s} H$, this can be expressed as

$$t_\nu \simeq \frac{2}{3\alpha\Omega}\left(\frac{r}{H}\right)^2, \tag{1.15}$$

with Ω being the Keplerian angular velocity, c_s the sound speed and H the disc scale height. For example, in a Shakura–Sunyaev disc (Shakura & Sunyaev, 1976) with $H/R \approx 0.05$ and $\alpha = 0.1$, the viscous timescale at $r = 1000\,R_\mathrm{s}$ around a $10^6\,M_\odot$ SMBH is of order $t_\nu \sim 10^5\,\mathrm{yr}$.

The efficiency of this process depends sensitively on the binary mass ratio and disc properties. For nearly equal-mass binaries, disc-driven migration may stall once the cavity becomes too large to refill before gravitational-wave (GW) emission takes over, whereas for unequal-mass binaries, the ratio between the secondary mass and the enclosed disc mass ($q_{2,\rm disc}$) becomes critical in setting whether migration proceeds at the viscous rate or slows down (Lodato et al., 2009; Haiman et al., 2009). Importantly, the sign and strength of gas torques are highly sensitive to disc thermodynamics: while thick, hot discs (high H/R) can cause binaries to outspiral (Tang et al., 2017; Moody et al., 2019; Muñoz et al., 2019, 2020), thinner, cooler discs—closer to AGN conditions—tend to promote inspiral instead (Duffell et al., 2020; Tiede & D'Orazio, 2024; Heath & Nixon, 2020; Franchini et al., 2022).

Dynamical interactions with the surrounding gas also play a central role in shaping the orbital eccentricity of the binary. Analytical studies show that Lindblad resonances generally excite eccentricity, whereas co-rotation resonances act to circularize the orbit (Goldreich & Tremaine, 1980; Artymowicz et al., 1991). The balance between these competing effects depends strongly on the binary mass ratio: for $q_{\rm b} \gtrsim 0.2$ and initially circular orbits, (Artymowicz, 1992; Lubow, 1992) found that binaries tend to evolve toward moderate eccentricities of $e_{\rm b} \sim 0.5$. More recent hydrodynamical simulations confirm this trend, showing that equal-mass binaries reach an *equilibrium* (or *attractor*) eccentricity of $e_{\rm b,eq} \simeq 0.45$ (Zrake et al., 2021; D'Orazio & Duffell, 2021). This behavior is illustrated in Fig. 1.4, which shows the time-averaged evolution of the semi-major axis and eccentricity for a wide range of binary and disc parameters from the 2D simulations of (Siwek et al., 2023b). In particular, binaries with $e_{\rm b} \lesssim 0.5$ tend to increase their eccentricity, while those with $e_{\rm b} \gtrsim 0.5$ circularize, converging toward the equilibrium value.

A precise understanding of this gas-driven phase is crucial for predicting MBHB properties at the point of GW decoupling and their potential detection for example by LISA. The binary–disc decoupling radius is typically defined by equating the viscous timescale of the disc with the GW inspiral timescale, implying that gas interactions may influence residual eccentricities at the mHz regime (Cuadra et al., 2009; Roedig et al., 2011; Roedig & Sesana, 2014; Muñoz et al., 2019). However, fully relativistic MHD simulations suggest that gas may continue accreting onto the binary up to merger, challenging the notion of a clean decoupling (Farris et al., 2012; Gold et al., 2014; Khan et al., 2018). Significant uncertainties remain, as current simulations are often idealized (e.g. 2D treatments, simplified thermodynamics, neglect of radiative feedback, or absence of self-gravity), underscoring the need for more realistic theoretical models.

Formation of circumstellar mini-discs

Gas that crosses the circumbinary cavity can form mini-discs around each MBH (see Fig. 1.1). Their survival depends on the thermal state of the circumbinary disc: colder, thinner discs yield less massive, short-lived mini-discs, while hotter, thicker discs produce more persistent ones (Ragusa et al., 2016). Although typically of low mass (Chang et al., 2010; Tazzari & Lodato, 2015; Fontecilla et al., 2017), mini-discs regulate accretion and spin evolution (Bourne et al., 2024) and can influence binary migration. 2D simulations

$\dot{a}_b/a_b\,[\dot{M}_b/M_b]$, $g + a$

	$e_b = 0.0$	$e_b = 0.1$	$e_b = 0.2$	$e_b = 0.3$	$e_b = 0.4$	$e_b = 0.5$	$e_b = 0.6$	$e_b = 0.8$
$q_b = 0.1$	-1.28	-5.06	1.03	3.43	3.74	4.0	3.0	-6.32
$q_b = 0.2$	-0.77	-1.51	-0.16	0.92	2.87	2.59	-1.3	-7.09
$q_b = 0.3$	1.15	-2.05	-1.89	-0.19	-1.44	-0.93	-2.34	-3.49
$q_b = 0.4$	1.29	-1.3	-0.65	-2.41	-2.5	-2.93	-1.48	-3.61
$q_b = 0.5$	1.43	-0.69	-0.15	-2.43	-2.1	-3.73	-1.26	-3.52
$q_b = 0.6$	1.58	-0.69	-0.42	-2.37	-2.96	-4.33	-0.3	-2.73
$q_b = 0.7$	1.67	-0.75	-0.46	-2.38	-5.16	-4.36	0.28	-2.85
$q_b = 0.8$	1.72	-0.94	-0.67	-2.52	-6.23	-0.28	0.52	-3.0
$q_b = 0.9$	1.74	-0.88	-1.02	-4.15	-6.23	0.86	0.47	-2.89
$q_b = 1.0$	1.76	-0.95	-1.31	-4.79	-6.1	0.6	0.38	-2.74

$\dot{e}_b\,[\dot{M}_b/M_b]$, $g + a$

	$e_b = 0.0$	$e_b = 0.1$	$e_b = 0.2$	$e_b = 0.3$	$e_b = 0.4$	$e_b = 0.5$	$e_b = 0.6$	$e_b = 0.8$
$q_b = 0.1$	0.0	1.55	0.78	-1.84	-4.15	-4.78	-5.95	-7.7
$q_b = 0.2$	0.0	1.32	2.14	0.16	-2.02	-3.96	-4.62	-5.47
$q_b = 0.3$	0.0	3.73	5.59	0.23	-0.4	-2.73	-3.95	-3.46
$q_b = 0.4$	0.0	4.29	3.5	2.52	0.23	-1.64	-2.81	-2.61
$q_b = 0.5$	-0.0	4.33	3.75	3.38	1.33	-1.82	-2.37	-2.15
$q_b = 0.6$	0.0	4.73	4.9	4.52	3.33	-0.04	-2.2	-1.96
$q_b = 0.7$	0.0	4.88	5.48	5.26	5.6	0.58	-2.14	-1.86
$q_b = 0.8$	-0.0	5.28	5.95	5.97	6.48	-1.15	-2.08	-1.7
$q_b = 0.9$	-0.0	5.16	6.6	8.33	7.02	-1.83	-2.12	-1.69
$q_b = 1.0$	0.0	5.33	7.07	9.43	6.91	-1.67	-2.11	-1.85

Figure 1.4: Orbital evolution of binaries embedded in circumbinary discs across a wide parameter space, from 2D simulations by Siwek et al. (2023b). **Top panel:** Time-averaged evolution of the semi-major axis a_b. Red regions indicate orbital expansion, while blue denotes orbital contraction. Circular, low-mass-ratio binaries tend to expand, whereas more eccentric systems generally shrink. **Bottom panel:** Time-averaged eccentricity evolution $\dot{e}_b$. Red corresponds to eccentricity growth, blue to circularization. The results reveal a clear trend toward an equilibrium (or attractor) eccentricity of $e_{b,eq} \simeq 0.45$, consistent with previous studies.

suggest that torques are dominated by gas near mini-disc edges, making results sensitive to their numerical treatment, including sink prescriptions and boundary conditions (Tang et al., 2017; Muñoz et al., 2019; Moody et al., 2019; Tiede et al., 2020). Their dynamical importance has been confirmed in 3D simulations (Franchini et al., 2022), underscoring the need for systematic studies of mini-disc modeling.

Relativistic simulations, however, have yielded more mixed results. GRMHD studies often fail to find persistent mini-discs (Noble et al., 2012; Farris et al., 2012; Gold et al., 2014; Khan et al., 2018). Bowen et al. (2017); Bowen et al. (2018), who began with

mini-discs in place, reported structures that survive but undergo cycles of depletion and replenishment. Gold et al. (2014) argued that at small separations the ISCO around each MBH exceeds its Hill sphere, so bound material is rapidly accreted, a scenario confirmed in recent full GR simulations (Paschalidis et al., 2021). Despite advances, the role of mini-discs in regulating accretion, spin alignment, and orbital migration remains uncertain, requiring more realistic modeling to fully capture their impact on MBHB evolution.

1.3.2 AGN Feedback

AGN feedback—i.e., the injection of energy from accreting MBHs—can significantly influence the hardening phase of a binary, regardless of the dominant migration mechanism. For binaries embedded in circumbinary discs, this effect has been studied via smooth-particle-hydrodynamics (SPH) simulations only at relatively large separations (parsec scales) by del Valle & Volonteri (2018). They explored two evolutionary regimes: in the "gap" regime, viscous torques are inefficient and a low-density cavity is carved, so accretion is suppressed and feedback outflows escape through the cavity without strongly impacting orbital evolution; in the "no-gap" regime, effective angular momentum transport allows dense gas to feed the MBHs, enabling winds that disrupt the disc, carve a "feedback gap," and stall binary migration. Although these simulations assumed isotropic feedback, real outflows may be collimated or anisotropic, potentially altering this picture and producing observable signatures. More recently, Bollati et al. (2024) investigated how AGN radiative feedback limits gas inflow onto MBHs, finding that such feedback can regulate accretion and suppress inflow on sub-galactic scales, which may further complicate the gas–binary coupling in dense environments.

In cases where stellar hardening dominates, the role of AGN feedback remains largely unexplored. One might expect that injecting thermal or kinetic energy has minimal immediate effect on the orbits of existing stars, but could hinder the formation of new stars capable of replenishing the loss cone. If new star formation is suppressed in a gas-rich nucleus, this could slow down or stall further binary evolution in a mixed environment where both stars and gas contribute (Liao et al., 2024). In gas-poor systems, this effect is likely negligible, but in gas-rich contexts, AGN feedback may play a nontrivial role in modulating binary decay.

1.4 Triple and Multiple Massive Black Holes

The high-redshift Universe provides a fertile environment for the formation of multiple massive black holes (MBHs), as frequent halo interactions and galaxy mergers lead to complex dynamical systems. Observational evidence, such as the Jackpot nebula at $z \sim 2$, which hosts several AGN within a 400 kpc Ly-α nebula, illustrates the prevalence of such environments (Hennawi et al., 2015). Mergers between galaxies can deposit several MBHs into the same halo, with the possibility of either bound MBH binaries or, if binary formation fails, wandering MBHs that temporarily coexist in the same system (Pfister et al., 2019).

These failures influence the merger rate across redshift, mass, and mass ratio (Klein et al., 2016; Bonetti et al., 2016; Barausse et al., 2020). As a result, MBH triplets or even higher-order multiplets can naturally emerge, introducing a richer landscape of few-body dynamics (Mikkola & Valtonen, 1990; Heinämäki, 2001; Blaes et al., 2002; Hoffman & Loeb, 2007; Amaro-Seoane et al., 2010; Kulkarni & Loeb, 2012; Rantala et al., 2017; Ryu et al., 2017c; Bonetti et al., 2019; Mannerkoski et al., 2021).

MBH triplets typically begin as hierarchical systems, composed of an inner binary and an intruder MBH on a wider orbit. These systems may undergo von Zeipel–Kozai-Lidov (ZKL) oscillations (von Zeipel, 1910; Kozai, 1962; Lidov, 1962), where angular momentum exchanges drive the inner binary to high eccentricity, enhancing GW emission (Ford et al., 2000; Naoz, 2016; Lim & Rodriguez, 2020). Relativistic or apsidal precession can, however, quench these oscillations (Bonetti et al., 2016), suppressing eccentricity growth. Intriguingly, the orbital decay of the intruder MBH, driven by interactions with the galactic background, can re-strengthen the ZKL mechanism, further shortening oscillation timescales and potentially leading to coalescence (Bonetti et al., 2018). Yet, in many configurations, secular evolution alone does not trigger mergers—insufficient mutual inclination, low perturber mass, or wide binaries can inhibit GW-driven inspirals. In such cases, the system often transitions to dynamical instability once the intruder approaches closely, entering a chaotic regime of strong encounters, exchanges, and ejections (Mikkola & Valtonen, 1990).

The outcomes of this chaotic evolution are diverse. An ejected MBH may wander within the galaxy, or it may return on a bound trajectory to perturb the binary further, possibly triggering a merger after repeated interactions. Over cosmic timescales, additional galaxy mergers can introduce further MBHs, leading to quadruplets (e.g., Herwig et al., 2025) or higher-order multiplets (Ryu et al., 2017c). For example, the merger of two galaxies hosting MBH binaries can initially resemble a triplet before the full four-body dynamics emerge, resulting in highly stochastic evolution. Such multiplet dynamics often drive binaries to very high eccentricities, a potential observational signature that can persist well into the GW-driven phase (Bonetti et al., 2019). Ultimately, the complex interplay between secular mechanisms, chaotic encounters, and environmental influences renders MBH triplet and multiplet dynamics a critical—and highly non-linear—pathway toward MBH coalescence in the Universe.

1.5 Final stage: Gravitational Wave Driven Coalescence

As the MBHB continues to interact efficiently with its surrounding environment, losing energy and angular momentum through stellar and gas-driven processes (e.g. Hills, 1991), the binary is gradually driven to sub-pc and eventually mpc separations. At these scales, the evolution becomes dominated by the emission of gravitational radiation. In this relativistic regime, the dynamics are governed primarily by the MBH masses and spins, together with the binary's separation and eccentricity.

1.5.1 Post-Newtonian Dynamics

General-relativistic effects influence the orbital evolution of a MBH binary already in the previous stage (e.g. the hardening phase), but taking them into account at short separations ($\sim$ mpc) becomes a necessity (Will, 2006; Poisson & Will, 2014). The post-Newtonian (PN) formalism provides a perturbative expansion of Einstein's field equations in the regime of weak gravitational fields and relatively low velocities. Within this framework, relativistic corrections—originally encoded in the full geodesic equations—are systematically incorporated as higher-order terms beyond Newtonian gravity. For a system with characteristic velocity v, total mass M, and length scale R, the expansion is governed by a dimensionless small parameter ϵ that quantifies the departure from the Newtonian limit,

$$\epsilon \sim \left(\frac{v}{c}\right)^2 \sim \left(\frac{GM}{c^2 R}\right), \tag{1.16}$$

where G is Newton's gravitational constant and c is the speed of light. In the limit $\epsilon \to 0$, one recovers Newtonian gravity, while $\epsilon \sim 1$ marks the onset of the strong-field regime. Each PN correction is denoted such that its contribution to the acceleration scales with a power of ϵ,

$$|\boldsymbol{a}_{i\mathrm{PN}}| \propto \epsilon^i \sim \left(\frac{v}{c}\right)^{2i} \sim \left(\frac{R_s}{R}\right)^i, \tag{1.17}$$

where v and R denote the relative velocity and separation between two BH particles, and $R_\mathrm{s} = 2GM/c^2$ is the Schwarzschild radius of a binary of mass M. The total PN-corrected acceleration can then be expressed as

$$\boldsymbol{a} = \boldsymbol{a}\mathrm{N} + \boldsymbol{a}\mathrm{PN1} + \boldsymbol{a}\mathrm{PN2} + \boldsymbol{a}\mathrm{PN3} + \boldsymbol{a}\mathrm{PN2.5} + \boldsymbol{a}\mathrm{PN3.5} + ..., \tag{1.18}$$

where $\boldsymbol{a}_\mathrm{N}$ is the Newtonian term, and the PN contributions arise exclusively from BH interactions. Integer-order PN terms are *conservative*, associated with corrections to energy and angular momentum conservation, whereas half-integer orders represent *dissipative* contributions, corresponding to radiation reaction due to GW emission.

The PN corrections—and consequently the associated gravitational-wave (GW) emission—remain negligible when the binary separation is of the order $a \sim a_\mathrm{h}$ (see Eq. (1.5)). The dissipative PN terms, which describe radiative losses, begin to dominate the orbital evolution only once the separation decreases to $a \sim a_\mathrm{GW} \sim 0.01 \times a_\mathrm{h}$ (e.g., Quinlan, 1996; Sesana et al., 2006; Rantala et al., 2018). For equal-mass binaries with individual MBH masses of $M_\mathrm{BH} \sim 10^6$–$10^7, M_\odot$, this corresponds to a characteristic physical scale of $a_\mathrm{GW} \sim 10^{-4}$–$10^{-3}$, pc, with proportionally smaller separations required for lower-mass MBHs.

Nonetheless, a gaseous component may remain coupled to the binary nearly down to coalescence, implying that gas can still influence the dynamics even during the GW-driven stage (see Section 1.3, Farris et al., 2014; Tang et al., 2018). More recently, Zwick et al. (2020) presented a systematic attempt to quantify the interplay between environmental

perturbations (e.g. gas dynamical friction and torques) and PN effects, deriving simple analytic criteria that delineate the regions of phase space where the two contributions become comparable.

1.5.2 Gravitational-Wave-Driven Inspiral

If the evolution of an MBHB is assumed to be driven solely by GW emission, the secular evolution of its Keplerian orbital parameters can be approximated to leading order following the seminal treatment by (Peters, 1964). The orbital period scales as

$$t_{\rm orb} \sim \left(\frac{a}{r_g}\right)^{3/2}, \tag{1.19}$$

where a is the semi-major axis and $r_g = GM/c^2$ is the gravitational radius. By contrast, the radiation-reaction timescale scales as

$$t_{\rm rad} \sim \left(\frac{a}{r_g}\right)^{4}. \tag{1.20}$$

Since $a \gg r_g$ for astrophysical binaries, the inequality $t_{\rm orb} \ll t_{\rm rad}$ holds, meaning that the system is approximately Keplerian, with orbital parameters a and e evolving slowly under GW backreaction.

Averaging over one orbital period, the secular evolution of the semi-major axis is given by (Peters & Mathews, 1963; Peters, 1964):

$$\left\langle \frac{da}{dt} \right\rangle_{\rm GW} = -\frac{64}{5}\frac{G^3 m_1 m_2 M}{c^5 a^3 \left(1-e^2\right)^{7/2}}\left(1+\frac{73}{24}e^2+\frac{37}{96}e^4\right) = -\frac{64}{5}\frac{G^3 m_1 m_2 M}{c^5 a^3} f(e), \tag{1.21}$$

where m_1, m_2, and $M = m_1 + m_2$ denote the component and total masses of the binary, and

$$f(e) = \left(1+\frac{73}{24}e^2+\frac{37}{96}e^4\right)\left(1-e^2\right)^{-7/2} \tag{1.22}$$

is the eccentricity enhancement function. The eccentricity itself evolves as

$$\left\langle \frac{de}{dt} \right\rangle_{\rm GW} = -\frac{304}{15}\frac{G^3 m_1 m_2 M}{c^5 a^4 \left(1-e^2\right)^{5/2}} e \left(1+\frac{121}{304}e^2\right). \tag{1.23}$$

The negative sign in both equations ensures that both a and e decrease monotonically, yielding a binary that becomes progressively tighter and more circular. In the limit $e \ll 1$, Eqs.(1.21)-(1.23) imply that eccentricity decays more rapidly than semi-major axis, leading to efficient circularization unless the initial eccentricity is extremely high. A key caveat is that when PN corrections up to a given order (e.g., 3.5PN) are included, the Keplerian

elements cease to be constants of motion: they oscillate over the orbit, particularly near pericentre passages of eccentric binaries (e.g., Will, 2006; Memmesheimer et al., 2004; Mannerkoski et al., 2019). Furthermore, if the MBHs are spinning, both the magnitude and orientation of the spins affect the dynamics and the emitted GWs, introducing additional modulations and precession effects (Cutler & Flanagan, 1994; Apostolatos et al., 1994; Kidder, 1995; Kesden et al., 2015; Gerosa et al., 2015).

Although the PN expansion accurately describes inspiral down to separations of order $a \sim 6r_g$, at smaller distances the strong-field regime renders the perturbative approach unreliable. In this domain, fully non-linear general relativistic simulations are required to capture the dynamics (e.g., Pretorius, 2005; Campanelli et al., 2006; Baker et al., 2006).

Time to Coalescence

For a binary entering the GW-driven phase with initial orbital parameters (a_0, e_0), one can estimate the time it will take to merge. A precise answer requires numerical integration of Eqs.(1.21)-(1.23). Nevertheless, for mildly eccentric binaries, a widely used analytical estimate is the so-called Peters' time-scale (Peters, 1964):

$$t_P = \frac{5c^5(1+q)^2}{256G^3M^3q}a_0^4 f\left(e_0\right) \approx 0.32\frac{(1+q)^2}{qf\left(e_0\right)}\left(\frac{a_0}{\mathrm{AU}}\right)^4\left(\frac{M}{10^6M_\odot}\right)^{-3}\mathrm{yr}, \tag{1.24}$$

where $q = m_2/m_1$ is the mass ratio, a_0 and e_0 are the initial semi-major axis and eccentricity, respectively, and $f(e_0)$ is the eccentricity enhancement function introduced in Eq. (1.21). The interpretation is intuitive: more massive and compact binaries decay faster, and for a given semi-major axis, highly eccentric binaries coalesce more rapidly because the MBHs approach closer at pericentre, maximizing GW energy loss.

Due to its simplicity, Peters' formula is commonly used for order-of-magnitude estimates of GW-driven decay, and has been applied throughout previous sections to compare GW-induced evolution against other processes affecting the binary orbit. However, it has two key limitations. First, it provides only a lower bound and can underestimate the merger time by a factor of $\sim$ 1–8 (Peters & Mathews, 1963). Second, the derivation assumes a purely Keplerian orbit and quadrupole GW emission, which are valid only at lowest PN order.

More accurate corrections accounting for relativistic effects have been developed. Zwick et al. (2020) provided first-order PN corrections, while Zwick et al. (2021) included spin-dependent modifications for highly eccentric binaries. The corrected time-scale reads:

$$t_{\rm PN}\left(a_0, e_0, s_1\right) = \frac{5c^5(1+q)^2}{256G^3M^3q}a_0^4 f\left(e_0\right)\underbrace{R\left(e_0\right)\exp\left[2.8\frac{r_S}{p_0} + \frac{s_1}{0.3}\frac{r_S}{p_0} + |s_1|^{3/2}\left(1.1\frac{r_S}{p_0}\right)^{5/2}\right]}_{\text{eccentricity, spin, and PN correction}} \tag{1.25}$$

where $p_0 = a_0(1-e_0)$, $r_S = 2GM/c^2$ is the Schwarzschild radius, $R(e_0) = 8/(1-\sqrt{1-e_0})$, and $s_1 = S_1\cos\theta$, with S_1 being the spin magnitude of the primary MBH and

θ the angle between its spin vector and the orbital angular momentum. Adopting these more accurate GW time-scales is particularly important for studies of MBHB dynamics and merger rates relevant for LISA observations.

1.5.3 Gravitational Wave Recoil from Massive Black Hole Binaries

At coalescence, gravitational waves carry away not only energy and angular momentum but also linear momentum (Bonnor & Rotenberg, 1961; Peres, 1962; Bekenstein, 1973), imparting a recoil ("kick") to the merger remnant. The recoil depends on the binary's mass ratio, spins, and eccentricity, and is strongly peaked during the final orbits (Brügmann et al., 2008; Gerosa et al., 2018). While PN estimates exist (Fitchett, 1983; Kidder, 1995; Blanchet et al., 2005), accurate modeling requires numerical relativity (Campanelli et al., 2007a; González et al., 2007; Lousto & Zlochower, 2011). Simulations show that "superkicks" can reach $\sim 5000, \mathrm{km}, \mathrm{s}^{-1}$, with several fitting formulae and surrogate models available to interpolate across parameter space (Campanelli et al., 2007b; González et al., 2007; Lousto & Zlochower, 2008; Varma et al., 2019).

Recoils of $\sim 10^3, \mathrm{km}, \mathrm{s}^{-1}$ may eject remnants from their host galaxies (Redmount & Rees, 1989; Merritt & Poon, 2004; Gerosa & Sesana, 2014), with far-reaching astrophysical implications: altering MBH–galaxy scaling relations, suppressing MBH growth in low-mass galaxies, producing wandering MBHs and AGN, and hindering the early assembly of $> 10^9 M_\odot$ SMBHs (Haiman, 2004; Boylan-Kolchin et al., 2004; Volonteri, 2007; Blecha et al., 2011; Dunn et al., 2020; Rawlings et al., 2025). Spin alignment driven by gas can mitigate recoil velocities (Schnittman & Buonanno, 2007; Bogdanović et al., 2007; Berti et al., 2012), making environmental coupling crucial for predicting the impact on LISA event rates. Recoils may also yield electromagnetic counterparts, such as off-nuclear AGN with displaced broad emission lines (Komossa, 2012; Blecha & Loeb, 2008; Civano et al., 2012; Koss et al., 2014), though candidate identifications remain challenging.

Finally, recoiling remnants can leave GW signatures, including Doppler shifts between inspiral and ringdown, distinctive higher-mode content, and correlations with spin orientations, all potentially observable by LISA

1.6 Observational Evidence of Massive Black Hole Binaries

1.6.1 Dual AGN

Dual AGN are systems hosting two actively accreting supermassive black holes (SMBHs) in merging galaxies, typically separated by less than 30kpc before becoming gravitationally bound. They are identified using multi-wavelength techniques, with early searches relying on optical spectroscopy to detect double-peaked narrow emission lines (e.g. [O III] λ5007), which can indicate two distinct narrow-line regions (Zhou et al., 2004; Comerford et al.,

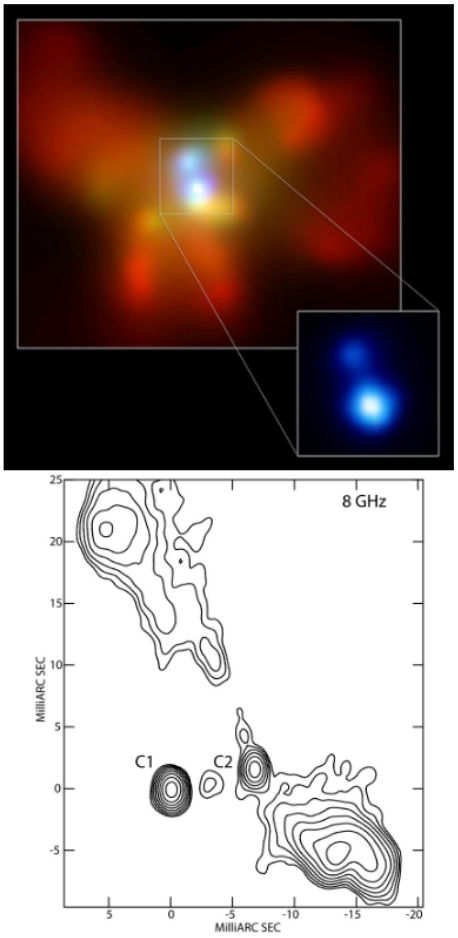

Figure 1.5: Directly resolved dual AGN systems. **Top:** Chandra X-ray observations of the merger remnant NGC 6240, showing soft-band (0.5–1.5 $\sim$ keV, reddish) and hard-band (5–8 $\sim$ keV, bluish) emission. The detection of two distinct X-ray cores confirms the presence of two active SMBHs with a projected separation of $\sim$1 kpc (Komossa et al., 2003). **Bottom:** 8 $\sim$ GHz VLBA radio map of the galaxy $0402+379$ (Rodriguez et al., 2006), revealing two compact radio cores separated by only $\sim$ 7pc. The fainter component is associated with a radio jet, confirming one of the closest known dual AGN.

2009). However, such features can also arise from alternative mechanisms like bipolar outflows or rotating disks, requiring spatially resolved confirmation of each nucleus.

High-resolution imaging—particularly in radio wavelengths—provides the most direct confirmation of dual AGN, resolving compact radio cores at parsec scales (Rodriguez et al., 2006; Bansal et al., 2017). The tightest known dual AGN candidate shown in Fig. 1.5, $0402+379$, has a projected separation of only $\sim$ 7pc Yet, radio identification is limited to systems where both AGN are radio-bright ($\sim$ 15% of all AGN) and exhibit compact, flat-spectrum cores. Additional infrared observations are often needed to distinguish true

dual AGN from starburst regions, which can mimic AGN-like compactness and emission properties.

Optical band

Optical surveys have identified numerous dual AGN candidates across a wide redshift range, including tens at $z > 1$ (e.g., Hennawi et al., 2006; Myers et al., 2008; Kayo & Oguri, 2012; Eftekharzadeh et al., 2017), and even up to $z > 5$ using recent spectroscopic and photometric campaigns (Yue et al., 2023). At lower redshifts ($0.2 < z < 2.5$), Stemo et al. (2021) analyzed 2585 AGN host galaxies with *HST*, identifying 204 offset or dual AGN candidates based on multiple stellar bulges. New high-precision astrometric techniques, such as *Gaia*-based varstrometry (Shen et al., 2019; Hwang et al., 2020; Shen et al., 2021), exploit uncorrelated flux variability between unresolved SMBH pairs to detect positional shifts. These methods have revealed a confirmed dual AGN at $z > 2$ (Chen et al., 2023) and additional candidates at $z > 1$ through the Gaia Multi-peak (GMP) approach (Mannucci et al., 2022; Ciurlo et al., 2020).

X-ray band

Optical searches for dual AGN are often limited by extinction and contamination from star formation, particularly in highly obscured mergers (e.g., Kocevski et al., 2015; Koss et al., 2016; Ricci et al., 2017; Blecha et al., 2018). X-ray observations, especially with *Chandra*, provide more reliable confirmation by penetrating dense gas and resolving closely separated nuclei, as in *NGC* 6240 (Komossa et al., 2003). To date, fewer than 50 X-ray–confirmed dual AGN are known (Chen et al., 2022), mostly in the local universe ($z < 0.1$), since high-redshift ($z > 0.1$) surveys are limited by *Chandra*'s small field of view and sensitivity (Sandoval et al., 2023).

Dual AGN fraction

Predictions of the dual AGN fraction at high redshift primarily come from cosmological simulations (e.g., Steinborn et al., 2016; Rosas-Guevara et al., 2019; Volonteri et al., 2022; Chen et al., 2023), but observed fractions remain poorly constrained and generally higher than simulations suggest (e.g., Koss et al., 2012; Barrows et al., 2017). Optical surveys have provided some constraints: Silverman et al. (2020) identified ∼100 dual AGN candidates out to $z = 4.5$ using the Subaru HSC, with no evidence of redshift evolution, while Shen et al. (2023) analyzed 60 Gaia-resolved double quasars at $z < 1.5$ and found a similar lack of evolution. X-ray studies at higher redshift remain limited; Sandoval et al. (2023) find no dual AGN detections among 66 AGN at $2.5 < z < 3.5$, implying an upper limit of $\sim 4\%$ for the dual AGN fraction at $z \sim 3$.

1.6.2 Sub-parsec Massive Black Hole Binaries

At sub-parsec separations, we approach the regime where gravitational radiation dominates the inspiral of binary SMBHs. Despite decades of observational efforts, no sub-parsec binary SMBHs have yet been unambiguously confirmed. The closest known candidate, often cited as the most promising case of a compact binary, has a projected separation of ∼7 pc and was discussed above Fig. 1.5.

Optical techniques

Optical searches for sub-parsec SMBH binaries have primarily relied on two indirect techniques: detecting quasi-periodic variability in AGN light curves and identifying velocity shifts in broad optical emission lines. Searches for periodic or repeating optical variability (e.g., Graham et al., 2015; Charisi et al., 2016) have uncovered numerous candidate systems, but their interpretation is limited by short observational baselines (sampling only ∼ 1.5–3 orbital cycles) and contamination from red-noise variability, with inferred binary rates exceeding gravitational-wave background limits (Sesana et al., 2018). Spectroscopic searches for velocity offsets between broad and narrow emission lines—first systematic in SDSS data (Boroson & Lauer, 2009; Eracleous et al., 2012)—have yielded few robust candidates: only 3 of 88 sources remain viable after a decade of monitoring. Broader multi-epoch studies (e.g., Ju et al., 2013; Wang et al., 2017) have shown that stochastic "velocity flickering" in single AGN can mimic orbital motion. However, future large time-domain surveys, such as SDSS-V (Fries et al., 2023) and LSST (Ivezić et al., 2019), promise significant progress by statistically characterizing AGN variability and enabling long-baseline, high-cadence searches for coherent periodicity or velocity trends—potentially identifying sub-parsec binaries and providing electromagnetic counterparts to LISA detections (Xin & Haiman, 2024; Cocchiararo et al., 2024).

Dual jets

High-resolution radio observations have revealed that precessing or oscillating AGN jets can serve as indirect indicators of binary SMBHs. Jet precession may arise from either binary-induced perturbations of a misaligned accretion disc or from *Lense–Thirring* (Lense & Thirring, 1918; Thirring, 1918) precession around a single spinning SMBH. Among the strongest candidates, OJ287 exhibits an ∼ 11-year optical periodicity and a corresponding ∼ 22–23-year radio jet precession cycle (Britzen et al., 2018), consistent with a binary system in which the smaller black hole crosses the accretion disc of the primary twice per orbit. This model links optical outbursts, jet precession, and Doppler-boosted radio variability, with recent VLBI and ALMA imaging showing jet structures consistent with precession (Zhao et al., 2022). The spectral energy distribution of OJ287 also varies with precession phase, reinforcing the connection between jet orientation and observed emission (Britzen et al., 2021). Similar binary-induced jet signatures are seen in $0402 + 379$, where the jet structure reflects the orbital motion of a SMBH pair.

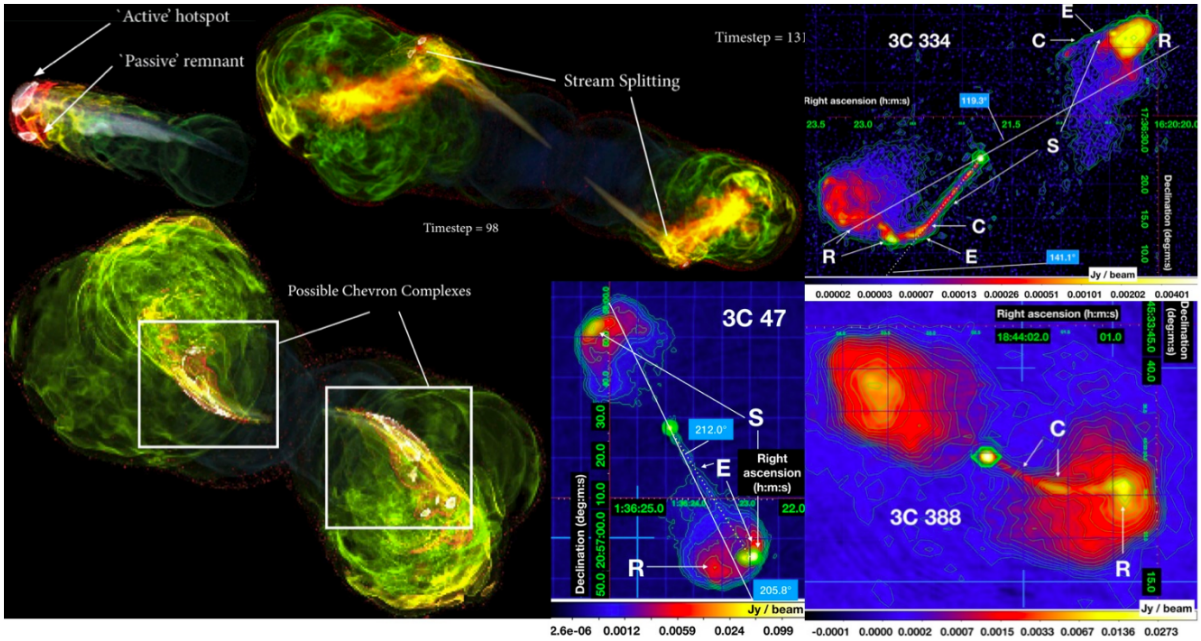

Figure 1.6: Comparison between 3D hydrodynamical simulations of precessing jets (left; (Horton et al., 2023)) and observed $\sim$ 5–8 GHz VLA radio maps of powerful radio galaxies and quasars (right; (Krause et al., 2019)). The simulations, computed with varying precession parameters, reproduce key morphological features seen in real systems—such as jet curvature (C), edge alignment (E), S-shaped symmetry (S), and multiple or ring-like hotspots (R)—which are consistent with long-term geodetic precession in binary SMBH systems. The observed jets span projected sizes of $\sim$ 70–330 kpc and reveal precession signatures in 24 out of 33 sources.

Large-scale precessing radio jets provide compelling indirect evidence for close SMBH binaries, as their long-term, periodic morphological distortions can arise from geodetic precession of the black hole spins around the orbital angular momentum (Begelman et al., 1980). Characteristic precession signatures include jet–lobe misalignment, curvature, S-shaped symmetry, and multiple or ring-like hotspots (Krause et al., 2019) Fig. 1.6), all reproduced in hydrodynamic simulations. Observationally, powerful kpc-scale jets—such as those in Cygnus A and Hydra A—show these features, implying SMBH separations $\lesssim 0.2$ pc and precession periods of $\sim 10^6$–10^8 yr. Surveys with LOFAR have identified over a thousand strong precession candidates (Horton et al., 2025), suggesting that binary-induced precession may be widespread among radio-loud AGN. Since Lense–Thirring precession cannot sustain such long-term stability, these findings point toward geodetic precession driven by close SMBH binaries as the dominant mechanism behind large-scale jet bending and complex radio morphologies.

1.6.3 Spin measurements

Spin measurements of supermassive black holes (SMBHs) provide indirect evidence for the role of SMBH mergers in shaping their evolution. Observationally, coherent gas accretion tends to spin up SMBHs to near maximal values, whereas mergers produce more slowly rotating remnants. X-ray reflection spectroscopy of the inner accretion disc has been applied to over 50 SMBHs spanning masses $10^5 - 10^{10}\,M_\odot$, using relativistic reflection models of broadened iron Kα lines to infer spin magnitudes using relativistic reflection models of broadened iron Kα lines to infer spin magnitudes (García et al., 2014; Dauser et al., 2014; Reynolds, 2021). The observed distribution shows higher spins at low SMBH masses ($< 10^8\,M_\odot$) and lower spins at higher masses, consistent with cosmological simulation predictions where low-mass SMBHs grow primarily via coherent accretion, while high-mass SMBHs are more strongly influenced by mergers (Volonteri et al., 2005; Sesana et al., 2014; Bustamante & Springel, 2019; Sala et al., 2024). Some tension exists between different simulations, e.g., NEWHORIZONs Beckmann et al. (2025) and semi-analytic models incorporating jet-driven spin-down (Ricarte et al., 2025), but the overall trend supports a scenario in which SMBH spin serves as a fossil record of growth history. Selection effects, such as the preferential detection of high-spin SMBHs in flux-limited AGN samples, must also be accounted for (Brenneman et al., 2011; Taylor & Reynolds, 2018). These results suggest that tracing SMBH spins across mass and cosmic time may provide indirect constraints on the prevalence of SMBH binaries.

1.6.4 Accretion Signatures from Circumbinary Disks

Accretion onto supermassive black hole (SMBH) binaries in gas-rich environments can produce distinct observational signatures through warping, precession, and disc breaking. Misaligned accretion discs around each SMBH experience Lense-Thirring precession and viscous torques, leading to the Bardeen-Petterson effect where the inner disc aligns with the black hole spin while the outer disc remains tilted (Bardeen & Petterson, 1975; King et al., 2005; Gerosa et al., 2015). Simulations have shown that this process is highly dependent on the disc geometry, viscosity, and binary mass ratio (Bourne et al., 2024; Koudmani et al., 2024). In cases where the binary and circumbinary disc are initially misaligned, discs can break into discrete, precessing sub-discs rather than fully aligning, producing signatures such as warped or torn discs with independent precession Doğan et al. (2018); Nealon et al. (2022). Observationally, these warped or broken discs could manifest as variable X-ray reflection signatures, quasi-periodic luminosity modulations, or misaligned jets that trace the precessing inner disc regions.

The state-of-the-art simulations provide predictions for how these gas-driven processes affect SMBH spin alignment and the resulting gravitational wave signals. Bourne et al. (2024) found that, even for low mass-ratio binaries, BH-accretion disc alignment timescales are generally shorter than the inspiral timescales when discs remain continuous, but misaligned or broken discs reduce the efficiency of spin alignment. Semi-analytic and numerical models suggest that this leads to sub-populations of aligned and misaligned SMBHs that

could be probed by future gravitational wave missions such as LISA (Steinle & Gerosa, 2023). These results imply that the presence of warped or broken discs introduces an important degeneracy: misaligned BH mergers could arise from either gas-poor environments or gas-rich systems where disc breaking prevents alignment. Observationally, signatures of disc warping, precession, and potential disc tearing offer a complementary probe of SMBH binary evolution, their spin distribution, and the dynamics of accretion in the vicinity of tight binaries.

1.6.5 Gravitational Waves

Ground- and space-based gravitational wave (GW) observatories probe different parts of the GW spectrum, providing complementary insights into compact object populations. Current ground-based detectors such as LIGO, Virgo, and KAGRA operate at frequencies of $\sim$ 10Hz–1kHz, enabling the detection of stellar-mass black hole and neutron star binaries (LIGO Scientific Collaboration et al., 2015; Abbott et al., 2023). Supermassive black hole (SMBH) binaries, however, emit at much lower frequencies ($\sim$ nHz $-$ mHz), accessible only to pulsar timing arrays (PTAs) and the future LISA mission (Foster & Backer, 1990; Colpi et al., 2024). PTAs use long-term observations of millisecond pulsars to detect correlated timing deviations indicative of a gravitational-wave background, potentially dominated by the ensemble of inspiraling SMBH binaries (Sesana, 2013; Antoniadis et al., 2022; Reardon et al., 2023). Recent PTA datasets (EPTA, NANOGrav, PPTA, CPTA, MPTA) show increasing evidence for a common stochastic signal that may have a gravitational-wave origin, with reported significance between 2σ and 4σ (Agazie et al., 2023; Xu et al., 2023; Miles et al., 2025). These observations provide a first window into the population of low-frequency SMBH binaries and their merger rates.

To interpret these signals, Bayesian population analyses combining astrophysical priors and PTA measurements have been developed (Steinle & Gerosa, 2023; Middleton et al., 2023; Chen et al., 2017, 2019). Astrophysically-informed models, constrained by galaxy formation and SMBH evolution simulations, suggest high merger rates and short delay times between galaxy and SMBH binary mergers, implying an active population of inspiraling binaries detectable by PTAs (Barausse et al., 2023; Steinle & Gerosa, 2023). In the future, space-based observatories such as LISA will access the higher-frequency band ($\sim 0.1\,\mathrm{mHz} - 1\,\mathrm{Hz}$), allowing direct observation of individual SMBH binary mergers and precise parameter estimation, potentially to $< 1\%$ in component mass for favorable systems (Amaro-Seoane et al., 2023; Pratten et al., 2023a,b). If the PTA signal is indeed due to SMBH binaries, it can be extrapolated to predict LISA detection rates, with recent estimates giving 95% upper limits of $R < 134\,\mathrm{yr}^{-1}$ for binaries in the $10^7 - 10^8\,\mathrm{M}_\odot$ range (Steinle & Gerosa, 2023). Together, PTA and LISA observations promise multi-band gravitational-wave astrophysics, bridging the inspiral and merger phases of SMBH binaries and opening a new window on galaxy and black hole co-evolution.

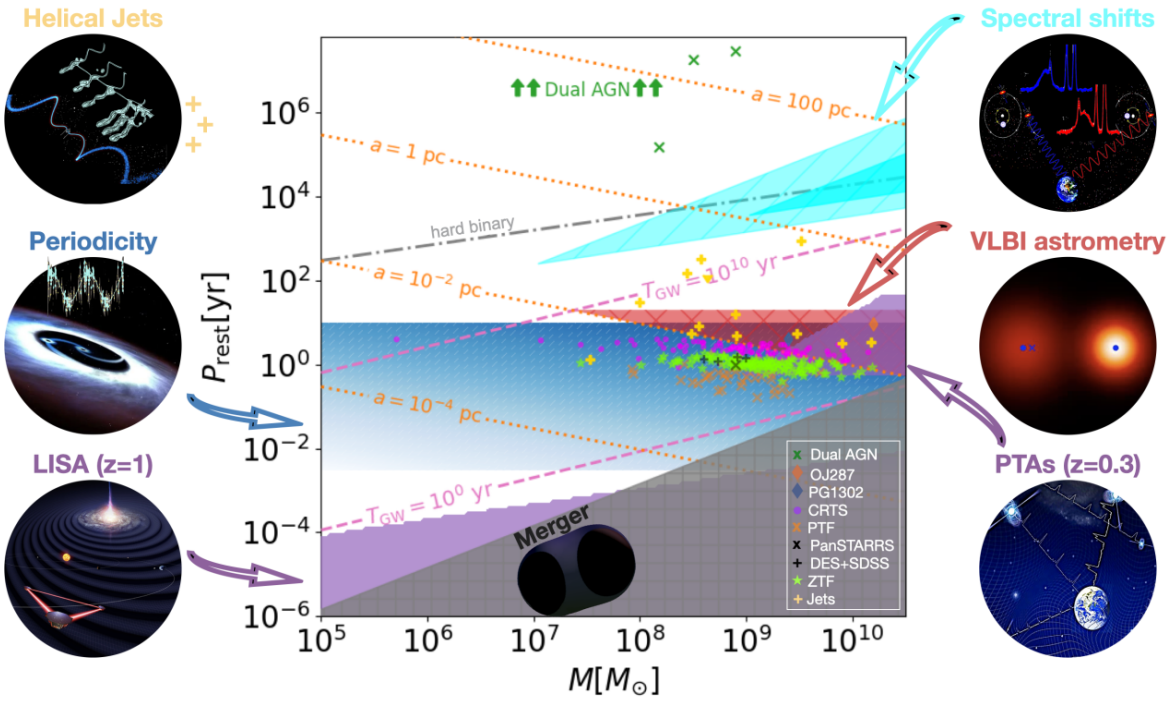

Figure 1.7: Observational signatures of supermassive black hole binaries (SMBHBs) across parameter space. The y-axis corresponds to the period of the source in the rest frame $P_{\rm rest}$. The grey dot–dashed line marks the hard-binary limit (Milosavljević & Merritt, 2003), below which systems are bound binaries. Green crosses indicate dual AGN candidates (Goulding et al., 2019; Koss et al., 2023) and the most compact imaged pair (Rodriguez et al., 2006). The cyan region shows where kinematically offset broad lines are detectable (Kelley et al., 2021), and the blue–white region denotes where periodic light curves are observable in optical time-domain surveys, with darker shading indicating longer residence times and higher luminosities. Photometric variability candidates from CRTS, PTF, Pan-STARRS, DES, and ZTF are shown as magenta dots, orange and black markers, and chartreuse stars (Graham et al., 2015; Charisi et al., 2016; Liu et al., 2019; Chen et al., 2020, 2022). Helical jet candidates are marked by yellow crosses, while the red region indicates where direct orbital tracking is possible. Purple regions show the sensitivity ranges of LISA and PTA observatories. Figure credit by D'Orazio & Charisi (2023).

1.6.6 Overview

An overview of the different observational methods of SMBH binaries across different scales by D'Orazio & Charisi (2023) is given in Fig.1.7 .

Chapter 2

Single and Binary Massive Black Holes in Merging Star Clusters

The content of this chapter has been published in the Monthly Notices of the Royal Astronomical Society, Volume 539, Issue 1, May 2025, Pages 45–68, and reported here with slight modifications.

Abstract

Star clusters can interact and merge in galactic discs, halos, or centers. We present direct N-body simulations of binary mergers of star clusters with $M_\star = 2.7 \times 10^4\,\mathrm{M}_\odot$ each, using the N-body code `BIFROST`with subsystem regularisation and post-Newtonian dynamics. We include 500 $\mathrm{M}_\odot$ massive black holes (MBHs) in the progenitors to investigate their impact on remnant evolution. The MBHs form hard binaries interacting with stars and stellar black holes (BHs). A few Myr after the cluster merger, this produces sizable populations of runaway stars ($\sim$800 with $v_{\rm ej} \gtrsim 50\mathrm{kms}^{-1}$) and stellar BHs ($\sim$30) escaping within 100 Myr. The remnants lose $\sim 30\%$ of their BH population and $\sim 3\%$ of their stars, with $\sim$30 stars accelerated to high velocities $\gtrsim 300\mathrm{kms}^{-1}$. Comparison simulations of isolated clusters with central hard MBH binaries and cluster mergers without MBHs show that the process is driven by MBH binaries, while those with a single 1000 $\mathrm{M}_\odot$ MBH in isolated or merging clusters produce fewer runaway stars at lower velocities. Low-eccentricity merger orbits yield rotating remnants ($v_{\rm rot} \sim 3\mathrm{kms}^{-1}$) , but probing the presence of MBHs via kinematics alone remains challenging. We expect the binary MBHs to merge within a Hubble time, producing observable gravitational-wave (GW) events detectable by future GW detectors such as the Einstein Telescope and LISA. The results suggest that interactions with low-mass MBH binaries formed in merging star clusters are an important additional channel for producing runaway and high-velocity stars, free-floating stellar BHs and compact objects.

2.1 Introduction

Numerous escaping stars and compact objects with velocities large enough to escape the galaxy have been detected or proposed in recent years. At the same time the dynamical evolution of star clusters in the presence of massive black holes (MBHs) has been widely studied, while evidence about interacting or merging star clusters is growing. In this section, we first outline the observational evidence of escaping stars and compact objects (Section 2.1.1) , then we present evidence for the presence and formation pathways of MBHs in star clusters (Section 2.1.2) and the interactions and/or mergers of star clusters (Section 2.1.3) .

2.1.1 High-velocity escaping stars and compact objects

The leading scenario of stellar ejections from the Galactic Centre (GC) with velocities exceeding the escape velocity of the Galaxy is based on the 'Hills mechanism' (Hills, 1988), i.e., when a stellar binary comes sufficiently close to the supermassive black hole (SMBH) Sgr A* (GRAVITY Collaboration et al., 2020; Event Horizon Telescope Collaboration et al., 2022) in the GC, it can be tidally disrupted. This refers to the dynamical break up of the binary in analogy to the disruption of a single star by a massive black hole. This results in the capture of one of the stars on a wide eccentric orbit and the ejection of the companion star with extreme velocities of 1000 km s^{-1}, by far larger than the escape velocity of the Milky Way (MW) . The ejection due to close encounter with the massive BH (MBH) and velocities higher than escape velocity are the two properties that define a hyper-velocity star (HVS). The first HVSs were discovered by Brown et al. (2005) and Hirsch et al. (2005) with heliocentric radial velocities of 709 km s^{-1} and 708 km s^{-1} and at 50 kpc and 19 kpc heliocentric distances respectively, both consistent with GC origin. The very high velocities of those stars allow them to travel long distances following radial trajectories, which makes them ideal probes of the mass distribution of the Galaxy (Gnedin et al., 2005; Kenyon et al., 2008). In order to reveal their origin, those stars are backwards integrated in a Galactic MW-like potential (Price-Whelan, 2017, e.g.). The respective trajectory can then be used to probe the shape of the potential and dark matter halo profile (Gnedin et al., 2005; Yu & Madau, 2007; Perets et al., 2009; Contigiani et al., 2019). An additional confirmation of the Hills mechanism was the discovery of a HVS with an extreme velocity of 1800 km s^{-1} and a backwards trajectory pointing towards the GC and Sgr A* (Koposov et al., 2019). The discovery of the first HVS has lead to numerous dedicated searches (Li et al., 2011; Zheng et al., 2014; Huang et al., 2017; Du et al., 2019; Kreuzer et al., 2020), reporting a large number of HVSs candidates in the Galactic halo (review in Brown (2015) and references therein) but the true origin for many of those still remains a mystery. An additional channel for the production of HVSs was proposed by Begelman et al. (1980), and Yu & Tremaine (2003), extending the classical Hills mechanism: the interaction of single or binary stars with a binary SMBH. Alternatively, the inspiral of an intermediate mass (in the range of 100 $M_\odot \lesssim M_\bullet < 10^6\ M_\odot$) black hole (IMBH) towards the GC (Baumgardt et al., 2006; Sesana et al., 2007, 2009a; Wang et al., 2018; Rasskazov et al., 2019; Evans

et al., 2023) could also explain the origin and ejection mechanism of HVSs.

Another class of high-velocity stars is observed to have large peculiar velocities, in the range of 40 km s^{-1} $\leq v_{\rm pec} \leq$ 200 km s^{-1} (Blaauw, 1961a; Gies & Bolton, 1986; Hoogerwerf et al., 2001; Perets & Šubr, 2012), commonly called 'runaway stars' (RASs). Those are usually early type (O-type, B-type) stars with a Galactic disk origin. Their ejection mechanisms are usually divided in two types (Blaauw, 1993; Hattori et al., 2019; Carretero-Castrillo et al., 2023) : (a) the dynamical ejection mechanism (DEM), where strong 3- and 4- body encounters between stars and/or BHs in dense stellar environments lead to the ejection of one of the members (Poveda et al., 1967; Aarseth & Hills, 1972; Hut & Bahcall, 1983; Ryu et al., 2017a,b; Weatherford et al., 2023) and (b) the binary ejection mechanism (BEM), where primary of the binary members undergoes a supernova explosion (SN) and the secondary (the runaway star) moves on with close to its original orbital velocity. The primary remnant receives a kick from the SN which might unbind it from the secondary (Zwicky, 1957; Blaauw, 1961b; Portegies Zwart, 2000; Justham et al., 2008; Pakmor et al., 2013; Neunteufel, 2020; Rajamuthukumar et al., 2024) . Heber et al. (2008) have discovered an unbound star travelling with heliocentric radial velocity of $>$ 400 km s^{-1} with a Galactic disk origin and have classified it as a hyper-runwaway star (HRS) . Finally, alternative mechanisms for the origin of high-velocity stars include the encounters with satellite galaxies and nearby galaxies such as the Large Magellanic Cloud (LMC) (Gualandris & Portegies Zwart, 2007; Boubert et al., 2017; Erkal et al., 2018) and the Andromeda Galaxy (Sherwin et al., 2008) and from star clusters tidally interacting with a single or a binary SMBH (Capuzzo-Dolcetta & Fragione, 2015; Fragione & Capuzzo-Dolcetta, 2016; Fragione et al., 2017).

Our knowledge on stellar populations in the Milky Way has been vastly expanded by the *Gaia* satellite mission of the European Space Agency (ESA) and the unprecedented quality of astrometric and photometric data it provides. Already from the first data release (DR1) (Gaia Collaboration, 2016) , the number of HVS candidates has significantly increased (Marchetti et al., 2018a) , contributing at least 14 more objects with a total velocity in the Galactic rest frame of $>$ 400 km s^{-1} and one classified as a HVS. A crucial step towards the improvement of modern astrometry came with the second data release (DR2) (Gaia Collaboration, 2018) providing us positions and proper motions of more than one billion stars and the radial velocities for about 7 million of those. The number of HVS candidates reported in the literature before Gaia's DR2 was close to 500 (Hirsch et al., 2005; Brown et al., 2006, 2008, 2012, 2014; Li et al., 2011, 2015; Huang et al., 2017; Vennes et al., 2017), with about 20 of them being faint and blue stars located in the Galactic halo with very high radial velocities and being classified as HVSs. Utilizing Gaia DR2 Hattori et al. (2018) found 30 ($>$ 480 km s^{-1}) old metal-poor stars, with 2-3 having LMC and 1-2 GC origin. Three white dwarfs (WDs) with extreme velocities of 1000 s^{-1} $\leq v \leq$ 3000 km s^{-1}, were also discovered in DR2 from Shen et al. (2018). Marchetti et al. (2018b) found 20 stars unbound ($>$ 80% probability) from the Galaxy, seven of which are consistent with a GC origin and 13 with an origin outside of the Milky Way. By combining Gaia DR2 and the 7th data release of the Large Sky Multi-object Fiber Spectroscopic Telescope (LAMOST), Li et al. (2021) reported a total of 591 high-velocity candidates with 43 of them having more

than 50% probability of being unbound from the Galaxy, increasing the number of known candidates by a factor of two. Despite the additional proper motions and radial velocities of 34 million stars that the third Gaia data release (DR3) (Gaia Collaboration, 2023) has provided, Marchetti et al. (2022) found no additional HVS candidates $> 400\,\mathrm{km\,s^{-1}}$ and Liao et al. (2023) reported only two with radial velocities larger than $500\,\mathrm{km\,s^{-1}}$ without strong evidence for a GC origin. Finally, the recent discovery (Huang et al., 2024) of high-velocity star (J0731+3717) with $v_{\rm ej} \approx 548\,\mathrm{km\,s^{-1}}$, whose backward trajectory 21 Myr ago, reveals its origin from MW globular cluster M15.

2.1.2 Evidence for massive black holes in star clusters

The existence and formation pathway of IMBHs remains an open question. Dense stellar environments like dwarf galaxies and massive star and globular clusters are ideal sites for their formation and growth (Askar et al., 2024). Although limited, observational evidence of IMBHs have been growing recently (see e.g. Mezcua, 2017; Greene et al., 2020, and references therein). One of the most recent and clear piece of evidence to date, is the detection GW190521 (Abbott et al., 2021) of an IMBH with $M_\bullet \sim 150\,\mathrm{M}_\odot$ via gravitational waves (GW) from two coalescing stellar-mass black holes of $m_\bullet \sim 66\,\mathrm{M}_\odot$ and $m_\bullet \sim 85\,\mathrm{M}_\odot$ each. Apart from GWs numerous candidates of accreting IMBHs have been proposed due to X-ray emission detected in galaxies nearby, in the mass range of $200 \lesssim M_\bullet \lesssim 10^5\,\mathrm{M}_\odot$ (Matsumoto et al., 2001; Strohmayer & Mushotzky, 2003; Farrell et al., 2009; Mezcua et al., 2013; Mezcua et al., 2015; Mezcua, 2017). Moreover, an IMBH of $M_\bullet \sim 10^4\,\mathrm{M}_\odot$ was recently proposed (Wen et al., 2021) as a the X-ray source of a tidal disruption event (TDE) in a massive object of $M_\star \sim 10^7\mathrm{M}_\odot$ (Lin et al., 2018), which corresponds either to a stripped galactic nucleus or a globular cluster.

Evidence for the existence of IMBHs or central populations of stellar BHs in various stellar and globular clusters is supported by dynamical signatures from observations and dynamical modeling. However, making a clear distinction between the two alternatives remains challenging. Among the top candidates of galactic (MW) globular clusters hosting an IMBH are ωCentauri (ωCen) and 47 Tucanae (47 Tuc). For the former dynamical models (van der Marel & Anderson, 2010; Noyola et al., 2010; Jalali et al., 2012; Baumgardt, 2016) have proposed a central IMBH in the $1.2 \times 10^4\,\mathrm{M}_\odot \lesssim M_\bullet \lesssim 5 \times 10^4\,\mathrm{M}_\odot$. Only recently observations of proper-motions of fast-moving stars in the inner 0.08 pc of ωCen from HST have been analyzed by Häberle et al. (2024), who found that the excess velocities can be explained by the presence of an IMBH with a corresponding lower mass limit of $M_\bullet \sim 8.8 \times 10^3\,\mathrm{M}_\odot$. On the other hand, the situation in 47 Tuc is still under debate. X-ray (Grindlay et al., 2001) and radio (de Rijcke et al., 2006) data observations have provided upper mass limits of $\sim 470\,\mathrm{M}_\odot$ and $\sim 2060\,\mathrm{M}_\odot$ for a central IMBH in 47 Tuc, while recent dynamical modeling (Kızıltan et al., 2017a,b) supports this evidence predicting a mass of $M_\bullet \sim 2300\,\mathrm{M}_\odot{}^{+1500}_{-800}$. Further observations of millisecond pulsars (MPS) have shown that the presence of an IMBH is not required to explain the data (Freire et al., 2017; Abbate et al., 2018) , in line with multi-mass dynamical modeling results (Mann et al., 2019; Hénault-Brunet et al., 2020). Updated dynamical models by Croce et al. (2023) place

an upper limit of $\sim 578\,\mathrm{M}_\odot$ and only the latest ultradeep Australia Telescope Compact Array (ATCA) have revealed a central compact radio source associated with a faint X-ray emission corresponding to an IMBH of $M_\bullet \sim 54 - 6000\,\mathrm{M}_\odot$.

Numerous studies have been conducted providing additional evidence of a central IMBH or a dark central cluster (Ibata et al., 2009; Kamann et al., 2014; Baumgardt, 2016; Nguyen et al., 2017; Gieles et al., 2018; Vitral et al., 2022) in such environments. A detailed analysis of 3D spectroscopic data by Kamann et al. (2016) revealed the presence of a $M_\bullet \sim 600\,\mathrm{M}_\odot$ IMBH in the core-collapsed cluster NGC6397, while Rui et al. (2021) suggested a central sub-system of stellar remnants supported by Vitral et al. (2022) who utilized Gaia and HST proper motion data, consistent with a dark concentration mass of $\sim 1000\,\mathrm{M}_\odot$. A less debated case of whether the central mass corresponds to a single IMBH or to a sub-system of dark objects is that of NGC6388. Combining spectroscopic data from the *Very Large Telescope* (VLT) and HST, Lützgendorf et al. (2011) proposed an IMBH of $M_\bullet \sim (1.7 \pm 0.9) \times 10^4\,\mathrm{M}_\odot$ confirmed by Lanzoni et al. (2013) who placed an upper limit of $\sim 2000\,\mathrm{M}_\odot$ for the mass of the IMBH. Finally, similar findings have been proposed for Andromeda (M31) galaxy. For example, with the use of *Hubble Space Telescope* (HST) data, Gebhardt et al. (2002) reported the detection of a $M_\bullet \sim 2 \times 10^4\,\mathrm{M}_\odot$ IMBH in G1 cluster of M31 galaxy. Dynamical models by Baumgardt & Makino (2003) proposed that the presence of an IMBH in G1 is not needed to explain the observed data, while X-ray emission detected by *XMM-Newton* could not distinguish between an accreting IMBH or a low-mass X-ray binary (Pooley & Rappaport, 2006). Additionally, there has been recent evidence for a $M_\bullet \sim 10^5\,\mathrm{M}_\odot$ IxsMBH in G078 (Pechetti et al., 2022), which is the most massive globular cluster of M31, originating from the tidally stripped nucleus of a dwarf galaxy (Fuentes-Carrera et al., 2008).

One of the leading mechanisms for the formation of an IMBH, is the growth of low-mass BHs ($m_\bullet < 50\,\mathrm{M}_\odot$) in dense stellar environments via successive stellar and compact object collisions (Stone et al., 2017; Arca-Sedda et al., 2021; Rizzuto et al., 2020, 2022b; Arca-Sedda et al., 2023a). The high densities in the centre of such environments leads to a sequence of mergers capable of producing BHs on the intermediate mass range $100\,\mathrm{M}_\odot \lesssim M_\bullet < 10^4\,\mathrm{M}_\odot$ (Atallah et al., 2023; Arca-Sedda et al., 2021; Fragione et al., 2022; Mapelli et al., 2021; Rizzuto et al., 2022b). Such merger products can receive velocity kicks ranging from tens up to 5000 km s^{-1} (Campanelli et al., 2007b; Lousto & Healy, 2019) due to the GW-induced recoil. Consequently, it is rather unlikely that the final product can be retained in low escape velocity environments such as stellar and globular clusters (Gerosa & Berti, 2019). The extreme densities of nuclear star clusters (NSCs) combined with the increased escape velocities $v_{\rm esc} \gtrsim 100$ km s^{-1} (Neumayer et al., 2020), makes them ideal sites for the retention of IMBHs. The hierarchical assembly of massive star clusters and NSCs makes retaining the merger products more likely as the black holes end up residing in environments with higher escape velocities than their original birth clusters (Rantala et al., 2024a).

The theory of pair-instability (PPSN) and pulsation pair-instability supernovae (PSN) predicts a mass gap on BH formation ranging between $\sim 50 - 130\,\mathrm{M}_\odot$, due to single stellar evolution only (Fowler & Hoyle, 1964; Woosley et al., 2007; Woosley, 2017). In young

and massive star clusters, a star can grow to very high masses (very massive star with $m_\star > 150\,\mathrm{M}_\odot$, therefore VMS) via repeated stellar collisions which collapses to an IMBH within or above the mass gap, which may further grow through accretion during TDEs. This so-called *fast runaway collision* scenario, has been numerically studied (Portegies Zwart et al., 1999; Portegies Zwart & McMillan, 2002; Freitag et al., 2006a,b; Rizzuto et al., 2020, 2023; Arca-Sedda et al., 2023b,a; Arca-sedda et al., 2024; Prieto et al., 2024; Rantala et al., 2024a) where VMSs are efficiently formed, resulting in MBHs of $M_\bullet \gtrsim 10^2 - 10^4\,\mathrm{M}_\odot$ when they collapse. Finally, it is important to mention, that the mass-loss from VMSs is still unclear and further research in stellar evolution models is needed to understand if and how long such stars could survive even if they do form (Sabhahit et al., 2022, 2023).

The formation of IMBHs and the co-evolution of massive star cluster hosts has been studied mostly in isolated numerical setups (Wang et al., 2016; Rizzuto et al., 2023; Arca-Sedda et al., 2023b) and only recently in full hierarchical by Rantala et al. (2024a). Recent observations by James Webb Telescope (JWST) suggest the formation of clumped clusters like the Cosmic Grapes at $z > 6$ redshift (Fujimoto et al., 2024). Furthermore, five massive ($M_{cl} \sim 10^6\ \mathrm{M}_\odot$) star clusters, the so-called Cosmic Gems, have been detected by JWST at $z = 10.2$, providing additional evidence to such hierarchical assembly. This is also supported by previous observations of star cluster forming regions (e.g. Zhang et al., 2001; Bastian et al., 2005; Grasha et al., 2017; Menon et al., 2021) and simulations of star-burst environments (Lahén et al., 2020), where a monolithic collapse seems unlikely.

The conditions required to produce massive clusters, such as globular clusters, occur in interacting galaxies and star forming regions during the collapse of giant molecular clouds (see e.g. Krumholz et al., 2019, and references therein). The combined effects of the properties of the collapsing cloud and the tidal field from the forming galaxy may lead to efficient angular momentum transport in the star cluster forming region, resulting in rotating clusters Lahén et al. (2020). Although debated in the past, there is clear observational evidence nowadays of rotating GCs in the Milky Way (Bellazzini et al., 2012; Fabricius et al., 2014) with rotational velocities of the order of a few $\mathrm{km\,s^{-1}}$. Rotation can have significant effects on the overall evolution Fiestas & Spurzem (2012) of a star cluster, for example spinning up its core and increasing the stellar ejection rate (Einsel & Spurzem, 1997; Ernst et al., 2007) or when combined with stellar evolution of the system Kamlah et al. (2022).

Similar to the coupled formation and evolution of IMBHs and massive star clusters, the properties of NSCs and SMBHs are closely related to those of their host galaxies (Ferrarese et al., 2006; Leigh et al., 2015; Capuzzo-Dolcetta & e Melo, 2017) which indicates that the formation and evolution of the two is tightly related (Antonini et al., 2015; Neumayer et al., 2020). Two scenarios have been proposed for the formation of NSCs. Galactic nuclei with sufficiently high gas densities can trigger in-situ star formation (Loose et al., 1982; Mihos & Hernquist, 1994; Milosavljević, 2004; Nayakshin et al., 2007; Aharon & Perets, 2015) leading to the formation of a NSC, or by cluster inspirals and mergers towards the galactic centre due to dynamical friction (Tremaine et al., 1975; Capuzzo-Dolcetta, 1993; Loose et al., 1982; Agarwal & Milosavljević, 2011; Tsatsi et al., 2016). The latter suggests that clusters may interact with each other during their infall towards the GC. In conclusion

though, the diversity of stellar age and metallicity observed in galactic nuclei implies that both scenarios contribute to the overall evolution of NSCs (Antonini et al., 2015; Guillard et al., 2016; Neumayer et al., 2020; Do et al., 2020; Arca-Sedda et al., 2020) .

2.1.3 Binary star clusters: interactions and mergers

The interaction and merging of star clusters is theoretically expected and observed during their formation (see e.g. de La Fuente Marcos & de La Fuente Marcos, 2009; Lahén et al., 2020). Especially for LMC, it has been found that the fraction of binary star clusters is roughly $\sim 12\%$ (Dieball et al., 2002) , while a similar number ($\sim 10\%$) is expected for the Milky Way (de la Fuente Marcos & de la Fuente Marcos, 2010). Bhatia et al. (1991) published a catalogue with numerous binary star cluster candidates in LMC, but their formation path for most of them remains unclear. Apart from forming together at birth, star clusters undergo tidal interactions and mass exchange at later evolutionary phases in the disks of galaxies (Khoperskov et al., 2018; Mastrobuono-Battisti et al., 2019; Camargo, 2021; Ishchenko et al., 2024). Recent high resolution observations of LMC, provided evidence of pairs of star clusters in collision course due to tidal capture (Mora et al., 2019; Giusti et al., 2023). The kinematic properties of almost the entire population of the MW globular clusters is nowadays available thanks to the Gaia DR3 release (Gaia Collaboration, 2018, 2023). A detailed investigation on 16 Galactic binary cluster candidates from Gaia DR3 (Gaia Collaboration, 2023) was recently done by Angelo et al. (2022) who found 4 pairs of bound open clusters. Ishchenko et al. (2023) conducted a statistical analysis for the interaction probability of the galactic globular clusters utilizing the Gaia DR2 release (Gaia Collaboration, 2018) and found a significant rate of close encounters and an average of 10 intersecting with-each-other trajectories per cluster. Additionally, Chemerynska et al. (2022) integrated the orbits of the 150 clusters in a static MW-like potential up to 5 Gyr and found a probability above 20% for cluster collisions. Finally, recent studies have shown that many globular clusters inhibit disk-like kinematics (Casetti-Dinescu et al., 2010; VandenBerg et al., 2013) providing evidence of close orbital passages and angular momentum gain leading to rotation. This leads to the formation of IMBH binaries potentially leading to GW-driven coalescence.

In this chapter we investigate the presence of single and binary MBHs in star clusters as the potential origin for high velocity stars. We use direct N-body simulations of idealised isolated and merging star clusters with and without central massive black holes (MBH). We find that, in particular in the presence of MBH binaries, stars and compact objects (COs) can be accelerated to velocities up to 800 km s^{-1}. The paper is structured as follows: in Section 2.2 we describe the various mechanisms leading to the production of high velocity stars and COs. The simulation methods and initial conditions are presented in Section 3.3, while the results about cluster evolution, the formation and evolution of MBH binaries and the demographics of ejections in the Sections 2.4, 2.5, 2.6 respectively. Finally, we summarize our conclusions in Section 3.6 .

2.2 Dynamical Ejection Mechanisms (DEM) in Star & Globular Clusters

In this section we review the basic DEM processes operating in star clusters, where a single or binary MBH and/or a sub-cluster of stellar-mass BHs are present (Kulkarni et al., 1993; Quinlan, 1996; O'Leary et al., 2006; Sesana et al., 2006; Trenti et al., 2007; Morscher et al., 2015; Fragione & Capuzzo-Dolcetta, 2016; Fragione & Gualandris, 2019; Šubr et al., 2019; Rasskazov et al., 2019; Weatherford et al., 2023). If runaway and hyper-velocity stars are observed and a star cluster origin is confirmed, it would be smoking gun evidence for the existence of massive black hole seeds in the heart of such systems. Additionally, understanding their dynamical production channels can be used to disentangle the tension between the presence of a single massive or a collection of stellar-mass 'dark' objects (BHs) in the cores of massive clusters (Anderson & van der Marel, 2010; Noyola et al., 2010; Lu & Kong, 2011; Strader et al., 2012; Chomiuk et al., 2013; Feldmeier et al., 2013; Peuten et al., 2016; Zocchi et al., 2017, 2018; Bellini et al., 2018; Vitral et al., 2022; Häberle et al., 2024; Paduano et al., 2024; Huang et al., 2024) .

2.2.1 Single Stellar Encounters and 2-Body Relaxation

The gravitational interaction between two stars in the vicinity of a BH, with masses m_1 and m_2, results in a change in the velocity of the m_1 (Yu & Tremaine, 2003) ,

$$\begin{aligned}\delta v_1 &= \frac{2Gm_2}{\left[G^2\left(m_1+m_2\right)^2/v_{12}^2+b^2v_{12}^2\right]^{1/2}}\\ &\leq \frac{2Gm_2}{\left[2G\left(m_1+m_2\right)b\right]^{1/2}}\\ &= 440\ \mathrm{km\ s^{-1}}\left(\frac{2m_2}{m_1+m_2}\right)^{1/2}\left(\frac{m_2}{1\mathrm{M}_\odot}\right)^{1/2}\left(\frac{1\mathrm{R}_\odot}{b}\right)^{1/2}\end{aligned} \tag{2.1}$$

where v_{12} is the relative velocity of the two stars and b is the impact parameter (Binney & Tremaine, 2008). Although rare, an encounter of this type with small enough impact parameter can result in significant velocity kick. For example, if $m_1 = m_2 = 1\mathrm{M}_\odot$ and $b = 10^{-6}$pc, then $\delta v_1 \geq 30$ km s^{-1}.

The collective motion of objects in a N-body system, induces time-varying perturbations on the background potential of the system. A non-smooth potential introduces energy and angular momentum exchange between the cluster members, causing them to randomly diffuse in the phase space. The net effect of all the uncorrelated 2-body encounters can lead to a change of each body's velocity by order of itself $\Delta v/v \sim 1$ (Chandrasekhar, 1942; Spitzer, 1987; Heggie & Hut, 2003; Aarseth et al., 2008), allowing an object to escape within the relaxation timescale and velocity of the order $v_{2b} \approx 2\sqrt{\sigma}$, where σ is the velocity dispersion the cluster. A star located in the outskirts of a cluster with local velocity dispersion $\sigma \approx 2\,\mathrm{km\,s^{-1}}$, could then escape through that process with $v_{2b} \approx 2.8\,\mathrm{km\,s^{-1}}$.

2.2.2 Encounters of Singles with Binary Stars

Interactions between single and binary stars are common in star clusters and play a key role to binary evolution (Heggie, 1975). Those interactions can lead to the formation of new binaries from single ones or through the exchange of binary members (Valtonen & Karttunen, 2006). Lower mass objects are accelerated to high velocities when encounters between unequal mass stars take place (Spitzer, 1987), potentially leading to their escape from the host cluster. The critical velocity of a star (member of the cluster) capable of ionizing (the process where an encounter leads the break up of a bound system to its individual components) the binary in the centre-of-mass of a triple system is given by (Hut & Bahcall, 1983; Hills, 1975a; Sigurdsson & Phinney, 1993)

$$\begin{aligned} v_c &= \sqrt{G\frac{m_1 m_2}{m_3}\frac{(m_1+m_2+m_3)}{(m_1+m_2)}\frac{1}{a}} \\ &= \sqrt{\frac{G m_{123}}{a}\frac{\mu_{12}}{m_3}}, \end{aligned} \tag{2.2}$$

Here $\mu_{12} = m_1 m_2/(m_1+m_2)$, $m_{123} = m_1+m_2+m_3$ and a is the semi-major axis of the binary with $m_1 \geq m_2$, where the least massive body being the most likely to escape. For a binary with $m_1 = 2\,M_\odot$, $m_2 = 1\,M_\odot$ and $a = 2$ AU, a third star of $m_3 = 1\,M_\odot$ would need $v_c = 33.8\,\mathrm{km\,s^{-1}}$ to ionize the binary. The stochastic nature of such process makes it very challenging to predict the ejection velocity of the escaping body from generic initial conditions, but numerous detailed numerical 3-body scattering experiments have been conducted (e.g. Hut & Bahcall, 1983; Hills, 1975a; Sigurdsson & Phinney, 1993) for the equal-mass case and recently from Forastier et al. (2024) for unequal masses. Finally, Samsing et al. (2017) have investigated the role of stellar tides and post-Newtonian (PN) dynamics on such encounters and found that including those effects lead to higher stellar coalescence rates.

2.2.3 Binary Encounters with a Single Massive Black Hole

The strong tidal forces a star experiences once exerted by an SMBH, are capable of tearing it apart once it gets sufficiently close. This tidal disruption event (TDE) takes place when the orbital pericentre distance $r_{\rm peri} \leq r_t$, where r_t is the tidal radius given by (Hills, 1975b)

$$r_t \approx \left(\frac{M_{\rm SMBH}}{m}\right)^{1/3} r_*. \tag{2.3}$$

Consider now a binary system with mass $m_{\rm b}$ and semi-major axis $a_{\rm b}$ approaching an SMBH. The same process (replacing r_* with $a_{\rm b}$ and $m = m_{\rm b}$) will lead to the tidal break-up of the binary, where one member is captured by the SMBH and the other ejected with $v_{\rm ej}$ (Hills, 1988). This happens when it passes closer to the SMBH than the tidal radius, i.e., when

$$a_b \left(\frac{M_{\rm SMBH}}{m_1+m_2}\right)^{1/3} \simeq 10{\rm AU}\left(\frac{a_b}{0.1{\rm AU}}\right)\left[\frac{M_{\rm SMBH}}{10^6\,(m_1+m_2)}\right]^{1/3}. \tag{2.4}$$

For a star cluster with an IMBH at its centre and a number of binaries inside its core, the above mechanism may efficiently produce high-velocity stars escaping the cluster. During the tidal breakup, the stars receive a velocity change of the order of the velocity relative to the centre of mass of the binary, which for m_1 in this case is (Hills, 1988; Yu & Tremaine, 2003),

$$\begin{aligned}\delta v_1 &\approx \sqrt{\frac{G\,(m_1+m_2)}{a_{\rm b}}}\left(\frac{m_2}{m_1+m_2}\right)\\ &\approx 67\ {\rm km\ s^{-1}}\left(\frac{2m_2}{m_1+m_2}\right)^{1/2}\left(\frac{m_2}{1{\rm M}_\odot}\right)^{1/2}\left(\frac{0.1{\rm AU}}{a_{\rm b}}\right)^{1/2},\end{aligned} \tag{2.5}$$

or in a more practical form by Bromley et al. (2006), the velocity of the ejected star is,

$$v_{\rm ej} \approx 460\left(\frac{a_{\rm b}}{0.1{\rm AU}}\right)^{-1/2}\left(\frac{m}{2{\rm M}_\odot}\right)^{1/3}\left(\frac{M_{\rm IMBH}}{10^3{\rm M}_\odot}\right)^{1/6}\ {\rm km\ s^{-1}}. \tag{2.6}$$

Using Eq. 2.6, for a binary of $m_{\rm b} = m = 1{\rm M}_\odot$ approaching an IMBH of $M_{\rm IMBH} = 1000\ {\rm M}_\odot$, the ejection velocity can vary from $v_{\rm ej} \approx 136$ km s^{-1} for $a_{\rm b} = 0.1$mpc up to $v_{\rm ej} \approx 1360$ km s^{-1} for $a_{\rm b} = 0.01$mpc . For star clusters with large binary fractions, this channel acts as the major contribution to the production of RAs and HVSs (Šubr et al., 2019; Fragione & Gualandris, 2019; Weatherford et al., 2023). Finally, Ryu et al. (2023a) showed by means of hydrodynamics simulations that in the special case where a tight stellar binary interacts with a stellar-mass BH, both stars can be tidally disrupted if the impact parameter is small enough or end up with one of the members becoming unbound (*micro-Hills* mechanism). If the binary consists of a star and a BH, then the stellar ejection could also be accompanied by the formation of a binary BH via binary member exchange Ryu et al. (2023b).

2.2.4 Encounters with (Massive) Black Holes Binaries

Star clusters are expected to host a population of binary BHs and compact objects (Kulkarni et al., 1993; Portegies Zwart & McMillan, 2000; Downing et al., 2010; Tanikawa, 2013; Morscher et al., 2015; Rodriguez et al., 2015; Park et al., 2017; Anagnostou et al., 2020; Torniamenti et al., 2022). The presence of bodies with a range of masses in a star cluster lead to the exchange of kinetic energy and ultimately more massive objects tend to shrink to the centre of the cluster. During this stage, the density of the star cluster core is increased leading to the efficient dynamical formation of stellar and stellar remnant binaries. Encounters between single stars and COs with BH binaries can lead to sufficiently high velocity kicks and result in ejections. Especially when their semi-major axis $a_{\rm BHB}$ becomes small enough, such that $a_{\rm b} \leq a_{\rm h} \equiv GM_2/4\sigma_c^2$ (Sesana et al., 2006), where σ_c is the local

dispersion velocity (Quinlan, 1996). Additionally, a single star approaching a black hole binary (BHB) can be tidally disrupted and further harden the binary up to 20% for retrograde encounters (Ryu et al., 2022). The velocity kick of a single or multiple encounters of a star or CO with a BHB is then given by (Yu & Tremaine, 2003),

$$\delta v \approx 1500 \text{ km s}^{-1} \left(\frac{2M_2}{M_1+M_2}\right)^{1/2} \left(\frac{M_2}{10^6 \text{M}_\odot}\right)^{1/2} \left(\frac{1\text{mpc}}{a_\text{b}}\right)^{1/2}. \tag{2.7}$$

During the hierarchical formation of a massive star cluster (Gieles & Portegies Zwart, 2011; Rantala et al., 2024a), lower mass seed BHs can also form binaries. Those BH binaries are usually more massive than stellar remnants, since they can grow by successive mergers or as by products of runaway collisions (Arca-Sedda et al., 2023a; Arca-sedda et al., 2024; Fujii et al., 2024). Moreover, similar to how galaxies merge (e.g. Milosavljević & Merritt, 2001) leading to the formation of SMBH binaries, galactic globular clusters can also interact and merge. If such clusters contain a massive MBH, their merger remnant becomes the host of an MBH binary, which can then scatter single and binary stars around resulting to their ejection from the cluster. Finally, an MBH-host star or globular cluster on an inspiral orbit towards the galactic centre captured by the SMBH (e.g. Baumgardt et al., 2006; Sesana et al., 2007, 2009a), may lead to the formation of an SMBH-IMBH binary which can eject stars at high speed (Rasskazov et al., 2019) once it gets hard ($a_\text{b} < a_\text{h}$).

In the special but common in dense stellar environments like globular clusters and the galactic centre case where all interacting bodies are BHs, single-binary encounters in star clusters can efficiently lead to the production of GW-driven merger events (Samsing & Ilan, 2018; Samsing et al., 2018b,a), where one of the BHs receives a strong velocity kick enough to be ejected from the cluster.

2.3 Methods

To investigate the influence of (MBHs) on the merging of stellar clusters and the resulting population of escaping stars and compact objects (i.e. white dwarfs, neutron stars and black holes), we conduct a series of direct N-Body simulations. These simulations involve merging pairs of stellar clusters, where either both, only the primary or none of them hosts an MBH at their centre. The systems are evolved for 100 million years (Myr) using the direct N-Body code `BIFROST` (Rantala et al., 2023), which we describe briefly in Subsection 3.3.1.

2.3.1 N-Body Code (`BIFROST`)

Throughout this study we used the GPU-accelerated direct-summation N-Body code `BIFROST` (Rantala et al., 2023), which is the updated version of the `FROST` code (Rantala et al., 2021). The code employs a fourth-order forward symplectic integrator (FSI) technique (Chin, 1997; Chin & Chen, 2005; Dehnen & Hernandez, 2017), using a hierarchical implementation (Rantala et al., 2021). Beyond traditional Newtonian accelerations, FSI incorporates

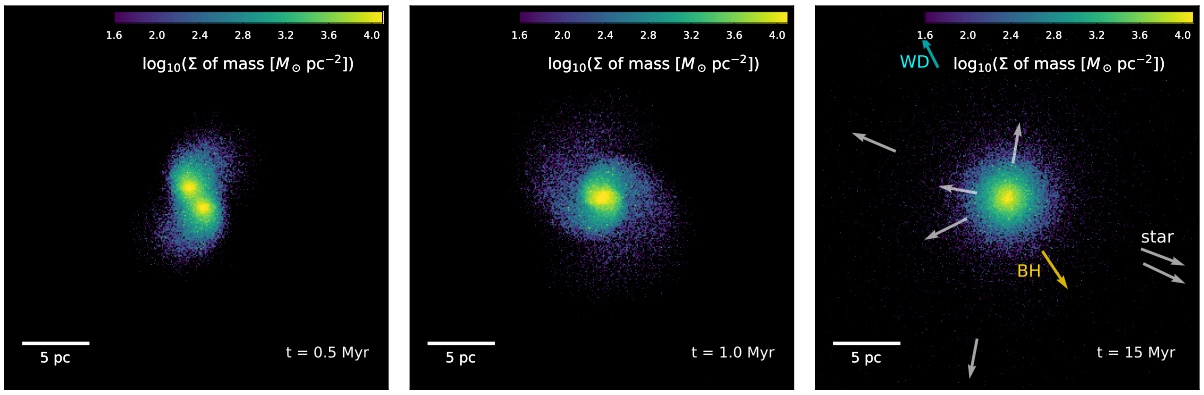

Figure 2.1: Time sequence of the stellar surface density distribution of a typical star cluster merger simulations with an orbital eccentricity e = 0.05 and an MBH in each cluster centre. We show the simulation at an early interacting phase (left panel, t = 0.5 Myr), at the time of the merger of the cluster cores (middle panel, t = 1 Myr) and after the central MBHs have formed a hard binary in the centre of the merger remnant (right panel, t = 15 Myr). By interactions with the MBH binary stars (star, white arrows), stellar BHs (BH, orange arrow) and white dwarfs (WD, cyan arrow) can be ejected at high velocities after interacting with the MBH binary (a few examples are shown). The arrow length scales with velocity and the BH has a velocity of $v_{\rm ej} \approx 80$ km s^{-1}.

gradient accelerations to cancel second-order error terms, resulting in a fourth-order time integration cycle with strictly positive sub-steps. This method was found to be more effective (Chin, 2007) e.g. for the Kepler problem than traditional Yoshida-type symplectic integrators (Yoshida, 1990) which use negative sub-steps for higher than second integration order. Furthermore, within the hierarchical integration approach, rapidly evolving components of the simulated systems decouple from slowly evolving components, a feature which makes the code particularly efficient when applied to N-body systems characterized with a large dynamical range (Pelupessy et al., 2012).

The code handles sub-systems such as binary and multiple systems, fly-bys and small clusters around supermassive black holes, through the use of secular and regularized few-body integrators (Rantala et al., 2020). The code also includes the option of enabling post-Newtonian equations of motion up to order PN3.5 utilizing the formulas given in Thorne & Hartle (1985) and Blanchet et al. (2006). In binary systems the PN corrections account for relativistic effects such as periastron precession and radiation-reaction (circularization and shrinking of the orbit) due to the emission of gravitational waves. Another feature which few codes share (Wang et al., 2020) is the ability to efficiently simulate massive systems with arbitrary fraction of primordial binary systems.

`BIFROST` makes use of four different criteria for stellar and compact object mergers, which we describe in detail Section 2.3.3. Those involve merging events of compact objects, disruption of a star by a CO or stellar collisions. For unbound stars at large distances from the centre-of-mass of the system, we employ a user-defined threshold at which the particles

Table 2.1: The BIFROST user-given parameters relevant for simulations of this study. Parameter definitions correspond to the ones in Rantala et al. (2023).

Parameter	Symbol	Value
Forward integrator time-step factor	$\eta_{\rm ff}, \eta_{\rm fb}, \eta_{\nabla}$	0.2
Subsystem neighbour radius	$r_{\rm rgb}$	10 mpc
Regularization GBS tolerance	$\eta_{\rm GBS}$	10^{-7}
Regularization GBS end-time tolerance	$\eta_{\rm endtime}$	0.01
Regularization highest PN order		PN3.5
Secular integration threshold	$N_{\rm orb,sec}$	0
Secular highest PN order		PN2.5

are removed from the simulation. For a typical star cluster, stars and COs found beyond $r_{\rm esc} \sim 100\ r_{\rm h}$ are not considered cluster members anymore, since at such distances the gravitational pull from the parent cluster would be too weak against the galactic tides. We note that the simulations presented in this study do not for simplicity include any tidal potential. The main user-defined code parameters are listed in Table 2.1. Overall the parameters `BIFROST` used are similar to used in previous `BIFROST` studies (e.g. Rantala et al. 2023; Rizzuto et al. 2023).

2.3.2 Orbital evolution of binary systems

Binary systems that are strongly perturbed or post-Newtonian are treated in `BIFROST` through algorithmic regularization. We make use of secular binary integration when a binary is sufficiently isolated (no other stars or COs within 10 mpc) and the number of binary orbits per time-step ϵ, $N_{\rm orb} = P_{\rm bin}/\epsilon$ is larger than the user-defined threshold $N_{\rm orb,sec}$, where $P_{\rm bin}$ is the orbital period of the binary. We use $N_{\rm orb,sec} = 0$ throughout the study. The initial conditions of the simulations presented here do not contain a binary population. We only form binary systems dynamically.

The equations of motion responsible for the secular evolution are characterised by the semi-major axis a, orbital eccentricity e and the argument of periapsis ω, taking into account leading-order relativistic effects which originate from the post-Newtonian PN1.0, PN2.0 and PN2.5. The advance of the orbital periapsis is due to PN1.0 and PN2.0 given by

$$\left\langle \frac{d\omega}{dt} \right\rangle_{\rm sec} = \frac{6\pi G}{c^2 P} \frac{M}{a(1-e^2)} + \frac{3(18+e^2)\pi}{2c^4 P} \left[\frac{GM}{a(1-e^2)} \right]^2 . \tag{2.8}$$

The PN2.5 term refers to gravitational wave radiation reaction due to energy and angular momentum losses, leading to the circularization and shrinkage of the orbit described by the rate of change of binary semi-major axis and eccentricity (Peters, 1964) as

$$\begin{aligned}\left\langle \frac{da}{dt} \right\rangle_{\rm sec} &= -\frac{64}{5}\frac{\beta(m_1,m_2)}{a^3}F(e) \\ \left\langle \frac{de}{dt} \right\rangle_{\rm sec} &= -\frac{304}{15}\frac{\beta(m_1,m_2)}{a^4}eG(e)\end{aligned} \tag{2.9}$$

in which the auxiliary functions $\beta(m_1, m_2)$, $F(e)$ and $G(e)$ are defined as

$$\begin{aligned}\beta(m_1,m_2) &= \frac{G^3 m_1 m_2 (m_1+m_2)}{c^5} \\ F(e) &= \frac{1+\frac{73}{24}e^2+\frac{37}{96}e^4}{(1-e^2)^{7/2}} \\ G(e) &= \frac{1+\frac{121}{304}e^2}{(1-e^2)^{5/2}}.\end{aligned} \tag{2.10}$$

The secular equations of motion are integrated with the use of a second-order leapfrog integrator, as described in detail in Rantala et al. (2023).

2.3.3 Merger Criteria

During a simulation run two objects can merge if any of the four merger criteria is satisfied. Stars can become gravitationally unbound due to strong encounters with the other cluster members. The type of merging pairs can either be compact objects (white dwarfs, neutron stars, BHs) , tidal disruptions (BH with star) and stellar mergers (stars with stars). The first criterion for a compact binary merger depends on the gravitational-wave driven inspiral timescale $\mathrm{t_{gw}}$. If $\mathrm{t_{gw}}$ is shorter that the binary's current time-step in the time-step hierarchy, then the particles are merged. Compact objects also merge if the radius of the (relativistic) innermost stable circular orbit ($R_{\rm ISCO}$) is larger than their mutual separation. Finally, stars can be tidally disrupted by a compact object (TDE) if the pericentre distance becomes smaller than the tidal disruption radius or in case of a direct collision between two stellar particles, i.e. when their radii overlap.

A common approach for detecting compact object mergers (e.g. Rizzuto et al., 2020; Arca-Sedda et al., 2021; Rizzuto et al., 2022a; Arca Sedda et al., 2023c) is to compute the timescale $\tau_{\rm gw}$ related to the time $\tau_{\rm gw}$ a compact binary needs to reach coalescence. This timescale can be evaluated through the integral expression (Peters, 1964)

$$\tau_{\rm gw} = \frac{15}{304}\frac{a_0^4}{\beta(m1,m2)}\frac{1}{g^4(e_0)}\int_0^{e_0}\frac{g^4(e)(1-e^2)^{5/2}}{e\left(1+\frac{121}{304}e^2\right)}de, \tag{2.11}$$

where a_0 and e_0 are the initial semi-major axis and eccentricity of the binary, $\beta(m_1, m_2)$ is the function defined in Eq. (2.10) and $g(e)$ is defined (Maggiore, 2007) by

$$g(e) = \frac{e^{12/19}}{1-e^2}\left(1+\frac{121}{304}e^2\right)^{870/2299}. \tag{2.12}$$

The expression for $\tau_{\rm gw}$ for $e = 0$, i.e. circular orbits, is then

$$\tau_{\rm gw} = \frac{5}{256} \frac{a_0^4}{\beta(m_1, m_2)}. \tag{2.13}$$

We tabulate the values of this integral by evaluating it separately (before the actual runs) for a large number of e_0, in order to avoid computing it every time-step. Then by interpolating for those table values, we have an estimate for $\tau_{\rm gw}$ throughout the simulation. However, extra caution should be taken when using the $\tau_{\rm gw}$ criterion due to the strong dependence of eccentricity in the computed integral value. Even tiny fluctuations of eccentricity (e.g. from weak 3- body and fly-by encounters) would result in significant underestimation of $\tau_{\rm gw}$ and false merger identification.

The second criterion for merging compact objects is based on the innermost stable circular orbit (ISCO) with radius

$$r_{\rm isco} = \frac{6GM_\bullet}{c^2} = 3R_{\rm sch}, \tag{2.14}$$

where c is the speed of light and $R_{\rm sch}$ the Schwarzschild radius of the black hole. Two COs are then merged if their mutual distance is lower than $r_{\rm isco}$.

If one of the particles is a compact object and the other one is a star, then the latter could be disrupted. This happens when (Rees, 1988a; Kochanek, 1992)

$$r_{\rm peri} < r_{\rm tde} = 1.3 \left(\frac{m_\star + M_\bullet}{m_\star} \right)^{1/3} r_\star, \tag{2.15}$$

where $m_\star$ and $r_\star$ is the mass and radius of the star and $M_\bullet$ is the mass of the compact object. Two stars are assumed to merge when they overlap i.e., when their distance is shorter than the sum of their radii

$$r < r_{\rm overlap} = r_{\star,1} + r_{\star,2}. \tag{2.16}$$

2.3.4 Initial Conditions and Simulations

We generate initial conditions (ICs) for pairs of two identical star clusters of $N = 64000$ single stars without primordial binaries and a total mass of $M_\star = 2.7 \times 10^4 M_\odot$, each using the `McLuster` code (Küpper et al., 2011). The single star cluster model follows a King density profile (King, 1966) with a fixed half-mass radius of $R_h = 1$ pc and central potential parameter related to the compactness of the cluster $W_0 = 5$, which represents a moderately compact cluster. The age of the clusters is $t_{\rm age} = 1$ Gyr and the stellar masses are sampled from a Kroupa initial-mass-function (IMF) (Kroupa, 2001) as zero-age main sequence stars in the range of $0.08 M_\odot$ up to $100 M_\odot$. The age of the cluster has been selected such that stellar evolution processes do not contribute to the overall evolution of the system, allowing us to focus on the long-term dynamical evolution. The mass range of stellar particles in the simulations is $0.08 \leq m_\star \lesssim 1.89$ M$_\odot$, $0.88 \leq m_{\rm WD} \lesssim 1.37$ M$_\odot$

for WDs, $1.1 \leq m_{\rm NS} \lesssim 1.91\,{\rm M}_\odot$ for NSs and $5.6 \leq m_{\rm BH} \lesssim 40.5\,{\rm M}_\odot$ for stellar-mass BHs. From the initial conditions, we have initially $N_{\rm BH} = 250$, $N_{\rm NS} = 944$ and $N_{\rm WDs} = 4100$. The number of retained NSs in the initial conditions is related to the way natal kicks for supernova remnants are assigned in Küpper et al. (2011) , i.e., when the recoil velocities are low so the remnant cannot escape the cluster. With the use and calibration of pulsar proper motions (Hobbs et al., 2005; Kapil et al., 2023) the recoil kicks reach high velocities resulting in small fraction (only a few) of retained NSs in the initial system. Examples of a more sophisticated prescription for the number of retained NSs in the ICs can be found in Banerjee et al. (2020). The NS population in our simulations does not significantly contribute to the overall ejection demographics, but could potentially lead to false rates of escaping NSs and the formation of a larger number of NS binaries.

We use three different initially bound orbits for the merging star clusters. Each orbit has the same fixed semi-major axis $a_{\rm semi} = 2$ pc (and thus a fixed orbital energy, since $E = -GM_1M_2/2a_{\rm semi}$) and three different values of eccentricity $e = [0.05, 0.5, 0.99]$. The second cluster is located at the apocentre of the orbit with $r_{\rm apo} = [1.9, 1.0, 0.02]$ pc for the three orbits. For each of the merger initial setups, we explore three scenarios: neither of the clusters host an MBH, the primary cluster host an MBH of $M_\bullet = M_1 = 1000\,M_\odot$ and finally when both clusters host an MBH of $M_1 = M_2 = 500\,M_\odot$. Furthermore, we run three additional simulations where we consider a star cluster with $N = 128000$, $M_\star = 5.4 \times 10^4\,M_\odot$ and $R_h = 1\,{\rm pc}$ without a prior merger. For these simulations we either place a single, a binary with $a_{\rm b} = 0.01$ pc and $e_{\rm b} = 0.5$, or no MBH at all. We follow the evolution of the merger remnants or the single clusters up to $t = 100\,{\rm Myr}$. An overview of the merger progenitors and their orbital elements is presented on Table 2.2 .

In the next sections, we present the main outcomes of our stellar cluster merger simulations. We discuss how the presence of a single or a binary MBH affects the evolution of the merger remnants, their kinematic and structure properties as well as the demographics of the escaping stellar and compact object populations, which is the main focus of this work. An example outlook (here for the $e = 0.05$ cluster orbits) of the simulations at different times ($t = 0.5, 1, 15\,{\rm Myr}$), is shown in Fig. 2.1. In the figure we show the surface stellar density and highlight the velocity vector $\vec{V}$ field of unbound stars and COs.

If an MBH is present in both of the merging clusters, a massive black hole binary (MBHB) forms. The binary orbit keeps shrinking (monotonic decrease of $a_{\rm b}$) until the end of the simulation, due to interactions with the background stars and COs. We describe the evolution of the MBHBs in detail in Section 2.5.

2.4 Properties of the star clusters

Adopting the definition by Trenti et al. (2009), the core size or *core radius* of a star cluster following a King density profile is given by Casertano & Hut (1985),

$$r_{\rm c} = \sqrt{\frac{\sum_i \rho_i^2 \left|\mathbf{r}_i - \mathbf{r}_{\rm d}\right|^2}{\sum_i \rho_i^2}}, \tag{2.17}$$

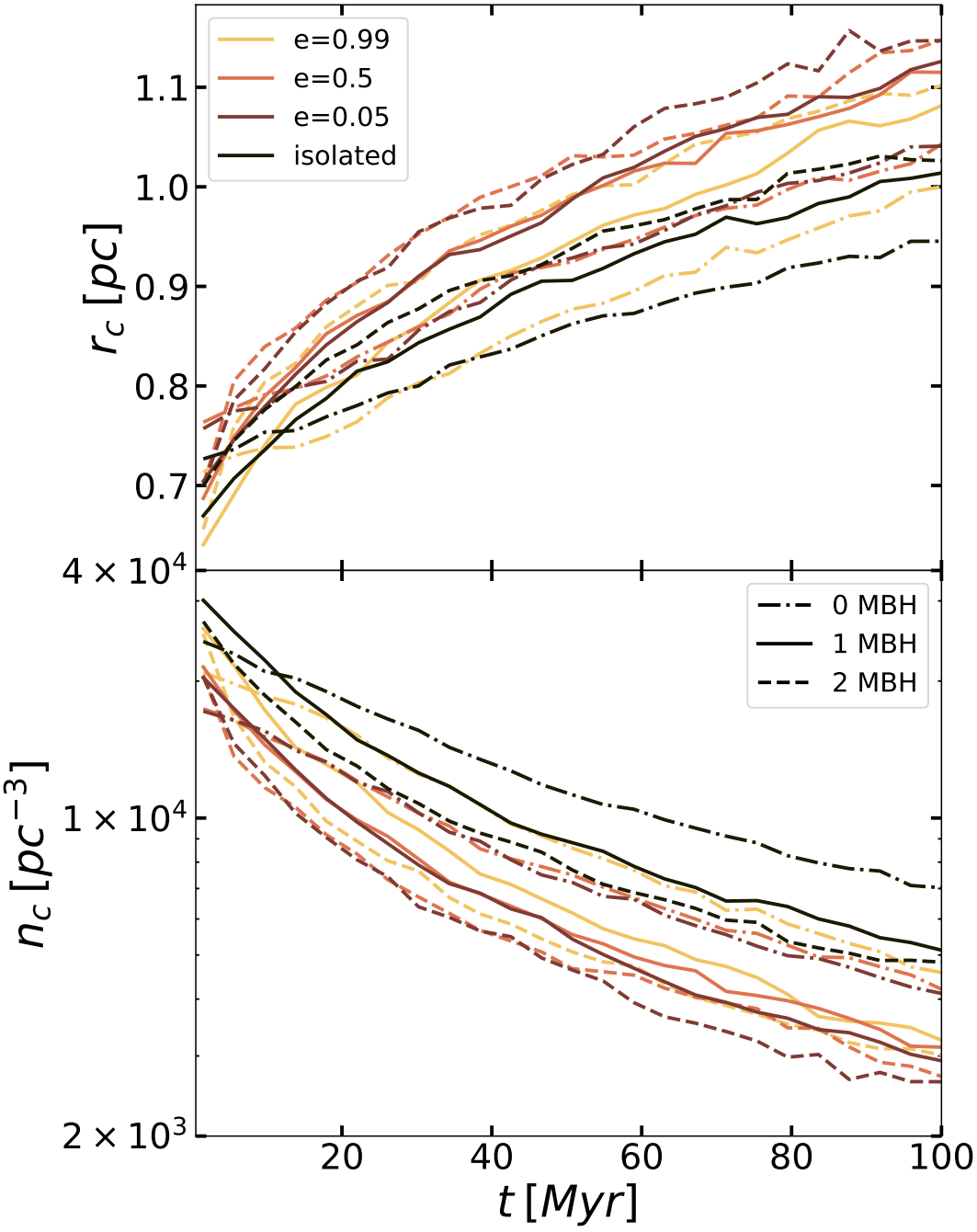

Figure 2.2: Evolution of the core for the three cases. Top panel: Core radius r_c. Bottom panel: Number density inside r_c. The expansion rate (decreasing number density) is higher for remnants with more MBHs and lower values of eccentricity.

Table 2.2: List of cluster merger simulations with two (2MBH), one (1MBH) or no MBH (noMBH) with three cluster orbital eccentricities e (fourth column). The semi-major axis of all merger orbits is 2 pc. We also give the MBH masses ($M_{\bullet,1}, M_{\bullet,2}$), the pericentre distance and velocity ($r_{\rm peri}, v_{\rm peri}$), and the apocentre velocity ($v_{\rm apo}$) of the initial star cluster orbits. Since the star clusters are not point masses, they do not follow this initial orbit exactly but merge due to dynamical friction. The bottom three simulations (*_iso*) correspond to isolated setups with $e = 0.5$.

Simulation	$M_{\bullet,1}$ [$M_\odot$]	$M_{\bullet,2}$ [$M_\odot$]	e	$r_{\rm peri}$ [pc]	$v_{\rm peri}$ [km/s]	$v_{\rm apo}$ [km/s]
2MBH_e099	500	500	0.99	0.02	151.89	0.76
2MBH_e05	500	500	0.50	1.0	18.65	6.22
2MBH_e005	500	500	0.05	1.9	11.32	10.24
1MBH_e099	1000	-	0.99	0.02	151.89	0.76
1MBH_e05	1000	-	0.50	1.0	18.65	6.22
1MBH_e005	1000	-	0.05	1.9	11.32	10.24
noMBH_e099	-	-	0.99	0.02	150.48	0.75
noMBH_e05	-	-	0.50	1.0	18.47	6.16
noMBH_e005	-	-	0.05	1.9	11.21	10.15
2MBH_iso	500	500	-	-	-	-
1MBH_iso	1000	-	-	-	-	-
noMBH_iso	-	-	-	-	-	-

where ρ_i is the local density around a star i defined as

$$\rho_i = \frac{\sum_{j=1}^{5} m_j}{\frac{4}{3}\pi r_n^3} \tag{2.18}$$

and r_n is the distance to the n-th nearest neighbor i, while $\mathbf{r}_{\rm d}$ is the position of the density centre:

$$\mathbf{r}_{\rm d} = \frac{\sum_i \rho_i \mathbf{r}_i}{\sum_i \rho_i}. \tag{2.19}$$

When the cores of the two progenitor clusters overlap, i.e., when their relative distance d_{12} becomes shorter than r_c, we assume that the clusters have merged. The evolution of the core radii and the respective enclosed number density is shown in Fig. 2.2. From Fig. 2.2 we see that the presence of a single or binary MBH in the remnants leads to more rapid expansion due to a higher mass-loss rate. Essentially, particles interacting with the MBHs are radially scattered outwards, leading to constant decrease of the number density inside the core (bottom panel in Fig. 2.2) which indicates mass-loss inside r_c.

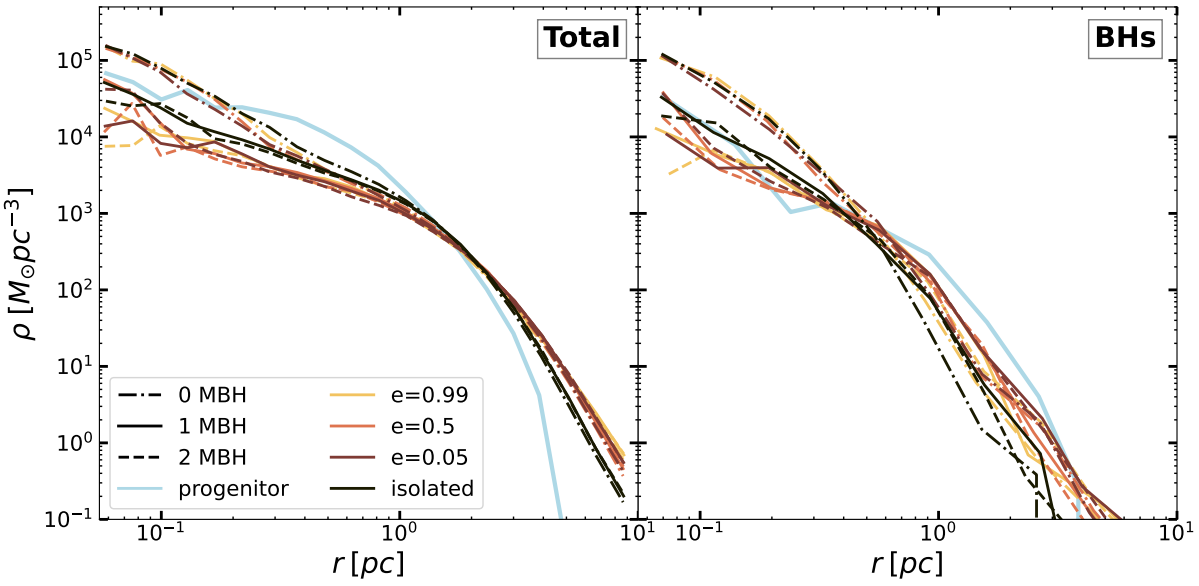

Figure 2.3: Final density ($t = 100$ Myr) profiles of the merger remnants. Left panel: density profiles including all cluster members. Right panel: density profiles of the stellar BH sub-systems. Remnants hosting a single or binary MBH result in lower density in the central regions. For BH sub-systems in the absence of MBHs to provide a counteracting source of contraction, the corresponding density profiles become more cuspy.

Since the core radius r_c is not exactly the same (ranging between $0.6\text{pc} < r_c < 0.8\text{pc}$) for the various progenitor clusters, we define a threshold distance such that when $d_{12} < d_{\rm crit} = 2\text{pc}$, the two clusters have merged. The timescale of this process depends on the orbital eccentricity of the merger and on the number of MBHs in the system. Specifically for remnants with two MBHs, this happens at $t = 1$ Myr while for the other cases ranges between $t = 1.25$ Myr and $t = 2$ Myr.

The density evolution for $t > 2$Myr until the end of the run, is only moderately affected by the merger process and its mainly driven by the presence of the single or binary MBHs. Figure 2.3 shows the final (at $t = 100$Myr) density profiles of the merger remnants and that of the stellar BHs only. Overall we observe an increase of the central density, which inversely scales to the presence and number of MBHs in the remnant, with an even more clear signature for the sub-system of BHs (right panel in Fig. 2.3). The binary transfers its orbital energy

$$E = -\frac{GM_1M_2}{2a_{\rm b}}, \tag{2.20}$$

to the surrounding stars either through dynamical friction (DF) (Begelman et al., 1980; Varisco et al., 2021) or three-body encounters Hills (1991) accompanied by stellar ejections which carry out energy and angular momentum, leading to a decrease of stellar density around the MBHB. This process, known as *core scouring*, is likely responsible for the

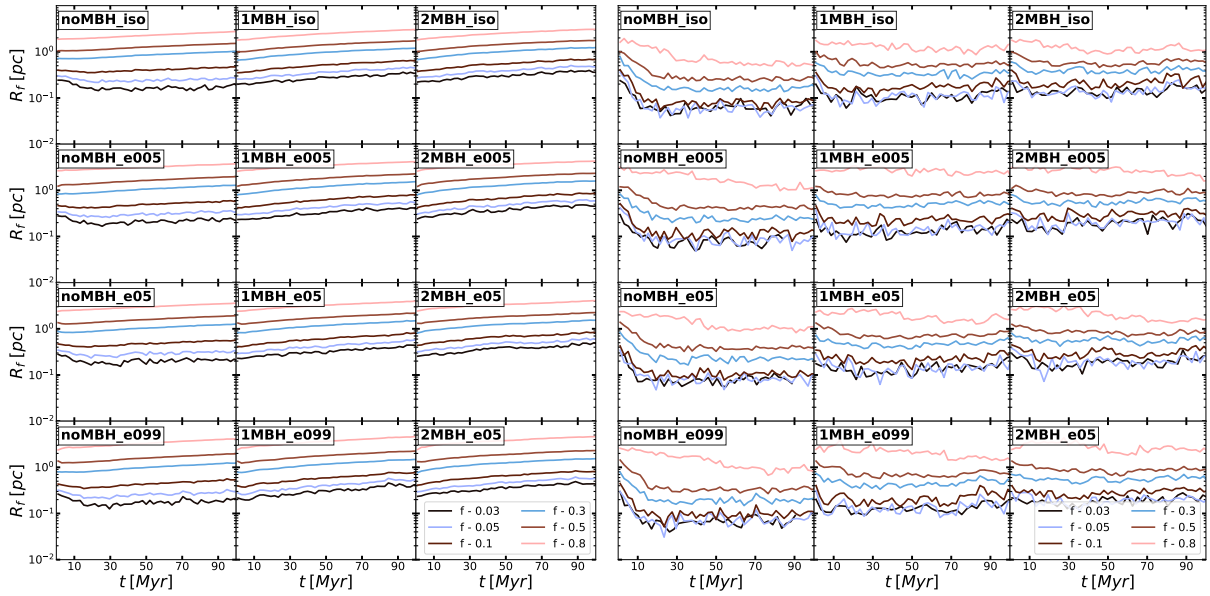

Figure 2.4: Lagrangian radii for the $3-80\%$ enclosed mass of the entire system (top plot) and for the respective BH subsystems only (bottom plot). Columns from left to right refer to different number of MBHs, while rows to different orbital eccentricities of the merger orbits. The top row in each panels shows the isolated runs. An initial central collapse phase is clearly seen in the runs without MBHs (left columns).

presence and formation of flat central cores in luminous galaxies (e.g. Rantala et al. 2018), and can likely affect the central properties of merged star cluster remnants as well. The characteristic timescale over which the energy is extracted from the binary is given by Merritt (2013),

$$T_{\rm E} = \left| \frac{1}{E} \frac{{\rm d}E}{{\rm d}t} \right|^{-1} \approx \frac{\sigma^3}{CG^2 M_2 \rho}, \tag{2.21}$$

where σ and ρ are the three-dimensional velocity dispersion and density of the stellar background and C is a constant that depends on the energy transfer mechanism[1]. In our simulation models we have $T_{\rm E} = 1 - 3.7$ Myr, which is consistent with the time needed (~ 1 Myr) for the respective progenitor clusters to merge.

2.4.1 Star cluster evolution

A bound self-gravitating system admits negative heat capacity $C_{\rm V}$, allowing the release of energy from the centre to the outer parts, leading to the formation of a contracting core with radius r_c (Eq. 2.17) and an expanding halo (Lynden-Bell et al., 1968; Lynden-Bell, 1999).

[1] $C \approx 10$ for DF or 3-body encounters.

In the absence of an additional energy source in the centre to halt the contraction the core will eventually collapse, a process called the *gravothermal catastrophe* (Antonov, 1960, 1961, 1962). The core undergoes a series of contraction-expansion phase, known as *gravothermal oscillations* (Sugimoto & Bettwieser 1983; Heggie 1993). For a single and equal mass component system in isolation, the core collapse would happen at about $15t_{\rm rh}$ (Cohn, 1980), where $t_{\rm rh}$ is the half-mass relaxation time (Spitzer, 1987).

$$t_{\rm rh} = \frac{0.138N^{1/2}}{\ln\Lambda}\left(\frac{R_{\rm h}^3}{G\bar{m}}\right)^{1/2}. \tag{2.22}$$

Here N is the star/particle number of the system, R_h and $\bar{m}$ the half-mass radius and average stellar mass and finally $\Lambda = \gamma N$ is the Coulomb logarithm. In our simulations we sample the stellar masses from a Kroupa IMF[2], which corresponds to $\gamma = 0.02$ (Giersz & Heggie, 1997) for multi-mass clusters. In realistic (multi-mass) star clusters, higher-mass stars have lower velocity dispersion than the low-mass ones, driving the system towards energy equipartition, i.e., evenly distributing the kinetic energy of the system (Spitzer, 1969, 1987). The massive stars segregate to the centre by transferring their kinetic energy to low mass stars, thus expanding the orbits of the latter. The segregation time (Spitzer & Hart, 1971; Portegies Zwart et al., 2004b) is defined as

$$t_{\rm s} = \frac{\bar{m}}{m_{\rm max}}\frac{0.138N}{\ln\left(0.11M_{\rm cl}/m_{\rm max}\right)}\left(\frac{R_{\rm h}^3}{GM_{\rm cl}}\right)^{1/2}, \tag{2.23}$$

where $M_{\rm cl}$ is the total mass of the cluster and $m_{\rm max}$ is the mass of the most massive object. Since we don't assume any degree of primordial mass segregation in our initial conditions, we compute the segregation time of the merger remnants at $t = 2$ Myr, when all the progenitors have merged. Using Eq. 2.23 for the remnant clusters without an MBH, we find $t_{\rm s} \sim 8 - 10$ Myr. In timescales of the order of $\sim t_{\rm s}$ compact objects, i.e., the most massive particles sink towards the centre of the remnant (Baumgardt & Makino, 2003).

The evolution of the radii enclosing $3 - 80\%$ of the cumulative total mass (Lagrangian radii) of all stellar and compact objects for all simulations is shown in the top panel of Fig. 2.4. The left, middle and right columns show the systems with no, single, or binary MBHs. For the isolated cluster the centre of the system without MBH (left) undergoes core contraction on a timescale of $\sim$ 20 - 30 Myr while the half-mass radius expands. The systems with single and binary MBH (middle and right) show no core collapse as rapidly forming binaries with the central MBH prevent this (see e.g. Rizzuto et al., 2023, and references therein). Stars and compact objects bound to MBHs interact, heating up the core and lead to its mild but constant expansion. The evolutionary behaviour is very similar for cluster merger remnants (second to bottom row). For mergers without a MBH the one with the highest eccentricity (bottom left panel) shows most core contraction. For systems with one or two MBHs the eccentricities of the merger orbits do not change the structural evolution.

[2]For a single-mass system $\gamma = 0.11$ (Giersz & Heggie, 1994).

In the bottom panel of Fig. 2.4 we show the Lagrangian radii evolution of the respective BH subsystems only. Initially, the general behaviour is the same as for the entire cluster (left panels in Fig. 2.4). However, the BH subsystem contracts faster on a $\sim$ 10 Myr timescale which is the expected mass segregation timescale (see Eq. 2.23) in all cases without MBHs (left column). However, the presence of just one MBH does not prevent the collapse in for the BH subsystem. In addition the BHs form a central, stable subcluster which is not expanding like the entire cluster population. The dynamical interactions in this central BH cluster provide a continuous source of energy for ejections of stars and compact objects.

The sphere around an MBH of mass $M_\bullet$ where its presence dominates the gravitational potential of the system is called *sphere of influence* (SOI) . The radius of this sphere $r_{\rm SOI}$ is then given by (Merritt, 2013)

$$M_\star(r < r_{\rm SOI}) = 2M_\bullet, \tag{2.24}$$

where $M_\star$ refers to the stellar mass.

The interactions of stars within $r_{\rm SOI}$ with the MBH/MBHB can significantly effect their growth through TDEs Rizzuto et al. (2023) or GW-merger events, but also play an important role on the evolution of the remnant cores (e.g. Aros et al., 2020, and references therein). Figure 2.5 shows the fraction of bound stars to the single or binary MBH, i.e., stars with negative orbital energy $E = \frac{m_* v^2}{2} - \frac{G m_* M_{\rm BH}}{r} < 0$, where m_* is the mass of the individual star and r, v are the relative distance and velocity w.r.t. the MBH or the centre of mass of the MBH binary. After the cluster mergers the bound fractions are $f_{\rm bound} \sim 0.14$–0.22 in our simulations. The MBH case behaves in a qualitatively similar manner as the binary MBH setup: the bound fractions reach values of $f_{\rm bound} \sim 0.1$ in both cases. This reflects the similar overall evolution of central cluster properties such as stellar densities and velocity dispersions. We however note that the bound fraction decreases somewhat more rapidly in the MBHB setups. For clusters with a single MBH we find similar behavior to that of the $M_\bullet = 2000\ M_\odot$ case in (Rizzuto et al., 2023). We note though, that their clusters are more dense and that stellar-mass BHs were not present in their ICs. The remnants with an MBH binary, maintain approximately the same fraction of bound stars until the end of the simulation. The bounds stars in the vicinity of the MBH or the MBHB provide enough energy supply to support the expansion of the core (Fig. 2.2) and the remnant itself. Moreover, encounters with the MBHB lead to 3- and 4- body encounters (Section 2.2.4), capable of kicking stars and COs in the outer parts of the cluster. The lower panel of Figure 2.5 depicts the total energy loss from the bound cloud of stars inside $r_{\rm SOI}$ leading to its growth. Those encounters drain orbital energy from the MBH binaries, leading to the shrinking of their orbits (decrease of semi-major axis) . This hardening process is further discussed in Section 2.5. The energy inside the cloud in the form of dynamical heating combined with that from the BH sub-system (Mackey et al., 2008) leads to the expansion of the remnant cores and monotonic decrease of the number density (bottom panel in Fig. 2.2). Subsequently, the drop of the number density is associated with a decrease in the mass of the bound cloud, i.e., the gravitational potential

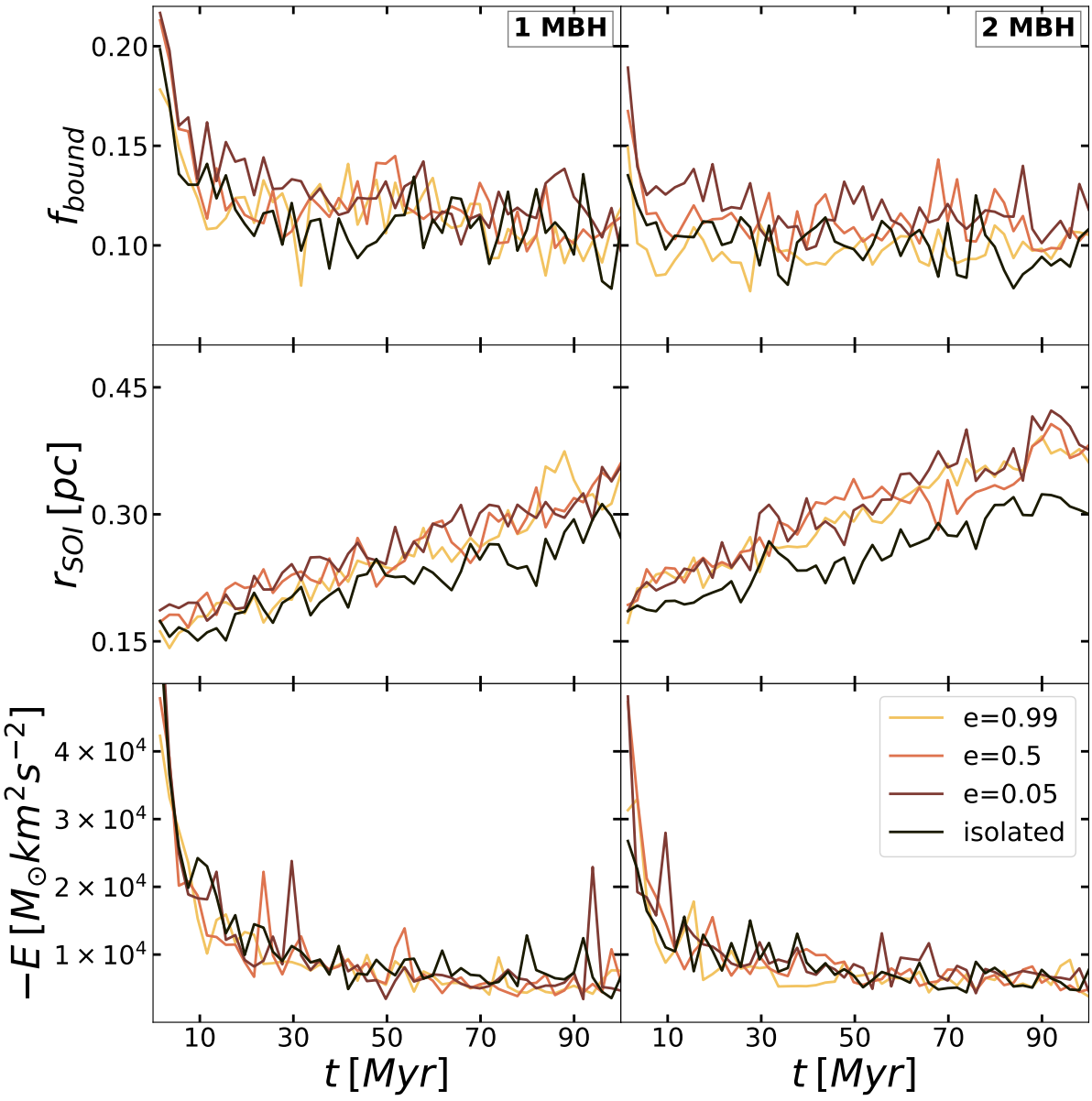

Figure 2.5: Top: fraction of bound stars $f_{\rm bound}$ inside the sphere of influence $r_{\rm SOI}$ of the single/binary MBHs. Middle: MBH radius of influence. Bottom: Energy inside $r_{\rm SOI}$. Both Single and binary MBHs initially have a high fraction of bound stars, which is decreased over time due to encounters inside $r_{\rm SOI}$, leading to energy losses elevating its growth. The orbital energy released from the hardening of the MBH binary also contributes to the expansion.

of the core gradually becomes more shallow (i.e., a drop in the local escape velocity $V_{\rm esc}$), allowing more particles to escape to the outer parts of the cluster.

Finally the merger process itself has an effect on the differential energy distribution of the cluster stars. For a bound gravitational system in virial equilibrium $2T + V = 0$

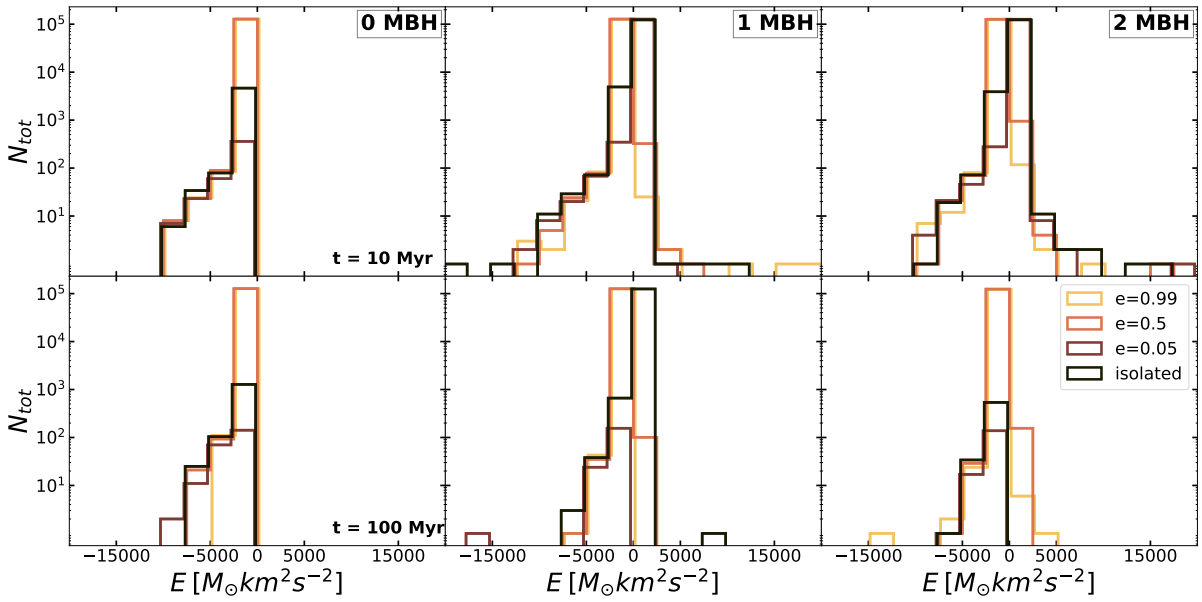

Figure 2.6: Binding energy distribution for stars and compact objects in all simulated clusters at $t = 10$ Myr (top) and $t = 100$ Myr (bottom). Once the systems contain at least one MBH (middle and left panels) objects can become unbound (positive energies). In particular at early times ($t = 10Myr$, middle panel) the high energy objects can be clearly seen. At later times many of the early escapers have travelled beyond 100 pc and have been removed from the simulation. There is no clear trend with the shape of the cluster merger orbit or the merging process itself.

(kinetic energy T and potential energy V) with $T = -E$ and $V = 2E$. The total energy is simply $E = T + V$. During the merger, the system is not in equilibrium which means that although the total energy E remains constant, T and V will oscillate around their values leading to the widening of the differential energy distribution (Hilz et al., 2012). This results to the most bound particles become even more bound, while weakly bound particles might gain enough energy to escape from the local gravitational potential.

This process, known as *violent relaxation* further contributes to the expansion of the core and the cluster itself, comparing to clusters without any prior merger (dashed lines in 2.2) .

Figure 2.6 shows the particle energy distribution at $t = 10$ and $t = 100$ Myr. We see that clusters with MBHs hold a large fraction of unbound particles at early times corresponding to potential ejections. It is clear that the presence of MBHs broadens the energy distribution, especially for stars with $E > 0$ we observe a persistent tail in the distribution even after $t = 100$Myr. Especially, from the radial velocity V_r distribution (Fig. 2.7), we see that single MBH clusters develop a positive V_r tail which is larger for MBH binaries. This tailed distribution is closely connected to the number and velocity of ejected bodies as we describe in Section 2.2.

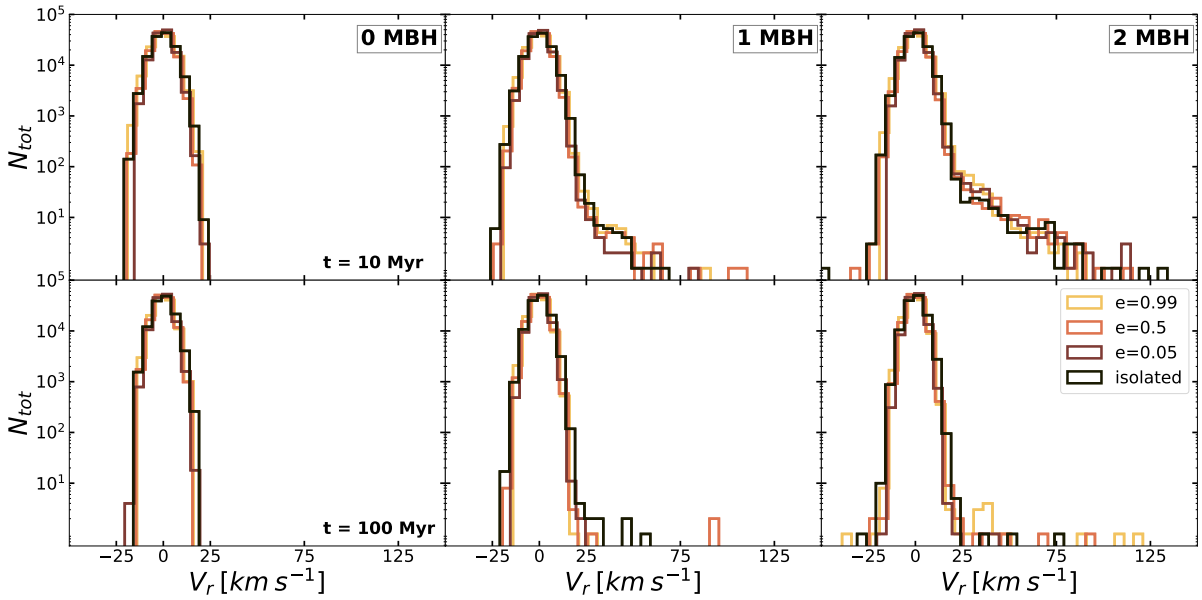

Figure 2.7: Distribution of the radial velocity of all stars and compact objects in all simulations at $t = 10$ Myr (top) and $t = 100$ Myr (bottom). The systems without MBHs (left panels) show a distributions with absolute radial velocities ≤ 23 km s^{-1}. This is the escape velocity from the cluster centres. Once an MBH is present, the distributions extend towards ~ 75 km s^{-1} for one MBH (middle panels) and to values $\gtrsim 120$ km s^{-1} for binary MBHs (right panels). The unbound part of the distributions in Fig. 2.6 is caused by objects within the high velocity tail.

2.4.2 Star cluster shapes

In order to determine the inherent three-dimensional structure of the star clusters, we compute the reduced inertia tensor given by given by Gerhard (1983); Bailin & Steinmetz (2005)

$$I_{ij} = \sum_k m_k \frac{r_{k,i} r_{k,j}}{r_k^2}, \tag{2.25}$$

where k is the total particle number. The eigenvectors and eigenvalues of this tensor correspond to the directions of the principal axes a, b, c (major, intermediate and minor axis respectively, i.e., $a > b > c$) of the remnant. Their ratios can then be used to define the triaxiality parameter T (Jesseit et al., 2005; Binney & Tremaine, 2008) given by

$$T = \frac{1 - (b/a)^2}{1 - (c/a)^2}. \tag{2.26}$$

Fig. 2.8 shows the evolution of the principal axes ratios and the triaxiality parameter within the half-mass radius $r_{\rm h}$, where $T = 1$ correspond to prolate, $T = 0.5$ to triaxial and $T = 0$ to oblate shapes.

The shape of merger remnants is an indicator of the orbital families that are generated

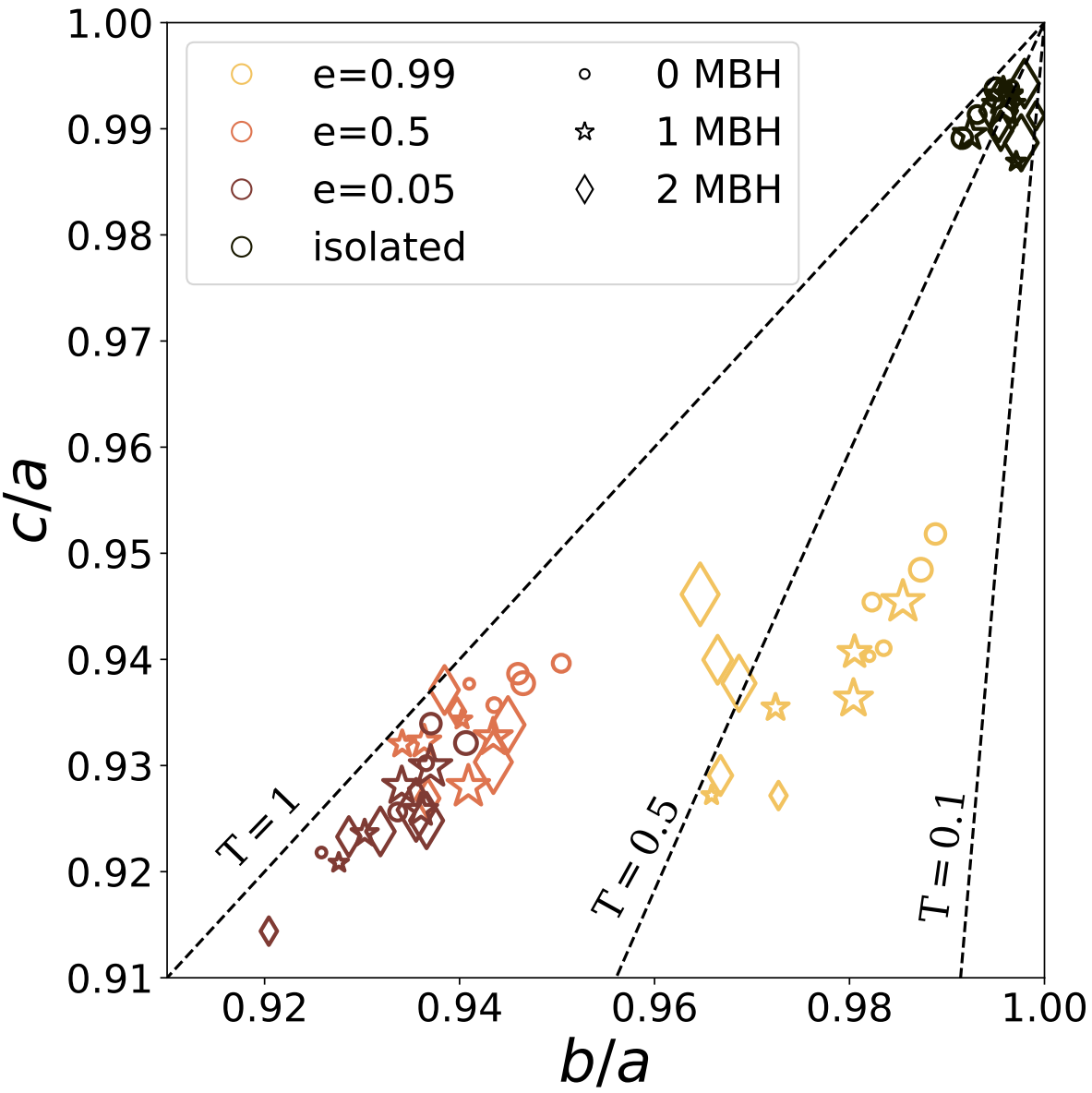

Figure 2.8: Axis rations of the three principal axes of the moment-of-inertia tensor within the $r_{\rm h}$. The dashed lines correspond to constant triaxiality T, where $T = 1$: prolate, $T = 0.5$: triaxial, $T = 0.1$: oblate. Different colours here correspond to different values of eccentricity, while markers to the number of MBHs. The size of the markers grows with time, i.e., the smaller one is at $t = 0$.

during the merger process (for a detailed analysis on a galaxy merger context, see for example Frigo et al. 2021). In Fig. 2.8 we present the time evolution of the remnant shapes. The size of the markers indicates the time-evolution of cluster shapes, where the largest ones correspond to $t = 100$ Myr (end of the simulation). Constant triaxiality T

is marked with the three dashed lines. This provides a qualitative way to classify the resulting shapes for the various models based on their evolution and initial merger orbit. First of all, we notice that the clusters without prior merger are initially spherical and isotropic and maintain their shape (black markers in the top-right corner of Fig. 2.8) until the end of the simulation.

The eccentricity of the merging star cluster orbits plays an important role in determining the shape and kinematics of the remnant. Low e orbits carry more angular momentum, since $\mathcal{L} = \mu\sqrt{GMa\,(1-e^2)}$ (where $M = M_1 + M_2$ and $\mu = M_1 M_2/M$) which is then transferred to the stars. Our merger simulations result in a narrow range of c/a with a clear trend of low ($e = 0.05$) and medium eccentricities ($e = 0.5$) towards less oblate systems (brown and orange markers in Fig. 2.8). Very eccentric ($e > 0.9$) merger orbits on the other hand, tend to scatter stars in radial orbits resulting in more oblate and triaxial shapes as can be seen in Fig. 2.8 (yellow markers). We conclude that merger remnants have less spherical shapes than isolated clusters, the process driven by the eccentricity of the progenitor cluster orbits.

2.4.3 Star cluster kinematics

In a spherical coordinate system, the two angular velocity dispersion components $\sigma_\theta, \sigma_\phi$ can be combined into a tangential velocity dispersion σ_t as

$$\sigma_\mathrm{t} = \sqrt{\frac{\sigma_\theta^2 + \sigma_\phi^2}{2}}. \tag{2.27}$$

The non-isotropic nature of the kinematic structure of the stellar system can be characterized by the velocity anisotropy parameter β (Binney & Tremaine, 2008), defined as

$$\beta = 1 - \frac{\sigma_\theta^2 + \sigma_\phi^2}{2\sigma_\mathrm{r}^2} = 1 - \frac{\sigma_\mathrm{t}^2}{\sigma_\mathrm{r}^2}. \tag{2.28}$$

The velocity anisotropy β is closely related to the orbital structure of a stellar population. When the stellar orbits are purely radial, then $\sigma_\mathrm{t} = 0$ and $\beta = 1$. Conversely, for a stellar population with exclusively circular orbits, $\sigma_\mathrm{r} = 0$ and $\beta = -\infty$. The system is isotropic ($\beta = 0$) if the two components $\sigma_\mathrm{r}, \sigma_\mathrm{t}$, are equal.

To compute velocity dispersion profiles for our star cluster setups and to reduce the noise we construct average dispersion profiles. To do so we use 10 simulation snapshots from the last 5×10^4 yr in our runs. Each snapshot is centred in space and velocity to the region of highest stellar density using the shrinking sphere approach (Power et al., 2003). The velocity dispersion and anisotropy profiles (Fig. 2.9) of stars (thick solid lines) and of COs (thin dotted lines) of the remnants at and $t = 100$ Myr are presented in Fig. 2.9. The left panels correspond to simulations without MBHs. Both σ_r and σ_t have values of about $\lesssim 10$ km s^{-1} and decrease with increasing radius. The $\beta \sim 0$ profiles indicate isotropic velocity dispersion in the inner parts of all clusters. The merger orbits do not change the

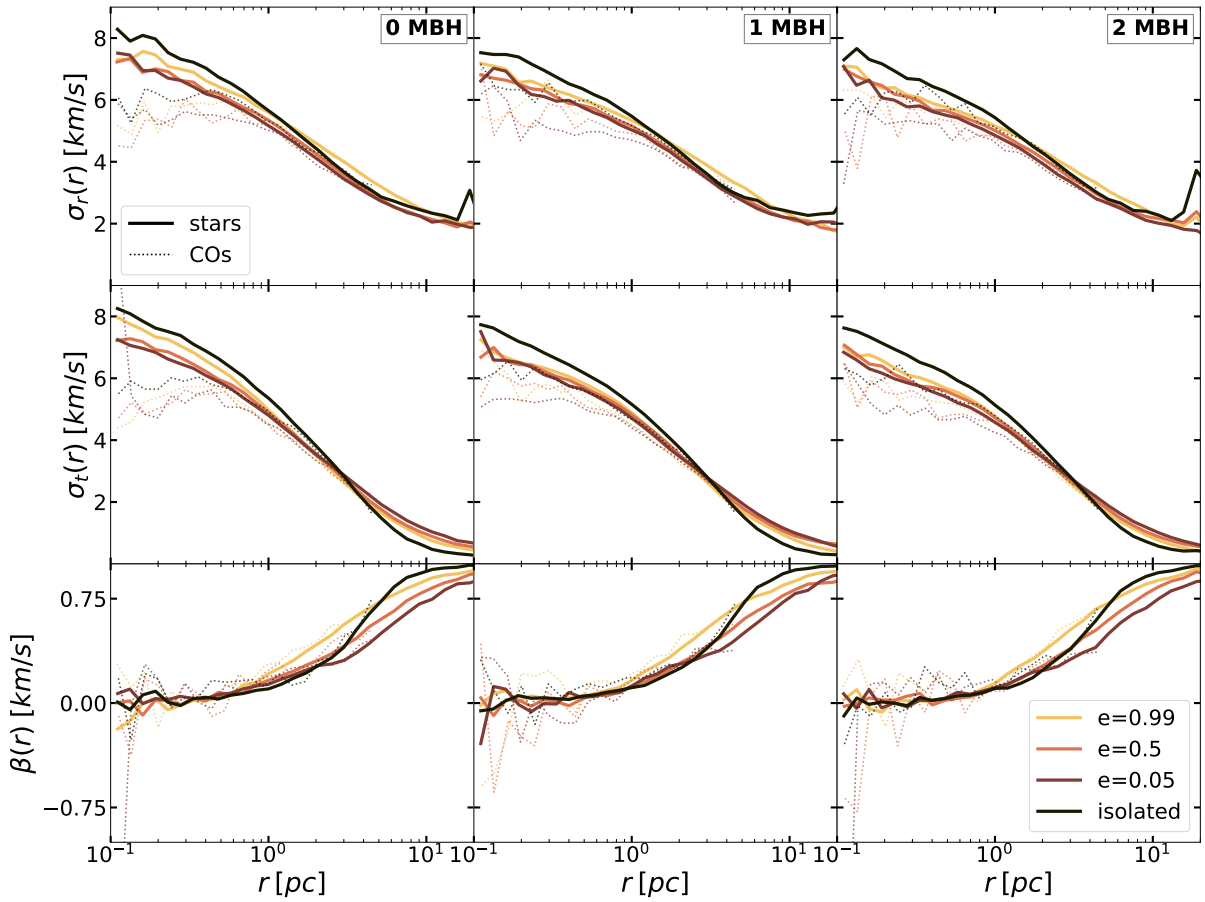

Figure 2.9: Radial $\sigma_{\rm r}$ (top panels) and tangential σ_ϕ (middle panel) velocity dispersion profiles and the anisotropy parameter β (bottom panels) for simulations without (left column) with one (middle column) and with two (right column) MBHs after 100 Myr. The thick solid lines correspond to stars only, while the thin dotted lines to the contribution of compact objects. All systems show isotropic velocity dispersions in the centre and more massive particles, i.e., compact objects have lower velocity dispersion, as expected from energy equipartition.

dispersion profiles significantly. The presence of one (middle column) or two (right column) MBHs also does not change the kinematic structure significantly.

Rotation of cluster merger remnants

For the simulated cluster mergers, orbital angular momentum is transferred to internal angular momentum. The effect is strongest for low eccentricity orbit (i.e. $e = 0.05, 0.5$) which have the highest orbital angular momentum. This corresponds to higher merger remnant rotation velocities.

We present the two dimensional line-of-sight (LOS) velocity ($V_{\rm LOS}$) maps of the cluster merger simulations after 100 Myr of evolution in Fig. 2.10. The maps are constructed

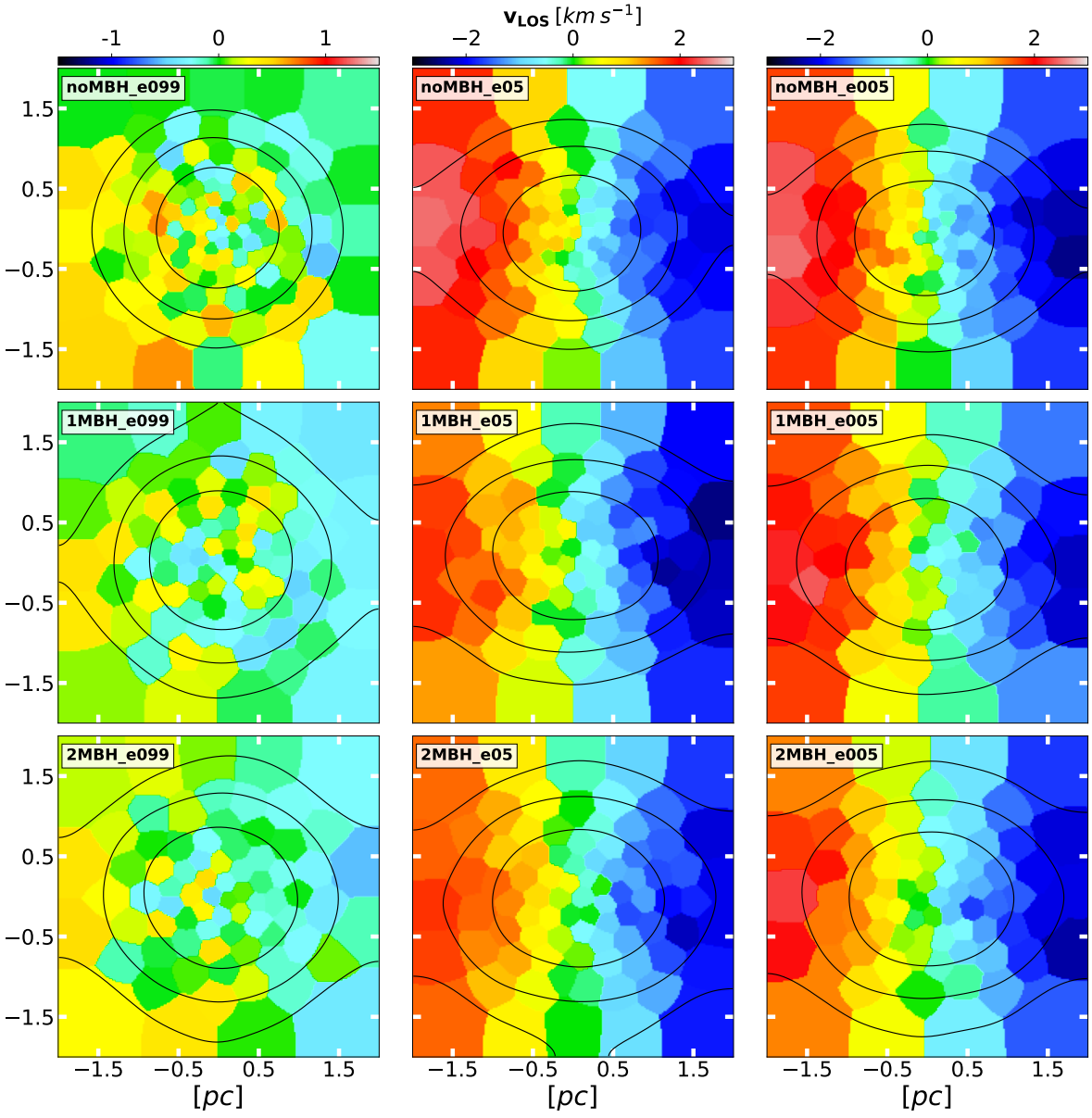

Figure 2.10: Two dimensional (x vs. z) line-of-sight velocity maps of the stars in the simulated cluster mergers at $t = 100$ Myr. From top to bottom we show the models with no, one, and two MBHs and the eccentricity of the merger orbit is decreasing from left (most radial) to right (most circular). The more circular merger remnants (middle and left panels) show no clear signs of rotation while the radial orbit remnant (left panels) show no rotation. The presence of an MBH does not affect the rotation properties. Contours of constant surface density are also displayed.

utilizing the analysis package `pygad` (Röttgers et al., 2020). Following Naab et al. (2014), these maps are produced similar to the analysis of observational integral field unit data (see e.g. Naab et al., 2014, for more details). We use the clusters' reduced moment of

inertia tensor given by Eq. 2.25 to align the major axis of the cluster with the $x-$axis and perform the analysis within the central region of about ~ 2 half-mass radii, corresponding to a spatial extent of 4 pc. The velocity data is represented by *spaxels* of constant signal-to-noise ratio (a fixed number of stars per spaxel) using a Voronoi tessellation algorithm (Cappellari & Copin, 2003). We also show contours of constant surface density.

The highly eccentric ($e = 0.99$) merger orbits carry the least angular momentum and the respective remnants show no sign of ordered rotation (left panels in Fig. 2.10) independent of whether the clusters host black holes or not. The mergers with higher angular momentum orbits produce remnants which clearly show ordered rotation with velocities up to ~ 3 km s^{-1} (middle and right panels of Fig. 2.10). In contrast to the velocity dispersion (see Sec. 2.4.3), the presence of MBHs in the clusters does not change the rotation features.

2.5 Formation and Evolution of Massive Black Hole Binaries

In this section we focus on the formation and evolution of the MBH binaries in the merger runs `2MBH_e005`, `2MBH_e05` and `2MBH_e099` with two MBHs and the isolated cluster, `2MBH_iso`, with a central MBH binary. The different cluster orbits affect the time when the MBH binaries become bound in the cluster mergers, while the `2MBH_iso` MBH binary is bound by definition. For the `2MBH_e05` and `2MBH_e005` runs, the MBH binaries become bound at 1 Myr and 1.3 Myr, respectively. For the merger with the highest eccentricity of $e = 0.99$ (`2MBH_e099`) the MBH binary becomes first bound at 1.1 Myr then unbound again at 1.5 Myr. During the first bound phase the semi-major axis of the binary shrinks from $a_\mathrm{b} \approx 1$ pc down to 0.1 pc. The binary reaches a steady bound state at ~ 3 Myr with $a_\mathrm{b} \leq 0.1$ pc. Interactions with the stellar background lead to a continuous energy exchange with the MBH binary. This leads to orbital energy being removed from the binary, resulting in decrease of their semi-major axes a_b. When the MBH binary separation becomes lower than a critical value a_h of the semi-major axis, the binary has reached the so called 'hard' phase at Quinlan (1996)

$$a_h \equiv \frac{GM_2}{4\sigma^2}, \tag{2.29}$$

where M_2 is the mass of the secondary MBH (in our case $M_1 = M_2 = 500\,\mathrm{M}_\odot$) and σ is the local velocity dispersion inside the r_SOI of the MBH binary. A typical value for the hard separation in our simulations is $a_\mathrm{h} \approx 2 \times 10^{-3}$ pc. The first time the MBH binaries in our simulations pass this threshold is at $t_\mathrm{hard} = 1.7$, 4.0, 4.8 and 7.5 Myr for the `noMBH_iso`, `2MBH_e005`, `2MBH_e05`, and `2MBH_e099` models, respectively. We note that on galactic scales, the eccentricity e_b of formed bound SMBH binaries is strongly affected by stochastic effects (Rawlings et al., 2023).

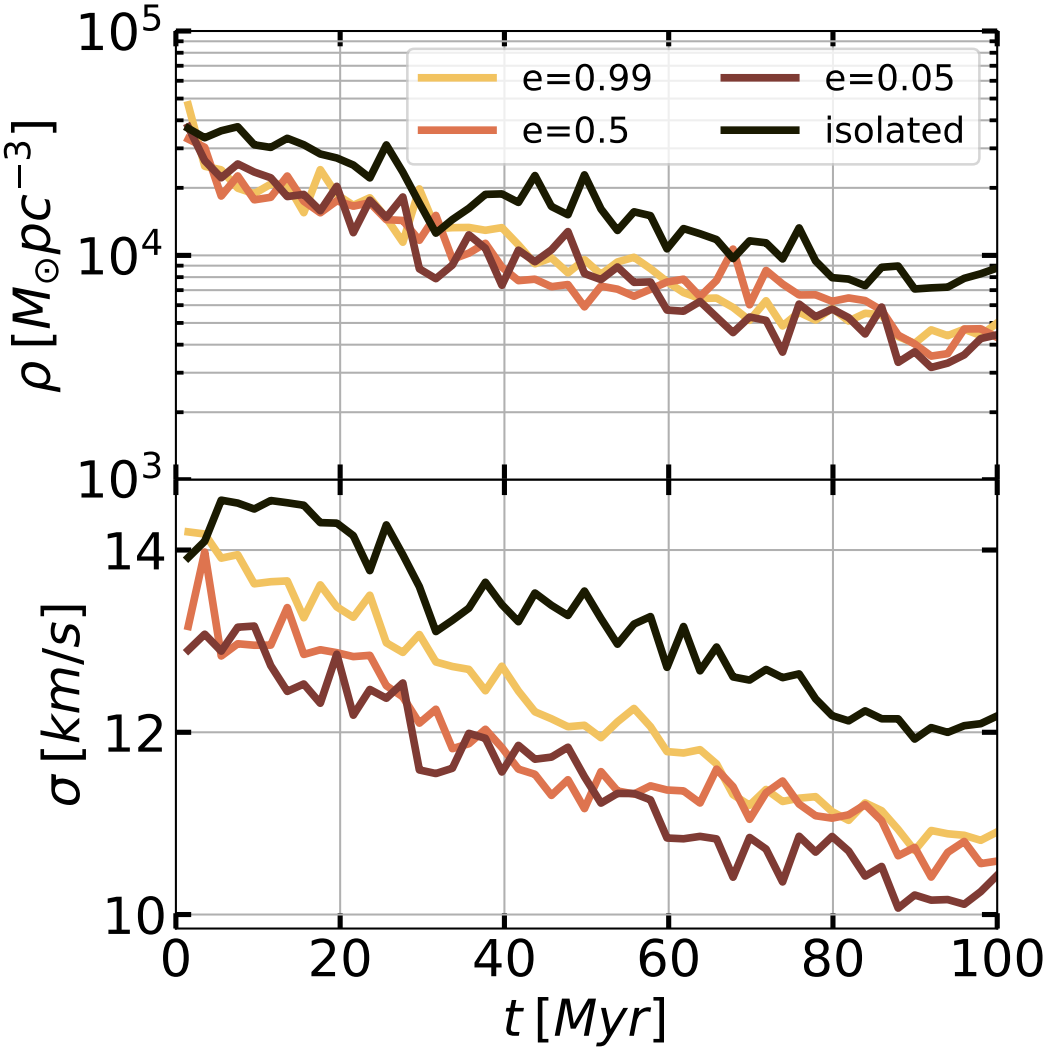

Figure 2.11: Time evolution of the density (top panel) and velocity dispersion (bottom panel) for simulations with MBH binaries. The values are computed within the sphere of influence $r_{\rm SOI}$ of the MBHs.

2.5.1 Hardening and eccentricity growth of MBH binaries in a stellar background

The hardening of an MBH binary depends on the properties of its stellar environment, i.e., the velocity dispersion and mass density of the stars. For a fixed stellar background, the

hardening rate H and eccentricity growth K are given by (Quinlan, 1996),

$$H = \frac{\sigma}{G\rho}\frac{\mathrm{d}}{\mathrm{d}t}\left(\frac{1}{a_\mathrm{b}}\right), \qquad K = \frac{\mathrm{d}e_\mathrm{b}}{\mathrm{d}\ln(1/a_\mathrm{b})}, \tag{2.30}$$

where ρ and σ are the stellar density and velocity dispersion inside the sphere of influence r_SOI (Eq. 2.24) of the binary. Equation 2.30 assumes fixed values for ρ and σ and has been used in various studies on the efficiency of MBH hardening and its effect on the production of gravitational wave merger events and the production of RAs and HVs (Sesana et al., 2006, 2008b, 2009a; Leigh et al., 2017; Rasskazov et al., 2019; Gualandris et al., 2022; Evans et al., 2023). In our simulations, ongoing dynamical interactions of the MBH binaries with the stellar background change the average central stellar density and velocity dispersion continuously. In Fig. 2.11 we show that the density inside the sphere of influence (top panel) of the MBH binaries continuously decreases with time, by a factor 4 - 5 during the 100 Myr of evolution. Over the same time interval, the stellar velocity dispersion (bottom panel in Fig. 2.11) is decreased by 4 km s^{-1} for the merger remnants. The decrease in central density is caused by the ejection of stars which have interacted with the central MBH binary whose semi-major axis is continuously shrinking for all simulations with MBH binaries (the top panel of Fig. 2.12). Individual strong encounters with the central MBH binary result in visible jumps (see e.g. the e = 0.5 merger, orange line, in the top panel of Fig. 2.12) in the semi-major axis evolution and result in the eject of high velocity objects (see discussion in Sec. 2.6).

The evolution of the eccentricity of the central MBH binary is not smooth (bottom panel of Fig. 2.12) and fluctuates significantly. This adds uncertainties on the further post-Newtonian evolution of the MBH binary as the eccentricity has a strong impact the process of coalescence through gravitational wave emission (e.g. Bonetti et al., 2020; Gualandris et al., 2022) and may also imprint distinct signatures on the number and velocity distribution of captured or ejected stars (Sesana et al., 2006, 2008b; Rasskazov et al., 2019). We estimate the hardening rate coefficients H and K from the slope of linear fits on the $1/a_\mathrm{b}$ and $e_\mathrm{b}/\ln(1/a_\mathrm{b})$ time evolution. The values are given in Tab. 2.3. The coefficients H and K have been typically evaluated (e.g. Sesana et al. 2006) using scattering experiments assuming a fixed stellar background.

Eccentricity growth has been observed again in previous studies (Amaro-Seoane & Freitag, 2006; Amaro-Seoane et al., 2009; Arca-Sedda & Mastrobuono-Battisti, 2019) in the context of merging star and globular clusters hosting IMBHs. It's origin can be due to the collective effect of many stars interacting with the MBHB or through strong encounters with individual and/or binary stars (Askar et al., 2021).

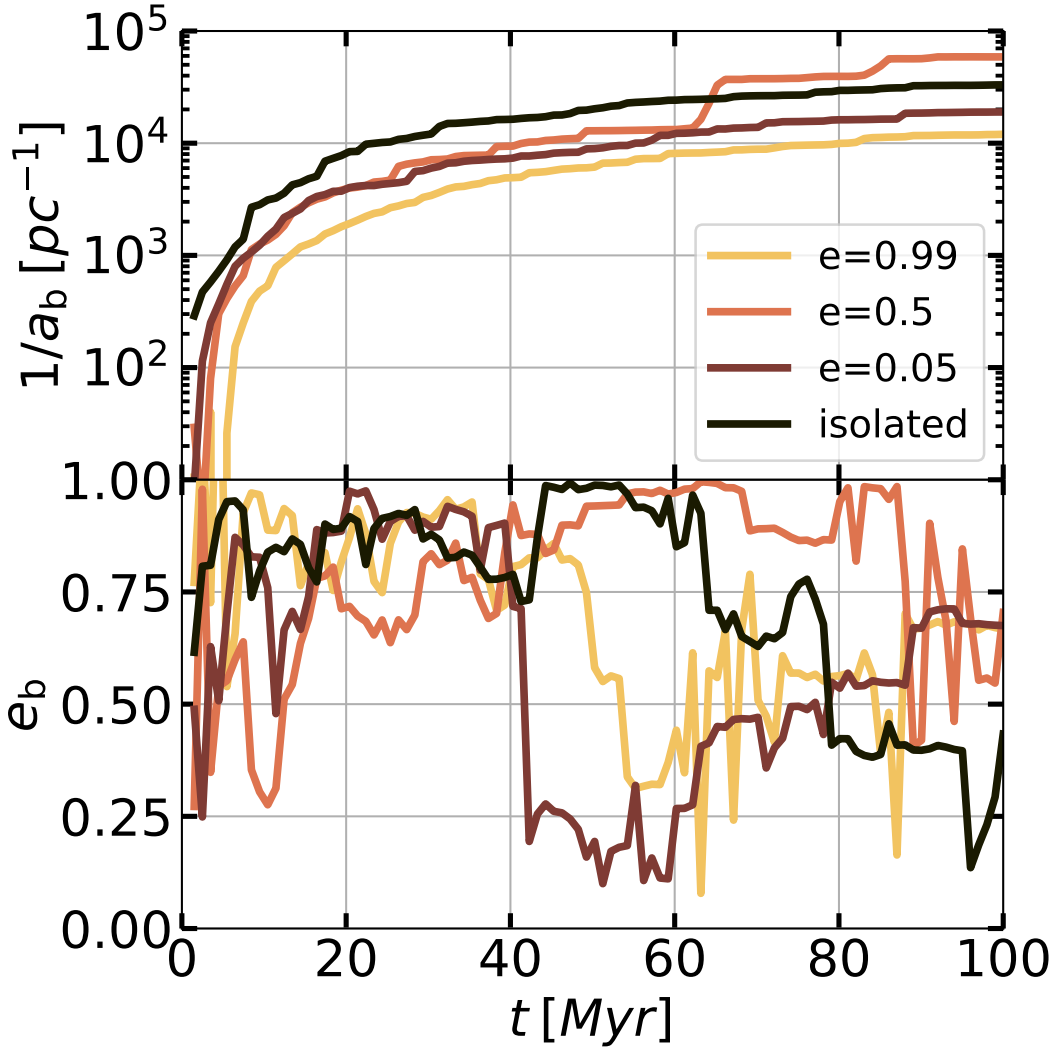

Figure 2.12: Time evolution of the MBH binaries' inverse semi-major axis $1/a_\mathrm{b}$ (top panel) and eccentricity e_b (bottom panel) evolution of the MBH binaries. The semi-major axis is monotonously decreasing due to continuous interactions with the central MBH binaries while the eccentricity shows strong variations.

2.5.2 Gravitational wave driven evolution and coalescence of MBH binaries

In this section we explore the evolution of our MBH binaries after $t = 100$ Myr where our simulations are stopped. To do so, we assume that the orbital elements evolve due to interactions of the MBH binary with the stellar background and GW emission which dominates at late times. The differential equations describing the evolution of semi-major axis and eccentricity are therefore written as

Table 2.3: Hardening rate H and eccentricity growth K from linear fitting. a_{100} and e_{100} are the semi-major axis and eccentricity of the MBH binaries, while ρ_{100} and σ_{100} denote the density and velocity dispersion inside $r_{\rm SOI}$ at $t = 100$ Myr.

Simulation	H	K	a_{100} $[10^{-5}\mathrm{pc}]$	e_{100}	ρ_{100} $[M_\odot \mathrm{pc}^{-3}]$	σ_{100} [km/s]
2MBH_e099	134.5	-11	8.3	0.667	5000	12.15
2MBH_e05	263.2	-9.6	1.7	0.704	4300	20.7
2MBH_e005	204.7	-7.1	5.3	0.675	4400	10.86
2MBH_iso	352.3	-8.7	3.0	0.433	8800	16.53

$$\begin{aligned} \frac{da_{\rm b}}{dt} &= \left.\frac{da_{\rm b}}{dt}\right|_{\star} + \left.\frac{da_{\rm b}}{dt}\right|_{\rm GW}, \\ \frac{de_{\rm b}}{dt} &= \left.\frac{de_{\rm b}}{dt}\right|_{\star} + \left.\frac{de_{\rm b}}{dt}\right|_{\rm GW}, \end{aligned} \tag{2.31}$$

where the terms with $\star$ refer to stellar interactions and GW to GW-emission respectively. The former are described by Quinlan (1996),

$$\begin{aligned} \left.\frac{da_{\rm b}}{dt}\right|_{\star} &= -a_{\rm b}^2 \frac{HG\rho}{\sigma} \\ \left.\frac{de_{\rm b}}{dt}\right|_{\star} &= a_{\rm b} \frac{HKG\rho}{\sigma}, \end{aligned} \tag{2.32}$$

where G is the gravitational constant and ρ and σ are the stellar density and velocity dispersion inside the sphere of influence $r_{\rm SOI}$ (Eq. 2.24) of the binary as before and H, K correspond to the fitted values for the hardening rate and eccentricity growth given in Table 2.3. The GW-driven part is modelled via Eq. 2.9 where, a, e correspond to the binary elements $a_{\rm b}, e_{\rm b}$.

The initial values used for solving Eq. 2.31 correspond to the values at the end of the simulation, i.e. $(a_{100}, e_{100}, \rho_{100}, \sigma_{100})$. The results are presented in Fig. 2.13 (solid lines), where all MBH binaries merge before $t < 4$ Gyr. Although e_{100} has some fixed value for each simulation but due to the stochastic nature of strong encounters, this value would vary if the simulation runs were slightly longer. For this reason and in order to capture the effect of $e_{\rm b}$ in the full range of possible values, we integrate system eq. 2.31 for an almost circular and a highly eccentric binary, whereas the e_{100} from the actual runs serve as intermediate ones. Assuming a fixed high initial eccentricity ($e_{\rm b} = 0.9$) the binaries merge earlier, in less than 2 Gyr. For almost circular orbits ($e_{\rm b} = 0.01$) the MBH binaries can take up to ∼5 Gyr to merge. The above estimates indicate that the MBHs formed in mergers of dense stars clusters will merge within a Hubble time. The main takeaway from this experiment is that given a sufficiently dense environment, hard MBH binaries could potentially merge regardless of how eccentric they are and can be observed with future space-born and ground-based GW detectors like LISA (Amaro-Seoane & Freitag,

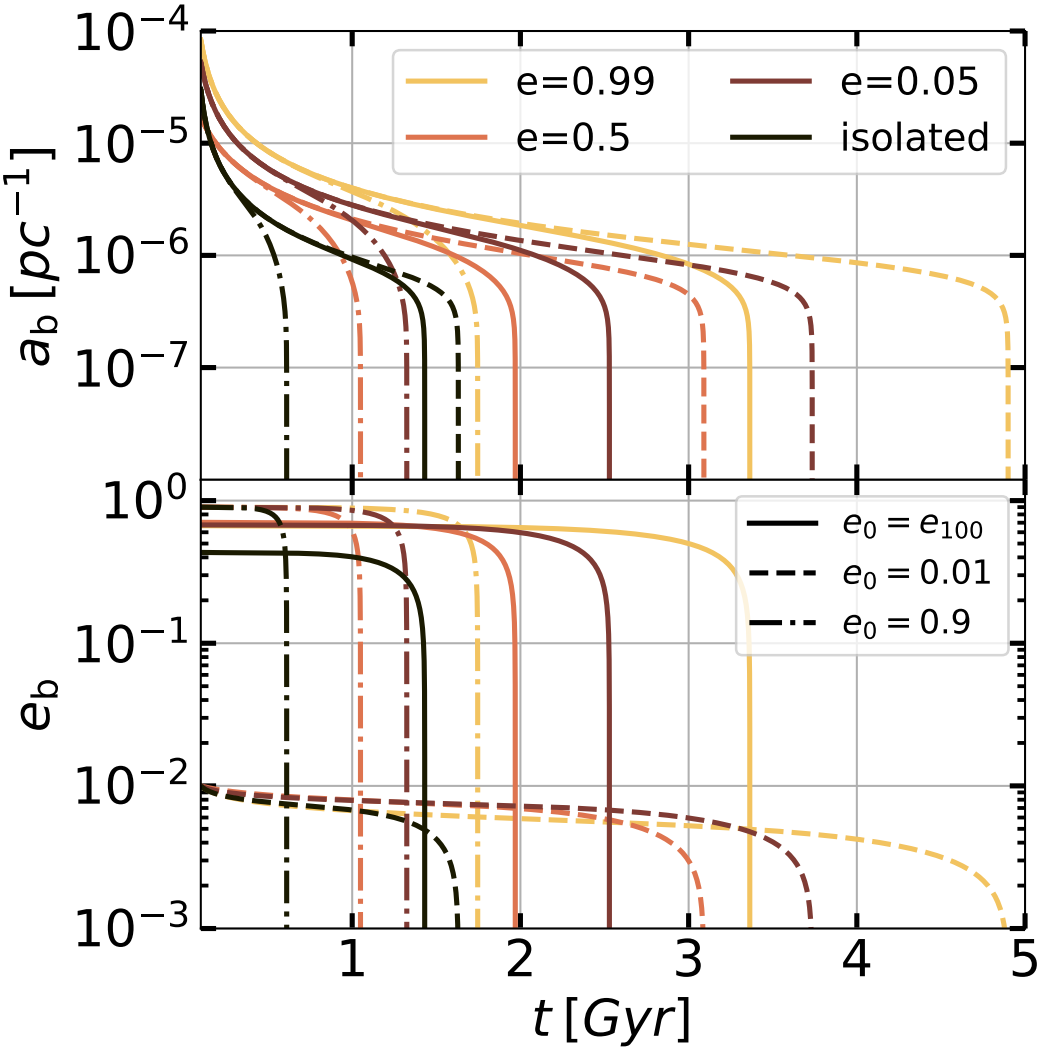

Figure 2.13: Predicted time evolution of the MBH binaries' orbital elements beyond $t = 100$Myr until coalescence. The solid lines corresponds to final values of MBHB eccentricities, therefore e_{100}. We repeat the integration of Eq. 2.31 for nearly circular orbits with $e = 0.01$ (dashed lines) and very eccentric ones $e = 0.01$ (dot-dashed lines) , to test whether the binaries would still merge. All MBH binaries merge within $t < 6$ Gyr, with larger values of e leading to earlier coalescence times.

2006; Amaro-Seoane et al., 2017; Arca-Sedda & Mastrobuono-Battisti, 2019) and Einstein Telescope (Maggiore et al., 2020).

2.6 The ejection of stars and compact objects

2.6.1 Classification and overview

In each simulation, we monitor the stars and compact objects (COs) which become unbound and eventually escape the cluster at a fixed distance of $r_{\rm esc} = 100$ pc. As outlined in Sec. 2.2, the various dynamical ejection channels have characteristic ejection velocities. In this section, we give an overview of the properties of ejected stars and COs in our simulations and connect them to the most likely ejection mechanisms. We classify the ejected objects as follows:

- Low-velocity escapers ($v_{\rm ej} < 50$ km s^{-1}), originating mostly from weak 2-body encounters and 2-body relaxation in the vicinity of an MBH.
- Runaway stars (RA) and COs (50 km s^{-1} $\leq v_{\rm ej} <$ 300 km s^{-1}), most likely from from 3- or 4-body encounters of single or binary stars with BH+star and BH+BH or MBH+star and MBH+MBH binaries and/or binary encounters with a single MBH (a Hills-like mechanism) or a binary MBH.
- Hyper-runaway (HR) stars and COs (300 km s^{-1} $\leq v_{\rm ej} <$ 700 km s^{-1}) , which are the extreme version of the previous channel from interactions with hard binaries.
- Hyper-velocity stars (HV) and COs ($v_{\rm ej} \geq 700$ km s^{-1}), most likely due to strong 3- and 4-body interactions with a single and/or binary MBHs.
- Extreme-velocity stars and COs ($v_{\rm ej} \geq 1000$ km s^{-1}), which are a handful of extreme and rare cases for which we suggest the most likely scenario of ejection.

In Fig. 2.14 we show the evolution of the cumulative number of escapers (top panel) and the escape rate (bottom panel) for all simulations. The characteristic timescale for escaping our clusters can be estimated from the escaper removal distance and the cluster centre escape velocity yielding 100 pc / 22 km s^{-1} ~ 4.4 Myr. The total number of escapers raises rapidly after 10 - 15 Myr (the post merger phase) when the first stars cross the 100 pc boundary. After 100 Myr about 1000 stars have escaped for all simulations without MBHs. The escape rates (bottom left panel) are almost constant (though a moderate peak develops for the most circular merger) at ~ 0.2/Myr. For simulations with one MBH (middle panels in Fig. 2.14) the total number of escapers (~ 2000) is about a factor two higher compared to the run without MBHs, and the escape rates peak at ~ 1.0/Myr after ~ 20 Myr . At the end of the simulation the escape rate drops to similar values as the no MBH simulations. In the presence of two MBHs (right panels) the total number of escapers raises to $\gtrsim 3000$ objects and the escape rates peak earlier (due to the higher speeds of the escapers) at values of ~ 3.0/Myr. After 100 Myr the rates have dropped to similar values as the simulations with one and no MBH. Even though the escape rates are similar towards the end of the simulations, the velocities of the objects are significantly higher in the presence of MBHs. We will discuss this fact more below.

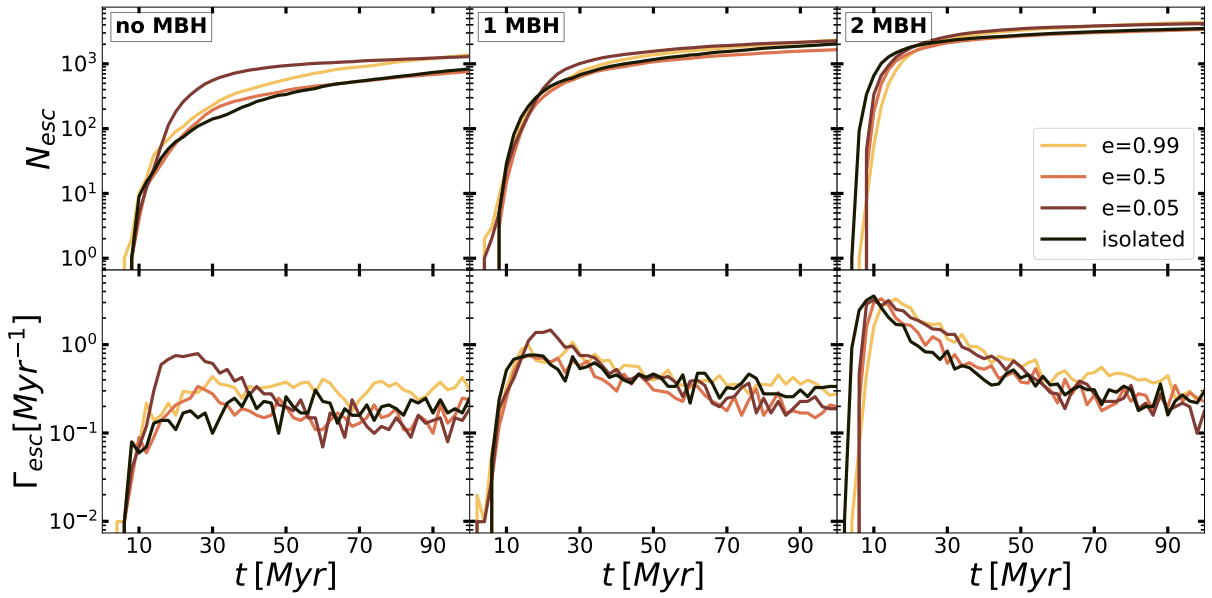

Figure 2.14: Time evolution of the cumulative number of escaping objects (stars and compact objects) at 100 pc (top panels) and the respective escape rate (bottom panels) of escaping stars and COs. For the binary MBH simulations the average (t ¡ 30 Myr) escape velocity (up to 39 km s^{-1}) can be about a factor two higher than for the single MBH cases, which explains the earlier peak in the escape rates.

The number Nesc and rate Γ_{esc} of ejections do not strongly correlate with the orbital eccentricity of the mergers. The results indicate a weak dependence to our ICs, thus suggesting that the our escaper numbers and rate estimates are robust and a generic feature of star cluster mergers with and without MBHs. For clusters without MBHs, only the `noMBH_e005` remnant shows an increased number and rate of 1/Myr of escapers in the first 15Myr compared to the ($\Gamma_{esc} < 0.5$ ejection per Myr) other runs, which could be due to the higher number of dynamically formed binaries during that time (Section 2.6.2). When MBHs are present, the merger orbit itself does not significantly affect the overall number and rates of ejection, as we see from the bottom panels (middle, right) in Fig. 2.14 where Γ_{esc} from the isolated runs is similar to those of the merger remnants.

The velocity distribution of the escapers in all simulations are shown in Fig. 2.15 separated into stars (top panels), stellar BHs (middle panel) and white dwarfs (WD) bottom panels. The assumed velocity limits for runaway stars, hyper-runaway stars and hypervelocity stars are indicated. The total number of escaping stars, BHs, and WDs for these three classes are given in first four columns of Tab. 2.4 and the total mass and fraction of the respective population lost by escapers is given in the five columns on the right. For the isolated cluster without MBHs all escapers are low velocity escapers and we do not find stars with velocities in excess of the assumed runaway star limit of 50 km s^{-1}. Merger of clusters without MBHs can produce a small population of runaway stars ($\lesssim 10$) and, in rare cases, a hyper-runaway BH. Already in the presence of one MBH the isolated

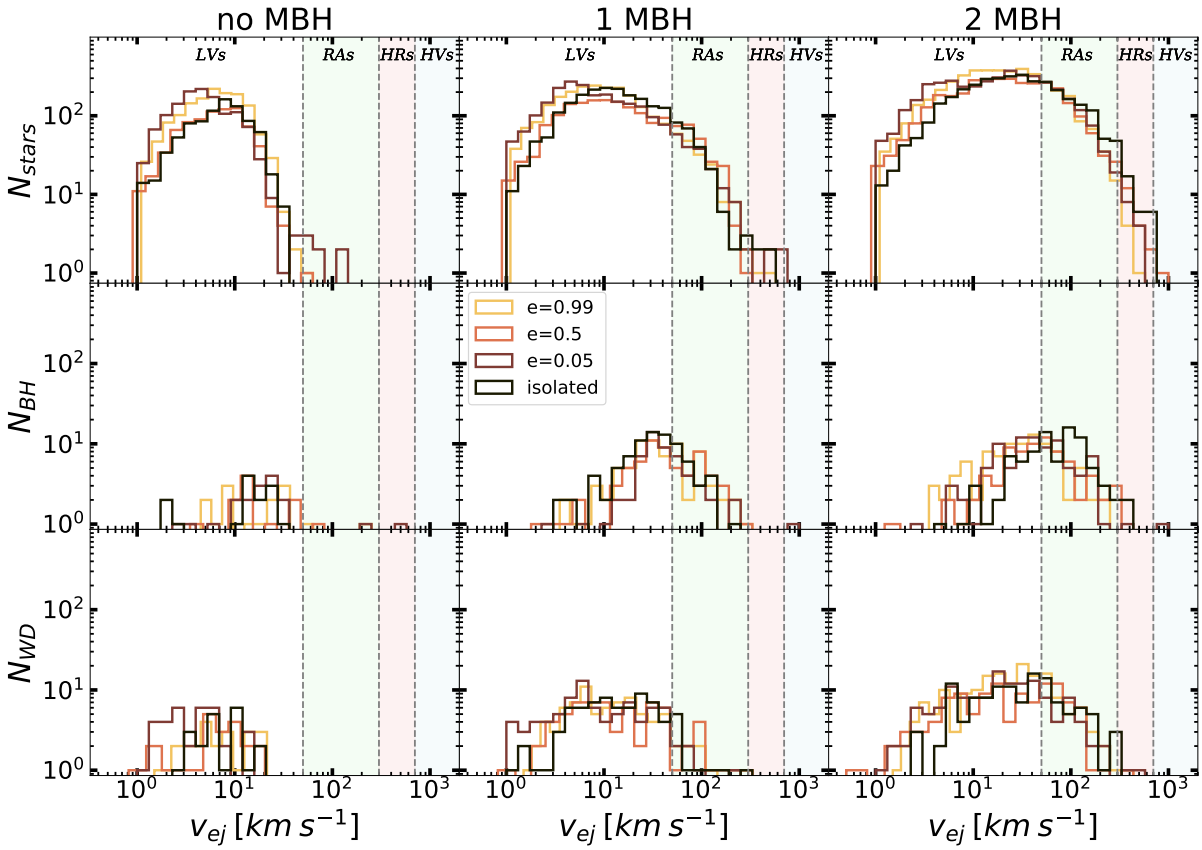

Figure 2.15: Distribution of ejection velocities for objects crossing 100pc distance for simulations without (left panels), with one 1000 $M_\odot$ (middle panels), and with two 500 $M_\odot$ MBHs (right panels). From top to bottom we show stars, stellar-mass BHs and WDs. The different colors indicate different orbital setups. The different shaded areas indicate the velocity regimes for runaway objects (RA, 50 km s^{-1} $\leq v_{\rm ej} <$ 300 km s^{-1}), hyper-runaways (HR, 300 km s^{-1} $\leq v_{\rm ej} <$ 700 km s^{-1}), and hyper-velocity objects (HV, $v_{\rm ej} \geq$ 700 km s^{-1}), respectively. In particular the simulations with binary MBHs (right panels) produce a new population of stars, BHs, and WDs in the RA and even HV velocity regime.

and merger simulations produce a sizable population of $\sim$ 250 runaway objects, up to five hyper-runaway stars. The presence of a MBH also results in the ejection of a significant fraction of the initial BH population (from $\sim$ 22 to $\sim$ 37 per cent), some with runaway velocities, and a few percent of the stellar, white dwarf, and neutron star population in the runaway velocity regime. If both clusters have an MBH which is forming a binary in the remnants, the runaway population increases to $\sim$ 800 and up to 45 hyper-runaway and 3 hyper-velocity stars can be formed. The number of the escaping BHs increases slightly. These results clearly indicate the existence of a single or binary MBH in a star cluster will create a new population of runway stars and compact objects.

In Fig. 2.16 we show the distribution of ejection velocities for objects crossing a distance

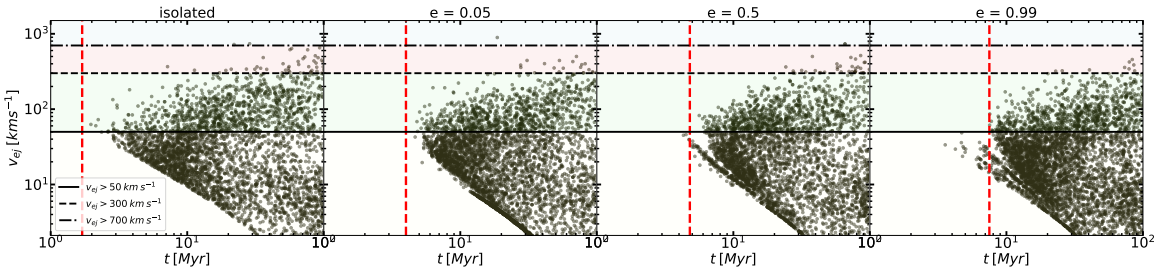

Figure 2.16: Distribution of ejection velocities versus time for stars and compact objects crossing a 100 pc sphere around the clusters with MBH binaries. The solid, dashed, and dashed-dotted horizontal lines indicate the velocity boundaries for low-velocity ejections ($v_{\rm ej} < 50$ km s^{-1}), runaway objects (RA, 50 km s$^{-1} \leq v_{\rm ej} < 300$ km s^{-1}), hyper-runaways (HR, 300 km s$^{-1} \leq v_{\rm ej} <$ 700 km s^{-1}), and hyper-velocity objects (HV, $v_{\rm ej} \geq 700$ km s^{-1}), respectively. The red vertical lines indicate the time when the central MBH becomes hard. The lower velocity boundary is determined by the arrival time of the objects at a distance of 100 pc. The maximum escape velocities increase with time as the ejected objects result from interactions with more bound (more hardened) central MBH binaries (see Fig. 2.12).

of 100 pc as a function of time for all simulations with binary MBHs. The results are not sensitive to the choice of 100 pc as the particle removal radius, since this would only slightly affect (increased/decreased for lower/higher values) the low-end of the the $v_{\rm ej}$ distribution. After the central MBHs become a hard binary (horizontal red dashed lines) objects are ejected with velocities exceeding 50 km s^{-1} which is the velocity limit for runway stars. The ejection velocity of a star ejected via a strong encounter with an MBH binary, typically scales with the orbital velocity of the binary $v_{\rm b}$ (Valtonen & Karttunen, 2006; Merritt, 2013)

$$v_{\rm ej} \sim v_{\rm b} = \left(\frac{2GM_\bullet}{a_{\rm b}}\right)^{1/2}, \tag{2.33}$$

where $M_\bullet = M_1 + M_2$. At later times, when the central MBH binary becomes harder with $a_{\rm b} \lesssim 10^{-3}$ pc (see Fig. 2.12) the maximum escape velocities increase into the hyper-runaway velocity regime. The lower velocity boundary for data points in this figure is determined by the flight times to the 100 pc particle removal distance, with the particle ejection velocities from the central parts of the cluster.

2.6.2 Ejection mechanisms

Dynamically formed binary systems

Single-binary and binary-binary interactions play a central role in the ejections of stars from their host clusters. Besides from being formed in multiples, stars may form binary systems via dynamical processes, especially in dense cluster environments. These dynamical processes are present in our simulations and they include tidal captures (TC) (Press

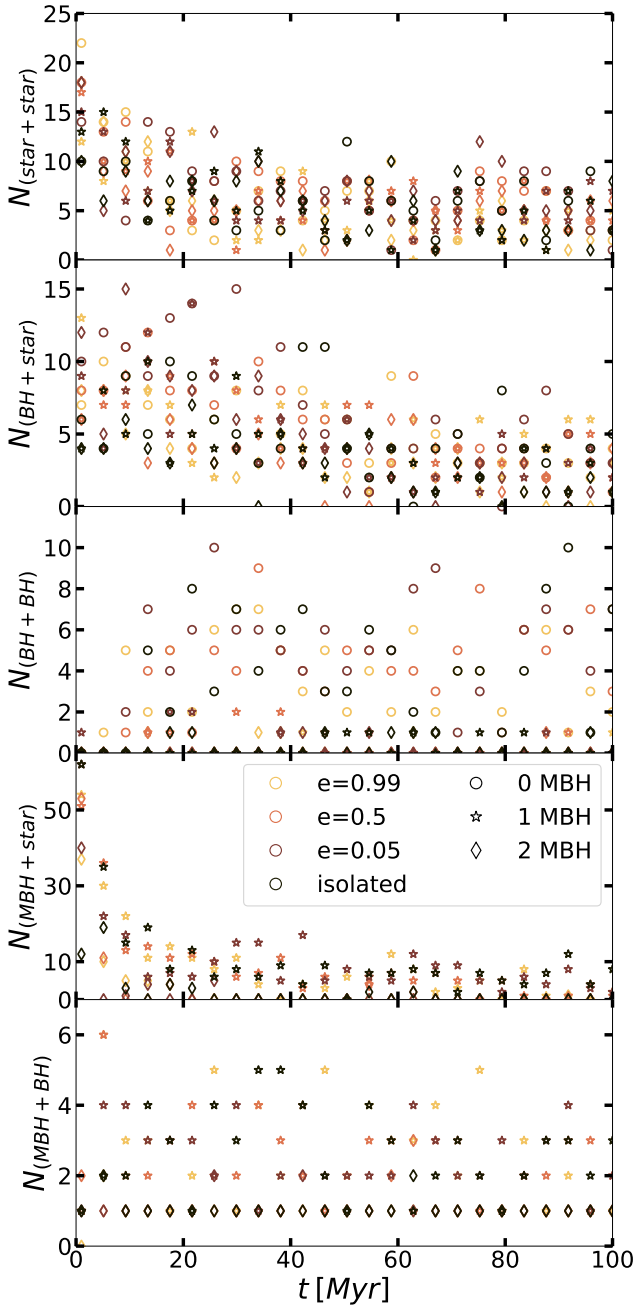

Figure 2.17: Number of dynamically formed binaries in all simulations as a function of time for snapshots with 4 Myr separation. From top to bottom we show star–star, stellar BH–star, stellar BH–BH, MBH–star, and MBH–BH (stellar) binaries. The simulations with MBHs hardly form any BH–BH binaries (third panel).

Table 2.4: Escaper demographics for all simulations. For each simulation we give, from left to right, the number of stars, BHs, and WDs in the LV, RA, HR, and HV velocity regimes. The total escaped fraction in total mass and in numbers of BHs, NSs, WDs, and stars are given in columns 6 to 10.

simulation	$N_{\rm LV}$ stars/BHs/WDs	$N_{\rm RA}$ stars/BHs/WDs	$N_{\rm HR}$ stars/BHs/WDs	$N_{\rm HV}$ stars/BHs/WDs	$M_{\rm tot,esc}$ [%]	$N_{\rm BH,esc}$ [%]	$N_{\rm NS,esc}$ [%]	$N_{\rm WD,esc}$ [%]	$N_{\rm stars}$ [%]
2MBH_e099	3607 / 65 / 134	813 / 29 / 41	8 / 0 / 1	0 / 0 / 0	7.4	36.9	4.0	4.2	3.5
2MBH_e05	2616 / 41 / 76	786 / 36 / 39	34 / 0 / 1	3 / 0 / 0	5.8	30.5	2.5	2.8	2.7
2MBH_e005	3343 / 51 / 116	837 / 37 / 27	19 / 1 / 2	0 / 1 / 0	6.9	34.9	3.2	3.5	3.4
2MBH_iso	2568 / 31 / 88	935 / 55 / 33	40 / 3 / 2	2 / 0 / 0	6.4	38.7	2.8	2.9	2.8
1MBH_e099	2182 / 37 / 79	167 / 28 / 8	2 / 0 / 0	0 / 0 / 0	5.1	30.3	1.8	2.1	1.9
1MBH_e05	1442 / 41 / 57	242 / 23 / 10	0 / 0 / 1	0 / 0 / 0	4.3	25.8	1.8	1.6	1.3
1MBH_e005	2118 / 37 / 79	167 / 18 / 6	5 / 0 / 0	0 / 1 / 0	4.2	22.7	1.4	2.0	1.8
1MBH_iso	1870 / 62 / 67	204 / 22 / 10	4 / 0 / 0	0 / 0 / 0	5.0	37.2	1.9	1.8	1.7
noMBH_e099	1427 / 13 / 26	1 / 2 / 0	0 / 0 / 0	0 / 0 / 0	1.6	6.0	0.7	0.6	1.1
noMBH_e05	805 / 10 / 22	1 / 1 / 0	0 / 0 / 0	0 / 0 / 0	1.1	4.4	0.6	0.5	0.6
noMBH_e005	1308 / 16 / 36	7 / 1 / 0	0 / 1 / 0	0 / 0 / 0	1.7	7.2	0.5	0.8	1.1
noMBH_iso	869 / 14 / 21	0 / 0 / 0	0 / 0 / 0	0 / 0 / 0	1.2	6.2	0.5	0.4	0.7

& Teukolsky, 1977; Giersz, 1986; Generozov et al., 2018; Rizzuto et al., 2023) or 3-body encounters known as *three-body binary formation* (3BBF) (Mansbach, 1970; Aarseth & Heggie, 1976; Goodman & Hut, 1993; Portegies Zwart & McMillan, 2000; Heggie & Hut, 2003; Atallah et al., 2024; Ginat & Perets, 2024). We briefly discuss the dynamical binary formation in Appendix A.

We show the number of dynamically formed binaries for snapshots with 4 Myr separation in Fig. 2.17. The initial conditions do not contain binary stars or compact objects. All simulations form stellar (low mass) binaries. Initially ($t < 4$Myr) up to 25 such systems form and the numbers drop to up to 10 later on throughout the runs (top panel) without a clear trend with initial conditions. For stellar BH+star binaries (second panel) the trend is similar with slightly lower (about 10 less on average) numbers. For stellar BH+BH binaries (third panel, Fig. 2.17) there is a clear trend. Simulations with central MBHs have at most two such systems. Meanwhile, the simulations without central MBHs can have up to 10 BH-BH binaries. In these simulations, more BHs escape and binaries can be disrupted by the interaction with the central MBHs which leaves one BH directly bound to the central MBHs (see bottom panel). After $\sim$ Myr up to 10 stars are bound to the single MBHs and up to three to the binary MBHs (fourth panel). This trend also holds for MBH - BH binaries (bottom panel, Fig. 2.17). Binaries with white dwarfs WD+WD or WD+star do form occasionally with an average number of $N_{\rm WD+WD} \approx N_{\rm WD+star} \approx 1-2$, but most of them do not survive due to multiple dynamical encounters and the fact that they form in relatively wide configurations.

Ejections from clusters without MBHs

First we examine the ejections from clusters without an MBH. In Fig. 2.14 we see these clusters mostly produce low-velocity escapers ($v_{\rm ej} \lesssim 10$ km s^{-1}) corresponding to 2-body relaxation and weak encounters between single stars. Still, there is a noteworthy population of ejections above 10 km s^{-1} which could be the result of encounters of single

stars/COs with star+star, star+BH or BH+BH binaries (see Fig. 2.17). An encounter with a star+star binary leads to velocity kicks of the same order as 2-body relaxation driven escapers, whereas encounters with star+BH or BH+BH binaries can explain the higher velocities. The range of velocities for these ejection processes strongly depends on the binary semi-major axis and mass ratio q. For example, for a hard binary with $a = 2\,\mathrm{AU}$ and $q = 1/25$, Eq. 2.7 implies a velocity kick of $v_{\rm ej} > 100$ km s^{-1}. From Fig. 2.14 we notice that the `noMBH_e005` remnant is able to produce a few RAs even in the absence of an MBH as there is a sufficient number of BH+star and BH+BH binaries present in the simulations (Fig. 2.17) to fuel the few-body ejection channels. Especially the hyper-runaway ($v_{\rm ej} \approx 473$ km s^{-1}) object, which is a BH (see middle-left panel in Fig. 2.14), is ejected at $20\,\mathrm{Myr} < t < 25\,\mathrm{Myr}$. At this time the star cluster remnant contains $N_{\rm BH+star} = 15$ and $N_{\rm BH-BH} = 10$ which is the largest number of those types of binaries throughout the run. As such, the ejection time coincides with the most probable moment for a strong few-body ejection.

Ejections from clusters with a single MBH

Next we discuss ejections from clusters and remnants with a single MBH. In addition to the ejection channels in the case without any MBHs, now there is a significant fraction of MBH+star and MBH+BH binaries. The numbers of those binaries vary from $N_{\rm MBH+star} \approx 50$ at early times to $N_{\rm MBH+star} \gtrsim 10$ at later times and $N_{\rm MBH+BH} \approx 3-6$ (Fig. 2.17) and essentially generate ejections covering the full range of $v_{\rm ej}$ (given a broad distribution of semi-major axes and mass spectrum of stars and BHs). The Hills mechanism also contributes and can explain some rare but strong encounters of binaries with the MBH. The number of stellar and BH binaries is significantly lower compared to the simulations without MBHs. The MBH+star and MBH+BH channel is likely dominant in this case. The number of Hills-like encounters is low due to the lack of available dynamically formed stellar-mass binaries. The number of RAs lies in the range of $192 < N_{\rm RAs} < 280$ for all cases, with a handful $(0-5)$ of HRs, and $0-2$ HVs. We see from Fig. 2.14 that none of them is a BH. Most HRs and stars with higher $v_{\rm ej}$ are produced in the `1MBH_e005` run, which has a larger number of MBH+star and MBH+BH binaries (Fig. 2.17), implying stellar encounters with these types of binaries.

A notable (classified as 'extreme' and not shown in Fig. 2.14) ejection is one at $t \approx 87\,\mathrm{Myr}$ of the `1MBH_e005` run with $v_{\rm ej} > 1000$ km s^{-1}. Specifically, a star of $m_\star = 0.7\,\mathrm{M}_\odot$ accompanied by a $m_\bullet = 14\,\mathrm{M}_\odot$ BH, where the two used to be members of a bound binary system before the ejection. A MBH and star+BH interaction, i.e., a Hills ejection, is the most probable reason for this escape event. The binary semi-major axis in the last snapshot about 1000yr before the ejection was $a \approx 27\,\mathrm{AU}$, which gives an estimated ejection velocity using Eq. 2.6 of $v_{\rm ej} \approx 900$ km s^{-1}. This ejection velocity, close to 1000 km s^{-1}, is very well consistent with the Hills mechanism. We highlight the potential importance of the Hills mechanism for the production of high velocity stars in the context of star clusters and BHs in the IMBH mass regime as the Hills mechanism is commonly associated with galactic nuclei and their SMBHs.

Ejections from clusters with a binary MBH

Finally, we focus on ejections from clusters with a binary MBH at their centre. We note that although all the previous ejection channels are possible in those clusters, the vast majority does not involve interactions with stellar or BH binaries, since their numbers are very low (see Fig. 2.17). The dominant additional ejection mechanism here is the interaction of an MBH+MBH binary with a star or a stellar BH. The MBH binaries become hard, i.e., $a_{\rm b} \leq a_{\rm h}$, already in the early $t < 5\,$Myr post-merger phase as we discussed in Sec. 2.5. The MBH binaries efficiently produce additional RAs, HRs and even HVs. Fig. 2.16 marks (red dashed lines) the time at which the MBH binaries become hard, while the different horizontal (black) lines correspond to the various ejection velocities ($v_{\rm ej}$ is the velocity of the ejected object at $r_{\rm esc} = 100$ pc) classes. High-velocity ejections are initiated only after $a_{\rm b} = a_{\rm h}$. With enough available stars and COs in the vicinity of the MBH binary (top-right panel in Fig. 2.5, the number of ejections rises from $1830 < N_{\rm esc} < 2450$ for the single MBH clusters to $3600 < N_{\rm esc} < 4800$ for the ones with an MBHB (top panels in Fig. 2.14).

2.7 Summary and Conclusions

Star clusters in galaxies are expected to frequently interact and occasionally merge. This can happen during their hierarchical assembly or for evolved star clusters in the spiral arms of galactic discs, in galactic halos, or in galactic centres. In this study we explore the consequences of the merging star clusters hosting massive black holes for the cluster evolution and the production of escaping stars and COs. With $M_\bullet = 500\,{\rm M}_\odot$ the MBHs have masses about one order of magnitude higher than the most massive observed massive stellar BH (see e.g. Gaia Collaboration et al., 2024). Such low mass MBHs might naturally form by rapid stellar collisions in hierarchically forming young and dense star clusters (see e.g. Gieles & Portegies Zwart, 2011; Rantala et al., 2024a) and be retained in the clusters at later times.

We have performed a suite of simulations of mergers of star clusters with individual cluster masses of $M_\star = 2.7 \times 10^4$ M$_\odot$ and $N = 64000$ individual stars and compact objects. In one set of simulations, each of the merging star clusters has a central MBH of $M_\bullet = 500\,{\rm M}_\odot$. For comparison we perform simulations without initial MBHs, and with only one MBH of $M_\bullet = 1000\,{\rm M}_\odot$. We merge the clusters on a circular, a very radial and an intermediate eccentricity orbit. To estimate the effect of the merger process itself we also simulate isolated clusters with $M_\star = 5.4\times10^4{\rm M}_\odot$ without any MBHs, with one MBH (1000 M$_\odot$), and including a binary (2×500 M$_\odot$) MBH. The simulations are performed with the hierarchical forward fourth-order, GPU accelerated N-body code `BIFROST` (Rantala et al., 2023) which includes a regularisation scheme for binaries and post-Newtonian dynamics up to order PN3.5. We study the impact of the presence of MBHs on the star cluster merger remnants. Specifically we study how they affect the i) kinematic and structure of the remnant clusters, ii) the formation and evolution of MBH binaries and their coalescence time and iii) the production and populations of ejected stars and compact objects.

The clusters merge rapidly and the merger remnants are almost spherical with isotropic velocity dispersions. The two more circular merger orbits with $e = 0.05$ and $e = 0.5$ result in remnant star clusters with rotational velocities of $v_{\rm LOS} = v_{\rm rot} \sim 3{\rm km\,s^{-1}}$, similar to observations (e.g. Bellazzini et al., 2012; Fabricius et al., 2014) who find a few km s^{-1}. Apart from a slightly reduced central density of the order of $\sim 300 - 700\,{\rm M_\odot\,pc^{-3}}$, we find no strong evidence for a measurable/observable impact of the MBHs on the structural and kinematic properties of the merger remnants themselves. In conclusion, it's difficult to probe the presence of MBHs in merger remnants based on their kinematic properties alone.

In the cluster merger remnants the sinking MBHs rapidly form binaries and harden by interactions with stars and compact objects. This process produces a new population of escaping stars and compact objects with velocities $\gtrsim 50$ km s^{-1}, which is absent in the star cluster mergers without MBHs. Within 100 Myr, ~ 800 stars with $v_{\rm ej} \gtrsim 50$ km s^{-1} are ejected and would be classified as runaway stars. In addition about 30 stellar black holes escape with similar velocities within 100 Myr. Of order 30 stars can be accelerated to high velocities ~ 300 km s^{-1}. On average ~ 3000 stars escape at velocities lower than 50 km s^{-1}. Overall, the remnants lose ~ 30 percent of their BH population and ~ 3 to 4 per cent of their white dwarf (WD) and star population if MBHs are present.

In the absence of MBHs the fraction of escaping BHs drops to ~ 6 per cent and to below one per cent for white dwarfs and stars. Comparison simulations of isolated clusters of the same mass as the merger remnants and initialised with central MBH binaries as well as star cluster mergers without MBHs show that the high velocity ejection process is driven by the MBH binaries and not the cluster merger process itself. For merger simulations without MBHs of order ~ 1000 stars and ~ 10 BHs escape the system at velocities below 50 km s^{-1}. Comparisons with a single MBH of 1000 M$_\odot$ in isolated or merging cluster show a smaller population of runway stars at lower velocities. Recently, Polak et al. (2024) have highlighted the role of star cluster mergers for the formation of runaway stars. Their simulations feature a more realistic hydrodynamical, hierarchical setup and do not include MBHs. When compared to our idealised star cluster mergers without MBHs we find that one of their 'runaway' star group with a velocity of ~ 39 km s^{-1} is consistent with our simulations. As we assume a runaway velocity limit of 50 km s^{-1} they would fall in our low velocity (LV) escaper regime. The second runway group in Polak et al. (2024) has a velocity of ~ 87 km s^{-1}. We do not reach such high velocities by cluster mergers alone, As discussed in Polak et al. (2024), the more realistic and more dynamical setup in their simulation might allow for higher escape velocities during cluster mergers.

Based on the evolution of the structural and dynamical cluster properties and the MBH binary hardening rates we expect the binary MBHs in our simulations to merge in less than a Hubble time and produce observable gravitational wave (GW) emission events, detectable by future gravitational wave detectors like Advanced LIGO, the Einstein Telescope, or the Laser Interferometer Space Antenna (LISA). The gravitational recoil kicks exerted on the MBH merger remnants might easily eject the MBHs from the star clusters leaving no detectable evidence for their prior existence apart from a strongly reduced stellar BH sub-population.

Low mass MBHs might form naturally by stellar collisions in dense stars clusters (see e.g. Portegies Zwart et al., 2004a; Rizzuto et al., 2021; Rantala et al., 2024a, and references therein), in particular in the dense, star forming, low metallicity interstellar medium in the early Universe. Mergers of these clusters are very likely during their hierarchical formation, during nuclear star cluster assembly or in the disks of early compact galaxies. In this case, the results of our study imply that interactions with low mass MBH binaries formed in merging stars clusters are an important additional channel for producing runaway and high-velocity stars as well as free floating stellar BHs and compact objects which are produced at high redshift and still populate the disks and halos of present day galaxies.

Chapter 3

Relativistic Dynamics near Single and Binary SMBHs

The content of this chapter is based on the submitted paper "Elusive Plunges and Heavy Intermediate-mass-ratio Inspirals from Single and Binary Supermassive Black Holes" (Souvaitzis et al., 2025a).

Abstract

The most massive galaxies in the Universe also host the largest supermassive black holes (SMBHs), with masses of $10^9\,\mathrm{M}_\odot$ and above. During their hierarchical assembly, these galaxies have experienced only a few major mergers at low redshift, but have accreted many low-mass galaxies across cosmic time, possibly hosting intermediate mass black holes (IMBHs). If some of these IMBHs migrate to the galactic center, they may form compact subsystems around the central SMBH. We investigate the evolution of such subsystems, consisting of ten $10^5\,\mathrm{M}_\odot$ IMBHs at three different concentrations around a $10^9\,\mathrm{M}_\odot$ SMBH. We evolve these systems both in isolation and in the presence of a companion SMBH, using `MSTAR`, a regularized integration method including relativistic effects up to post-Newtonian order 3.5PN. Our analysis focuses on gravitational-wave–driven intermediate-mass-ratio inspirals (heavy IMRIs) and direct plunges. We show that perturbations from a secondary SMBH enhance the number of IMBH direct plunges by more than a factor of two, making them the dominant merger channel. These plunges and IMRIs with a central $10^9\mathrm{M}_\odot$ SMBH will contribute to SMBH growth but will likely evade detection with future gravitational-wave interferometers and pulsar timing arrays. However, for galaxies with lower-mass SMBHs ($M_\bullet \lesssim 10^8\,\mathrm{M}_\odot$), heavy IMRIs will be detectable with LISA and can provide direct observational constraints on the existence of IMBHs, while the more numerous plunges will still remain hidden.

3.1 Introduction

Supermassive black holes (SMBHs) are expected to be located at the centers of practically all massive galaxies, with masses spanning approximately $10^6 - 10^{10}$ $M_\odot$ (Kormendy & Richstone, 1995; Menci et al., 2004; Kormendy & Ho, 2013). Within the framework of the ΛCDM paradigm of structure formation, galaxies assemble hierarchically: the systems form small and subsequently grow and merge to produce more massive ones (Ostriker & Hausman, 1977; White, 1980; Lacey & Cole, 1993). If the galaxies contain massive black holes, galactic mergers naturally lead to the creation of SMBH pairs, with the two black holes initially separated by kpc distances within the merger remnant (Barnes & Hernquist, 1992). Their subsequent orbital evolution is driven by a range of dynamical processes, that remove energy and angular momentum from the pair, bringing them closer together and potentially culminating in their coalescence (Begelman et al., 1980). Understanding the origin and subsequent growth of such SMBHs remains one the fundamental research topics in modern astrophysics (Rees, 1988b; Volonteri et al., 2021).

Major galaxy mergers—interactions between galaxies of comparable mass—play a key role in the assembly of massive galaxies and have been extensively studied out to high redshift (Conselice, 2003; Bluck et al., 2009, 2012; Lotz et al., 2011; Man et al., 2016; Mundy et al., 2017; Mantha et al., 2018; Duncan et al., 2019; Ferreira et al., 2020; Dai et al., 2021; Huško et al., 2022; Shibuya et al., 2022). Their dynamical and morphological evolution, also including their supermassive black holes, has been investigated with numerical simulations (e.g., Mihos & Hernquist, 1996; Hopkins et al., 2008; Johansson et al., 2009; Dekel et al., 2009; Hilz et al., 2012; Pillepich et al., 2018; Hani et al., 2018; Rantala et al., 2018; Mannerkoski et al., 2021). Mergers with more unequal mass ratios like *minor* mergers with mass ratios of $4 \lesssim M_1/M_2 < 10$, *very minor* or *mini* mergers with mass-ratios $10 \lesssim M_1/M_2 < 100$, and so-called accretion events $M_1/M_2 > 100$ are much more common (e.g. Nipoti, 2025). Semi-analytical, empirical, and numerical cosmological models all agree that the most massive early-type galaxies these merger and accretion events dominate the mass assembly of massive early-type galaxies, in particular at low redshift (e.g. De Lucia & Blaizot, 2007; Moster et al., 2013; Rodriguez-Gomez et al., 2016; Moster et al., 2018; Behroozi et al., 2019; Moster et al., 2020) such that most of their stellar mass is of ex-situ origin. There is theoretical evidence that the accreted stellar mass mixes well in case of major mergers and the central supermassive black holes sink to the center and eventually merge (e.g. Springel et al., 2005; Di Matteo et al., 2008). For minor mergers and accretion events, the accreted stars assemble at larger radii (e.g. **?**) which is supported by observations as well as simulations (e.g. van Dokkum et al., 2010; Hilz et al., 2012; D'Souza et al., 2014; Williams et al., 2025). Additional observational evidence for galaxy growth through mergers up to redshift $z < 3$ has been reported by Conselice et al. (2022), who find that galaxies with stellar masses above $M_\star > 10^{11}$ $M_\odot$ undergo on average $0.84^{+0.30}_{-0.20}$ major mergers and $1.43^{+0.50}_{-0.23}$ minor mergers. Moreover, cosmological hydrodynamical simulations (e.g. **?**) have shown that the average number of mergers for massive galaxies increases with increasing galaxy stellar mass. Thus, the most massive early-type galaxies in the Universe may have experienced up to ∼ 5–10 mergers and more with a mass ratio exceeding 10 since

$z \sim 3$. The potential lower mass central massive black holes brought in through minor mergers and accretion events that are expected to be more numerous might eventually sink to the center on longer timescales and assemble there without immediate coalescence (see e.g. Partmann et al., 2024). It is therefore possible that a central SMBH is surrounded by lower mass black holes while a major galaxy merger brings in another SMBH sinking to the center.

Once an additional SMBH enters a galaxy through galaxy merger processes, it can sink towards the remnant center through dynamical friction (Chandrasekhar, 1942; Begelman et al., 1980; Tremmel et al., 2015). Once bound at $\sim$ 10pc, binaries harden via 3-body interactions with stars (Quinlan, 1996; Sesana et al., 2006, 2008c), a process enhanced in triaxial merger remnants that provide stars with low-angular-momentum orbits capable of interacting with the central SMBH binary (Khan et al., 2016; Gualandris et al., 2017; Bortolas et al., 2018; Rantala et al., 2018, 2019). Such binaries are primary sources of gravitational waves (GWs), which can be individually resolved in the millihertz band by the Laser Interferometer Space Antenna (LISA) (Sesana et al., 2005; Berti, 2006; Amaro-Seoane et al., 2013; Amaro-Seoane et al., 2017; Katz et al., 2020; Mangiagli et al., 2022), or detected through their collective emission in the form of a gravitational-wave background (GWB) in the nanohertz regime with Pulsar Timing Arrays (PTAs) (Sesana et al., 2008a, 2009c; Babak & Sesana, 2012; NANOGrav Collaboration et al., 2025). Considerable effort has also been devoted to modeling the expected GWB spectrum from massive black hole binary populations using cosmological and semi-analytic simulations, in order to reproduce and interpret PTA measurements (e.g., Kelley et al., 2017b; Fastidio et al., 2025).

To date, while dozens of SMBH binary candidates have been proposed, only a handful can be considered robust. For example, Rodriguez et al. (2006) report a resolved binary in the radio galaxy 0402+379 with a projected separation of $\sim 7\,\mathrm{pc}$. Valtonen et al. (2008) studied OJ287, whose quasi-periodic optical outbursts (12-year cycle, two peaks per cycle) agree to within ~ 1 day with predictions from a binary SMBH model and are consistent with orbital energy loss via gravitational radiation. In the quasar PG1302-102, Graham et al. (2015) detected a smooth optical periodicity of ~ 1884 days ($\sim 5.2\,\mathrm{yr}$) over nearly a decade, which is best explained by a sub-parsec SMBH binary. And more recently Kharb et al. (2017) reported a candidate dual SMBH at a projected separation of only $\sim 0.35\,\mathrm{pc}$ in the Seyfert galaxy NGC7674 (Mrk533), using VLBI imaging of radio cores. Recently, JWST observation have revealed binary and even triple SMBHs already at redshifts $z \sim 5$ (Übler et al., 2024, 2025). However, such studies are not sensitive to SMBH masses lower than $\sim 10^6 M_\odot$.

Despite the well-established mechanisms of dynamical friction and three-body scattering that drive massive black holes (MBHs) toward the galactic center, these processes do not necessarily guarantee rapid coalescence (e.g., Partmann et al., 2024), especially for low-mass MBHs and gas poor environments (e.g., Van Wassenhove et al., 2014). Instead, minor and mini mergers may result into a buildup of a population of MBHs orbiting the central SMBH, which may stall on sub-parsec scales for extended periods of time (Milosavljević & Merritt, 2001; Dosopoulou & Antonini, 2017). This accumulation of multiple MBHs in galactic nuclei (e.g., Matsui et al., 2012; Tanikawa & Umemura, 2014; Askar et al., 2021)

can have important implications for both the dynamics of the central region and the rates of subsequent mergers. Motivated by this scenario, we explore the evolution of a system in a galactic nucleus in which a central SMBH is surrounded by a population of MBHs that has formed via minor and mini mergers. The host galaxy of the system may later undergo a major merger that introduces a secondary SMBH into the nucleus, providing an ideal laboratory to study the interplay between hierarchical galaxy assembly and multiple black hole coalescence.

On small spatial scales, the dynamics of stars, stellar mass compact objects (CO) as well as IMBHs in the immediate vicinity (sphere of influence) of an SMBH are governed by a competition between coherent torques, Newtonian mass precession, relativistic precession and stochastic two-body encounters (Rauch & Tremaine, 1996; Hopman & Alexander, 2006; Merritt et al., 2011). In a near-Keplerian potential the orbits of stars can be considered 'wires' acting as long-range gravitating rods that exert slowly varying torques on one another, thus their motion becomes correlated. Such torques lead to the diffusion of orbital angular momentum changing both its direction and magnitude via a process known as *resonant relaxation* (RR; Rauch & Tremaine 1996; Hopman & Alexander 2006; Perets et al. 2009; Merritt et al. 2011; Hamers et al. 2014; Bar-Or & Alexander 2016). In dense stellar environments such as galactic nuclei, RR becomes very efficient at randomizing the angular-momentum vectors driving stars and COs to highly eccentric orbits, leading to close passages to the SMBH. When the pericentre distance falls below the tidal radius the star is shredded as a tidal-disruption event (Rees, 1988b) or ejected as a hyper-velocity star (Hills, 1988), whereas compact remnants that survive the plunge become extreme- or intermediate- mass-ratio inspirals (EMRIs/IMRIs), spiralling into the SMBH hole via gravitational-wave emission (Merritt et al., 2011; Amaro-Seoane, 2018; Broggi et al., 2022; Rom et al., 2024) . In the special case where the inspiral of an IMBH ($10^2\mathrm{M}_\odot \lesssim M_\bullet \lesssim 10^5\mathrm{M}_\odot$) into an SMBH results in a merger, the event is referred to as a *heavy IMRI* (Amaro-Seoane et al., 2023; Bellovary et al., 2025).

Building on the analytic picture, a series of numerical studies introduced more realistic treatments of RR including relativistic effects. Using statistical methods such as Fokker–Planck and Monte Carlo simulations, Merritt et al. (2011) demonstrated that the inclusion of post-Newtonian (PN) corrections substantially alters the dynamical evolution of compact objects around SMBHs. In particular, the relativistic precession induced by the PN terms suppresses the efficiency of resonant torques in driving angular momentum diffusion. As a consequence, the rate at which objects can be driven to the EMRI regime is significantly reduced. This dynamical suppression was termed the *Schwarzschild barrier*, a phenomenon that has since been independently confirmed and further explored in subsequent studies (Brem et al., 2014; Hamers et al., 2014).

EMRIs constitute one of the key science objectives of space-based gravitational-wave observatories such as LISA (Babak et al., 2017; Amaro-Seoane et al., 2017). Their gradual orbital evolution and the accumulation of a very large number of cycles around an MBH allow for exceptionally high signal-to-noise ratios (SNR) (Amaro-Seoane, 2018). This, in turn, enables precise mapping of the spacetime geometry in the strong-gravity regime (Ryan, 1995), making EMRIs powerful probes for testing the predictions of General Rela-

tivity (GR) (Pappas & Sotiriou, 2015; Cardoso & Gualtieri, 2016; Cárdenas-Avendaño & Sopuerta, 2024). Furthermore, since their orbital evolution and consequently their GW-waveform is extremely sensitive to external perturbations, such events can also provide valuable information on: the presence of a an MBH companion (Yunes et al., 2011b) or a gaseous disc in the system (Narayan, 2000; Yunes et al., 2011a).

An important quantity in studies of compact object dynamics around massive black holes is the relative occurrence of direct plunges (DPs) versus EMRIs. In the classical picture, DPs are expected to arise mainly from orbits with large initial semi-major axes, while EMRIs originate from more tightly bound orbits with smaller semi-major axes. Because DPs follow highly eccentric, nearly radial trajectories, they emit only weak gravitational radiation, making their signals difficult to detect with current GW detectors due to the resulting low signal-to-noise ratio (SNR). However, Qunbar & Stone (2024) recently showed that this dichotomy breaks down for lower-mass SMBHs ($M_\bullet \lesssim 10^5$ M$_\odot$). In this regime, they identified a new class of inspirals—termed *cliffhanger* EMRIs—that do not follow the standard semi-major axis dependence, that were subsequently confirmed and further characterized by Mancieri et al. (2025a).

In analogy to the dynamical evolution around a single SMBH, the presence of a second SMBH introduces additional layers of complexity, giving rise to a broader range of rich and distinctive dynamical phenomena. In such systems, the interplay between two-body relaxation, relativistic precession, and secular mechanisms such as the eccentric von Zeipel-Kozai–Lidov (ZKL) oscillations (von Zeipel, 1910; Kozai, 1962; Lidov, 1962; Naoz, 2016; Ito & Ohtsuka, 2019), combined with the inherently chaotic nature of multi-body interactions, can significantly alter the orbital evolution of surrounding compact objects and stars. It has been found that this channel can enhance the rate of EMRIs (Nate Bode & Wegg, 2013; Naoz et al., 2022; Mazzolari et al., 2022) and tidal disruption events (TDEs) (Chen et al., 2008, 2009, 2011; Chen & Liu, 2013; Li et al., 2015; Ricarte et al., 2016), thereby enriching the astrophysical signatures expected from galactic nuclei hosting SMBH binaries.

Building on these ideas, Nate Bode & Wegg (2013); Naoz et al. (2022); Mazzolari et al. (2022) examined scenarios in which a primary SMBH, comparable in mass to Sgr A* at the Galactic Centre (GRAVITY Collaboration et al., 2020; Event Horizon Telescope Collaboration et al., 2022), is embedded within a nuclear star cluster (NSC) of stars and compact objects, while the mass of a secondary MBH is varied. Using semi-analytic methods and direct integrations of the secular hierarchical three-body equations of motion, these studies demonstrated that the presence of a second MBH can substantially increase the rate of EMRI formation relative to the single-SMBH case, with the ZKL mechanism acting as the dominant driver. More recently, Naoz & Haiman (2023) extended this line of investigation to assess observational prospects, concluding that LISA could potentially detect several hundred such EMRIs with SNR≥ 8 over a four-year mission.

Our study departs from previous works on EMRI formation and the dynamics around SMBHs in galactic nuclei in several key aspects: (i) we consider systems hosting a very massive SMBH of $M_\bullet = 10^9$ M$_\odot$ surrounded by a small cluster of 10^5 M$_\odot$ MBHs, formed as the outcome of successive minor/mini galaxy mergers and accretion events; (ii) the secondary, equal-mass SMBH is introduced through a major galaxy merger; and (iii) the

Table 3.1: Characteristic timescales of different dynamical processes for an example system: $N = 10$ lower-mass MBHs around the primary SMBH of mass $M_\bullet$. Primary and secondary mass $M_\bullet = 10^9 M_\odot$, $m = 10^5 M_\odot$, semi-major axis $a = 0.01$pc, eccentricity $e = 0.5$ for two different values of the number of MBHs N inside a. For $t_{\rm ZKL}$, we consider an equal mass companion SMBH, with on an outer orbit at $a_{\rm out} = 1$pc and $e = 0.5$.

Physical mechanism	Timescale	$N = 1$ [yr]	$N = 10$ [yr]
Keplerian period	P	3.0	3.0
Mass precession	$t_{\rm MP}$	1.71×10^4	1.71×10^3
Schwarzschild precession	$t_{\rm GR}$	77.4	77.4
Resonant relaxation	$t_{\rm RR}$	4.71×10^3	1.49×10^3
Non-resonant relaxation	$t_{\rm NR}$	2.96×10^8	2.96×10^7
GW inspiral	$t_{\rm GW}$	8.75×10^7	8.75×10^7
von Zeipel-Kozai-Lidov	$t_{\rm ZKL}$	3.27×10^5	3.27×10^5

dynamical evolution of these black hole systems is followed using direct N-body simulations that incorporate relativistic corrections up to 3.5PN order. A setup similar to our single-SMBH runs, but involving lower-mass SMBHs and MBHs, was recently examined by Hochart & Portegies Zwart (2024), who focused on how the PN formalism accelerates the ejection of MBHs and how varying SMBH masses can favor ejections over mergers. In this paper, we investigate merger rates in the presence of single versus binary SMBHs and examine the differences in their formation pathways, focusing on the relative fractions of DPs and IMRIs, as well as their detectability with LISA. We find that the presence of a second SMBH leads to a substantial enhancement in merger events, by a factor of 2–5, with the majority corresponding to highly eccentric DPs. We also find that, although the absolute number of IMRIs is lower in the single-SMBH runs, their relative fraction is larger compared to the binary-SMBH case.

This chapter is organized as follows. In Section 3.2, we provide an overview of the theoretical framework for orbital evolution and dynamical timescales around SMBHs. Section 3.3 presents our N-body code, including a new adaptive timestep implementation and two complementary definitions of orbital elements suited for resolving both DPs and IMRIs. In Section 3.4, we analyze the evolution of our systems across different dynamical regimes and discuss the resulting merger demographics and classifications. Section 3.5 explores the gravitational-wave frequency bands of our mergers and their detectability prospects. Finally, Section 3.6 summarizes our conclusions and outlines directions for future work.

3.2 Theoretical Background - Motion around Supermassive Black Holes

To better understand the motion and dynamics of a system of N bodies in the vicinity of a single SMBH, in this section we brifely describe the basic concepts of resonant relaxation

(Rauch & Tremaine, 1996; Hopman & Alexander, 2006), precession due to general relativity (Einstein, 1915; Weinberg, 1972) and the eccentric Kozai-Lidov effect (von Zeipel, 1910; Kozai, 1962; Lidov, 1962; Naoz, 2016) induced by a tertiary object. Additionally we outline the characteristic timescales of each process, which are crucial for identifying the dominant mechanisms under different conditions.

3.2.1 Mass Precession

For a purely Keplerian orbit the radial $P_{\rm r}$ and angular P_ϕ orbital periods correspond to the same motion, so $P_{\rm r} = P_\phi$. In the presence of a distribution of mass around the SMBH those two periods are not the same anymore, leading to retrograde precession of the argument of periastron ω. For a spherically symmetric mass distribution the time ω takes to precess by π is approximately (Rauch & Tremaine, 1996; Merritt, 2013)

$$t_{\rm MP} \approx \frac{1}{2}(1-e^2)^{-1/2}\frac{M_\bullet}{M(a)}P, \tag{3.1}$$

where $M(a)$ is the distributed mass inside a and therefore the process is called *mass precession* (MP). For a system of $N = 10$ MBHs of mass $m = 10^5\,{\rm M}_\odot$ orbiting a primary SMBH of mass $M = 10^9\,{\rm M}_\odot$, an MBH with semi-major axis $a = 0.01$pc and eccentricity $e = 0.5$ would require $t_{\rm MP} = 1710\,{\rm yr}$ for MP to significantly affect its orbit (see Table 3.1).

3.2.2 Relativistic Precession

For a non-spinning SMBH, the leading-order effect of general relativity to the orbital motion leads to prograde precession of ω. This so called *Schwarzschild precession* (or GR-precession) (Einstein, 1915) does not affect the orientation of the orbital plane, while the time needed for ω to precess by π is (Weinberg, 1972; Rauch & Tremaine, 1996; Merritt, 2013)

$$t_{\rm GR} = \frac{1}{6}(1-e^2)\frac{c^2 a}{GM_\bullet}P, \tag{3.2}$$

where c is the speed of light. In a system of $N = 10$ MBHs with individual masses $m = 10^5\,{\rm M}_\odot$ orbiting a primary SMBH of mass $M = 10^9\,{\rm M}_\odot$, an MBH with semi-major axis $a = 0.01$pc and eccentricity $e = 0.5$ would experience relativistic precession on a timescale of $t_{\rm GR} = 7.74\,{\rm yr}$ (Table 3.1), making GR precession by far the most rapid and dominant process in such a configuration.

3.2.3 Resonant Relaxation

In galactic nuclei dominated by a central point mass $M_\bullet$ (e.g. an SMBH), orbits are nearly Keplerian, and their orientations remain fixed over many orbital periods. This leads to the phenomenon of *resonant relaxation* (RR) (Rauch & Tremaine, 1996; Hopman & Alexander, 2006; Perets et al., 2009; Merritt et al., 2011; Hamers et al., 2014; Bar-Or

& Alexander, 2016), whereby small, long-lived torques between objects result in a rapid evolution of angular momentum vectors. In the *coherent* RR regime, these torques act in a fixed direction over a coherence time $t_{\rm coh}$ (the time for which orbits stay fixed), leading to a net change in angular momentum that grows linearly with time. The total torque T on a test particle due to N randomly oriented background ones at radius $r \lesssim a$ is of order

$$T \sim \frac{Gm\sqrt{N}}{a}, \tag{3.3}$$

where G is Newton's gravitational constant, m is the average mass of background objects and a the semi-major axis of the test particle. On timescales shorter than $t_{\rm coh}$, this leads to an approximately linear angular momentum change of the order of $|\dot{\mathbf{L}}| \approx \sqrt{N}(Gm/a)$, while $|\dot{E}| \approx 0$. Expressed in terms of orbital period P and the angular momentum of a circular orbit $L_{\rm c} = \sqrt{GM_\bullet a}$ the change in L for $\Delta t < t_{\rm coh}$ is then (Merritt, 2013),

$$\frac{\Delta L}{L_{\rm c}} \approx \sqrt{N}\frac{GM}{a} \times \frac{\Delta t}{\sqrt{GM_\bullet a}} \approx 2\pi \frac{m\sqrt{N}}{M_\bullet}\frac{\Delta t}{P}. \tag{3.4}$$

The change of $\mathbf{L}$ translates to the precession of the orbital plane, on a characteristic timescale (Rauch & Tremaine, 1996)

$$t_{\rm RR} \equiv \frac{P}{2\pi}\frac{M_\bullet}{m}\frac{1}{\sqrt{N}}. \tag{3.5}$$

In a system of $N = 10$ MBHs with individual masses $m = 10^5\,{\rm M}_\odot$ orbiting a primary SMBH of mass $M = 10^9\,{\rm M}_\odot$, an MBH with semi-major axis $a = 0.01$ pc and eccentricity $e = 0.5$ would experience relativistic precession on a timescale of $t_{\rm RR} = 1490\,{\rm yr}$ (Table 3.1), competing with $t_{\rm MP}$ while both mechanisms being suppressed by GR.

3.2.4 Non-resonant (two-body) relaxation

In contrast to resonant relaxation, classical two-body (non-resonant) relaxation arises from uncorrelated, close gravitational encounters. It affects both the energy and angular momentum of stars, and its timescale is much longer than that of resonant processes in a Keplerian potential. This leads to the change of orbital elements on a timescale given by (Rauch & Tremaine, 1996; Hopman & Alexander, 2006)

$$t_{\rm NR} \approx \frac{M_\bullet^2}{m^2 N}P, \tag{3.6}$$

and is typically orders of magnitude larger than both $t_{\rm MP}$ and the timescale of relativistic precession $t_{\rm GR}$ which we discuss in next sub-section. Although $t_{\rm NR}$ is orders of magnitude (see Table 3.1) longer than both $t_{\rm MP}$ and $t_{\rm GR}$, it is important to note that, unlike resonant relaxation, non-resonant relaxation is not suppressed by relativistic precession. This is because it arises from stochastic, uncorrelated two-body encounters rather than coherent torques, and thus remains effective even in regimes where GR rapidly quenches resonant processes (Rauch & Tremaine, 1996; Hopman & Alexander, 2006).

3.2.5 Gravitational Wave Inspiral

Compact binaries emit gravitational waves, which remove energy and angular momentum from the system, causing the orbit to shrink and circularize over time. Once a particle is sufficiently close to the SMBH and decoupled from the rest of the system, the characteristic timescale for the semi-major axis to decay due to GW emission is given by Peters & Mathews (1963) as

$$t_{\rm GW} = \frac{5}{64}\frac{c^5 a^4}{G^3 M m (M+m)} F(e), \tag{3.7}$$

where

$$F(e) = (1-e^2)^{7/2}\left(1 + \frac{73}{24}e^2 + \frac{37}{96}e^4\right)^{-1} \tag{3.8}$$

and a and e are the orbital semi-major axis and eccentricity, and m_1, m_2 are the component masses. This timescale sets the orbital decay rate for GW-driven inspiral and is strongly dependent on eccentricity.

Starting from the post-Newtonian equations of motion of a binary system, it is possible to (numerically) solve the GW merger timescale of the system. For highly eccentric and relativistic orbits the GW timescale defined above begins to deviate from the merger timescale (Vázquez-Aceves et al., 2021). A more general expression, valid for arbitrary eccentricities, was derived by Peters (1964), with an alternative formulation later presented by Bonetti et al. (2018). More recently, Zwick et al. (2020) introduced a correction factor $R(e)$,

$$R\left(e\right) = 8^{1-\sqrt{1-e}}, \tag{3.9}$$

which, when applied to Eq. (3.7), yields a timescale applicable across the full eccentricity range:

$$t_{\rm GW}^{\rm corr} = t_{\rm GW} R(e). \tag{3.10}$$

As an example, for a system with primary and secondary mass $M_\bullet = 10^9 {\rm M}_\odot$, $m = 10^5 {\rm M}_\odot$, semi-major axis $a = 0.01$pc, eccentricity $e = 0.5$, $t_{\rm GW}^{\rm corr} = 87.5$ Myr , while $t_{\rm GW} = 47.6$ Myr. In the following we adopt this definition for the GW-driven inspiral timescale and $t_{\rm GW}$ will therefore correspond to Eq.(3.10).

3.2.6 Eccentric von Zeipel-Kozai-Lidov Mechanism

Let us now consider the scenario where a second SMBH with mass M_2 at a sufficiently large distance forms a binary with the primary SMBH M_1 and semi-major axis of $a_{\rm out}$. Now assume that a test particle (in our case a lower-mass MBH) with mass m is orbiting the SMBH with semi-major axis $a_{\rm in}$, then a hierarchical three-body system is formed. A hierarchical triplet consists of two clearly separated binary orbits, i.e., $a_{\rm in}/a_{\rm out} \ll 1$, where

$a_{\rm in}$ is the semi-major axis of the inner binary. In this scenario the outer SMBH acts as a perturber leading to the exchange of angular momentum between the two orbits (von Zeipel, 1910; Kozai, 1962; Lidov, 1962). Especially, when the relative inclination between the two orbital planes is above a critical threshold ($i_{\rm crit} > 39.2°$) , oscillations between the inner binary eccentricity and the relative inclination are triggered, acting on a (quadrupole approximation) timescale (Antonini et al., 2015)

$$t_{\rm ZKL} \sim \frac{16}{30\pi}\frac{M_1+M_2+m}{M_2}\frac{P_{\rm out}^2}{P_{\rm in}}\left(1-e_{\rm out}^2\right)^{3/2}, \tag{3.11}$$

where $e_{\rm out}$ is the outer binary eccentricity and $P_{\rm in}$ and $P_{\rm out}$ the inner and outer orbital periods. The ZKL mechanism can induce large eccentricity oscillations on a timescale longer than P_2, potentially driving the inner orbit to very small pericenter distances. This enhances the likelihood of direct collisions (Thompson, 2011; Hamers et al., 2013; Antonini et al., 2017; Silsbee & Tremaine, 2017; Toonen et al., 2018; Hamers & Thompson, 2019; Liu et al., 2019) or rapid gravitational-wave–driven mergers, provided that GR precession does not suppress the oscillations (Holman et al., 1997; Bonetti et al., 2016; Lim & Rodriguez, 2020). Hierarchical triples that become dynamically unstable ($r_{\rm p,out}/a_{\rm in} \sim 1$) can also trigger collisions, mergers, or ejections. As an example, for an SMBH binary on an outer eccentric orbit with $a_{\rm out} = 1\,{\rm pc}$, $e_{\rm out} = 0.5$, equal masses $M_1 = M_2 = 10^9\,{\rm M}_\odot$, and an inner MBH of $m = 10^5\,{\rm M}_\odot$, the timescale for the tertiary to induce ZKL oscillations on the inner orbit is $t_{\rm ZKL} \sim 3.27 \times 10^4$ yr.

3.3 Methods

We explore the post-Newtonian dynamics and mergers of a system of massive black holes ($m = 10^5 M_\odot$) around a supermassive black hole ($M_\bullet = 10^9 M_\odot$). In half of our models a second SMBH is introduced on an outer orbit around the primary SMBH and its surrounding MBH system. To investigate the role of the spatial distribution of 10 MBHs around the primary SMBH and the impact of a companion SMBH on the merger demographics we have performed a series of 300 direct N-body simulations. The systems are evolved for 10 Myr with the use of the regularised post-Newtonian `MSTAR` integrator (Rantala et al., 2020) included in the direct N-body code `BIFROST` (Rantala et al., 2023). `BIFROST` is used for handling the input, on-the-fly analysis and outputs of the simulations but we do not use its main fourth order forward integrator in this study. In the following section, we briefly outline the main features of `MSTAR` and highlight the modifications we made to accurately capture plunging and highly relativistic inspiraling orbits.

3.3.1 N-body Code (`MSTAR`)

Throughout this study we utilized the `MSTAR` integrator (Rantala et al., 2020) included in the direct-summation N-body code `BIFROST` (Rantala et al., 2023). `MSTAR` enables the

accurate modelling non-softened gravitational dynamics around SMBHs using algorithmically regularised integration (Mikkola & Tanikawa, 1999; Mikkola & Merritt, 2006, 2008; Rantala et al., 2017). The algorithmic regularisation relies on three key numerical aspects. First, the equations of motion of the few-body systems are time transformed. Together with a leapfrog approach it is ensured that the Newtonian coordinate singularity at small separations is avoided. Next, the particles are organized in a minimum spanning tree coordinate structure (Rantala et al., 2020) which further reduces floating-point round-off errors (Mikkola & Aarseth, 1993; Mikkola & Tanikawa, 1999). The final aspect of the algorithm is the use of Gragg-Bulirsch-Stoer (GBS) (Gragg, 1965; Bulirsch & Stoer, 1966) extrapolation method. The GBS method ensures the high accuracy of numerical orbit integrations with the relative errors in the dynamical variables of the system being below a user-defined error tolerance ($\eta_{\rm GBS}$) .

3.3.2 Relativistic dynamics at 3.5PN order

The post-Newtonian formalism is a perturbative expansion technique applied to Einstein's field equations in the regime of weak gravitational fields and low velocities. In this approach, relativistic effects —originally encoded in the geodesic equations— are systematically introduced as higher-order corrections to Newtonian gravity. For a system characterized by typical velocity v , mass M and length scale R, the expansion is governed by a small parameter ϵ indicative of the deviation from the Newtonian limit

$$\epsilon \sim \left(\frac{v}{c}\right)^2 \sim \left(\frac{GM}{c^2 R}\right), \tag{3.12}$$

where G is Newton's gravitational constant and c is the speed of light. For $\epsilon \to 0$ we recover the Newtonian gravity, while $\epsilon \sim 1$ corresponds to the strong gravitational regime. The post-Newtonian correction terms of the order iPN are denoted such that each term scales with a specific power of the PN expansion parameter ϵ,

$$|\boldsymbol{a}_{i\rm PN}| \propto \epsilon^i \sim \left(\frac{v}{c}\right)^{2i} \sim \left(\frac{R_{\rm sch}}{R}\right)^i, \tag{3.13}$$

where v and R are now the relative velocity and separation between two BH particles and $R_{\rm sch} = 2GM/c^2$ is the Schwarzschild radius for a binary with total mass M. The PN-corrected acceleration can then be written as

$$\boldsymbol{a} = \boldsymbol{a}_{\rm N} + \boldsymbol{a}_{\rm PN1} + \boldsymbol{a}_{\rm PN2} + \boldsymbol{a}_{\rm PN3} + \boldsymbol{a}_{\rm PN2.5} + \boldsymbol{a}_{\rm PN3.5}, \tag{3.14}$$

where $\boldsymbol{a}_{\rm N}$ is the Newtonian acceleration. Terms associated with conservation of energy and angular momentum are called *conservative* and represented by integer order, while *dissipative* terms with half-integer terms are related to radiation reaction due to gravitation wave emission.

To account for general-relativistic effects of the orbital motion around SMBHs (e.g. Will, 2006; Poisson & Will, 2014), `MSTAR` includes an implementation of the post-Newtonian

velocity-dependent equations of motion (Rantala et al., 2017; Mannerkoski et al., 2021, 2023). The velocity-dependent equations of motion are solved using an auxiliary velocity algorithm (Hellström & Mikkola, 2010) which allows for the efficient implementation of the PN-corrected gravitational dynamics. We incorporate post-Newtonian correction terms up to 3.5PN order, derived for binary systems with arbitrary eccentricity in the modified harmonic gauge, following the formulation presented in (Mora & Will, 2004). Finally, for the purposes of this study we have neglected BH spin-dependent terms.

3.3.3 Post-Newtonian Orbital Elements

In Newtonian gravity, the orbit of a binary system can be described using Keplerian orbital elements such as the semi-major axis and eccentricity, which remain constant or vary only gradually due to external perturbations. However, when PN corrections are included —as is necessary for the orbital evolution of BH binaries— the standard Keplerian elements are no longer even approximately conserved over a single orbit (Damour & Deruelle, 1985). Instead, they exhibit significant oscillations, particularly near pericenter in eccentric orbits (Danby, 1988; Damour & Deruelle, 1985). At short binary separations where the orbit becomes highly relativistic, the Keplerian elements no longer describe the geometry of the orbit. This mismatch leads to a commonly found artifact of increasing Keplerian eccentricity towards merger (see e.g., Mannerkoski et al., 2019). To overcome this, one has to introduce some quasi-Keplerian parametrization which takes into account the PN-corrected orbital motion. We have implemented such parametrization in `MSTAR`, by computing on-the-fly the 3PN-accurate quasi-Keplerian elements following Memmesheimer et al. (2004). In previous studies using `MSTAR`, the instantaneous post-Newtonian orbital elements have been computed in post processing from the code output (e.g. Mannerkoski et al. 2019, 2021). The quasi-Keplerian elements correspond to the solution of the conservative part of the PN equations of motion for a non-spinning binary:

$$R = a\left(1 - e_R \cos u\right), \tag{3.15}$$

$$\begin{aligned} n\left(t - t_0\right) =& u - e_t \sin u + \left(\frac{g_{4t}}{c^4} + \frac{g_{6t}}{c^6}\right)(v - u) \\ &+ \left(\frac{f_{4t}}{c^4} + \frac{f_{6t}}{c^6}\right)\sin v + \frac{i_{6t}}{c^6}\sin 2v \\ &+ \frac{h_{6t}}{c^6}\sin 3v, \end{aligned} \tag{3.16}$$

$$\begin{aligned} \frac{2\pi}{\Phi}\left(\phi - \phi_0\right) =& v + \left(\frac{f_{4\phi}}{c^4} + \frac{f_{6\phi}}{c^6}\right)\sin 2v \\ &+ \left(\frac{g_{4\phi}}{c^4} + \frac{g_{6\phi}}{c^6}\right)\sin 3v + \frac{i_{6\phi}}{c^6}\sin 4v \\ &+ \frac{h_{6\phi}}{c^6}\sin 5v, \end{aligned} \tag{3.17}$$

$$\tan\frac{v}{2} = \sqrt{\frac{1+e_\phi}{1-e_\phi}}\tan\frac{u}{2}. \tag{3.18}$$

The coordinates R and ϕ represent the relative separation and angle in the orbital plane, with ϕ_0 setting the pericenter direction at $t = t_0$. The orbit remains elliptical with semi-major axis a, but the radial frequency $f_r = n/2\pi$ differs from the angular frequency, causing the angle ϕ to precess by $\Phi > 2\pi$ per orbit. The anomalies u and v generalize the eccentric and true anomaly, but involve additional PN correction factors (g, f, i, h). The Newtonian eccentricity e is replaced by three distinct ones: e_R, e_t, and e_ϕ, i.e., eccentricity is not a scalar anymore. In the Newtonian limit where PN corrections are negligible, this reduces to the standard Keplerian description. The conserved energy E and angular momentum L at 3PN (conservative) order are given by Memmesheimer et al. (2004),

$$\begin{aligned} E &= \mu\left(E_0 + c^{-2}E_1 + c^{-4}E_2 + c^{-6}E_3\right) \\ L &= \mu|\boldsymbol{R}\times\boldsymbol{V}|\left(L_0 + c^{-2}L_1 + c^{-4}L_2 + c^{-6}L_3\right), \end{aligned} \tag{3.19}$$

where $\mu = m_1 m_2/M$ is the reduced mass and $M = m_1 + m_2$ the total mass of the binary and $\boldsymbol{R}$ and $\boldsymbol{V}$ the relative separation and velocity vectors computed in `MSTAR`. Even in the absence of radiation reaction terms, E and L are not constant in time, leading to the oscillation of the corresponding 3PN orbital elements. Additional oscillatory behavior is induced when radiation reaction terms are included (Königsdörffer & Gopakumar, 2006), but we expect those to be negligible compared to the secular evolution. The components of the eccentricity vector do not exactly relate to the geometry of a Keplerian orbit, which makes their interpretation ambiguous. The time eccentricity e_t remains well defined, but it exhibits a modest growth as the system approaches merger. This increase, however, does not reflect a genuine rise in the physical eccentricity of the orbit, i.e. the orbit does not become more elongated when closing the merger. For nearly circular relativistic orbits, the 3PN expressions yield $e_R^2 < 0$ and $e_\phi^2 < 0$ (Mannerkoski et al., 2019), while e_t shows a behavior reminiscent of the Keplerian case without corresponding to a real eccentricity growth. For further discussion, see Mannerkoski et al. (2019).

Geometric Eccentricity

A more robust and gauge independent way to measure orbital eccentricity, which also applies to the strong relativistic regime can be defined by utilizing the pericentre $R_{\min}$ and apocentre $R_{\max}$ of a binary orbit (Csizmadia et al., 2012), given by

$$e_g = \frac{R_{\max} - R_{\min}}{R_{\max} + R_{\min}}, \tag{3.20}$$

and the corresponding semi-major axis a_g is then

$$a_g = \frac{R_{\max} + R_{\min}}{2}. \tag{3.21}$$

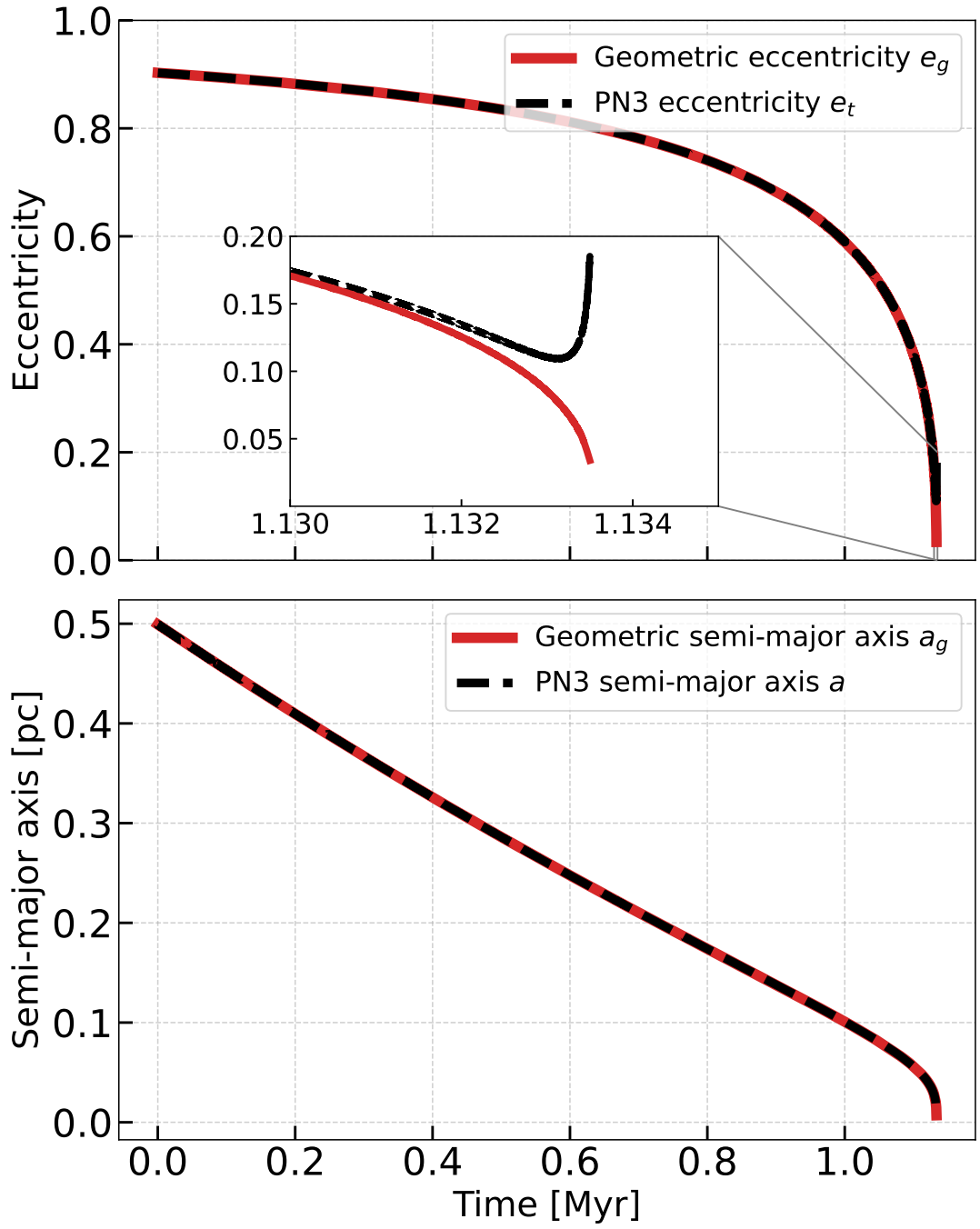

Figure 3.1: Orbital evolution of a merging SMBH binary with $M_1 = 10^{10}\,\mathrm{M}_\odot$, $M_2 = 10^9\,\mathrm{M}_\odot$. The initial eccentricity and semi-major axis are $e = 0.9.$ and $a = 0.5\,\mathrm{pc}$ respectively. The inset panel in the top panel highlights the well behaved geometric eccentricity close to merger. The increase of the 3PN radial component e_R does not correspond to a rise of the orbital eccentricity in the geometric sense.

This definition naturally accounts for the eccentricity evolution of binaries, while also encompassing the effects of precession and spin (Phukon et al., 2025) and it has recently been used in the late-time inspiral of binary BHs in GR-MHD simulations (Ressler et al., 2025). Notice that adopting the above definition, the orbital elements cannot be anymore computed on-the-fly using the instantaneous relative position and velocity vectors of a binary during a simulation run. Rather, a timeseries of the positions over at least a single orbital period is required. It is essential to ensure that the orbit output is sampled with sufficiently high time resolution so that the measurements of $R_{\rm max}$ and especially $R_{\rm min}$ are reliable. This is particularly important for strongly precessing orbits, where accurately capturing $R_{\rm min}$ may require adaptively reducing the output timestep as the system approaches merger. In our simulations we have adopted the geometrical orbital elements description for the binary BH merging orbits and in the next section we discuss our approach and criteria for the adaptive output timesteps. In Fig. 3.1 we provide an example of an eccentric binary SMBH merger initiated with eccentricity $e = 0.9.$, semi-major axis $a = 0.5\,{\rm pc}$ and component masses $M_1 = 10^{10}\,{\rm M}_\odot$, $M_2 = 10^9\,{\rm M}_\odot$. The ill-behaved rise of the 3PN eccentricity e_t (red curve) close to merger is highlighted in the inset plot of Fig. 3.1. This distinction is important, since spurious numerical eccentricity near merger could be misinterpreted as evidence for genuinely eccentric gravitational-wave events. Correctly identifying true eccentric mergers is crucial, as they provide valuable insights into the astrophysical environments and dynamical histories of the merging binaries.

3.3.4 Adaptive Output Timestep

The GBS extrapolation method in `MSTAR` is responsible for the adaptive timestepping and order control of the integration (Rantala et al., 2020; Mannerkoski et al., 2023). Compared to non-regularised techniques, regularised integrators are highly efficient and only require $\lesssim 10$ steps per orbit (especially for non-relativistic binaries) while still retaining a high integration accuracy. However, for the purposes of determining the geometric eccentricity this sparse stepping is not optimal. In our simulations, the final MBH orbits around the primary SMBH can enter the highly relativistic regime, where the precession is very rapid. Our goal is to ultimately distinguish between plunging or inspiral orbits, where the evolution of orbital elements close to merger has to be properly captured (Hochart & Portegies Zwart, 2024). At the same time, we wish to make sure that orbits with large separations are still handled by the default integration timesteps of `MSTAR` to achieve optimal performance, i.e., to avoid unnecessary slow-downs of the code when high-frequency output is not needed. For this, we introduce an adaptive time-stepping scheme that shortens the standard `MSTAR` integration step length if a better sampled orbit output is required. To do so, we start by finding the minimum relative distance $d_{\rm min}$ between MBH and SMBH particles and compute their combined Schwarzschild radius

$$R_{\rm sch} = \frac{2G(M_\bullet + m)}{c^2}, \tag{3.22}$$

where $M_\bullet$ and m are the masses of the SMBH and the MBH respectively. To test

whether the original timestep dt_0 (labelled H in Rantala et al. 2020) is capable of capturing the shortest-period close orbit, we compute the orbital P period of a circular orbit at $d_{\rm min}$,

$$P(r = d_{\rm min}) = \frac{2\pi d_{min}^3}{G(M_\bullet + m)}. \tag{3.23}$$

We can now directly compare the orbital period P to the base timestep dt_0 and determine whether a shorter timestep is required for resolving the geometry of the orbit from the code output. As a rule of thumb, we aim to resolve each orbit with at least $N_{\rm points} = 20$ outputs. However, to better adapt the output time resolution to the dynamics near the SMBH, we define three refinement zones based on the minimum relative distance to the binary, measured in units of the Schwarzschild radius $R_{\rm S}$:

$$N_{\rm points}(r) = \begin{cases} 100, & r < 25\,R_{\rm sch} \\ 50, & 25\,R_{\rm sch} \leq r < 52\,R_{\rm sch} \\ 20, & 52\,R_{\rm sch} \leq r < 236\,R_{\rm sch}. \end{cases}$$

These values serve as target output time resolutions: if an MBH is orbiting the SMBH at short distance, the orbit has to be increasingly better resolved due to rapid precession near the SMBH. For context, a binary SMBH-MBH orbit with $M_\bullet = 10^9\,{\rm M}_\odot$ and $m = 10^5\,{\rm M}_\odot$ at $r = 236\,R_{\rm sch}$ typically have periods $P \gtrsim 10$ yr, while at $r = 52\,R_{\rm S}$ we have $P \gtrsim 1$ yr. The innermost zone corresponds to the final inspiral stage, where maximal time resolution is critical. We have tested the adaptive output timestep criterion in practice and found that it performs well for all merger orbits in our simulation sample including eccentric mergers.

In the code we next check if $P(r = d_{\rm min}) \leq 10\,dt_0$ and if so, a refined timestep is adopted. The new timestep is estimated as

$$dt_{\rm new} = \frac{P}{N_{\rm points}}. \tag{3.24}$$

This ensures that the effective number of points per orbit is at least $N_{\rm points}$. We have also included the option to cap the maximum possible $N_{\rm points}$, in case an inspiral orbit demands indefinitely small dt to capture the final stage before merger. Once two particles merge, the timestep assignment process repeats and the code updates $dt_{\rm new}$ if needed, ensuring optimal integration performance.

3.3.5 Merger Conditions and Classification: Inspiral Vs Plunge

In our simulations the condition for a merger event between two BH particles is based on their instantaneous separation (e.g. Merritt et al., 2011; Mannerkoski et al., 2021; Rantala et al., 2023). This is defined as the distance of the innermost stable circular orbit (ISCO) around a Schwarzschild black hole with radius

$$r_{\rm isco} = \frac{6GM_\bullet}{c^2} = 3\,R_{\rm s}, \tag{3.25}$$

where R_s is the Schwarzschild radius for an SMBH with mass $M_\bullet$. To ensure that PN approximation does not break down at such distances, previous studies set the merger condition to $r \leq 4R_s$ (e.g. Merritt et al., 2011; Mazzolari et al., 2022). We highlight here that when the distance between an MBH and an SMBH is less than $\sim 6\, R_s$ the geometry of the spacetime has a strong influence on the orbit dynamics and a proper treatment requires the integration of geodesics coupled with dissipative PN radiation reaction terms (Gair & Glampedakis, 2006; Sopuerta & Yunes, 2011). An example of such implementation in N-body code has already been tested to study the dynamics and rates of EMRIs in the vicinity of a Schwarzschild or a Kerr SMBH (Amaro-Seoane et al., 2013; Brem et al., 2014), where radiation reaction terms have been neglected. For those reasons we have adopted a merger condition when

$$r \leq r_{\rm merge} = 6.5\, R_{\rm sch}, \tag{3.26}$$

which we have empirically found to be a lower threshold for well-behaved PN-corrected equations of motion for merging binaries in our simulation sample.

One of the primary goals of our work is to identify and classify different types of black hole merger events: direct plunges and inspirals. The first type of merger orbits arises from perturbations due to relaxation processes and/or strong chaotic encounters ($t_{\rm GW} > t_{\rm NR}, t_{\rm RR}, t_{\rm ZKL}$) leading to highly eccentric and radial capture orbits which directly plunge to an SMBH, i.e, when (Merritt et al., 2011; Brem et al., 2014; Amaro-Seoane, 2018; Mancieri et al., 2025a)

$$r_{\rm peri} < r_{\rm capt} = 6.5 R_s, \tag{3.27}$$

where $r_{\rm peri} = a(1-e)$ is the pericentre of the orbit and R_s the sum of the Schwarzschild radii of the two black holes from Eq.(3.22). For an orbit that barely intersects the capture sphere, the angular momentum and eccentricity are (Merritt et al., 2011),

$$L_{\rm plunge} = \sqrt{2GM_\bullet r_{\rm capt}}\,, \quad e_{\rm plunge} = 1 - \frac{r_{\rm capt}}{a}. \tag{3.28}$$

Using this definition, an orbit is classified as DP only if $e \geq e_{\rm plunge}$. More circularized orbits, on the other hand, decouple from external perturbations ($t_{\rm GW} < t_{\rm NR}, t_{\rm RR}, t_{\rm ZKL}$) and evolve primarily through energy and angular momentum losses due to gravitational-wave emission. These *inspirals* follow a coalescence pathway that is significantly different from that of DPs. Following the above criteria and in line with Amaro-Seoane (2018); Mazzolari et al. (2022); Mancieri et al. (2025a), we label as successful inspiral in post-processing, a merger orbit satisfying the following conditions:

$$\begin{cases} t_{\rm GW}\,(a,e) \leq (1-e)\, t_{\rm pert} \\ e < e_{\rm plunge} \\ r_{\rm peri} \geq r_{\rm capt} \end{cases} \tag{3.29}$$

where $t_{\rm pert}$ corresponds to any relevant mechanism timescale defined in Section 3.2 and in our case $t_{\rm pert} = t_{\rm NR}$.

Slowly evolving orbits, such as gravitational-wave-driven inspirals, are well resolved in the code output using the adaptive timestep scheme (Section 3.3.4), allowing their geometric orbital element, especially the geometric eccentricity $e_{\rm g}$ from Eq. (3.20) to be reliably computed. In contrast, the shape of strongly perturbed and rapidly evolving orbits cannot be well described by any set of instantaneous orbital elements. An example of this is shown in the right panels of Fig. 3.4, where the combined effects of an external perturbation from the companion SMBH and GR precession significantly alter the orbital shape prior to merger.

In Fig. 3.2, we compare the eccentricities at merger obtained from the geometric definition and the 3PN-corrected definition e_t, plotted as a function of the normalized angular momentum ($L/L_{\rm c}$), where L corresponds to Eq. (3.19) and $L_{\rm c} = \sqrt{2GM_\bullet a}$ denotes the circular-orbit angular momentum at merger. For slowly evolving inspirals, the geometric definition captures the eccentricity accurately as expected, whereas the 3PN-corrected definition overestimates the final eccentricity and fails to follow the inspiral down to $e = 0$. Conversely, for highly eccentric orbits, the geometric elements are unreliable due to resonant relaxation and strong encounters that rapidly modify the orbital shape. For those reasons we adopt a hybrid approach in the analysis of our results, where we use the geometric definition of orbital elements for mergers with $e < 0.6$ and the 3PN-corrected elements for $e \geq 0.6$. Our approach ensures that the shapes of both inspiralling and plunging merger orbits are accurately captured.

3.3.6 Initial Conditions and Simulations

We generate initial conditions (ICs) for a small cluster of MBHs around an SMBH, where $m = 10^5\,{\rm M}_\odot$ and $M_\bullet = 10^9\,{\rm M}_\odot$ (left panel in Fig. 3.3) . In a second set of simulations, we add a distant equal mass companion SMBH to the primary, on an outer orbit with binary semi-major axis $a_b = 1\,{\rm pc}$ and eccentricity $e_{\rm b} = 0.5$, corresponding to pericentre passage at $r_{\rm peri} = 0.5\,{\rm pc}$. All the semi-major axes of the MBH orbits are initially within this pericentre distance. We vary the spatial configuration of the MBHs by controlling the lower $a_{\rm min}$ and upper bound $a_{\rm max}$ of semi-major axis distribution, such that all MBHs are placed inside a radius of $r = r_{\rm peri}$, satisfying $a_{\rm max} \leq r_{\rm peri}$ (right panel in Fig. 3.3) . Our simulations do not account for the presence of a stellar population background; however, we discuss how such an environment would influence the initial dynamical state of our systems in Section 3.4.4.

Specifically, we produce ICs for three distributions given in Table 3.2. For each set of simulations (with and without the SMBH companion) , we run 50 realizations for every semi-major axis distribution, resulting in a total of $N_{\rm sim} = 2 \times 3 \times 50 = 300$ simulations. All simulations are run for a total time of $t_{\rm end} = 10\,{\rm Myr}$, so merger events are monitored only up to this timescale.

At coalescence, gravitational waves can impart a recoil *kick* to the remnant BH (Peres, 1962; Bekenstein, 1973). The magnitude depends on the binary's mass ratio and spins, and while our simulations neglect spins—implying only weak recoils—in more general configurations such kicks could eject remnants from their host nuclei with important astrophysical

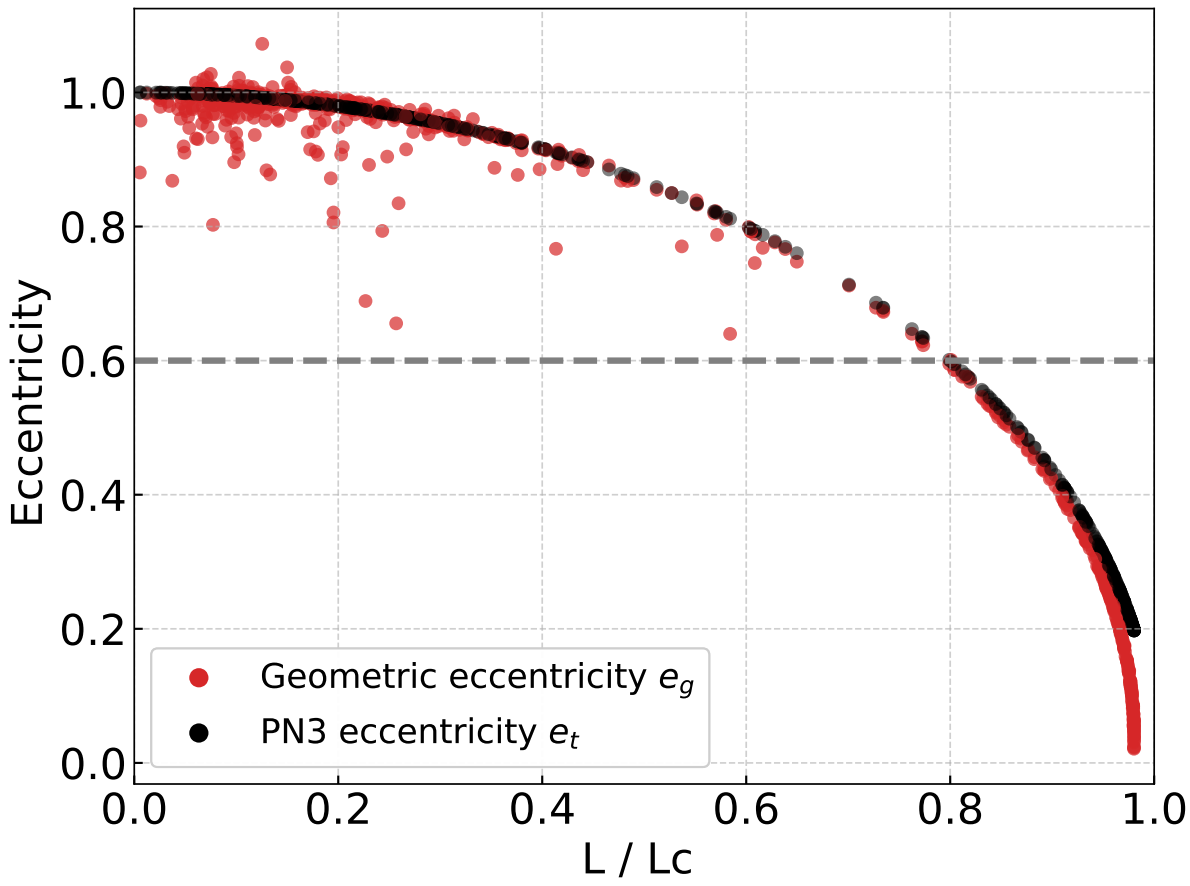

Figure 3.2: Final orbital eccentricity as a function of normalized angular momentum for all the merger events in our simulations. Different marker colors indicate the two definitions of orbital elements. For orbits with $e < 0.6$, the 3PN-corrected elements overestimate the eccentricity, as the inspirals do not reach $e = 0$. Conversely, for highly eccentric orbits ($e \geq 0.6$), the geometric elements fail to accurately represent the orbital properties due to rapid evolution and strong perturbations.

Table 3.2: Initial MBH configurations based on the distribution of semi-major axis.

Configuration	Semi-major axis
Compact	$0.005\,\mathrm{pc} < a \leq 0.05\,\mathrm{pc}$
Intermediate	$0.01\,\mathrm{pc} < a \leq 0.1\,\mathrm{pc}$
Wide	$0.05\,\mathrm{pc} < a \leq 0.5\,\mathrm{pc}$

consequences (e.g., Merritt & Poon, 2004; Volonteri, 2007; Rawlings et al., 2025).

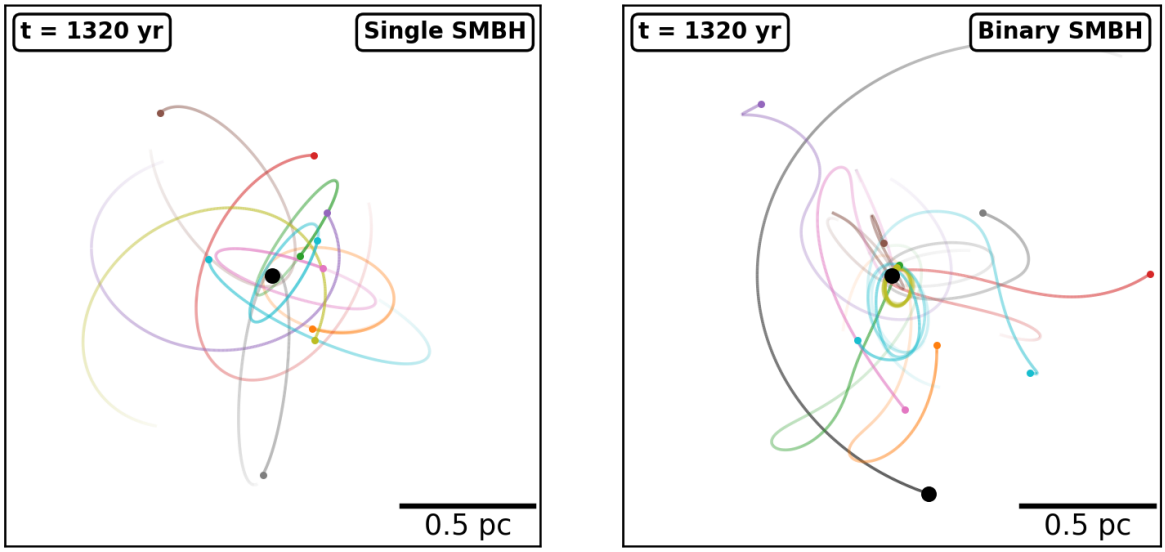

Figure 3.3: Initial configuration of the systems with wide semi-major axis distribution: $0.05\text{pc} < a \leq 0.5\,\text{pc}$. Left panel: single SMBH setup. Right panel: system with a companion SMBH on a fixed orbit with $a_\text{b} = 1\,\text{pc}$ and $e_\text{b} = 0.5$ corresponding to an orbital period of $P_\text{b} = 2000\,\text{yr}$. Both configurations are shown at $t = 1320\,\text{yr}$ after the start of the simulations, with trajectory tails tracing the preceding $t = 750\,\text{yr}$. Notice how the majority of orbits are being disrupted, already after the first pericentre passage of the companion SMBH. The animated versions of those runs are available at [zenodo link].

3.4 Dynamical Evolution of SMBH-MBH systems

3.4.1 Overview

The initial state of our systems consists of a population of lower-mass MBHs orbiting a central SMBH, with semi-major axes distributed over a wide range ($0.05\,\text{pc} < a \leq 0.5\,\text{pc}$). Figure 3.3 illustrates this setup for the case of a single SMBH (left) compared to a binary SMBH system (right). In the single-SMBH configuration, the MBHs remain bound in relatively undisturbed orbits around the primary. By contrast, introducing a companion SMBH on a fixed orbit with $a_\text{b} = 1\,\text{pc}$ and $e_\text{b} = 0.5$ ($P_\text{b} = 2000\,\text{yr}$) strongly perturbs the system: already by $t = 1320\,\text{yr}$, following the first pericentre passage ($t \approx 1000\,\text{yr}$) of the companion, the majority of orbits are disrupted or significantly altered. This demonstrates how the presence of a second SMBH can destabilize the configuration, whereas more compact MBH distributions are more resilient and harder to disrupt.

In Fig. 3.4, we present two representative examples of DP orbits from our simulations. The left panels show a case from a run with a single SMBH, where a lower-mass eccentric MBH orbits the primary while undergoing relativistic precession. The color map indicates the time to plunge. Around $t = 0.5\,\text{kyr}$ before merger, the orbiting MBH experiences a

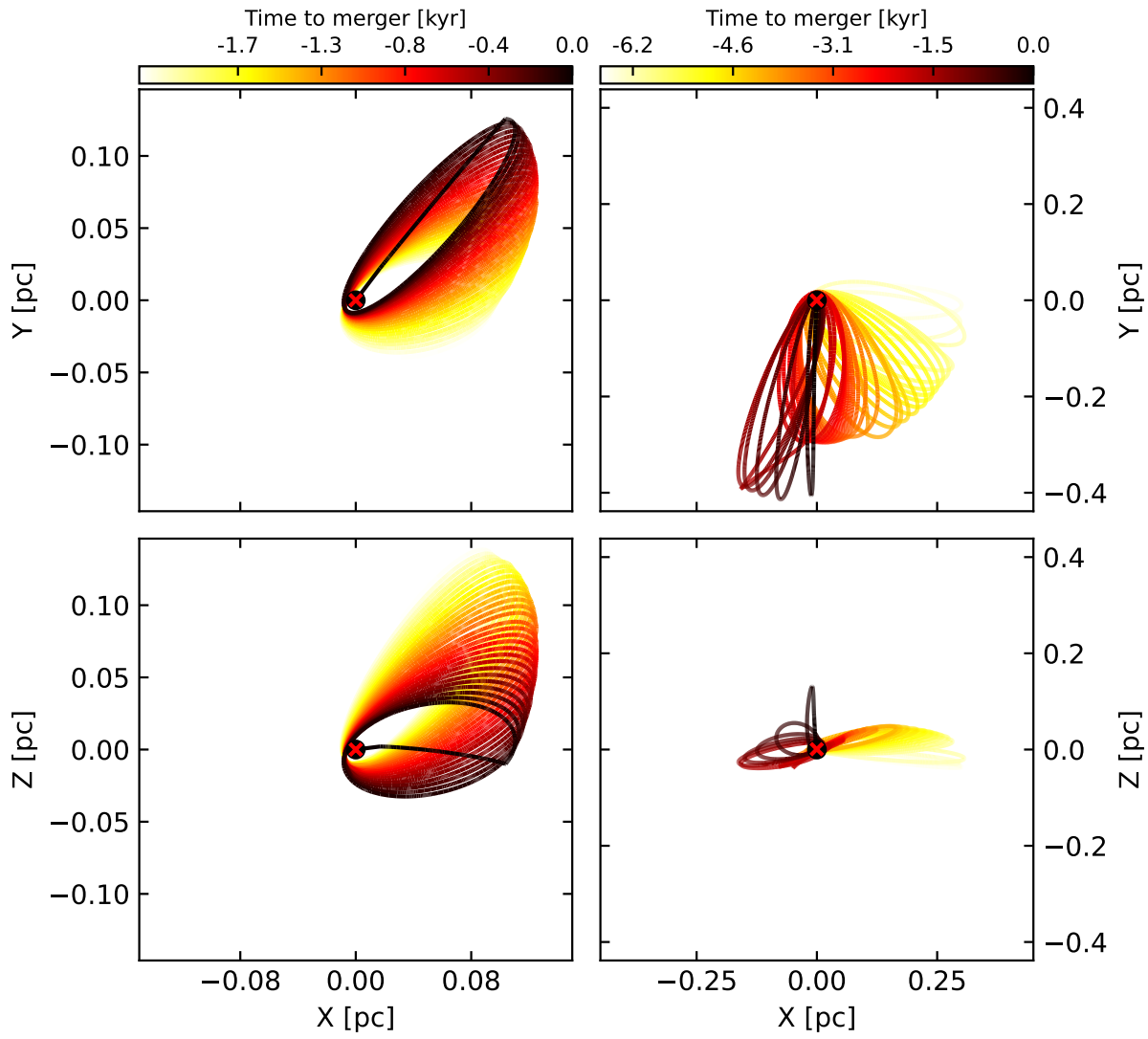

Figure 3.4: Examples of DP orbits. The colormap traces the time evolution until merger, marked with a red cross. Left panels: single-SMBH run, where a lower-mass MBH precesses due to GR and receives a strong kick from another MBH ~ 0.5 kyr before merger, leading to a rapid plunge. Right panels: binary-SMBH run, where a wider orbit precesses under GR but is perturbed by the companion SMBH ~ 2 kyr before merger, driving it to high eccentricity and eventual plunge. Upper panels show the x–y projection, while lower panels display the x–z view.

strong kick from an encounter with another MBH, which drives a rapid plunge onto the primary SMBH. The right panels illustrate an example from a run with a binary SMBH. In this case, the MBH also precesses due to GR, but with a semi-major axis larger by an order of magnitude. At this greater distance, the orbit becomes more susceptible to perturbations from the companion SMBH, which alters its trajectory around $t = 2$ kyr before merger, exciting a highly eccentric orbit and ultimately leading to the plunge onto

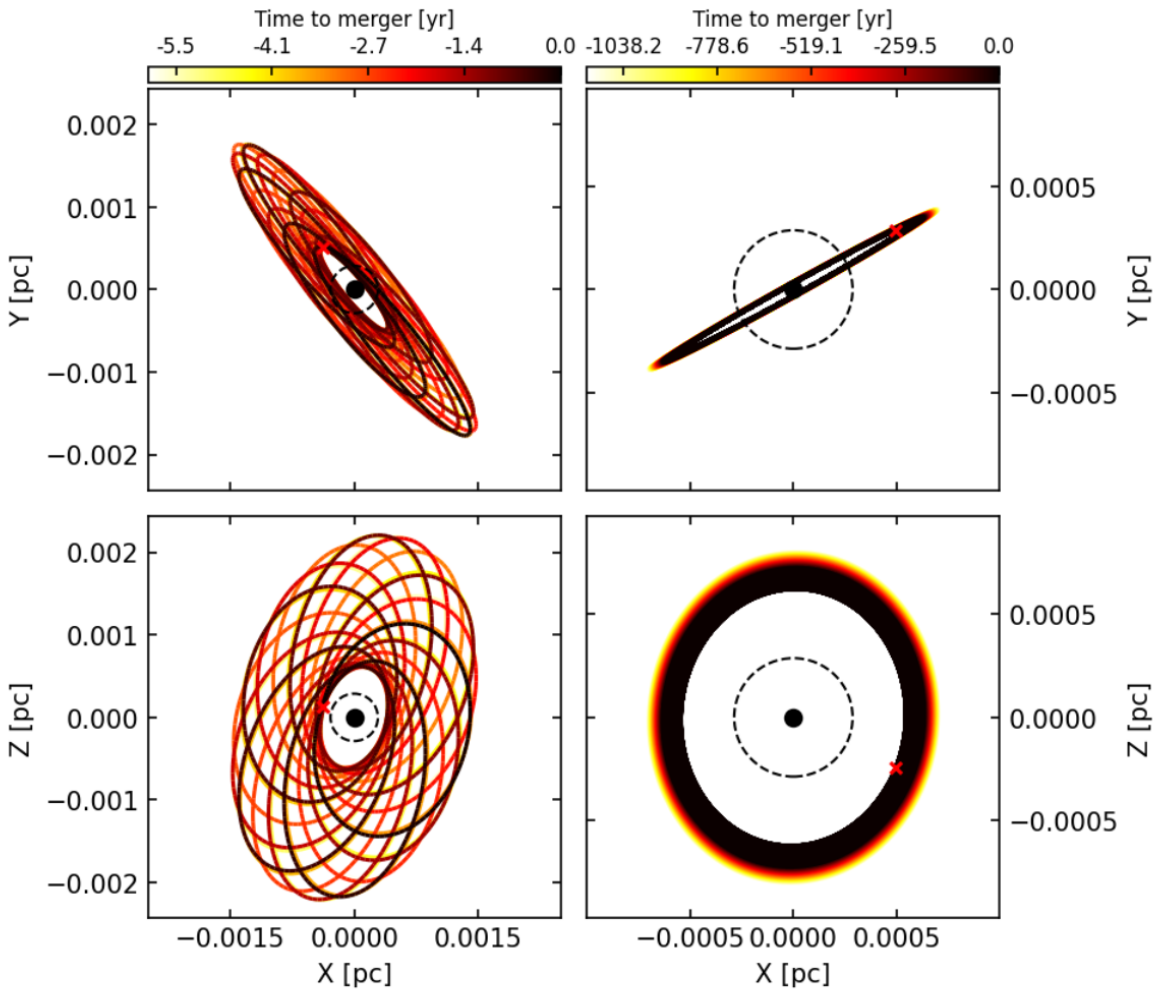

Figure 3.5: Inspiral example orbits. Left panels: single-SMBH run ($\sim 6\,\mathrm{yr}$ to merger), showing an eccentric orbit that precesses due to relativistic effects while simultaneously shrinking and circularizing via GW emission until $d \leq r_{\mathrm{merge}} = 6.5\,R_{\mathrm{s}}$. Right panels: binary-SMBH run (~ 1 : kyr to merger), where the inspiral is driven solely by GW emission. The color map indicates the time to merger (red cross), the dashed circle marks $R_{\mathrm{isco}} = 3R_{\mathrm{s}}$, and the primary SMBH is shown as a black dot. Upper panels display the x–y projection, while lower panels show the x–z view.

the primary.

Figure 3.5 presents examples of inspiral orbits. The left panels, taken from a run with a single SMBH, show a case about $\sim 6\,\mathrm{yr}$ before merger, where relativistic precession and gravitational-wave emission act simultaneously: the eccentric orbit precesses while gradually shrinking and circularizing until it reaches $d \leq r_{\mathrm{merge}} = 6.5\,R_{\mathrm{sch}}$, our adopted merger criterion. The right panels, corresponding to a run with a binary SMBH, illustrate an inspiral orbit that evolves slowly ($\sim 1\,\mathrm{kyr}$ until merger), driven by GW emission alone,

until it reaches $d = r_{\rm merge}$.

Following the merger criteria and classification outlined in Section 3.3.5, we present here an overview of the outcomes of our simulations. The total number of mergers, as well as the relative fractions of plunges and inspirals, are summarized in Table 3.3. Overall, the presence of a secondary SMBH substantially enhances the merger rate, particularly for wider initial semi-major axis distributions. In these cases, the number of mergers increases by a factor of ~ 5 compared to the single-SMBH runs. This enhancement remains significant even for more compact initial configurations, where the merger rate is still elevated by a factor ~ 2. All of our merger events involve MBH mergers, with only a small handful of exceptions that have been excluded from the analysis.

For wider initial configurations, the companion SMBH can disrupt the MBH system already during the first pericentre passage at $t \sim 1, \mathrm{Myr}$, capturing MBHs along its orbit while driving the remaining objects onto highly radial trajectories. This process results either in direct plunges or in the complete ejection of the system (see Section 3.4.4). The impact of this mechanism is evident in Table 3.3, where the number of plunges closely tracks the total number of mergers when comparing single- and binary-SMBH runs. In particular, for the two widest configurations, the total plunge fractions in the binary-SMBH case reach 93.2% and 97.7%, demonstrating that the overwhelming majority of mergers occur through direct plunges in the presence of a companion SMBH. Notably as shown in Fig. 3.6, in the widest configuration nearly $\sim 30\%$ of these events are hyperbolic plunges ($e \geq 1$), arising from strong few-body scatterings with the tertiary companion or other MBHs that eject the secondary from the system and drive it directly onto the primary SMBH.

An important outcome of our simulations concerns the relative fraction of inspiral mergers in single- versus binary-SMBH runs. For the wide configurations in the single-SMBH case, although the total number of mergers is lower than in the corresponding binary runs, the fraction of inspirals is substantially higher: 50% and 29.6% for $a_{\rm min} = 0.05, \mathrm{pc}$ and $a_{\rm min} = 0.01, \mathrm{pc}$, respectively. In contrast, the binary-SMBH runs yield only 2.3% and 6.8% inspirals for the same configurations (lower panels in Fig. 3.6), highlighting the efficiency of resonant and non-resonant relaxation in gradually driving MBHs towards the GW-dominated regime in the absence of a second SMBH. This result contrasts with previous studies (Naoz et al., 2022; Mazzolari et al., 2022) on less massive SMBH systems, which found that the presence of a secondary SMBH enhances the rate of EMRIs relative to single-SMBH cases. This could be both due to the fact that our systems consist of $10^9 \mathrm{M}_\odot$ SMBHs and $10^5 \mathrm{M}_\odot$ MBHs (in contrast to $10^6 \mathrm{M}_\odot$ SMBHs surrounded by stellar-mass BHs in the studies above) , as well as the background stellar and BH density and their spatial configuration. In loosely bound MBH systems, which occupy a larger spatial extent, the presence of a secondary SMBH can result in the complete ejection of the MBHs from the system (Section 3.4.4) and potentially from the host galaxy. This ejection mechanism becomes less efficient, producing lower ejection velocities ($V_{\rm ej}$), for more tightly bound systems (Fig. 3.9) . Finally, in the most compact configuration, the relative fractions of inspirals become more balanced: the binary-SMBH runs yield 20.7% inspirals, compared to 33.3% in the single-SMBH case (see Fig. 3.6), owing to the overall higher number of

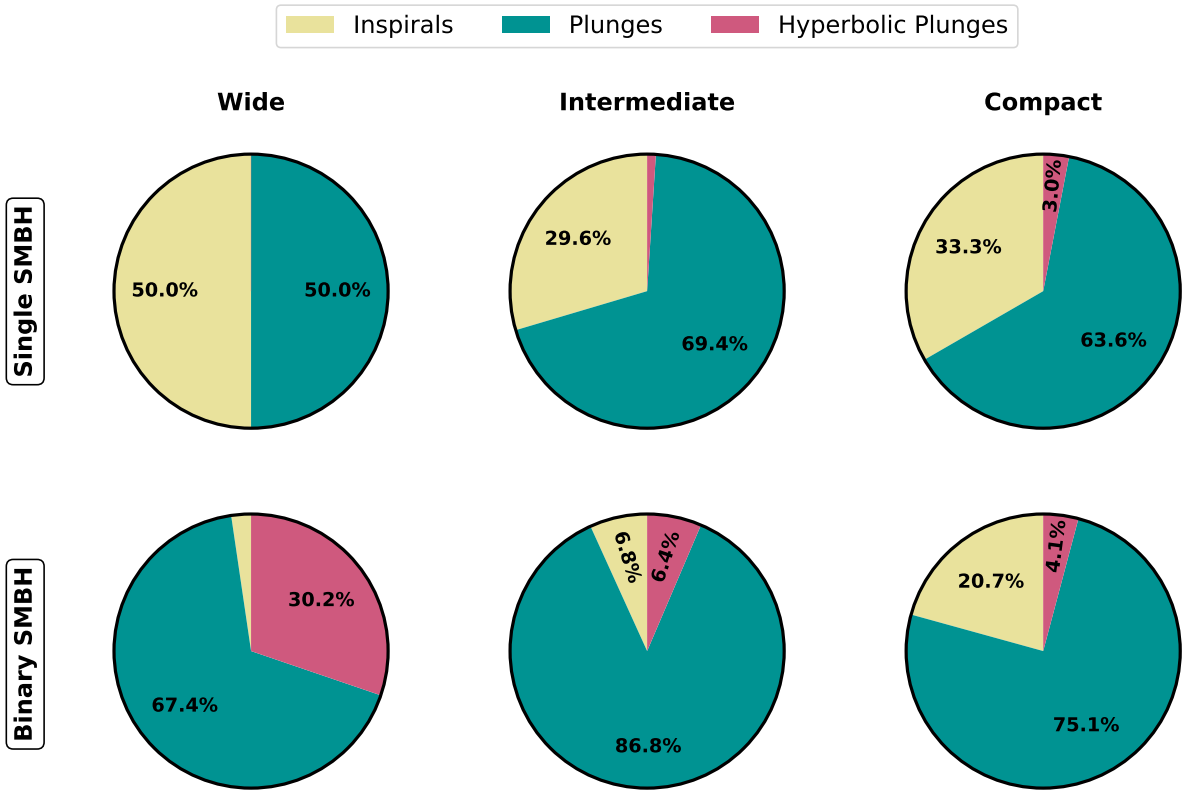

Figure 3.6: Pie charts illustrating the merger demographics in our simulations. Upper panels show results from single-SMBH runs, while lower panels correspond to binary-SMBH runs. Columns indicate the initial MBH configurations listed in Table 3.2. Single-SMBH systems exhibit a substantial fraction of inspirals, whereas the majority of mergers in binary-SMBH runs occur as direct plunges. For the widest MBH configurations, the presence of a companion SMBH produces a significant population of hyperbolic mergers ($e \geq 1$), accounting for $\sim 30\%$ of the total mergers, resulting from strong three-body interactions. In more compact configurations, the fraction of inspirals in binary-SMBH runs increases, reflecting the reduced ability of the secondary SMBH to efficiently disrupt tightly bound MBH systems.

mergers in the binary runs.

3.4.2 Initial State and Merger Pathways

To better understand the early dynamical state of our systems, we begin by discussing the key mechanisms driving the orbital evolution of the MBHs. In Fig. 3.7 we present the initial state of our simulations on the $(1-e, a)$ phase space, where different colored markers refer to the three different semi-major axes distributions. The figure is divided in four different regions where different dynamical processes are dominating the evolution of the system. The purple shaded region on the top-right corresponds to the region of phase

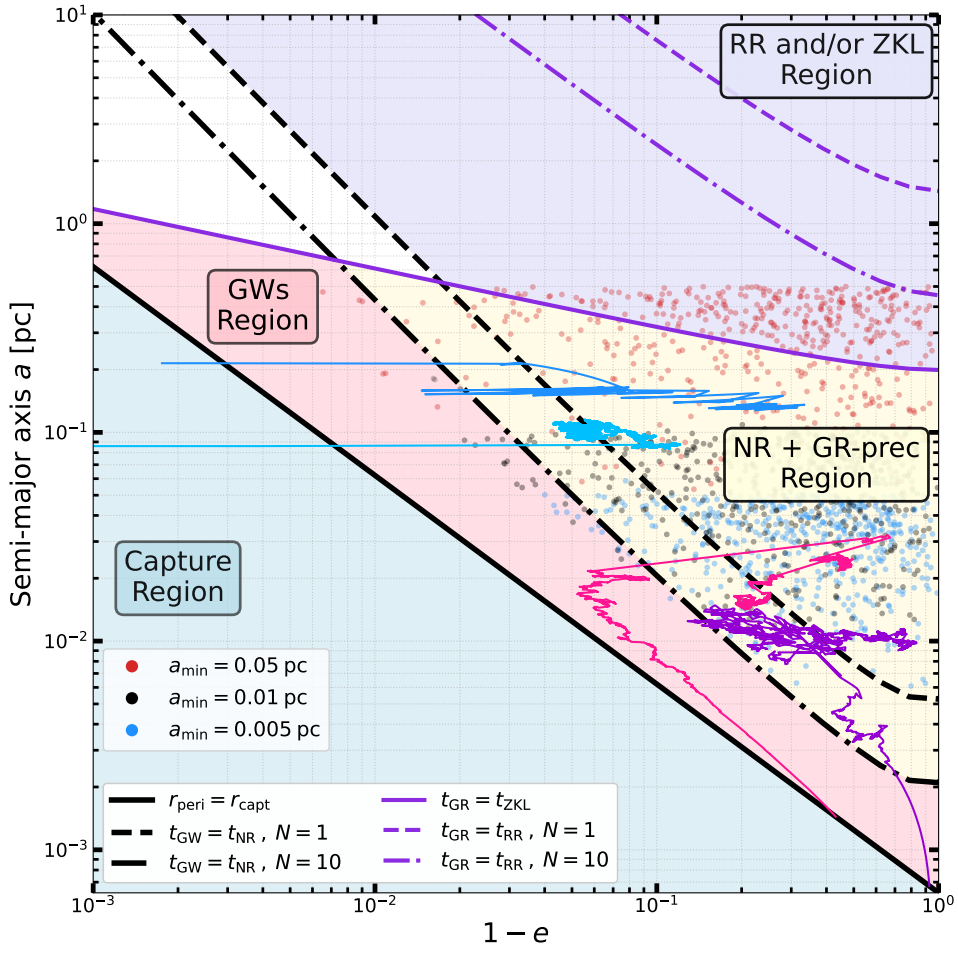

Figure 3.7: Initial distribution of our simulated systems. The phase space is divided in four different regions due to various key dynamical processes: resonant relaxation (RR) eccentric von Zeipel-Kozai-Lidov (ZKL), non-resonant relaxation (NR), relativistic precession (GR) and GW-driven inspiral (GW). The curves denote the semi-major axes at which the characteristic timescales of two competing processes governing the orbital evolution of a particle are equal. The dot-dashed and dashed purple curves are found by equating $t_{\rm RR} = t_{\rm GR}$ and they mark the region (purple) where resonant relaxation is the most rapid process against relativistic precession. Similarly the black curves correspond to $t_{\rm NR} = t_{\rm GW}$ and mark two regions: the pink one where gravitational wave emission dominates the orbital evolution and the yellow where the combined effects of non-resonant relaxation and relativistic precession act on shorter timescales. Different line-styles refer to different number of MBH particles N inside a reference semi-major axis. The black solid curve denotes orbits with $r_{\rm peri} = r_{\rm capt} = 6.5\,R$s marking the region (blue) where a particle in a highly eccentric orbit is captured by and directly plunges to the SMBH. When a companion SMBH with $a_{\rm b} = 1$ pc is included, it also induces perturbations on the particles via the ZKL mechanism. To find the critical semi-major axis (solid purple line) above which ZKL dominates over GR, we equate $t_{\rm ZKL} = t_{\rm GR}$. Notice how the wide (red) distribution is initially affected by this process. Finally the the light-blue and blue tracks correspond to plunges from a simulation with single and binary SMBH, whereas the pink and purple to inspiral orbits respectively.

Table 3.3: Merger outcomes for single and binary SMBH systems under different a distributions. Each entry shows the total number of mergers and their distribution among heavy IMRIs, direct plunges, and hyperbolic plunges (with percentages relative to the total in each column).

a [pc]	Single SMBH				Binary SMBH			
	Total	IMRIs	Plunges	Hyperbolic Plunges	Total	IMRIs	Plunges	Hyperbolic Plunges
0.05 – 0.5	8	4 (50.0%)	4 (50.0%)	0 (0.0%)	43	1 (2.3%)	29 (67.4%)	13 (30.2%)
0.01 – 0.1	98	29 (29.6%)	68 (69.4%)	1 (1.0%)	280	19 (6.8%)	243 (86.8%)	18 (6.4%)
0.005 – 0.05	165	55 (33.3%)	105 (63.6%)	5 (3.0%)	338	70 (20.7%)	254 (75.1%)	14 (4.1%)

space where resonant relaxation acts on a shorter timescale than relativistic precession and drives the orbital evolution. The characteristic semi-major axis at which the two processes operate on comparable timescales is obtained by equating Eqs. (3.5) and (3.2) and solving for a ,

$$t_{\rm GR} = t_{\rm RR} \;\Rightarrow\; \frac{1}{6}(1-e^2)\frac{c^2 a}{GM_\bullet}P = \frac{P}{2\pi}\frac{M_\bullet}{m}\frac{1}{\sqrt{N}}$$
$$\Rightarrow\; a^{\rm RR}_{\rm crit} = \frac{3GM_\bullet^2}{mc^2\sqrt{N}(1-e^2)},$$

where we have also used Kepler's third law for the orbital period with $m \ll M_\bullet$,

$$P = 2\pi\sqrt{\frac{a^3}{GM_\bullet}}. \tag{3.30}$$

Below $a^{\rm RR}_{\rm crit}$ relativistic precession becomes faster and suppresses resonant relaxation. The curve separating those two regimes has been identified and examined in earlier studies (Merritt et al., 2011; Brem et al., 2014; Hamers et al., 2014) and is also known as the *Schwarzschild barrier*. Notice how the curve moves upwards (dot-dashed line for $N = 10$, dashed line for $N = 1$) for decreasing MBH number N inside a reference semi-major axis. Since all simulated systems lie below this curve, we can safely neglect resonant relaxation effects in the subsequent analysis.

The yellow shaded region in Fig. 3.7 corresponds to the phase space region where orbital and dynamical evolution are governed by stochastic encounters due to two-body (non-resonant) relaxation coupled with relativistic precession. To separate this region from that where the orbital evolution is dominated by gravitational wave emission, we define another characteristic semi-major axis where the timescale at which non-resonant relaxation operates becomes comparable with GW-driven inspiral timescale. We obtain this semi-major axis by equating Eqs. (3.6) and (3.7) and again solving for a. After some algebra and use of Eqs. (3.8), (3.9) and (3.30), we then get

$$t_{\rm GW} = t_{\rm NR} \;\Rightarrow\; \frac{5}{64}\frac{c^5 a^4}{G^3 M_\bullet m (M_\bullet + m)} F(e) R(e) = \frac{M_\bullet^2}{m^2 N} P$$
$$\Rightarrow\; a_{\rm crit}^{\rm NR} = \left(\frac{128\pi G^{2.5} M_\bullet^{2.5} \left(M_\bullet + m\right)}{5 c^5 m N F(e) R(e)} \right)^{2/5}.$$

An MBH with $a < a_{\rm crit}^{\rm NR}$ is then decoupled from other dynamical perturbations and will evolve towards merger with the SMBH due to energy and angular momentum loses via the emission of gravitational waves alone (pink-shaded region in Fig. 3.7). We show the effect of particle number inside some reference semi-major axis with different line-styles, where again for decreasing N the curve moves upwards. This curve serves as a key diagnostic, delineating whether an orbit's evolution is dominated by stochastic perturbations—such as non-resonant relaxation and chaotic encounters—or by the gradual, decoupled inspiral driven by gravitational wave emission. It has been employed in previous studies to distinguish between direct plunges into the SMBH and slow inspirals that can lead to the formation of EMRIs (Merritt et al., 2011; Brem et al., 2014; Hamers et al., 2014; Mancieri et al., 2025a).

In addition, strong scatterings (see e.g., Teboul & Perets, 2025) with a tertiary SMBH or chaotic three-body interactions can drive MBHs onto hyperbolic trajectories ($e \geq 1$), resulting in high-velocity encounters or ejections from the system. Finally, if any of the above processes drive a particle to an extremely (almost radial) eccentric orbit, then it can by-pass the GW-dominated region and be captured by the SMBH when $r_{\rm peri} < r_{\rm capt} = 6.5\,R$s. The corresponding semi-major axis limit below which such direct capture occurs (blue-shaded region in Fig. 3.7) is then

$$r_{\rm peri} = r_{\rm capt} \Rightarrow a(1-e) = r_{\rm capt} \Rightarrow a_{\rm capt} = \frac{r_{\rm capt}}{1-e}. \tag{3.31}$$

It is important to mention at this stage, that the inclusion of a companion SMBH can alter significantly the early dynamical evolution of the system-especially for wide MBH configurations- causing eccentricity oscillations to an inner binary consisting of the primary SMBH and an MBH via the eccentric ZKL mechanism (Nate Bode & Wegg, 2013; Naoz et al., 2022; Mazzolari et al., 2022). The solid purple curve in Fig. 3.7 corresponds to the semi-major axis where the timescales between ZKL and GR-precession become comparable and is obtained by equating this time Eqs. (3.2) and (3.11). In the region above this line, ZKL dominates the early evolution of an MBH in the presence of the secondary SMBH.

Additionally, in Fig. 3.7 the evolutionary tracks for two plunge and two inspiral orbits are plotted. The light-blue line is an example of a plunging orbit in a simulation with a single SMBH, which initially evolves due to the cumulative effects of NR until it receives a strong perturbation enough to drive the MBH deep inside the capture radius. Similarly, the blue line corresponds to a plunging orbit in the presence of the second SMBH, where the MBH undergoes a 3-body encounter, boosting its eccentricity and resulting in a radial orbit crossing the capture radius. These tracks are representative of direct plunge events,

and the majority of such events in our simulations follow similar trajectories, exhibiting a rapid transition from mildly eccentric orbits to highly radial plunges into the SMBH.

In contrast, the pink track illustrates an inspiral orbit in a simulation with a single SMBH, where the early evolution is driven by non-resonant relaxation and GR precession. The MBH eventually enters the GW-dominated region and gradually inspirals toward merger via GW emission. The purple track shows a similar case in a binary SMBH simulation, but here the MBH enters the GW-dominated regime with low eccentricity and semi-major axis, producing an almost circular inspiral ($e \sim 0$). Inspiral tracks are generally more sensitive to the initial location in phase space (Fig. 3.7): depending on which region they enter from—whether dominated by NR, RR, or ZKL mechanisms—the resulting inspiral can exhibit substantially different semi-major axes and eccentricities at the onset of GW-driven evolution. Most inspiral events follow trajectories qualitatively similar to these examples, but their detailed properties are strongly influenced by the dominant dynamical processes in the region from which they enter the GW-dominated regime.

$$
\begin{aligned}
t_{\rm GR} &= t_{\rm ZKL} \\
&\Rightarrow \frac{1}{6}(1-e_{\rm in}^2)\frac{c^2 a}{GM_1}P_{\rm in} = \frac{16}{30\pi}\frac{M_1+M_2+m}{M_2}\frac{P_{\rm out}^2}{P_{\rm in}}\left(1-e_{\rm out}^2\right)^{3/2} \\
&\Rightarrow a_{\rm crit}^{\rm ZKL} = \left[\frac{16}{5\pi}\frac{GM_1\left(M_1+m\right)}{c^2}\frac{\left(1-e_{\rm out}^2\right)^{3/2}}{M_2}\frac{a_{\rm out}^3}{1-e_{\rm in}^2}\right]^{1/4},
\end{aligned}
$$

where M_1 and M_2 are the masses of primary and secondary SMBH and $P_{\rm in}$, $e_{\rm in}$ are the period and eccentricity of the inner binary. The outer binary is on a fixed orbit (Section 3.3.6) with $a_{\rm out} = 1$pc and $e_{\rm out} = 0.5$. This separating curve is essentially the *Schwarzschild barrier* for SMBH binaries (Nate Bode & Wegg, 2013). The key difference for the single SMBH simulations is that RR has no influence on the early dynamical evolution of the system and is already suppressed by GR-precession, whereas in the binary SMBH runs, the ZKL mechanism has a significant influence on the wide (red markers) configuration.

In general, eccentricity growth induced by the ZKL mechanism can be significantly suppressed by general relativistic precession (Bonetti et al., 2016; Bonetti et al., 2019; Lim & Rodriguez, 2020). Moreover, given that the evolution of our $N = 10$ systems is inherently chaotic, the hierarchical structure of the triple configuration will eventually be disrupted, rendering the secular ZKL formalism inapplicable. In the context of chaotic three-body dynamics, one may define a critical semi-major axis, $a_{\rm chaos}$, for the outer binary, which delineates the boundary between distinct dynamical regimes (Mardling & Aarseth, 2001; Vynatheya et al., 2022). A detailed investigation of these regimes requires alternative methodologies, which lie beyond the scope of the present work.

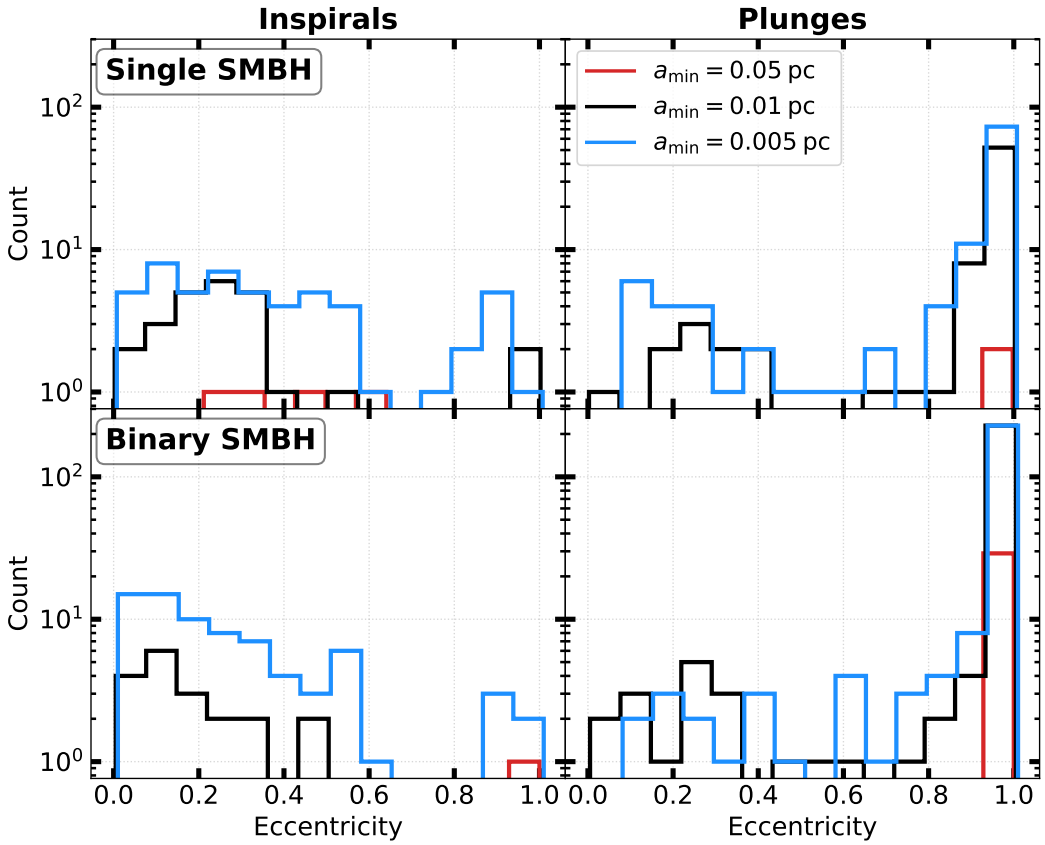

Figure 3.8: Distribution of final (at merger) eccentricity of direct plunges (right) and inspirals (left). The eccentricity for DPs peaks at $e \geq 0.9$, as expected for the majority of such events. MBHs on near-circular orbits with $a \gtrsim r_{\rm capt}$, can directly plunge to the SMBH, after receiving a perturbation from an another MBH, which explains the low-eccentricity DPs on the right panels. For IMRIs, there is not preferred eccentricity from single SMBH runs, with the majority of such events having $e \leq 0.6$ when a second SMBH is included. MBH orbits with small semi-major axes ($a \approx 0.01$pc) and large eccentricities can still reach the GW-dominated region of phase space, where they evolve into short-lived inspirals that merge while retaining high eccentricity.

The influence of the stellar background on the dynamical evolution

In our simulations and analysis we did not include a stellar background distribution. Here, we briefly assess how the relevant relaxation timescales would be affected in a typical massive early-type galaxy (ETG). We a typical ETG model (e.g. Rantala et al. 2018; Rantala et al. 2024b) characterized by a central density of $\rho_{\rm c} = 10^4\,{\rm M}_\odot{\rm pc}^{-3}$ at $r = 10$ pc and a Hernquist density profile (Hernquist, 1990) with an inner power-law slope $\rho(r) \propto r^{-\gamma}$, where $\gamma = 1$. For an average stellar mass of $m \approx 0.4\,{\rm M}_\odot$ from an evolved stellar population

within a radius of $r = 1$pc, this yields a total cumulative stellar mass $M_\star(r < 1\text{pc}) = 4.19 \times 10^4\,\mathrm{M}_\odot$ and a total number of stars $N_\star(r < 1\text{pc}) = 1.05 \times 10^5$. Thus, the SMBH dominates the mass budget of the central parsec of the system the entire MBH system is well embedded within the influence radius of the primary SMBH.

Considering an MBH orbiting a supermassive black hole with a semi-major axis of $a = 0.01$ pc and $e = 0.5$ (same as the example orbit used for the timescales in Table 3.1) , the expected number of stars in the above early-type galaxy within that radius is $N_\star(r < 0.01\text{pc}) \sim 0$. Consequently, both resonant relaxation (RR) and non-resonant relaxation (NR) from the stellar component play only a minor role in the dynamics at such small scales. For the same stellar distribution but with an MBH on a wider orbit ($a = 0.5$ pc), the enclosed number of stars rises to $N_\star(r < 0.5\text{pc}) \sim 5000$. At these distances, the corresponding relaxation timescales are $t_{\rm RR} \approx 1.45 \times 10^4$yr and $t_{\rm NR} \approx 8 \times 10^6$ yr. Relativistic precession weakens with increasing separation, yielding $t_{\rm GR} \approx 1.37 \times 10^6$ yr. Since $t_{\rm RR} < t_{\rm GR}$, relativistic precession cannot efficiently suppress RR at large separations, which therefore becomes the dominant and fastest mechanism governing orbital evolution. At those distances, for a subsystem of $N = 10$ MBHs, the RR and NR timescales are $t_{\rm RR} \approx 5.27 \times 10^5$ yr and $t_{\rm NR} \approx 1.05 \times 10^{10}$ yr, respectively, further confirming that RR governs the evolution of the MBH ensemble. Thus the presence of a stellar background would only enhance the overall efficiency of RR-driven evolution.

This highlights the importance of including a stellar background—particularly at larger orbital scales where GR effects are weaker and the MBH may initially reside—as the stellar torques can substantially enhance angular-momentum diffusion. In this regime, RR dominates over both NR and GR, while NR and GR act on comparable timescales ($t_{\rm NR} \sim t_{\rm GR}$) and thus compete. By contrast, the mass-precession timescale for the stellar background ($t_{\rm MP} \approx 1.15 \times 10^8$ yr) remains orders of magnitude longer than $t_{\rm GR}$, confirming that relativistic precession continues to limit its dynamical influence even at these separations. For an $N = 10$ MBH subsystem, however, $t_{\rm MP} \approx 6.05 \times 10^5$ yr, bringing it into direct competition with RR and further emphasizing the complex interplay of relaxation processes in the multi-MBH regime.

3.4.3 Merger eccentricity distribution

We focus on the eccentricity distribution of our merger events, as it encodes critical information about the dynamical environment in which the coalescence occurs. In particular, large residual eccentricities at merger can serve as a diagnostic of triple-MBH interactions, which can drive binaries to extreme values of $e \gtrsim 0.9$ and accelerate coalescence, requiring an accurate relativistic treatment (e.g., Bonetti et al., 2016). Recent work further demonstrates that high-eccentricity mergers are a natural outcome of chaotic three-body encounters among MBHs in galactic nuclei (Bonetti et al., 2019). Such signatures are especially relevant for LISA, since residual eccentricity leaves an imprint on their GW-waveform. Detecting eccentric mergers would thus not only provide evidence for triple-MBH interactions but also offer a unique probe of the dynamical assembly channels of MBHs in galactic centers.

Figure 3.8 shows the eccentricity distribution from our simulations measured at the time of merger. The right panels correspond to direct plunge (DP) events, with the expected peak at $e \geq 0.9$ in both single- and binary-SMBH cases. MBHs on near-circular orbits with $a \gtrsim r_{\rm capt}$ can still undergo direct plunges if perturbed by another MBH, which explains the presence of low-eccentricity DPs in the right panels. We do not observe significant differences between single- or binary-SMBH runs, nor a strong correlation with the compactness of the system. The broader (red) distribution from the binary-SMBH runs (bottom panel) is dominated by such highly eccentric mergers triggered by encounters with the secondary SMBH.

The eccentricity distribution of inspirals is presented in the left panels of Fig. 3.8. Most inspirals occur with $e < 0.5$, consistent with orbital evolution primarily driven by GW emission. For IMRIs, there is no preferred eccentricity in the single-SMBH runs, whereas in the binary-SMBH case the majority of events have $e \leq 0.6$. A small subset with $e \gtrsim 0.6$ corresponds to MBHs that enter the GW-dominated regime (highlighted in Fig. 3.7) on highly eccentric orbits, often as a result of chaotic three- or four-body interactions. These produce short-lived inspirals that merge while retaining substantial eccentricity. In particular, MBH orbits with small semi-major axes ($a \approx 0.01\,{\rm pc}$) and large eccentricities can evolve directly into this regime, leading to high-e mergers.

Finally, if the number of particles within the orbit of an MBH is sufficiently large (in our setup, $N_{\rm max} = 10$), two-body relaxation (NR) could, in principle, drive eccentricities to large values on longer timescales; however, this effect is not observed in our simulations. The limited number of inspirals in the wider (red) MBH configuration further prevents us from drawing robust conclusions for those systems.

3.4.4 Ejections from Single and Binary SMBHs

In our simulations, particles that become unbound are removed from the system once they reach a distance of $r_{\rm esc} = 1\,{\rm kpc}$. Figure 3.9 shows the distributions of ejection times, $t_{\rm ej}$ (left panels), and ejection velocities, $V_{\rm ej}$ (right panels), for the escaped MBHs, measured at $r_{\rm esc}$.

When MBH–SMBH binaries become sufficiently hard (Quinlan, 1996; Sesana et al., 2006), they can efficiently eject stars and COs that pass nearby. This dynamical slingshot mechanism (Hills, 1988) has been widely studied in the context of inspiralling star clusters hosting IMBHs, where an SMBH–IMBH binary can accelerate stars to high velocities (Baumgardt et al., 2006; Sesana et al., 2007, 2009b; Evans et al., 2023; Rasskazov et al., 2019). In merging star clusters hosting MBHs, Souvaitzis et al. (2025b) further demonstrated that hard MBH binaries not only increase the number of ejected stars and compact objects but also significantly boost their ejection velocities, highlighting the efficiency of such dynamical interactions. A related mechanism arises when a stalled MBH binary interacts with a third incoming MBH (Ryu et al., 2017c), forming a transient triplet: chaotic three-body encounters can both harden the surviving binary and eject the lighter component at high velocity (Mikkola & Valtonen, 1990). These processes underscore the role of few-body dynamics in shaping both the hardening of MBH binaries and the population of

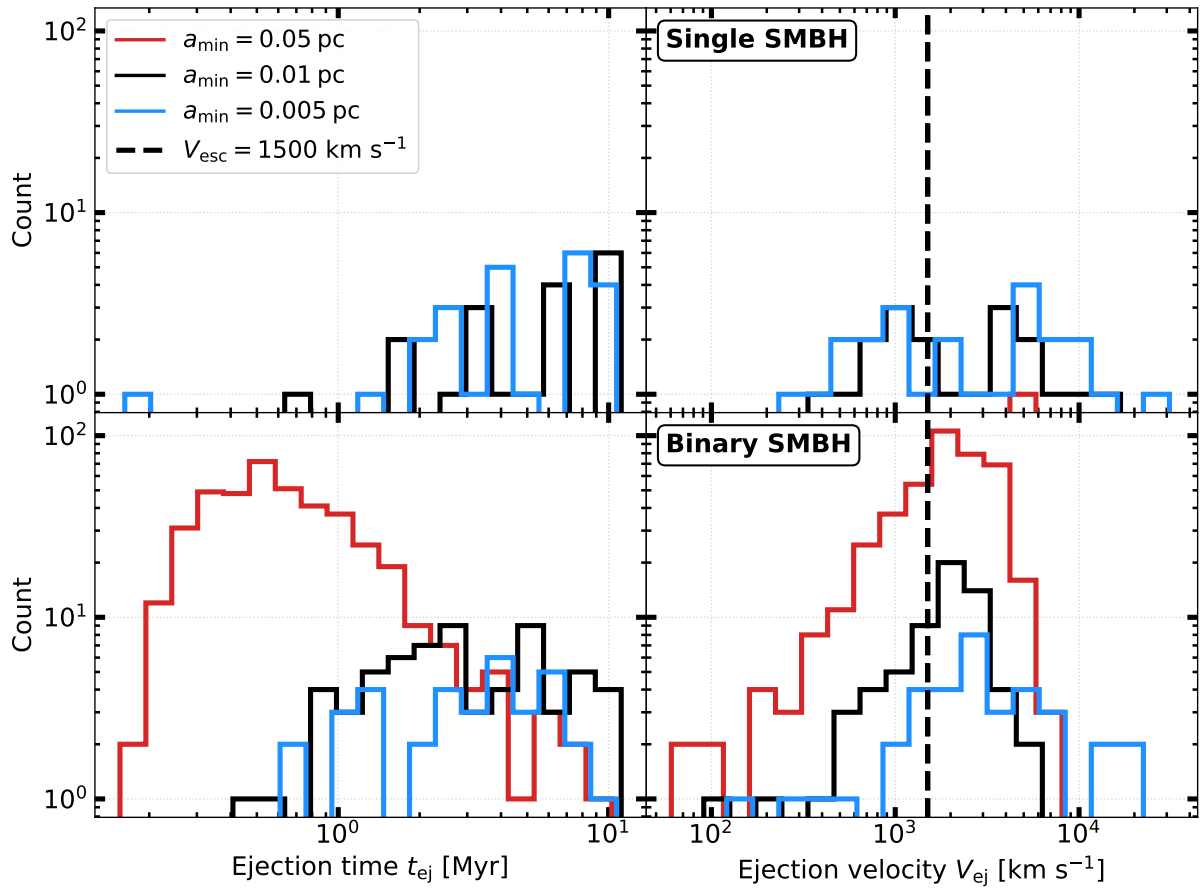

Figure 3.9: Distribution (top panel: single SMBH runs, bottom panel: binary SMBH runs) of ejection times t_{ej} (left) and ejection velocities (right) of MBHs which have escaped in the runs. The vertical black dashed line correspond to the escape velocity of a typical ETG, where $V_{esc} = 1500$ km s^{-1}.

wandering or ejected MBHs in galactic nuclei.

In our results, the presence of a second SMBH dramatically enhances the ejection rate for less bound MBH configurations (wide distribution shown in red). The peak of the red t_{ej} distribution occurs at $t_{ej} \sim 0.5$ Myr, which roughly corresponds to the typical fly-by time associated with the most common ejection velocities ($V_{ej} \approx 2000$ km s^{-1}). As a result, many of the escaping MBHs are expelled from the central system during the initial disruption phase, when the secondary SMBH first perturbs the configuration. This leads to a substantial excess of high-velocity ejections, with 283 out of 419 MBHs removed from the host galaxy due to these interactions.

The effect of the second SMBH in tightly bound systems is weaker, while they still increase the total number of ejections compared to runs with a single SMBH: from 12

(out of 19) to 44 (out of 64) for the intermediate configuration (black histograms) and from 15 (24) to 27 (out of 36) for the compact one (blue histograms). The effect of the compactness of the system is clearly visible in the $V_{\rm ej}$ distribution (bottom-right panel in Fig. 3.9), except from a few extreme cases in the compact configuration leading to $V_{\rm ej} > 10^4$ km s^{-1}.

3.5 Gravitational Waves

A binary system on a circular orbit emits gravitational waves at a frequency $f_{\rm GW}$ which is simply twice the orbital frequency (e.g. Blanchet et al., 2006; Maggiore, 2007) or

$$f_{\rm GW} = 2f_{\rm orb} = 2/P, \tag{3.32}$$

where P is the orbital period Eq.(3.30). However, for eccentric binaries, the GW emission is strongly concentrated near pericenter, resulting in a shift of the peak frequency towards higher harmonics. In accordance with the foundational work of Peters & Mathews (1963), which utilized the lowest-order (PN1) post-Newtonian approximation, it was demonstrated that the power of the n-th harmonic, with frequency $f_{\rm GW,n} = nf_{\rm orb}$ (with integer $n \geq 1$), is described by

$$P_{\rm n} = \frac{32}{5}\frac{G^4}{c^5}\frac{\mathcal{M}^5}{a^5}g(n,e), \tag{3.33}$$

where $\mathcal{M}$ is the chirp mass,

$$\mathcal{M} = \frac{(M_\bullet m)^{3/5}}{(M_\bullet + m)^{1/5}}. \tag{3.34}$$

The dimensionless function $g(n,e)$ quantifies the excess power emitted in the $n-$th harmonic relative to a circular orbit and is given by (Peters & Mathews, 1963)

$$\begin{aligned} g(n,e) = \frac{n^4}{32}\Bigg\{ &\Big[J_{n-2}(ne) - 2eJ_{n-1}(ne) + \frac{2}{n}J_n(ne) \\ &+2eJ_{n+1}(ne) - J_{n+2}(ne)\Big]^2 + \left(1-e^2\right)\left[J_{n-2}(ne)\right. \\ &\left.-2J_n(ne) + J_{n+2}(ne)\right]^2 + \frac{4}{3n^2}J_n(ne)^2\Bigg\}, \end{aligned} \tag{3.35}$$

where e is the orbital eccentricity and J_n are Bessel functions of the first kind.

3.5.1 Peak Gravitational Wave Frequency of Merger Events

The characteristic chirp mass of our binaries, with a primary SMBH of $M_\bullet = 10^9 M_\odot$ and a secondary MBH of $m = 10^5 M_\odot$, is $\mathcal{M} \simeq 4 \times 10^6$ M$_\odot$ computed via Eq. (3.34) . We

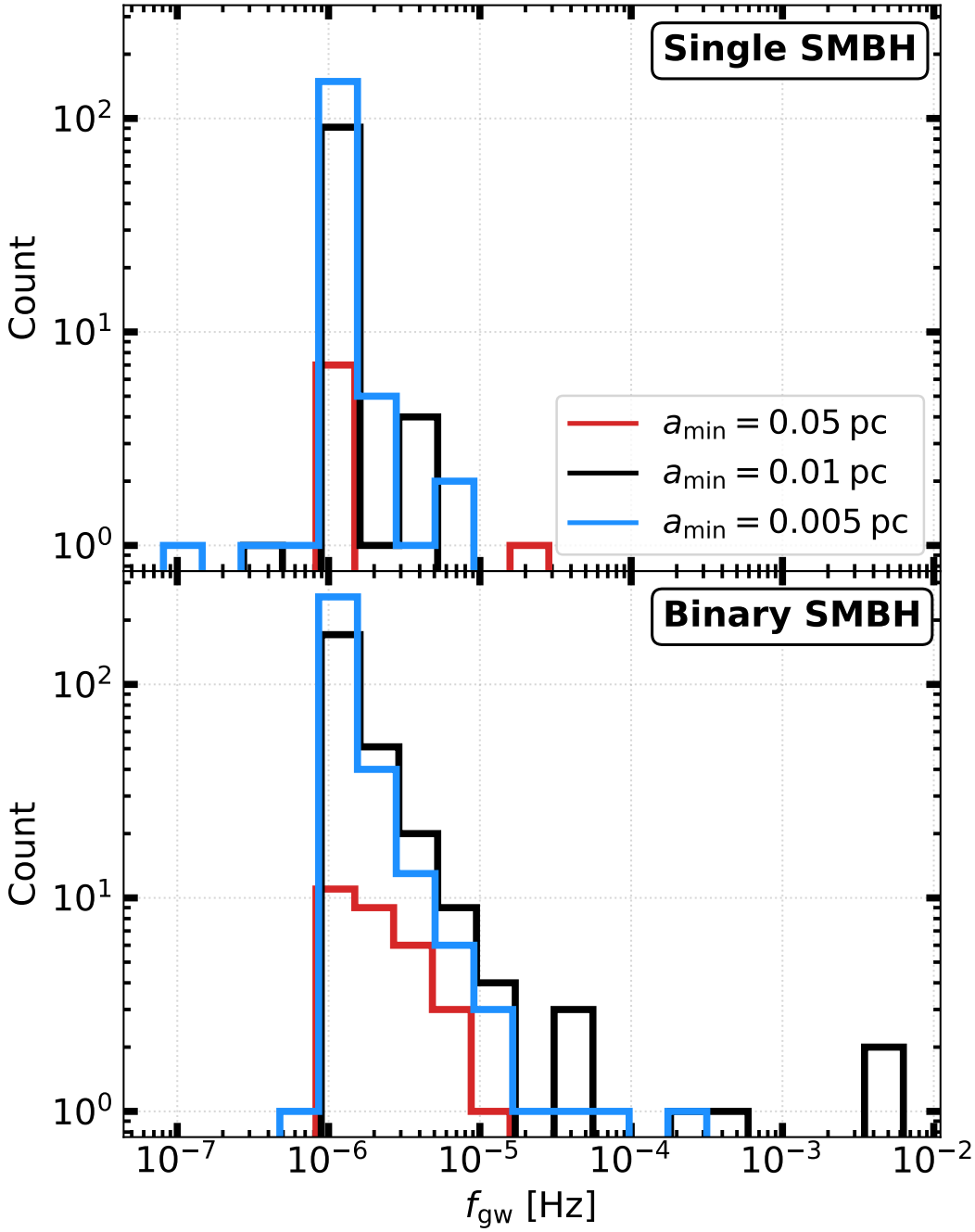

Figure 3.10: Distribution of the peak gravitational wave frequency $f_{\rm GW}^{\rm peak}$ for the merged systems in our simulations (top panel: single SMBH runs, bottom panel: binary SMBH runs). The presence of a companion SMBH systematically broadens the range of gravitational-wave frequencies at which mergers occur. Additionally, the compactness or spatial extent of the initial semi-major axis distribution (indicated by the different colors) further influences the spread of the frequency distribution, while also increasing the total number of merger events.

expect LISA to detect MBH binaries with $\mathcal{M} \sim 10^4 - 10^7$ M$_\odot$ (Klein et al., 2016; Amaro-Seoane et al., 2017), placing our system on that range, while remaining below the typical sensitivity threshold for PTAs $\mathcal{M} \sim 10^8 - 10^{10}$ M$_\odot$ (Hobbs et al., 2010; Sesana, 2013). Consequently, while the intrinsic chirp mass of our binaries falls within LISA's nominal sensitivity range, the redshift and mass ratio can shift the observed GW frequencies. We discuss the implications for their detectability with LISA and PTAs in the next section (Section 3.5.2).

To check whether our sources enter the frequency band of PTAs and/or LISA, we compute the distribution of the emitted GW frequencies. Since a large fraction of our sources are eccentric, it is important to make sure we account for the correct harmonics contribution for each case. This corresponds to the value of $n_{\rm peak}(e)$ for which Eq. (3.35) is maximum. The peak GW frequency then becomes

$$f_{\rm GW}^{\rm peak}(e) = n_{\rm peak}(e) f_{\rm orb}. \tag{3.36}$$

Wen (2003) provides a fitting function for $n_{\rm peak}(e)$, a prescription that has been widely adopted in studies of eccentric compact binary sources, (see e.g. Brown & Zimmerman, 2010; Gold & Brügmann, 2013; Samsing et al., 2014) capturing the frequency shift induced by eccentricity while remaining computationally efficient for large ensembles of binaries. However, Hamers (2021) have found that this fit behaves poorly for less eccentric sources ($e \lesssim 0.8$) and provided a corrected version of the fit capturing the full eccentricity range:

$$n_{\rm peak}(e) \simeq 2 \left(1 + \sum_{k=1}^{4} c_k e^k \right) \left(1 - e^2\right)^{-3/2}, \tag{3.37}$$

where $c_1 = -1.01678$, $c_2 = 5.57372$, $c_3 = -4.9271$, and $c_4 = 1.68506$. Using this approach, we can robustly estimate the GW signal from each merger, including highly eccentric systems, and construct the corresponding GW spectrum relevant for PTA experiments as well as LISA-related sources.

In Fig. 3.10 we present the distributions of the peak gravitational wave frequency of mergers from the simulations with a single (top panel) or a binary SMBH (bottom panel) . In all of our simulations we find the that the presence of the companion SMBH systematically broadens the frequency distribution pushing it towards higher values. This is essentially due to the excess of highly eccentric plunging orbits (right panels in Fig. 3.8), where the number of higher harmonics $n_{\rm peak}$ can be extremely large leading to increased peak gravitational wave frequencies $f_{\rm GW}$ at merger.

3.5.2 Characteristic Strain

To compute the characteristic strain $h_{\rm c,n}$ of MBH mergers, we follow the formalism of Peters & Mathews (1963) and Peters (1964), which describe the gravitational-wave (GW) emission from eccentric binaries as a sum over harmonics n of the orbital frequency $f_{\rm orb}$.

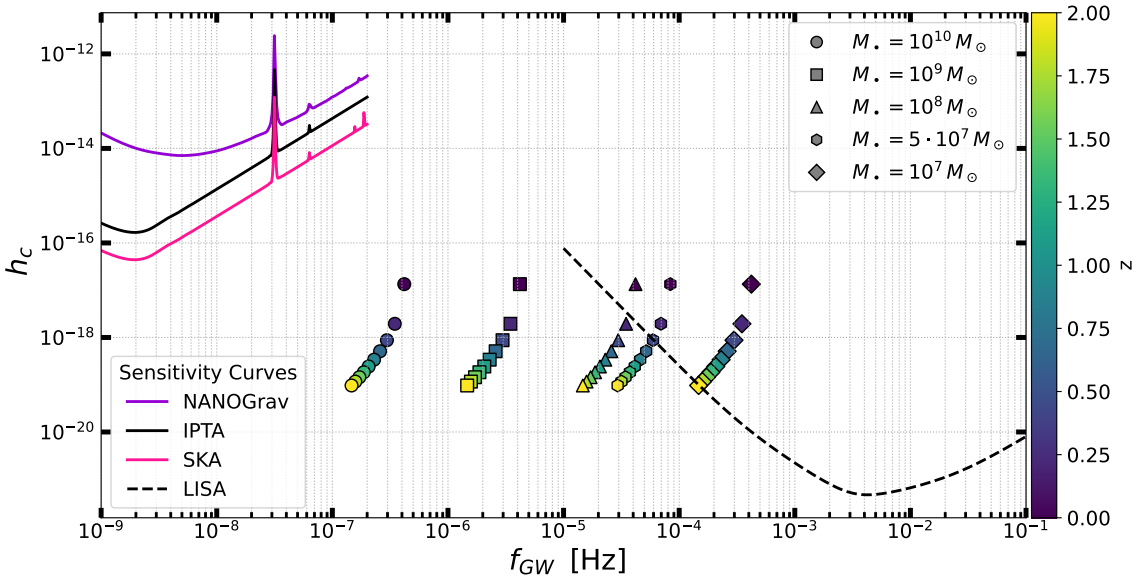

Figure 3.11: Characteristic strain for a range of heavy intermediate-mass-ratio inspiral (IMRI) sources. Different markers indicate varying primary SMBH masses and are color-coded by redshift in which we place the merging sources. Square markers represent our models, which lie just outside the LISA sensitivity band. Lower-mass primaries at modest redshifts can enter the LISA band, whereas higher-mass systems shift toward the PTA frequency range but remain below the detection threshold.

The strain amplitude $h_{\rm c,n}$ for the $n-$th harmonic with frequency $f_{\rm GW} = n f_{\rm orb}$ ($n \geq 1$) is then given by (Peters & Mathews, 1963; Finn & Thorne, 2000; Barack & Cutler, 2004)

$$h_{c,n}^2 = \frac{2}{3\pi^{4/3}} \frac{G^{5/3}}{c^3} \frac{\mathcal{M}^{5/3}}{D_L^2} \frac{g(n,e)}{n^{2/3}} f_{\rm orb}^{-1/3}, \tag{3.38}$$

where $\mathcal{D}_L$ is the luminosity distance and $n = 2$ circular orbits. Our goal is to assess whether these heavy IMRIs would be detectable by PTAs or LISA. To this end, we compute the characteristic strain $h_{\rm c}$ and GW frequency $f_{\rm GW}$ for circular binaries at $r = r_{\rm isco}$. In our models, the primary SMBH has a mass $M_\bullet = 10^9\,{\rm M}_\odot$ and the secondary $m = 10^5\,{\rm M}_\odot$, but we also explore how variations in the primary mass influence detectability. In addition, we examine the impact of different source redshifts on the prospects for detection.

Our IMRIs are indicated by the square markers in Fig. 3.11. For these systems, the characteristic strain is too low for PTA detection, while the gravitational-wave frequency falls outside the LISA sensitivity band. We expect systems with more massive primaries to approach the PTA frequency range, whereas those with lower-mass primaries may enter the LISA band depending on their redshift. Notably, IMRIs around a primary of $M_\bullet = 10^8\,{\rm M}_\odot$ could become detectable if they are sufficiently nearby, suggesting that SMBH growth via such processes may be observed by future space-based interferometers such as LISA.

To obtain a more reliable assessment of the detectability of these sources with LISA,

it is necessary to evaluate their signal-to-noise ratio (SNR), defined as (e.g., Moore et al., 2014; Robson et al., 2019).

$$\mathrm{SNR}^2 = \sum_n \left(\frac{h_{c,n}}{h_n\left(f_n\right)} \right)^2, \tag{3.39}$$

where $h_n(f) = \sqrt{f S_n(f)}$ is the characteristic noise strain and $S_n(f)$ represents the one-sided power spectral density (PSD) of the detector's noise. For a typical LISA detection, we require SNR ≥ 8 (e.g., Amaro-Seoane et al., 2017; Naoz & Haiman, 2023). We note that there may exist a population of GW-driven mergers that is effectively unobservable in GWs with current or near-future detectors due to their low masses, large distances, or orbital parameters. For these systems, electromagnetic signatures may offer complementary probes of their existence (e.g., D'Orazio & Charisi, 2023).

The estimates for primaries with $M_\bullet = 10^7, 10^8$ and $10^{10}\,\mathrm{M}_\odot$ shown in Fig. 3.11 are based on analytical estimates using Eqs. (3.36)–(3.39). These estimates assume circular binaries, a secondary mass of $m = 10^5 \mathrm{M}_\odot$, and, for illustrative purposes, are plotted at multiple redshifts to show how the same merger would appear when observed at different distances. By including these analytic points, we illustrate how the characteristic strain h_c and peak frequency scale with primary mass, highlighting the parameter space where future GW observatories may detect these heavy IMRIs. The sensitivity curve for LISA is taken from Robson et al. (2019), the NANOGrav curve from the public data release (The NANOGrav Collaboration, 2023), and for SKA and IPTA we have used the Hasasia package (Hazboun et al., 2019).

Binaries with primary masses of $M_\bullet = 10^7 \mathrm{M}_\odot$ can enter the LISA band out to redshifts as high as $z \sim 2$, although only systems with $z \lesssim 1.2$ reach a sufficiently large SNR for detection. For instance, a circular IMRI of this type would be observable at $z = 1.1$ with SNR $= 8.62$, while the same system with a modest residual eccentricity of $e = 0.1$ could be detected out to $z = 1.35$ with SNR $= 8.7$, underlining the critical role of residual eccentricity (Fumagalli et al., 2024; Garg et al., 2024) not only as a tracer of the astrophysical environment but also as a factor enhancing source detectability. By contrast, circular IMRIs with primaries of $M_\bullet = 10^8 \mathrm{M}_\odot$ remain detectable only within $z \lesssim 0.04$ with SNR ≥ 8, increasing to SNR ~ 14 for $e = 0.1$ at the same redshift. These examples highlight the strong potential of lower-mass primaries ($M_\bullet \sim 10^7$–$10^8 \mathrm{M}_\odot$) as promising hosts for heavy IMRIs detectable by LISA, motivating a systematic exploration of this regime in future work.

3.6 Discussion and Conclusions

Massive early-type galaxies grow through a hierarchical assembly process, potentially leading to a population of low-mass MBHs as well as multiple high-mass SMBHs in their nuclei. This process takes place via major galaxy mergers ($M_1/M_2 \lesssim 4$), minor mergers ($4 \lesssim M_1/M_2 < 10$), very minor or mini mergers ($10 \lesssim M_1/M_2 < 100$), and also through

accretion events ($M_1/M_2 > 100$), where the events with larger mass ratios are expected to be more common (e.g., Nipoti, 2025). In this study we explore a scenario in which the central (primary) SMBH of the galaxy is accompanied by a population of lower-mass MBHs and study the dynamics of such systems with and without the presence of a companion SMBH. We find that the secondary SMBH can increase the total merger rate up to a factor of ~ 5, depending on the initial compactness of the lower-mass MBH system.

We set up initial conditions consisting of a small cluster of MBHs with mass $M_{\rm MBH} = 10^5 {\rm M}_\odot$ orbiting a central SMBH of mass $M_{\rm SMBH} = 10^9 {\rm M}_\odot$. In the second set of simulations, we include an equal-mass companion SMBH on an outer binary orbit with semi-major axis $a_b = 1$ pc and eccentricity $e_{\rm b} = 0.5$, giving a pericentre distance of $r_{\rm peri} = 0.5$ pc. The MBHs are initialized within $r_{\rm peri}$, with semi-major axes drawn between $a_{\rm min}$ and $a_{\rm max}$, ensuring $a_{\rm max} \leq r_{\rm peri}$. We performed simulations for three choices of the compactness of the semi-major axis distributions and for each case—both with and without the SMBH companion—we carry out 50 independent random realizations, giving a total of 300 runs.

For the simulations, we have used the direct-summation N-body integrator `MSTAR` (Rantala et al., 2020), which enables the accurate modeling of non-softened dynamics via algorithmically regularised integration. The code incorporates relativistic effects with the inclusion of post-Newtonian corrections up to order 3.5PN and we have additionally implemented on-the-fly calculation of 3PN-accurate quasi-Keplerian elements following Memmesheimer et al. (2004). With the aim of classifying rapidly-evolving direct-plunge orbits on the primary SMBH versus the slowly-evolving GW-driven inspirals, we further implement an adaptive timestep method to properly capture (essential for a detailed output analysis) the latter type of merger orbits.

To address the unphysical behavior of the 3PN orbital elements for binaries approaching merger (Mannerkoski et al., 2019), we employ the geometric elements (Csizmadia et al., 2012), which more reliably describe the late stages of slowly evolving orbits provided that the pericentre region is sufficiently well resolved. This requirement is met in our simulations through the use of the adaptive timestep scheme mentioned above. An alternative approach, which would avoid switching between different orbital element definitions and ensures consistency with GW-driven evolution, would be to adopt a fully relativistic geodesic framework. In this case, the PN-corrected N-body integration would be terminated at a larger separation ($d \gg 10 R_{\rm s}$), and the final PN energy E and angular momentum L are extracted and mapped onto the semi-latus rectum p and eccentricity e (e.g., Hughes, 2024). The resulting (p, e) pair could then be used to compute and evolve the corresponding geodesic (e.g., Gair & Glampedakis, 2006). This methodology has recently been applied by Mancieri et al. (2025b) to infer EMRI eccentricity distributions and obtain robust event rates relevant for LISA, and we are currently pursuing a similar approach as part of a follow-up work.

The orbital and dynamical evolution of the lower-mass MBH system is dictated by the competition between various dynamical processes, like resonant and non-resonant relaxation (RR and NR), relativistic precession, von-Zeipel-Kozai-Lidov oscillations and the energy and angular momentum dissipation due to the emission of gravitational waves. In all systems considered, the characteristic timescale of GR precession is many orders of mag-

nitude shorter than that of RR, implying that RR is effectively quenched by relativistic effects (Merritt et al., 2011; Brem et al., 2014; Hamers et al., 2014). The presence of a companion SMBH can induce ZKL oscillations, though these are also largely suppressed by GR (Holman et al., 1997; Bonetti et al., 2016; Lim & Rodriguez, 2020), except in the case of the widest MBH configuration, where the secondary SMBH disrupts the system and produces an enhanced rate of DPs or a burst of ejections within the first $t \lesssim 0.6$ Myr. In contrast, the uncorrelated nature of gravitational encounters from NR are present, competing with GR and shaping the long-term evolution of the system. Diffusion of angular momentum through relaxation processes can gradually push MBHs toward higher eccentricities, while strong chaotic encounters provide a more violent pathway, rapidly scattering MBHs onto nearly radial orbits. Together, these mechanisms drive a substantial fraction of MBHs into highly eccentric trajectories, leading to a large number of DP merger orbits.

In our analysis we focus on the SMBH-MBH mergers involving the primary SMBH. Only four mergers with the secondary SMBH occurred in the entire sample of 300 simulations. No MBH-MBH mergers occurred in our simulation set. Our simulations demonstrate that the presence of a secondary SMBH substantially enhances the overall merger rate of MBHs, particularly for wide initial semi-major axis distributions. In these cases, the number of mergers increases by a factor of ~ 5 compared to the single-SMBH runs. Even for more compact initial configurations, the enhancement remains significant, with merger rates elevated by a factor of ~ 2. This strong boost in the SMBH-MBH merger efficiency highlights the importance of binary-SMBH environments for the evolution of central MBH subsystems.

The character of these mergers differs markedly between single- and binary-SMBH systems as presented in Figure 3.6. For wide configurations, the inspiral fraction is significantly higher in the single-SMBH case, reaching 50% for $a_{\rm min} = 0.05$ pc and 29.6% for $a_{\rm min} = 0.01$ pc. In contrast, binary-SMBH runs produce only 2.3% and 6.8% inspirals for the same configurations. The presence of the secondary SMBH efficiently drives MBHs onto nearly radial trajectories, suppressing gradual inspirals and instead producing rapid plunges. In the most compact configuration ($a_{\rm min} = 0.005$ pc), the inspiral fractions become more balanced, with 20.7% in the binary-SMBH case compared to 33.3% for the single-SMBH case. This indicates that relaxation processes dominate inspiral formation in isolated systems, while binary environments preferentially produce plunges. These findings contrast with studies of lower-mass systems (primary $M_\bullet \sim 10^6 M_\odot$), where secondary SMBHs enhance EMRI production (Naoz et al., 2022; Mazzolari et al., 2022).

An additional outcome concerns the production of hyperbolic plunges and high-velocity ejections. For the two widest configurations, plunge fractions in the binary-SMBH case reach 93.2% and 97.7% of the total mergers, with nearly ~ 30% of plunges in the widest setup (Fig. 3.6) occurring with $e \geq 1$, corresponding to hyperbolic encounters where MBHs are dynamically scattered and directly driven onto the central SMBH. The secondary SMBH also acts as an efficient channel for ejecting MBHs via the slingshot mechanism (Hills, 1988) from the system: in the wide configuration, 283 out of 419 MBHs are ejected from the host galaxy within the first ~ 0.5 Myr, coinciding with the early pericentre passages of the secondary. Intermediate and compact systems similarly show enhanced

ejection numbers compared to single-SMBH runs, from 12 (out of 19) to 44 (out of 64) for the intermediate configuration, and from 15 (out of 24) to 27 (out of 36) for the compact one.

On average out of 10 MBHs, the single-SMBH systems yield fewer than one escaper per realization across all initial configurations, whereas the binary-SMBH cases produce markedly higher ejection rates: ~ 8 escapers per run in the wide setup, ~ 1.3 in the intermediate one, and ~ 0.7 in the compact case. The reduced ejection numbers in more compact systems indicate that the efficiency of the slingshot mechanism is suppressed when the MBHs are more tightly bound, further highlighting the dominant role of the secondary SMBH in driving high-velocity ejections in wider configurations. Most ejections occur with velocities of a few $10^3\,\mathrm{km\,s^{-1}}$, though in rare compact cases velocities exceed $10^4\,\mathrm{km\,s^{-1}}$. These results demonstrate the efficiency of hard MBH binaries in producing high-velocity ejections, in agreement with previous studies of both SMBH–IMBH and MBH–MBH binaries in galactic nuclei and star clusters (Quinlan, 1996; Baumgardt et al., 2006; Sesana et al., 2006, 2007; Rantala et al., 2018; Rasskazov et al., 2019; Evans et al., 2023; Souvaitzis et al., 2025b).

The eccentricity distribution of merger events encodes key information about their dynamical environment. High residual eccentricities ($e \gtrsim 0.9$) can signal triple-MBH interactions or chaotic multi-body encounters, accelerating coalescence and requiring accurate relativistic treatment (e.g., Bonetti et al., 2016). In our simulations, most direct plunges occur at $e \geq 0.9$, while inspirals generally have $e < 0.5$, with a subset of IMRIs retaining $e \gtrsim 0.6$ due to chaotic encounters in compact configurations. Such high eccentricities leave distinct signatures on GW waveforms, which are particularly relevant for LISA (Bonetti et al., 2019). Moreover, the residual eccentricity encodes information about the surrounding stellar (Matsubayashi et al., 2007; Löckmann et al., 2008; Preto et al., 2009; Sesana, 2010; Gualandris et al., 2022) or gaseous (Sesana et al., 2005; MacFadyen & Milosavljević, 2008; Cuadra et al., 2009; Roedig & Sesana, 2012; Siwek et al., 2023b; Tiede & D'Orazio, 2024) environment, producing measurable modifications in the GW signal (Garg et al., 2024) that provide a unique probe of MBH assembly channels.

The characteristic chirp mass of our simulated binaries, with a primary SMBH of $M_\bullet = 10^9\,\mathrm{M}_\odot$ and a secondary MBH of $m = 10^5\,\mathrm{M}_\odot$, is $\mathcal{M} \simeq 4 \times 10^6\,\mathrm{M}_\odot$, placing them within the nominal LISA sensitivity range $\mathcal{M} \sim 10^4$–$10^7\,\mathrm{M}_\odot$ (Klein et al., 2016; Amaro-Seoane et al., 2017), but below the typical PTA sensitivity threshold $\mathcal{M} \sim 10^8$–$10^{10}\,\mathrm{M}_\odot$ (Hobbs et al., 2010; Sesana, 2013). Despite falling within LISA's chirp-mass range, the observed GW frequencies of our systems are generally shifted outside LISA's most sensitive band, mainly due to the large primary SMBH masses, while the characteristic strain h_c of our IMRIs is too low for PTA detection. For example, IMRIs around a primary of $M_\bullet = 10^9\,\mathrm{M}_\odot$ largely remain undetectable, while lower-mass primaries ($M_\bullet \sim 10^7$–$10^8\,\mathrm{M}_\odot$) can reach the LISA band at sufficiently low redshifts, illustrating the importance of both mass and distance in setting their GW detectability. These considerations also suggest that a population of mergers may remain essentially "invisible" to current GW observatories, motivating complementary electromagnetic searches (e.g., D'Orazio & Charisi, 2023).

To provide a broader perspective on detectability, we complement our simulations with

analytical estimates of binaries with primary masses $M_\bullet = 10^7, 10^8$, and $10^{10}\,\mathrm{M}_\odot$, assuming circular binaries, $m = 10^5\,\mathrm{M}_\odot$, and plotting them at multiple redshifts to illustrate how the same merger would appear at different distances (Fig. 3.11). For instance, a circular IMRI with $M_\bullet = 10^7\,\mathrm{M}_\odot$ would be detectable by LISA at $z = 1.1$ with SNR = 8.62, while a modest eccentricity of $e = 0.1$ increases the detectable horizon to $z = 1.35$ with SNR = 8.7 (Fumagalli et al., 2024; Garg et al., 2024). By contrast, IMRIs with $M_\bullet = 10^8\,\mathrm{M}_\odot$ are detectable only within $z \lesssim 0.04$, with SNR ~ 14 if $e = 0.1$. These results underscore the strong potential of lower-mass primaries as hosts for LISA-detectable IMRIs and motivate a systematic follow-up study to explore their occurrence rates, residual eccentricities, and observational signatures across a broader black hole mass range.

Chapter 4

MBH Binaries in Circumbinary Discs

4.1 Introduction

In the hierarchical framework of galaxy formation (Ostriker & Hausman, 1977; White, 1980; Blumenthal et al., 1984; Davis et al., 1985), galaxies assemble through successive mergers of smaller systems (Toomre & Toomre, 1972; Cox et al., 2006; Conselice, 2014). Each major merger brings together the central supermassive black holes (SMBHs) of the progenitor galaxies, leading to the formation of a bound SMBH binary once dynamical friction against the stellar and gaseous background becomes efficient (Begelman et al., 1980; Mayer et al., 2007; Khan et al., 2016). The subsequent orbital evolution proceeds through several distinct stages: large-scale dynamical friction driving the SMBHs toward the nucleus, a "hard binary" phase dominated by stellar and gaseous torques, and finally the gravitational-wave–driven inspiral and coalescence. In gas-rich mergers, substantial inflows funnel cold gas toward the nuclear region (Barnes & Hernquist, 1991; Mihos & Hernquist, 1996; Hopkins et al., 2006), forming a circumbinary disk (CBD) that mediates angular momentum exchange and can either accelerate or stall the inspiral (Artymowicz & Lubow, 1996; Ivanov et al., 1999; Cuadra et al., 2009; Roedig & Sesana, 2012; D'Orazio et al., 2013; Farris et al., 2014; Muñoz et al., 2019). Understanding the dynamics of such gas-embedded binaries—particularly how the disk's structure, orientation, and self-gravity affect accretion and orbital evolution—is essential for linking SMBH growth, galaxy evolution, and the gravitational-wave signals soon to be probed by pulsar timing arrays and space-based interferometers (Wyithe & Loeb, 2003; Haiman et al., 2009; Sesana, 2013).

Circumbinary disk (CBD) accretion plays an important role in the evolution of many binary systems, ranging from young stellar binaries to massive black hole binaries (MBHBs). In these systems, the combined effects of accretion and binary–disk gravitational interaction dictate the long-term orbital evolution. The accretion flow is complex, extending from the outer CBD through accretion streams and into circum-single mini-disks around the binary components. Numerical simulations are essential to capture these multiscale interactions and determine the net impact of accretion on the binary orbit. Long-term simulations are particularly important to average out the short-term variability and transient

structures that dominate the instantaneous flow. Only recently have consistent results begun to emerge regarding the long-term evolution of accreting binaries (Muñoz et al., 2019; Moody et al., 2019; Duffell et al., 2020).

The most important byproduct of binary–disk coupling is the change in the binary's semi-major axis $a_{\rm b}$. Early theoretical and computational studies (Artymowicz & Lubow, 1994, 1996) concluded that binaries surrounded by gas disks tend to shrink and eventually coalesce, as the tidal torques transfer angular momentum outward. However, these early works largely neglected the contribution of accretion inside the cavity, assuming that the gas inflow onto the binary components was negligible. Later studies that included accretion flows and resolved the mini-disks found that the net torque on the binary can, in some cases, become positive, leading to orbital expansion rather than contraction (MacFadyen & Milosavljević, 2008; D'Orazio et al., 2013; Farris et al., 2014; Miranda et al., 2017; Tang et al., 2017; Muñoz et al., 2019; Tiede et al., 2020; D'Orazio & Duffell, 2021; Siwek et al., 2023b). The direction of orbital evolution therefore depends sensitively on the relative importance of the torques from the inner cavity and the outer disk.

In prograde binaries, gravitational torques from the CBD have traditionally been invoked as the dominant mechanism for extracting angular momentum and driving the binary toward merger (Pringle, 1991; Artymowicz & Lubow, 1994; Ivanov et al., 1999; Armitage & Natarajan, 2002; Lodato et al., 2009). Yet, gas residing inside the cavity—streams and mini-disks—can contribute additional gravitational and accretion torques. Simulations that resolve these regions ($R < a$) typically find that torques from inside the cavity are positive while those from the outer disk are negative (Roedig & Sesana, 2012; Tang et al., 2017; Tiede et al., 2020; Franchini et al., 2022; Siwek et al., 2023b), and depending on their relative balance, the binary may either shrink or expand. Most of these studies employ locally isothermal equations of state and neglect disk self-gravity, though a few simulations including massive, self-gravitating disks (Cuadra et al., 2009; Roedig & Sesana, 2012, 2014; Franchini et al., 2021)—typically with β-cooling prescriptions—find consistent binary shrinking. This suggests that gas thermodynamics and self-gravity play critical roles in determining the long-term fate of SMBH binaries.

In reality, however, disks with masses exceeding their aspect ratio times the binary mass are gravitationally unstable and prone to fragmentation on short cooling timescales (Gammie, 2001; Goodman, 2003; Levin, 2006). Star formation and stellar feedback in such disks are extremely challenging to model numerically, and are therefore often suppressed artificially by assuming inefficient cooling, which may overestimate the efficiency of disk-driven coalescence. While star formation depletes the gaseous mass, newly formed stars may still contribute to orbital decay via three-body interactions (Sesana et al., 2007, 2008b), albeit less efficiently than gas due to the absence of dissipation. More likely, SMBH binaries interact repeatedly with successive low-mass gaseous disks formed by the infall and tidal disruption of molecular clouds (Nixon et al., 2011). These transient, misaligned, or even retrograde disks can significantly alter the orbital dynamics, sometimes accelerating coalescence through the accretion of counter-rotating gas that enhances binary eccentricity and reduces pericentre separation.

If accretion events in galactic nuclei are chaotic and randomly oriented (King & Pringle,

2006; King, 2008), SMBH binaries are naturally expected to be surrounded by misaligned circumbinary disks. The interaction between a misaligned disk and a binary resembles Lense–Thirring precession in tilted accretion disks around spinning black holes (Bardeen & Petterson, 1975; Pringle, 1992; Scheuer & Feiler, 1996). Analytical studies (King et al., 2005; Nixon et al., 2011, 2013) show that differential precession can cause the disk to either co-align or counter-align with the binary depending on the relative magnitudes of their angular momenta. In particular, counter-alignment occurs when

$$\cos\theta < -\frac{|L_{\rm disk}|}{2\,|L_{\rm b}|}, \tag{4.1}$$

where $L_{\rm disk}$ and $L_{\rm b}$ are the angular momenta of the disk and the binary respectively and θ is the inclination between the two. Three-dimensional hydrodynamical simulations (Nixon et al., 2013; Dunhill et al., 2014; Aly et al., 2015; Moody et al., 2019) have shown that misaligned disks can also break into independently precessing rings (Nixon, 2012), whose mutual interactions can enhance accretion and promote coalescence. Retrograde disks, in particular, which lack resonant torquing, can efficiently extract angular momentum from the binary and provide a promising pathway toward overcoming the *final parsec problem* (Nixon et al., 2011; Roedig & Sesana, 2014; Heath & Nixon, 2020; Tiede & D'Orazio, 2024).

Magnetic fields fundamentally alter the dynamics of circumbinary accretion and therefore merit explicit inclusion in follow-up studies. MHD processes — in particular the magnetorotational instability and magnetically driven winds — regulate angular-momentum transport, the structure of streams feeding the cavity, and the formation and evolution of circum-single (mini-)disks (Shi et al., 2012; Shi & Krolik, 2015). Recent work has demonstrated that magnetic stresses can change the balance of torques acting on the binary, modulating both the mean accretion rate and its variability and thereby affecting secular orbital evolution (Cattorini & Giacomazzo, 2024). Moreover, magnetic fields enable jet and outflow launching from mini-disks and from the circumbinary region, which carry away angular momentum and produce observable electromagnetic signatures that depend sensitively on field geometry and magnetization. In particular, magnetically arrested disk (MAD) states can emerge due to magnetic flux accumulation near the binary, leading to intermittent jets and enhanced EM emission (Most & Wang, 2024; Wang et al., 2025). Future work should therefore aim to incorporate magnetic fields self-consistently within MHD simulations, as this is essential for accurately capturing the impact of magnetic stresses on cavity structure, accretion dynamics, and binary evolution.

Even more crucially, the final stages of binary inspiral demand a fully general-relativistic magnetohydrodynamic (GRMHD) or radiation-MHD (RMHD) framework to model accretion, radiation, and jet formation under strong-field gravity. Recent efforts to couple general relativity and magnetohydrodynamics in a mesh-less framework have been demonstrated by (Lupi, 2023; Fedrigo & Lupi, 2025), offering a promising avenue to self-consistently follow the inspiral of massive black hole binaries from large separations down to horizon scales. Near coalescence, spacetime curvature, frame dragging, and relativistic orbital motion fundamentally alter the coupling between magnetic fields, plasma, and ra-

diation—effects inaccessible to Newtonian treatments (Manikantan et al., 2025; Ennoggi et al., 2025). Recent GRMHD simulations show that strong magnetic stresses and reconnection events produce short-lived EM transients coincident with merger, while changes in magnetic topology can drive quasi-periodic flaring and post-merger jet reorientation (Ressler et al., 2024, 2025). Importantly, first fully 3D RMHD simulations of sub-Eddington circumbinary disks around equal-mass SMBH binaries (Tiwari et al., 2025) reveal that including radiation modifies thermal pressure support, producing thinner, denser, and more filamentary disk structures. Radiation also reduces the prominence of inner-edge overdensities and enhances clumpy, filament-dominated morphology, highlighting the necessity of including both radiation and magnetic fields for robust predictions of EM counterparts in the GW-driven regime.

Despite significant progress, the majority of previous works have been limited to two-dimensional or locally isothermal setups. Full three-dimensional simulations are essential to capture warping, breaking, and precessional dynamics that govern the evolution of misaligned systems. The geometry of the disk–binary configuration not only determines the efficiency of angular momentum exchange and alignment but also imprints distinctive observational signatures, such as variable accretion rates and precessing jets. Consequently, the study of three-dimensional, misaligned, and potentially magnetized circumbinary disks represents the next frontier for understanding the coupling between SMBH binaries and their gaseous environments, with direct implications for both electromagnetic and gravitational-wave observations of coalescing black holes.

4.2 Methods

4.2.1 The AREPO Code

AREPO (Springel, 2010; Pakmor et al., 2016) is a second-order finite-volume Godunov code that solves the equations of hydrodynamics on a moving, unstructured mesh. The method is based on representing control volumes as the polygons or polyhedra of a Voronoi tessellation, constructed from a set of mesh-generating points that move with the local flow. A Voronoi tessellation divides space into non-overlapping cells such that each cell contains the region closest to one mesh-generating point, with cell faces lying equidistant between neighboring points. In contrast, the Delaunay tessellation is its topological dual: it connects points whose Voronoi cells share a common face, forming a triangulation (in 2D) or a network of tetrahedra (in 3D). While the Voronoi mesh defines the control volumes used to solve the fluid equations, the Delaunay tessellation provides their connectivity, ensuring that no mesh-generating point lies within the circumcircle (or circumsphere) of any Delaunay element. An example of the two tessellations is given in Fig. 4.1.

Because the Voronoi tessellation evolves continuously for smooth trajectories of these points, each cell can be viewed as a quasi-Lagrangian fluid element (e.g., Vogelsberger et al., 2012). In addition to ideal hydrodynamics coupled to self-gravity, the code includes modules for magnetohydrodynamics (see e.g., Pakmor et al., 2011; Pakmor & Springel,

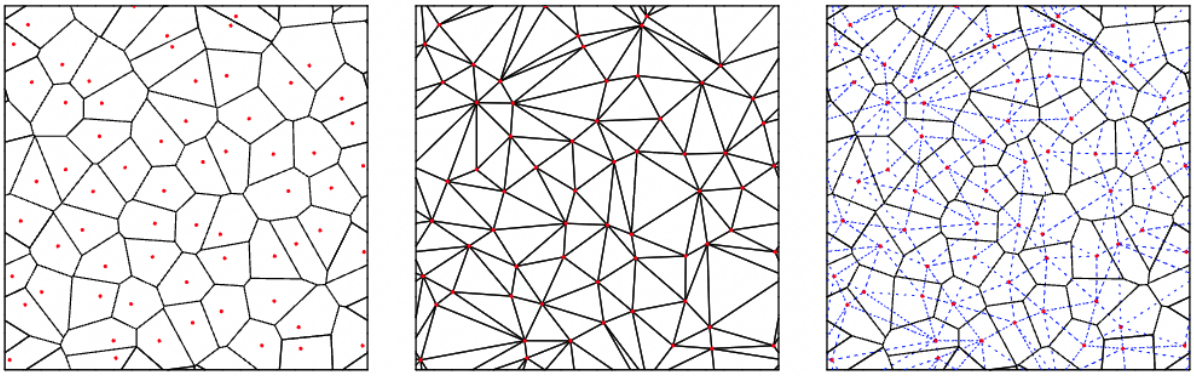

Figure 4.1: Example of two-dimensional Voronoi and Delaunay tessellations with periodic boundary conditions. The left panel shows the Voronoi tessellation for $N = 64$ mesh-generating points (red circles), the middle panel displays the corresponding Delaunay triangulation, and the right panel presents both together, with solid lines denoting the Voronoi cells and dashed lines the Delaunay connections. Figure credit: Springel (2010).

2013; Mocz et al., 2014), physical viscosity (Muñoz et al., 2013), and radiative transfer in various approximations (Petkova & Springel, 2011).

4.2.2 Finite Volume Hydrodynamics on a Moving Mesh

The Euler equations describe the conservation of mass, momentum, and energy in a fluid and form a system of hyperbolic partial differential equations. Introducing the state vector those can be expressed in compact form

$$\boldsymbol{U} = \begin{pmatrix} \rho \\ \rho\boldsymbol{v} \\ \rho e \end{pmatrix} = \begin{pmatrix} \rho \\ \rho\boldsymbol{v} \\ \rho u + \frac{1}{2}\rho\boldsymbol{v}^2 \end{pmatrix} \tag{4.2}$$

where ρ is the mass density, $\mathbf{v}$ the velocity field, and $e = u + \frac{1}{2}v^2$ the total specific energy. The quantity u denotes the internal energy per unit mass, which for an ideal gas is determined by the temperature. All fluid variables depend on position $\mathbf{x}$ and time t, although this dependence is omitted here for simplicity. Based on $\mathbf{U}$, the corresponding flux function can be written as

$$\boldsymbol{F}(\boldsymbol{U}) = \begin{pmatrix} \rho\boldsymbol{v} \\ \rho\boldsymbol{v}\boldsymbol{v}^T + P \\ (\rho e + P)\boldsymbol{v} \end{pmatrix}, \tag{4.3}$$

where the pressure P is given by the equation of state

$$P = (\gamma - 1)\rho u. \tag{4.4}$$

The Euler equations then take the conservative form

$$\frac{\partial \boldsymbol{U}}{\partial t} + \nabla \cdot \boldsymbol{F} = 0 \tag{4.5}$$

highlighting their nature as conservation laws. Over the past decades, numerous numerical methods have been developed to solve this coupled system of equations (e.g., LeVeque, 2002; Toro, 2009). Many of these are based on Godunov's method, which revolutionized computational fluid dynamics by solving exact or approximate Riemann problems at cell interfaces. This approach correctly captures the local wave structure and upwind direction, ensuring numerical stability. Although the original Godunov scheme is only first-order accurate and relatively diffusive, it can be extended to higher-order accuracy through various reconstruction techniques. In `AREPO` a finite-volume discretization is adopted, where the computational domain is divided into a finite number of non-overlapping cells. The fluid state in each cell is represented by the cell-averaged conserved quantities. Integrating over the volume V_i of the i-th cell we define the total mass m_i, momentum $\mathbf{p}_i$, and energy E_i contained within that cell as,

$$\boldsymbol{Q}_i = \begin{pmatrix} m_i \\ \boldsymbol{p}_i \\ E_i \end{pmatrix} = \int_{V_i} \boldsymbol{U} \, \mathrm{d}V. \tag{4.6}$$

With the Euler equations defined, the next step is to determine the time evolution of the conserved quantities $\boldsymbol{Q}_i$ in each cell. Using the divergence form of the Euler equations and applying Gauss's theorem, the rate of change of $\boldsymbol{Q}_i$ can be written as a surface integral over the boundary ∂V_i of the control volume:

$$\frac{\mathrm{d}\boldsymbol{Q}_i}{\mathrm{d}t} = -\int_{\partial V_i} \left[\boldsymbol{F}(\boldsymbol{U}) - \boldsymbol{U}\boldsymbol{w}^T\right] \mathrm{d}\boldsymbol{n} \tag{4.7}$$

where $\boldsymbol{n}$ is the outward normal vector of the cell surface, and $\boldsymbol{w}$ denotes the velocity of the moving cell boundary.

In a purely Eulerian scheme, the mesh remains fixed, such that $\boldsymbol{w} = 0$. In contrast, a fully Lagrangian formulation would allow each cell boundary to move with the local fluid velocity, i.e. $\boldsymbol{w} = \boldsymbol{v}$, resulting in constant cell masses. However, in multidimensional flows, the exact tracking of deforming fluid elements becomes impractical due to severe mesh distortion. Moving-mesh methods such as `AREPO` therefore adopt a quasi-Lagrangian approach, where the mesh-generating points move approximately with the flow, minimizing advection errors while maintaining mesh regularity. The general evolution equation (4.7) is thus retained in its full form.

Each control volume V_i is represented by a polyhedron (or polygon in 2D) with flat faces. Denoting by A_{ij} the oriented area vector of the face shared by cells i and j (pointing from i to j), we can define the average flux across that interface as

$$\boldsymbol{F}ij = \frac{1}{A}ij \int_{A_{ij}} [\boldsymbol{F}(\boldsymbol{U}) - \boldsymbol{U}\boldsymbol{w}^T], \mathrm{d}A, \tag{4.8}$$

so that the finite-volume discretization of the Euler equations becomes

$$\frac{\mathrm{d}\boldsymbol{Q}i}{\mathrm{d}t} = -\sum_j Aij\boldsymbol{F}_{ij}. \tag{4.9}$$

A discrete, conservative time integration can then be written as

$$\boldsymbol{Q}i^{(n+1)} = \boldsymbol{Q}i^{(n)} - \Delta t \sum_j Aij, \hat{\boldsymbol{F}}ij^{(n+1/2)}, \tag{4.10}$$

where $\hat{\boldsymbol{F}}ij^{(n+1/2)}$ is a suitably time-averaged approximation to the true flux across the interface between cells i and j. This formulation is manifestly conservative, since $\hat{\boldsymbol{F}}ij = -\hat{\boldsymbol{F}}_{ji}$ ensures exact pairwise flux cancellation.

The accuracy and stability of the finite-volume scheme crucially depend on how the numerical fluxes $\hat{\boldsymbol{F}}_{ij}$ are computed. A naive central averaging of the left and right cell-centered fluxes leads to unphysical oscillations and catastrophic numerical instabilities. Instead, modern Godunov-type schemes estimate these fluxes by solving a local Riemann problem at each cell interface. This approach correctly accounts for the upwind direction of information propagation and captures discontinuities such as shocks in a physically consistent manner.

In `AREPO`, the Riemann problem is solved in the rest frame of the moving interface, ensuring that the resulting scheme is both Galilean invariant and minimally diffusive. The moving Voronoi mesh adapts dynamically to the flow, providing a nearly Lagrangian character that reduces advection errors while avoiding mesh tangling. Combined with higher-order spatial reconstruction and slope limiting, this yields a second-order accurate, shock-capturing hydrodynamics method that smoothly transitions between Eulerian and Lagrangian behavior depending on the local flow.

A key step in finite-volume hydrodynamics is the accurate estimation of inter-cell fluxes $\hat{\boldsymbol{F}}_{ij}$, which is achieved in `AREPO` using a Godunov-type approach. Specifically, we employ the MUSCL-Hancock scheme (van Leer, 2006; Toro, 2009), which provides second-order accuracy in space and time. In this scheme, a slope-limited piecewise-linear reconstruction is performed within each cell, followed by a half-timestep prediction of the fluid state. The flux across each face is then computed by solving a one-dimensional Riemann problem in the frame moving with the face velocity $\boldsymbol{w}$, as illustrated in Fig. 4.2. This effectively up-winded approach ensures stability and physically consistent fluxes for the evolving fluid.

4.3 Simulations

We perform 3D hydrodynamic simulations of binaries embedded in circumbinary disks (CBDs) using the moving-mesh code AREPO (Springel, 2010; Pakmor et al., 2016) in its Navier–Stokes formulation (Muñoz et al., 2013). The code employs a Voronoi tessellation to construct a dynamically adaptive mesh around a set of discrete mesh-generating points. The MBH binary is modeled as two sink particles with mass ratio q_b and sink radii $r_\mathrm{acc} =$

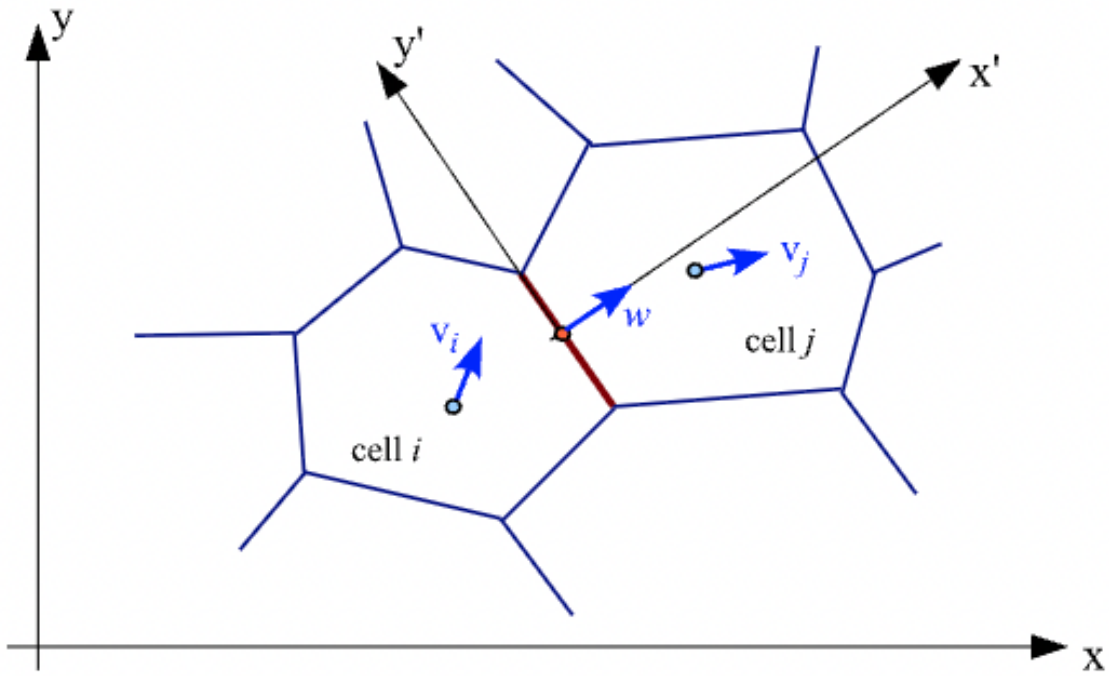

Figure 4.2: Geometry of the flux calculation. We employ an unsplit scheme in which the flux across each face is computed using a one-dimensional Riemann problem. The fluid state is evaluated in a frame moving with the face normal velocity $\boldsymbol{w}$ and aligned with the face. The face motion is fully determined by the velocities of the mesh-generating points of the cells on either side of the interface. Figure credit: Springel (2010).

$0.05\,a_b$, orbiting on a fixed Keplerian trajectory. The binary system is fully characterized by its eccentricity, e_b, and mass ratio, $q_b = M_2/M_1$. All distances are expressed in units of the binary semi-major axis, with $a_b = 1$. Likewise, the gravitational constant is $G = 1$ and the total binary mass $M_b = M_1 + M_2 = 1$. The orbital period of the binary is fixed at $P_b = 2\pi$, which is also used as the unit of time throughout our analysis, providing a natural reference for measuring disk and binary evolution. Finally, the mass resolution in the central region of our simulations corresponds to $m_{res} = 10^{-6}\Sigma_0 a_b^2$.

The parameter space explored in this preliminary study is summarized in Table 4.1. We consider binaries with circular ($e_b = 0$) and eccentric ($e_b = 0.5$) orbits, both coplanar ($i = 0°$) and moderately inclined ($i = 15°$) relative to the disk. For each combination of eccentricity and inclination, we simulate both prograde and retrograde configurations, resulting in a total of eight simulations, each evolved up to $\sim 500\,P_b$. These runs allow us to investigate the orbital evolution of the binaries and the degree of alignment or counter-alignment between the disk and the binary. The outcomes of this parameter survey will serve to motivate longer or more focused simulations in future studies. In the following, we present the mathematical and computational framework used to extract the quantities

Table 4.1: Orbital Configuration of gas-embedded MBH Binaries, varying eccentricity $e_{\rm b}$ and inclination angle i.

Model	Eccentricity	Inclination	Configuration
e0inc0	0.0	0°	prograde
e0inc15	0.0	15°	prograde
e0inc165	0.0	165°	retrograde
e0inc180	0.0	180°	retrograde
e05inc0	0.5	0°	prograde
e05inc15	0.5	15°	prograde
e05inc165	0.5	165°	retrograde
e05inc180	0.5	180°	retrograde

necessary to characterize the evolution of these systems.

4.3.1 Gravitational Potential of the Binary MBH

The binary is modeled using a prescribed, time-dependent gravitational potential,

$$\Phi(\mathbf{r}) = -GM_b \left[\frac{(1+q_b)^{-1}}{|\mathbf{r}-\mathbf{r}_1|} + \frac{q_b\,(1+q_b)^{-1}}{|\mathbf{r}-\mathbf{r}_2|} \right] \tag{4.11}$$

where $q_{\rm b} = M_2/M_1$ is the binary mass ratio and $M_{\rm b} = M_1 + M_2$ the total mass. The positions of the individual components are given by

$$\mathbf{r}_1(t) = q(1+q)^{-1}\mathbf{r}(t), \quad \mathbf{r}_2(t) = -(1+q)^{-1}\mathbf{r}(t), \tag{4.12}$$

where the relative position vector $\mathbf{r}(t)$ is expressed in terms of the binary's semi-major axis $a_{\rm b}$, eccentricity $e_{\rm b}$, and eccentric anomaly $E(t)$ as

$$\mathbf{r}(t) = a_{\rm b}\left(\cos E - e_{\rm b}, \sqrt{1-e_{\rm b}^2}\sin E\right). \tag{4.13}$$

The eccentric anomaly $E(t)$ is obtained by solving Kepler's equation (see, e.g., Danby 1988). To avoid numerical divergences near the sink positions, the potential around each component is softened using a softening length $s = 0.04a_{\rm b}$.

Gas is allowed to be accreted individually by the members of the binary through a sink-particle algorithm. Gas cells approaching within the critical distance $r_{\rm acc}$ of a sink are flagged for draining, with their mass partially removed—while the cells themselves are retained—at the end of each timestep. The fraction of gas removed from a cell depends on its radial distance $r_{\rm ij}$ from the j-th sink particle and is given by the dimensionless parameter

$$\gamma = \gamma_0 \times \left(1 - r_{\rm ji}/r_{\rm acc}\right)^2, \tag{4.14}$$

where $\gamma_0 = 0.05$, which regulates the efficiency of mass removal within the sink radius.

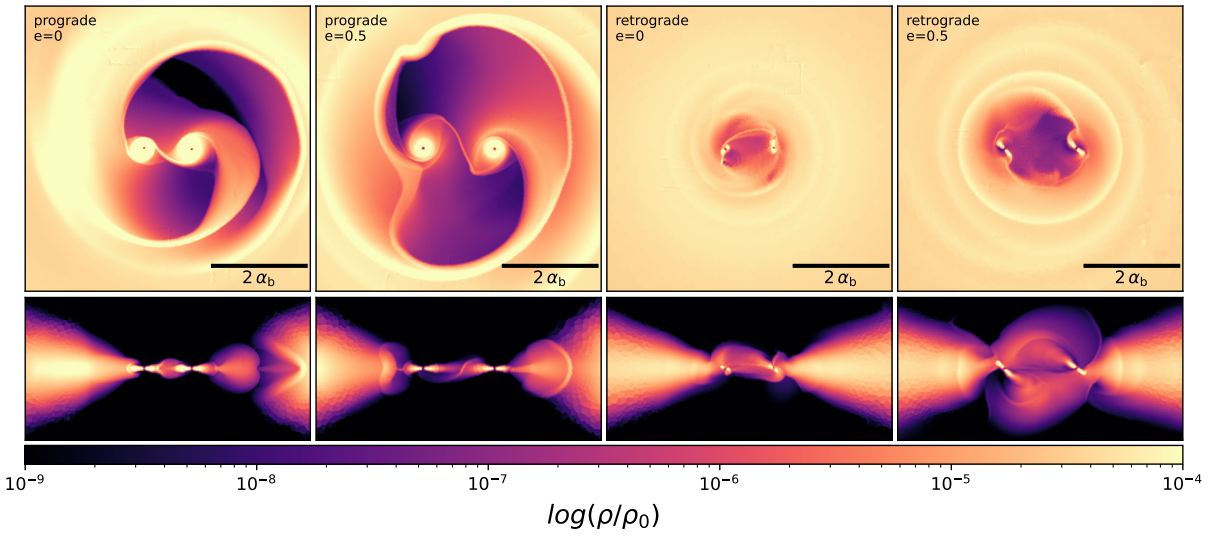

Figure 4.3: Coplanar binary–disk configurations after $t = 250$ binary orbits. Top panels show face-on projections, while bottom panels show edge-on density projections. From left to right: circular prograde, eccentric ($e_b = 0.5$) prograde, circular retrograde, and eccentric retrograde binary orbits.

4.3.2 Disk Model

The initial accretion disk is a finite, locally isothermal disk evolved within a computational domain with open boundary conditions. Figure 4.3 shows representative coplanar binary–disc configurations after 250 binary orbits, illustrating the resulting surface density distributions for circular and eccentric, prograde and retrograde binaries. Its surface density profile, $\Sigma(r)$, follows that adopted by Muñoz et al. (2020),

$$\Sigma(R) = f_t \Sigma_0 \left(\frac{R}{a_b}\right)^{-1/2} \left[1 - 0.7\sqrt{\frac{R}{a_b}}\right]. \tag{4.15}$$

The function f_t is a tapering function that initializes a finite disk with an inner cavity at radius $R_{cav} = 2\, a_b$ and an outer edge at $R_{out} \sim 50\, a_b$. This surface density profile is chosen such that $\Sigma(R) \propto R^{-1/2} \propto \dot{M}b/\nu(R)$, consistent with the steady-state solution of an accretion disk at large radii, $R/a_b \gg 1$. Although the detailed morphology of the inner regions of a CBD is expected to depend on the specific binary parameters, the impact on the outer disk at $R/a_b \gg 1$ is negligible. The vertical structure of the disk is modeled with a Gaussian profile, following the 3D prescription adopted by (see, for example, Duffell et al., 2024, and references therein):

$$\rho(r, z) = \frac{\Sigma(r)}{H} \frac{1}{\sqrt{2\pi}} \exp\left(-\frac{z^2}{2H^2}\right), \tag{4.16}$$

where $H = hr$ is the disk scale height and h the aspect ratio. Notice that the density

on the disk mid-plane is $\Sigma(r)/H = \rho(r, 0)$ and

$$\Sigma(r) = \int_{-\infty}^{+\infty} \rho(r, z) dz. \tag{4.17}$$

The simulations are performed in a computational domain of size $300a_{\rm b} \times 300a_{\rm b} \times 300a_{\rm b}$, providing sufficient space for the disk to spread viscously outward. The initial radial and azimuthal velocity profiles follow the prescription of Muñoz et al. (2019). The azimuthal velocity of the disk is initially Keplerian, with corrections due to the binary's quadrupole potential and the disk's pressure gradient,

$$v_\phi^2(R) = \frac{GM_{\rm b}}{R}\left[1 + 3QR^{-2}\right] - c_{\rm s}^2(R)\left[1 - R\frac{\partial \ln \Sigma_{\rm d}}{\partial R}\right], \tag{4.18}$$

where $G = 1$ is the gravitational constant, $M_{\rm b} = 1$ is the total binary mass, $c_{\rm s}$ is the sound speed, and Q represents the binary quadrupole moment given by

$$Q = \frac{a_{\rm b}^2}{4}\frac{q_{\rm b}}{(1+q_{\rm b})^2}\left(1 + \frac{3}{2}e_{\rm b}^2\right). \tag{4.19}$$

The initial radial velocity includes the viscous drift term, expressed as

$$v_R(R) = \frac{1}{R\Sigma}\frac{\partial}{\partial R}\left(\nu\Sigma R^3 \frac{{\rm d}\Omega}{{\rm d}R}\right)\left[\frac{\rm d}{{\rm d}R}(R^2\Omega)\right]^{-1}, \tag{4.20}$$

where ν is the kinematic viscosity and Ω the Keplerian angular velocity. A locally isothermal equation of state is adopted,

$$c_{\rm s}^2(R) = h^2\,|\Phi_{\rm b}(R)|, \tag{4.21}$$

where $\Phi_{\rm b}$ is the binary potential and the disk aspect ratio is $h = 0.1$.

4.3.3 Viscosity

The viscosity is modeled with an α-prescription both inthe CBD around the binary and on circumsingle disk (CSD) scales with a smooth transition in between similar to Siwek et al. (2023a). We model all accretion disks in our simulations using the standard α-disk prescription. The kinematic viscosity is expressed as

$$\nu(R) = \alpha h c_{\rm s}(R) R, \tag{4.22}$$

where $\alpha = 0.1$ is a constant viscosity parameter, h is the disk aspect ratio, and $c_{\rm s}$ is the locally isothermal sound speed, given by

$$c_{\rm s}(R) = h \times \sqrt{|\Phi_{\rm b}|}. \tag{4.23}$$

At large radii within the circumbinary disk (CBD), R corresponds to the distance from the center of mass of the binary, where the potential can be approximated by that of a single

point mass. Within the cavity region, however, and in the vicinity of either component, R is defined as the distance between a gas cell and its nearest sink particle. This ensures that each circumstellar disk (CSD) follows the same α-disk prescription with a consistent aspect ratio h as the CBD. Accordingly, we define a local viscosity ν_i around each sink particle, and the total viscosity ν is constructed as a weighted combination of these contributions,

$$\frac{1}{\nu^n} = \frac{1}{\nu_1^n} + \frac{1}{\nu_2^n}. \tag{4.24}$$

Choosing $n = 5$, and expressing the viscosity contributions from each sink particle as

$$\nu_1 = \alpha h c_\mathrm{s}(R_1) R_1, \quad \nu_2 = \alpha h c_\mathrm{s}(R_2) R_2, \tag{4.25}$$

where R_1 and R_2 denote the distances between the gas cell (where the viscosity is evaluated) and each sink particle, Eq. 4.24 simplifies to

$$\nu = \alpha h, c_\mathrm{s}(R_1) \frac{R_1 R_2}{(R_1^n + R_2^n)^{1/n}}. \tag{4.26}$$

For sufficiently large n (here, $n = 5$), this formulation smoothly transitions between the expected limits:

$$\nu \to \begin{cases} \alpha h c_\mathrm{s} R, & \text{for } R_1 \simeq R_2, \\ \alpha h c_\mathrm{s} R_1, & \text{for } R_1 \ll R_2 \ . \end{cases} \tag{4.27}$$

4.3.4 Torques acting on the MBH Binary

In the following, we outline our procedure for computing the binary's angular momentum change from simulation outputs during post-processing. Specifically, we describe how the direct torque on the binary can be decomposed into its relevant components. The orbital angular momentum of the binary is subject to torques due to accretion and gravitational interactions:

$$\begin{aligned} \frac{dL_\mathrm{b}}{dt} &= \left.\frac{dL_\mathrm{b}}{dt}\right|_\mathrm{acc} + \left.\frac{dL_\mathrm{b}}{dt}\right|_\mathrm{grav} \\ &= \dot{\mu}_\mathrm{b} l_\mathrm{b} + \mu_\mathrm{b} \left.\frac{dl_\mathrm{b}}{dt}\right|_\mathrm{acc} + \mu_\mathrm{b} \left.\frac{dl_\mathrm{b}}{dt}\right|_\mathrm{grav}, \end{aligned} \tag{4.28}$$

where

$$l_\mathrm{b} = a_\mathrm{b}^2 \Omega_\mathrm{b} \left(1 - e_\mathrm{b}^2\right)^{1/2} \tag{4.29}$$

is the binary's specific angular momentum and is defined by $L_\mathrm{b} = \mu_\mathrm{b} l_\mathrm{b}$ where $\mu_\mathrm{b} = M_1 M_2 / M_\mathrm{b} = q_\mathrm{b} M_\mathrm{b} / \left(1 + q_\mathrm{b}\right)^2$ is the reduced mass of the binary.

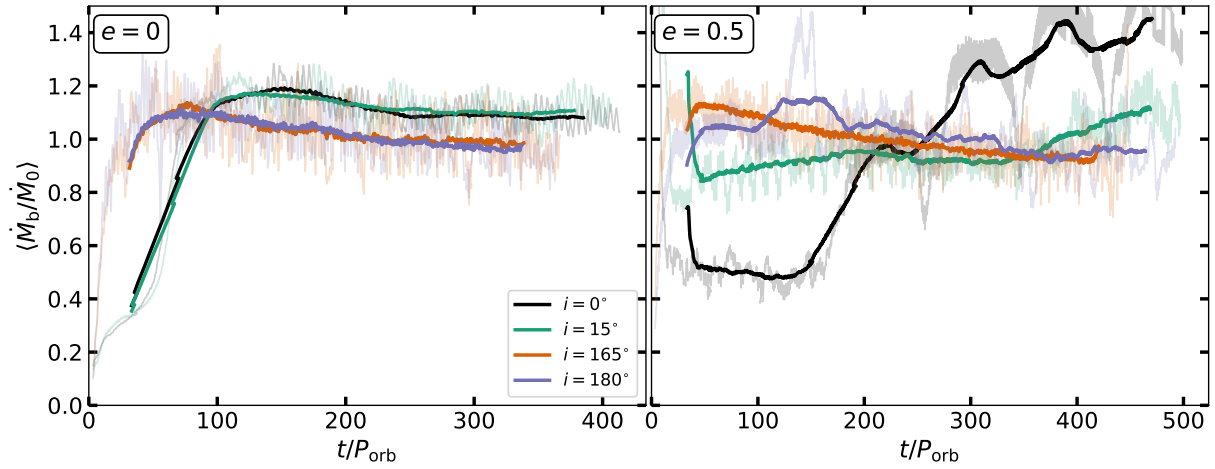

Figure 4.4: Time evolution of the normalized total accretion rate $\dot{M}_\mathrm{b}/\dot{M}_0$ for circular ($e_\mathrm{b} = 0$; left) and eccentric ($e_\mathrm{b} = 0.5$; right) binaries at various inclination angles ($i = 0°$, $15°$, $165°$, $180°$). Faint, low-opacity lines show the instantaneous accretion rates, while solid lines indicate the values smoothed over a 10-orbit window. Circular binaries tend to settle into a mildly decreasing, quasi-steady accretion regime, whereas eccentric binaries—particularly prograde ones—display a gradual increase in accretion rate over time, highlighting enhanced inflow and stronger variability in these configurations.

Mass Change

Even in the absence of explicit torques in Eq. (4.28), the binary's angular momentum can vary due to changes in the reduced mass, μ_b. These variations are directly related to changes in the mass ratio and the total mass (Muñoz et al., 2019),

$$\frac{\dot{\mu}_\mathrm{b}}{\mu_\mathrm{b}} = \frac{\dot{M}_\mathrm{b}}{M_\mathrm{b}} + \frac{1 - q_\mathrm{b}}{1 + q_\mathrm{b}} \frac{\dot{q}_\mathrm{b}}{q_\mathrm{b}}, \tag{4.30}$$

where

$$\dot{M}_\mathrm{b} = \dot{M}_1 + \dot{M}_2 \quad \text{and} \quad \dot{q}_\mathrm{b} = \frac{1 + q_\mathrm{b}}{M_\mathrm{b}} \left(\dot{M}_2 - q_\mathrm{b} \dot{M}_1 \right). \tag{4.31}$$

To study the time evolution of the total accretion rate onto the binary, we compute the sum of the individual mass accretion rates onto each sink particle, $\dot{M}_\mathrm{b}$, normalized by its long-term mean value, $\langle \dot{M}_\mathrm{b} \rangle$. Since accretion rates can fluctuate significantly on timescales comparable to the binary orbital period, we apply a temporal smoothing procedure to highlight secular trends. The accretion rate is convolved with a uniform moving-average kernel of width $\Delta t = N_\mathrm{w} \Delta t_\mathrm{samp}$, where N_w corresponds either to a fixed number of orbital periods or to a specified number of discrete time samples. In practice, this amounts to computing

$$\langle \dot{M}_{\rm b}(t_i) \rangle = \frac{1}{N_{\rm w}} \sum_{j=i-N_{\rm w}/2}^{i+N_{\rm w}/2} \dot{M}_{\rm b}(t_j), \tag{4.32}$$

which represents the accretion rate smoothed over a time window of $N_{\rm w}$ samples centered on t_i. The resulting smoothed curve suppresses short-term oscillations due to individual accretion events while preserving longer-term variability over many binary orbits.

Figure 4.4 presents the normalized accretion rate evolution $\dot{M}_{\rm b}/\dot{M}_0$ for circular ($e_{\rm b} = 0$) and eccentric ($e_{\rm b} = 0.5$) binaries with different inclination angles. The semi-transparent curves show the instantaneous values, while the solid lines display the smoothed profiles averaged over 10 orbits. Circular binaries tend to reach a mildly decreasing, quasi-steady accretion state, whereas eccentric systems—especially prograde configurations—exhibit an overall upward trend in accretion with time, suggesting sustained inflow enhancement.

Gravitational Torques

The specific gravitational torque acting on the binary has the general form:

$$\left.\frac{d\mathbf{l}_{\rm b}}{dt}\right|_{\rm grav} = \frac{M_1}{\mu_{\rm b}}\mathbf{r}_1 \times \mathbf{f}_{\rm grav,1} + \frac{M_2}{\mu_{\rm b}}\mathbf{r}_2 \times \mathbf{f}_{\rm grav,2} = \mathbf{r}_{\rm b} \times \left(\mathbf{f}_{\rm grav,1} - \mathbf{f}_{\rm grav,2}\right), \tag{4.33}$$

where $\mathbf{r}_{\rm b} = \mathbf{r}_1 - \mathbf{r}_2$ and $\mathbf{f}_{{\rm grav},i}$ is the force per unit mass acting on the i-th sink particle given by,

$$\mathbf{f}_{{\rm grav},i} = -G \sum_{\rm j} m_{\rm j} \frac{\mathbf{r}_{\rm i} - \mathbf{r}_{\rm j}}{\left|\mathbf{r}_{\rm i} - \mathbf{r}_{\rm j}\right|^3}, \tag{4.34}$$

Here, sink particle i is located at position $\mathbf{r}$i, measured from the simulation barycenter. The quantity mj denotes the mass of the j-th gas cell, and $\mathbf{r}_{\rm j}$ its position vector.

Accretion Torques

Accretion can exert an additional, specific torque on the binary (Roedig et al., 2011; Muñoz et al., 2019; Siwek et al., 2023b), distinct from the torque arising from changes in the binary mass itself. Analogous to Eq. (4.33), this torque can be expressed as

$$\left.\frac{d\mathbf{l}_{\rm b}}{dt}\right|_{\rm acc} = \mathbf{r}_{\rm b} \times \left(\mathbf{f}_{\rm acc,1} - \mathbf{f}_{\rm acc,2}\right) \tag{4.35}$$

Gas cells within the sink radius $r_{\rm s}$ are drained by a factor γ (defined in Eq. (4.14)) at each timestep (see Siwek et al. 2023a for further details on the numerical implementation). In addition to mass, the sinks also accrete linear momentum, giving rise to an asymmetric accretion force acting on each sink particle during every timestep (Roedig & Sesana, 2012; Muñoz et al., 2019).

The accretion force on sink i resulting from the accretion of mass and momentum from a given gas cell during a timestep δt is given by

$$\mathbf{f}_{\mathrm{acc,i}} = \left(\frac{\delta \mathbf{p}_\mathrm{i} - \delta m_\mathrm{i} \mathbf{v}_\mathrm{i}}{m_\mathrm{i} + \delta m_\mathrm{i}} \right) / \delta t \tag{4.36}$$

where δ**p**i and δm_i are the momentum and mass accreted by sink i during the current timestep, m_i is the sink mass prior to accretion, and $\mathbf{v}_\mathrm{i}$ is its velocity vector. Summing over all drained gas cells yields the total specific force due to accretion acting on each sink at a given timestep.

4.4 Preliminary Results

4.4.1 Orbital Evolution of Accreting Binaries

The specific angular momentum and specific energy of the binary are $\mathbf{l}_\mathrm{b} = \mathbf{r}_\mathrm{b} \times \dot{\mathbf{r}}_\mathrm{b}$ and $\mathcal{E}_\mathrm{b} = \frac{1}{2}\dot{\mathbf{r}}_\mathrm{b}^2 - \mathcal{G}M_\mathrm{b}/r_\mathrm{b}$ respectively. The equation of motion is then

$$\frac{d\dot{\mathbf{r}}_\mathrm{b}}{dt} = -\frac{GM_\mathrm{b}}{r_\mathrm{b}^3}\mathbf{r}_\mathrm{b} + \mathbf{f}_\mathrm{ext}\ , \tag{4.37}$$

where $\mathbf{f}_\mathrm{ext} \equiv \mathbf{f}_{\mathrm{ext},1} - \mathbf{f}_{\mathrm{ext},2}$ is an external force and $\mathbf{f}_{\mathrm{ext},i}$ is the force per unit mass acting on M_i. The external forces acting on the binary (as explained in the previous section) are

$$\mathbf{f}_\mathrm{ext} = \left(\mathbf{f}_{\mathrm{grav},1} - \mathbf{f}_{\mathrm{grav},2}\right) + \left(\mathbf{f}_{\mathrm{acc},1} - \mathbf{f}_{\mathrm{acc},2}\right), \tag{4.38}$$

where $\mathbf{f}_{\mathrm{grav},i}$ is given by Eq. (4.34) and $\mathbf{f}_{\mathrm{acc},i}$ by Eq. (4.36). The rates of change in $\mathbf{l}_\mathrm{b}$ and $\mathcal{E}_\mathrm{b}$ due to $\mathbf{f}_\mathrm{ext}$ and $\dot{M}_\mathrm{b}$ are (Muñoz et al., 2019; D'Orazio & Duffell, 2021)

$$\frac{d\mathbf{l}_\mathrm{b}}{dt} = \mathbf{r}_\mathrm{b} \times \mathbf{f}_\mathrm{ext} \tag{4.39}$$

and

$$\begin{aligned} \frac{d\mathcal{E}_\mathrm{b}}{dt} &= -\frac{\mathcal{G}\dot{M}_\mathrm{b}}{r_\mathrm{b}} + \frac{\mathcal{G}M_\mathrm{b}}{r_\mathrm{b}^3}\mathbf{r}_\mathrm{b} \cdot \dot{\mathbf{r}}_\mathrm{b} + \dot{\mathbf{r}}_\mathrm{b} \cdot \frac{d\dot{\mathbf{r}}_\mathrm{b}}{dt} \\ &= -\frac{\mathcal{G}\dot{M}_\mathrm{b}}{r_\mathrm{b}} + \dot{\mathbf{r}}_\mathrm{b} \cdot \mathbf{f}_\mathrm{ext}. \end{aligned} \tag{4.40}$$

From the orbital angular momentum $l_\mathrm{b}^2 = GM_\mathrm{b}a_\mathrm{b}\left(1 - e_\mathrm{b}^2\right)$, we get $e_\mathrm{b}^2 = 1 + 2l_\mathrm{b}^2\mathcal{E}_\mathrm{b}/\left(GM_\mathrm{b}\right)^2$. Substituting for specific binary energy, one gets the rates of change of eccentricity $\dot{e}_\mathrm{b}$ and semi-major axis $\dot{a}_\mathrm{b}$

$$\begin{aligned} -\frac{2e_\mathrm{b}\dot{e}_\mathrm{b}}{1 - e_\mathrm{b}^2} &= 2\frac{\dot{l}_\mathrm{b}}{l_\mathrm{b}} + \frac{\dot{\mathcal{E}}_\mathrm{b}}{\mathcal{E}_\mathrm{b}} - 2\frac{\dot{M}_\mathrm{b}}{M_\mathrm{b}} \\ \Rightarrow \dot{e}_\mathrm{b} &= \frac{1 - e_\mathrm{b}^2}{2e_\mathrm{b}}\left[2\frac{\dot{M}_\mathrm{b}}{M_\mathrm{b}} - \frac{\dot{\epsilon}_\mathrm{b}}{\epsilon_\mathrm{b}} - 2\frac{l_\mathrm{b}}{l_\mathrm{b}}\right] \end{aligned} \tag{4.41}$$

and

$$\frac{\dot{a}_\mathrm{b}}{a_\mathrm{b}} = -\frac{\dot{\mathcal{E}}_\mathrm{b}}{\mathcal{E}_\mathrm{b}} + \frac{\dot{M}_\mathrm{b}}{M_\mathrm{b}}. \tag{4.42}$$

In our simulations, we evaluate in real time the specific angular momentum $\delta\mathbf{l}$b and specific energy $\delta\mathcal{E}$b imparted to the sink (MBH) particles at each timestep,

$$\begin{aligned} \delta\mathbf{l}_\mathrm{b} &= (\mathbf{r}_\mathrm{b} \times \mathbf{f}_\mathrm{ext})\,\delta t, \\ \delta\mathcal{E}_\mathrm{b} &= (\mathbf{v}_\mathrm{b} \cdot \mathbf{f}_\mathrm{ext})\,\delta t, \end{aligned} \tag{4.43}$$

and determine their instantaneous rates of change by taking finite differences of Eqs. (4.43).

We now examine the early (100–350, P_b) orbital evolution of the gas-embedded MBH binaries, derived from the instantaneous changes in specific energy and angular momentum described above. Figures 4.5 and 4.6 show the temporal evolution of the semi-major-axis and eccentricity rates for binaries with varying inclination and initial eccentricity.

For the initially circular binaries ($e_\mathrm{b} = 0$; left panels), we find that only the coplanar prograde system `e0inc0` tends to expand on average, while all other configurations display net orbital shrinking. This contrasts with the typically expanding orbits found in 2D coplanar simulations (e.g., Muñoz et al., 2019), highlighting the importance of three-dimensional effects in determining the torque balance. This behaviour is particularly evident for the moderately inclined case `e0inc15`, suggesting that vertical disk structure and misaligned inflows may enhance angular-momentum loss. Both retrograde configurations `e0inc180` and `e0inc165` also show gradual contraction, consistent with the expectation that retrograde disks remove angular momentum from the binary more efficiently (Nixon et al., 2011; Roedig & Sesana, 2014).

The eccentric binaries ($e_\mathrm{b} = 0.5$; right panels) show a wider range of outcomes. Prograde systems generally exhibit expansion on average, while retrograde ones either maintain approximately constant separation or contract slightly. The prograde inclined `e05inc15` case in particular shows a sustained positive $\dot{a}_\mathrm{b}$, hinting that misaligned eccentric binaries may efficiently extract angular momentum from the surrounding gas. Conversely, the retrograde binaries remain dynamically stable or shrinking, consistent with the expectation that their gas interaction channels energy removal rather than transfer

As shown in Fig. 4.6, all circular binaries exhibit short-term fluctuations in eccentricity, even though the time-averaged $\langle\dot{e}_\mathrm{b}\rangle$ should nominally vanish. This variability likely reflects transient, non-axisymmetric inflows and the limited temporal span of our runs. Among the initially eccentric binaries, most configurations tend to grow more eccentric with time, particularly in the coplanar prograde `e05inc0` case. The sole exception is the coplanar retrograde `e05inc180` binary, which instead shows mild circularization, in line with expectations that retrograde accretion does not increase eccentricity (Tiede & D'Orazio, 2024; Bourne et al., 2024). These results, though preliminary, point to a strong dependence of the early orbital evolution on disk orientation and binary eccentricity. However, given that the simulations currently cover only a few hundred binary orbits, these findings should be regarded as indicative rather than conclusive. Extending the simulations to longer timescales

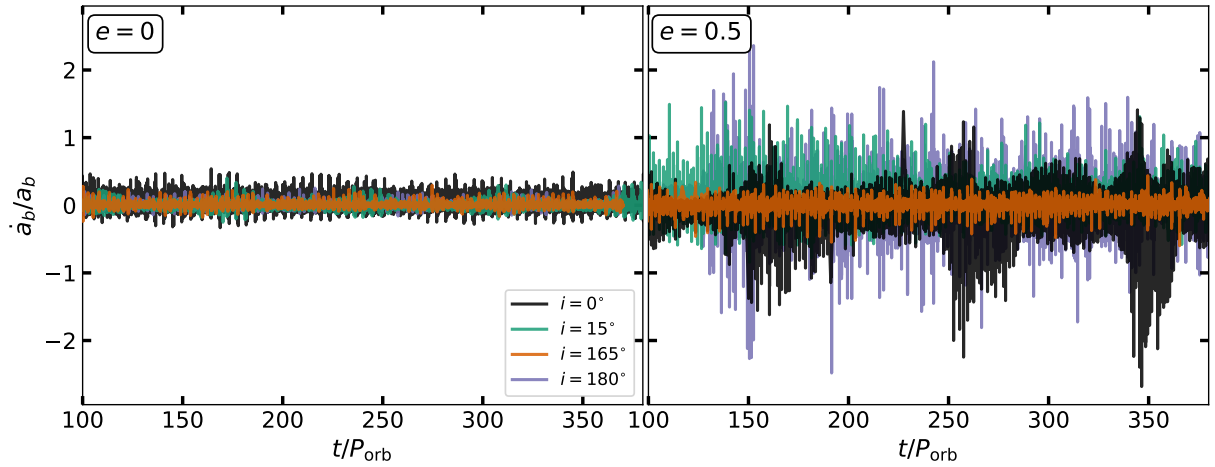

Figure 4.5: Time evolution of the binary semi-major-axis rate $\dot{a}$b for different inclinations and eccentricities over 100–350, Pb. The left panel shows circular binaries ($e_{\rm b} = 0$) and the right panel eccentric binaries ($e_{\rm b} = 0.5$). Apart from the `e0inc0` case, all circular binaries experience orbital shrinking, while eccentric prograde systems generally expand on average. Retrograde configurations tend to contract, consistent with results from previous 2D studies ().

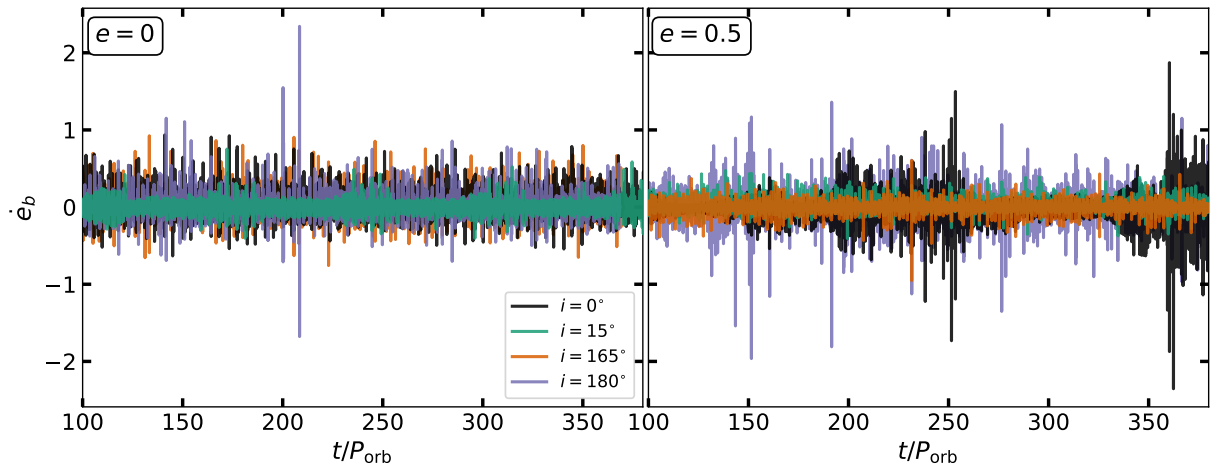

Figure 4.6: Time evolution of the binary eccentricity rate $\dot{e}$b for the same set of runs as in Figure 4.5. The left panel corresponds to initially circular binaries and the right to initially eccentric ones. Circular systems exhibit transient eccentricity variability despite an expected $\langle \dot{e}_{\rm b} \rangle \simeq 0$, while most eccentric binaries show a net increase in eccentricity over time. The coplanar retrograde case instead shows mild circularization, consistent with retrograde gas accretion. These preliminary results underscore the need for longer integrations to capture secular trends over viscous timescales.

will be necessary to assess whether these early-time trends persist in a quasi-steady regime.

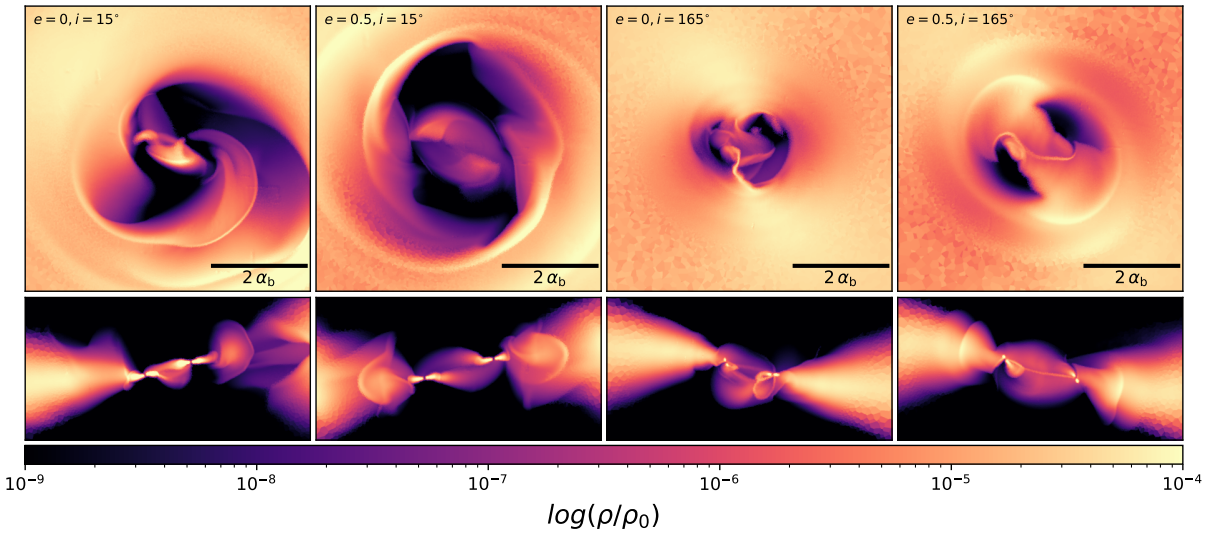

Figure 4.7: Misaligned binary–disk configurations after $t = 250$ binary orbits. The inclination angle is fixed at $i = 15°$, i.e., for retrograde binaries corresponds to $i = 165°$. Top panels show face-on projections, while bottom panels show edge-on density projections. From left to right: circular prograde, eccentric ($e_b = 0.5$) prograde, circular retrograde, and eccentric retrograde binary orbits.

4.4.2 Binary - Disk Misalignment

In our simulations of misaligned circumbinary disks (see Fig. 4.7), we compute the inclination angle δ across the disk to quantify the degree of alignment between the disk and the binary orbital plane. Following Fragner & Nelson (2010); Moody et al. (2019), the inclination is defined as

$$\cos\delta = \frac{\mathbf{L_b} \cdot \mathbf{L_{disk}}}{|\mathbf{L_b}|\,|\mathbf{L_{disk}}|}, \tag{4.44}$$

where $\mathbf{L_b}$ is the binary angular momentum vector and $\mathbf{L_{disk}}$ is the angular momentum vector of the disk, calculated within spherical shells at different radii (in units of a_b). This measure allows us to track how the disk responds to the binary's torque and estimate the realignment timescale—i.e., the time required for the circumbinary disk to adjust its orientation toward the binary orbital plane.

Figure 4.8 shows the radial profiles of δ (Eq. (4.44)) at different times in our simulations. We find that retrograde configurations ($i = 165°$) counter-align with the binary plane faster than prograde systems ($i = 15°$), achieving near-complete counter-alignment within roughly 350 binary orbits. In contrast, prograde disks realign more gradually. The circular prograde `e0inc15` case exhibits increased variability in the central regions, likely due to transient warping (Fragner & Nelson, 2010; Rabago et al., 2024) and differential precession (Nixon et al., 2013), whereas the eccentric prograde binary initially drives evolves toward disk breaking, followed by a slow trend toward alignment.

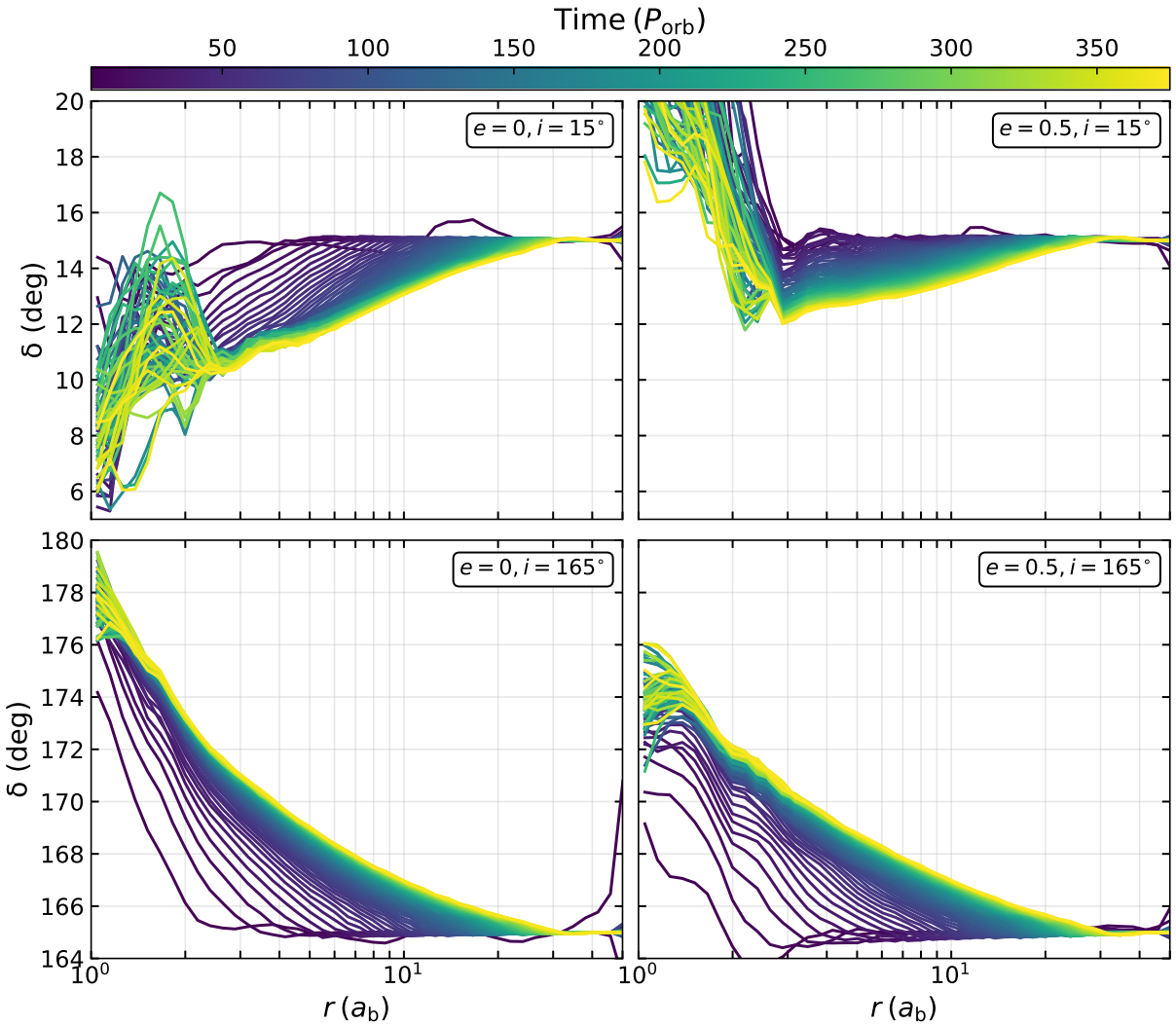

Figure 4.8: Radial profiles of the inclination angle δ between the binary orbital plane and the circumbinary disk at different times. Retrograde systems ($i = 165°$) achieve counter-alignment faster than prograde systems ($i = 15°$), while the circular prograde disk shows enhanced variability in the inner regions and the eccentric prograde disk initially develops a warp before slowly realigning.

These results highlight the strong dependence of disk realignment on the initial binary–disk inclination and the binary eccentricity. In particular, retrograde binaries efficiently drive the disk toward a long-lived counter-aligned configuration, consistent with the findings of Garg et al. (2024), who show that retrograde accretion channels generically lead to eccentricity growth and negative effective spins measurable by LISA. This combination arises from eccentricity pumping under retrograde accretion and the formation of stable retrograde circumbinary and mini-disks, providing a distinctive observational signature of gas-driven MBH binary mergers. By contrast, prograde systems—especially those with

significant eccentricity—tend to induce transient warps or partial misalignments in the inner disk before gradually relaxing toward alignment, in line with their predicted positive effective spins and largely non-measurable eccentricities. Extending our simulations to longer timescales will be essential to determine whether these early-time behaviors persist and to establish the final quasi-steady alignment state of the disk–binary system.

4.5 Summary and Discussion

In this work, we have explored the dynamics of massive black hole binaries embedded in circumbinary disks, focusing on the interplay between gas accretion, gravitational torques, and orbital evolution. Using 3D hydrodynamic simulations with the moving-mesh code `AREPO`, we resolved both the circumbinary disk and the inner cavity containing mini-disks, capturing the complex multiscale flows that regulate angular momentum exchange. This work serves as a first step towards long-term simulations needed to fully assess the evolution of the binary and the disk on viscous timescales.

We explored the effects of eccentricity $e_{\rm b}$ and inclination on accretion rates on overall MBH binary evolution. Circular binaries generally approach a quasi-steady accretion state, while eccentric binaries—particularly prograde systems—exhibit enhanced accretion and stronger variability. Inclined and retrograde configurations show markedly different dynamics, including the potential for orbital expansion or accelerated coalescence depending on the disk's angular momentum relative to the binary. These findings reinforce the importance of disk geometry, binary orbital parameters, and cavity flows in shaping long-term evolution, and they underscore the necessity of fully three-dimensional treatments to capture warping, precession, and disk breaking phenomena.

We also find that disk realignment strongly depends on the initial binary–disk inclination and the binary's eccentricity. Retrograde disks ($i = 165°$) counter-align with the binary plane rapidly, reaching near-complete alignment within $t \sim 350\ P_{\rm b}$ orbits, while prograde disks ($i = 15°$) realign more gradually. Circular prograde disks show variability in the inner regions due to transient warping and differential precession, whereas eccentric prograde binaries can induce temporary disk breaking before slowly approaching alignment. These trends suggest that long-term simulations are needed to determine the final quasi-steady configuration and the persistence of early misalignment features.

Apart from hydrodynamics alone, additional physics will be crucial for such studies. Magnetic fields, through the magnetorotational instability (Most & Wang, 2024) and magnetically driven winds, can modulate accretion and torque distributions, while radiation shapes the disk's thermal structure (Tiwari et al., 2025), thickness, and filamentary morphology. The final stages of inspiral, in particular, require general-relativistic magnetohydrodynamic (GRMHD) modelling via the use of a binary black hole metric (Lupi, 2023; Combi & Ressler, 2024; Fedrigo & Lupi, 2025) to capture strong-field effects, jet launching (Ressler et al., 2025), and electromagnetic signatures coincident with merger. Incorporating self-gravity, star formation, and feedback in massive disks remains an important frontier, as these processes can either stall or accelerate the binary's evolution in realistic

galactic environments (Ennoggi et al., 2025).

Looking forward, we plan to extend our 3D simulations to include misaligned disks with MHD and GR effects over long-term, high-resolution runs. This approach will enable robust predictions for both gravitational-wave signals and electromagnetic counterparts, linking theoretical models directly to observations from PTAs and space-based interferometers like LISA. Such studies will be essential for understanding the co-evolution of SMBH binaries and their host galaxies towards coalescence in the era of multimessenger astrophysics.

Chapter 5

Summary and Outlook

Massive black hole binaries (MBHBs) play a pivotal role in our understanding of galaxy evolution, gravitational-wave astrophysics, and the multi-scale coupling between stellar, gaseous, and relativistic processes in the Universe. Despite decades of theoretical and numerical efforts, many aspects of their formation, evolution, and eventual coalescence remain uncertain, largely due to the complexity of the physical environments in which they arise. This thesis has sought to address these challenges by combining direct N-body and hydrodynamical simulations to explore MBHBs across three distinct regimes: dynamical formation through cluster mergers, gravitational-wave–driven inspirals in galactic nuclei, and gas-assisted evolution within circumbinary accretion discs. Each of these studies highlights how the interplay between dynamics, relativity, and gas physics determines the evolutionary pathways and observable signatures of MBHBs.

5.1 Summary of Results

In Chapter 2, I study via means of direct N-body simulations, the process of merging star clusters. Each progenitor cluster has a stellar mass of $2.7\times10^4\mathrm{M}_\odot$ and hosts a $500\mathrm{M}_\odot$ MBH, which form a hard binary during the merger and efficiently interact with surrounding stars and stellar black holes (BHs). I find that these interactions drive strong dynamical ejections, producing hundreds of runaway stars with velocities exceeding $50\,\mathrm{km\,s^{-1}}$—including a small subset reaching above $300\,\mathrm{km\,s^{-1}}$—and ejecting a significant fraction of the stellar BH population within 100 Myr. By running additional simulations of isolated clusters or mergers without MBHs, I demonstrate that such high-velocity escapers are a distinctive outcome of MBH binary dynamics, while systems with only a single MBH generate fewer and slower ejections. The cluster remnants exhibit mild rotation for low-eccentricity mergers, though kinematic signatures of MBHs remain subtle. I find that the resulting MBH binaries are expected to merge within a Hubble time, making them potential gravitational-wave sources detectable by future observatories such as LISA and the Einstein Telescope. These results indicate that mergers of star clusters hosting low-mass MBHs provide a viable channel for producing runaway and high-velocity stars, free-floating compact objects,

and gravitational-wave–emitting massive black hole binaries.

In Chapter 3, I investigate the dynamical evolution of intermediate-mass black holes (IMBHs) orbiting around supermassive black holes (SMBHs) via direct direct post-newtonian N-body simulations. Motivated by the hierarchical assembly of massive galaxies, I model systems containing ten $10^5 M_\odot$ IMBHs distributed with varying degrees of concentration around a central $10^9 M_\odot$ SMBH, and I explore their evolution both in isolation and in the presence of a secondary SMBH. My results show that perturbations induced by a binary SMBH configuration significantly enhance the number of direct plunges (DPs) of IMBHs into the primary SMBH—by more than a factor of two—making this the dominant merger channel compared to gravitational-wave–driven intermediate-mass-ratio inspirals (heavy IMRIs). While these events contribute to SMBH growth, their rapid evolution and low signal-to-noise ratios imply that they are unlikely to be individually detected by LISA or pulsar timing arrays. However, for galaxies hosting lower-mass SMBHs ($M_\bullet \lesssim 10^8 M_\odot$), I find that heavy IMRIs will enter the LISA frequency band with detectable amplitudes, offering a promising avenue for probing the population of IMBHs and testing models of hierarchical black hole formation.

In Chapter 4, I explore the dynamics of massive black hole binaries embedded in circumbinary accretion disks using high-resolution three-dimensional hydrodynamical simulations performed with the AREPO code. This ongoing work focuses on understanding how gas accretion, gravitational torques, and disk orientation collectively influence the binary's orbital evolution. By resolving both the large-scale circumbinary disk and the small-scale mini-disks around each black hole, I capture the complex multiscale flows that regulate angular momentum exchange between the binary and the surrounding gas. Preliminary results show that circular binaries tend toward quasi-steady accretion, while eccentric and inclined systems exhibit stronger variability, potentially leading to either orbital expansion or accelerated coalescence. Moreover, I find that the rate and direction of disk realignment depend sensitively on the initial inclination and eccentricity: retrograde disks counter-align rapidly, while prograde configurations realign more gradually, often undergoing warping or temporary disk breaking. These findings highlight the critical role of three-dimensional gas dynamics in shaping binary–disk coevolution and motivate future long-term simulations that follow the system over viscous timescales to determine its final steady-state structure and implications for gravitational-wave source populations.

Overall, the results presented in this thesis underscore the fundamental role of massive black hole binaries (MBHBs) in shaping the dynamical, stellar, and gaseous environments across a wide range of astrophysical scales—from dense star clusters to galactic nuclei and circumbinary accretion disks. Through a combination of direct N-body and hydrodynamical simulations, I demonstrate that MBHBs act as powerful engines of energy and angular momentum redistribution, driving observable phenomena such as runaway stars, stellar-mass black hole ejections, GW-driven inspirals and direct plunges, and strong disk warping or realignment. These signatures not only trace the presence of otherwise undetectable MBHs but also provide valuable diagnostics for identifying the physical processes governing their evolution. The diverse environments explored in this work reveal a coherent picture in which MBHBs serve as both catalysts of dynamical transformation and

key progenitors of gravitational-wave sources, bridging the gap between small-scale stellar dynamics and the large-scale growth of supermassive black holes. This highlights their crucial importance as multi-messenger probes of galaxy formation, accretion physics, and relativistic dynamics in the era of current and next-generation observatories such as Pulsar Timing Arrays (PTAs), the Laser Inteferometer Space Antenna (LISA) and Einstein Telescope (ET) .

5.2 Future Prospects

The findings presented in this thesis open several avenues for follow-up investigations, each building upon the individual projects and their respective results. In the following, I outline several promising directions for future research, highlighting how each study can be extended, explore longer evolutionary timescales, and establish stronger connections with upcoming gravitational-wave and electromagnetic observations.

A natural extension of the project presented in Chapter 2 would be to incorporate the gravitational potential of the host galaxy in which the star clusters merge. In this scenario, the fate of the remnant cluster would be governed by the interplay between the internal merger dynamics and the external tidal forces exerted by the galaxy, potentially leading to an accelerated dissolution of the system. The resulting ejected stars and compact objects are expected to populate stellar streams, offering additional clues about their origin and the underlying dynamical mechanisms at work (see e.g., Roberts et al., 2025). The morphology of these streams could further reveal key information about the parent cluster's composition, including the presence of a central population of stellar-mass or intermediate-mass black holes (IMBHs). Moreover, introducing a realistic fraction ($f \sim 50\%$) of primordial binaries into the initial conditions would bring the simulations closer to observed stellar systems and naturally lead to the formation of gravitational-wave sources—either merging within the cluster or as ejected binaries that later coalesce in the galactic field, potentially detectable by current and future observatories such as LIGO, Virgo, and KAGRA.

As discussed in Chapter 3, the extension of this project is particularly well suited for studies of galactic nuclei, where the interplay between stellar dynamics, relativistic effects, and environmental influences governs the formation and evolution of extreme- and intermediate-mass-ratio inspirals (EMRIs and IMRIs) detectable by LISA. A natural next step will be to expand the current framework to more realistic galactic environments, such as nuclear star clusters (NSCs) and active galactic nucleus (AGN) disks. In the case of NSCs, incorporating a background gravitational potential (e.g., Dehnen, 1993; Tremaine et al., 1994) will account for the influence of the surrounding stellar population, which shapes relaxation timescales and modifies the overall dynamical evolution. Alternatively, modeling EMRI and IMRI formation within AGN disks by introducing a gas-drag force (Ostriker, 1999; Trani & Di Cintio, 2025) into the N-body code will enable the exploration of gas-assisted inspirals and mergers. In both scenarios, general relativistic effects remain essential, and as highlighted in Chapter 3, a significant advancement will be the inclusion of a geodesic solver—currently under development—to accurately capture the final inspiral

and plunge phases while coupling the binary evolution to environmental processes such as stellar hardening, fly-bys, and AGN-disk-related phenomena such as migration traps. Furthermore, future simulations will incorporate a realistic mass spectrum for the smaller black holes instead of a fixed particle mass, allowing for a more detailed investigation of capture probabilities, eccentricity and merger rate distributions, ultimately providing deeper insight into the dynamical channels that lead to EMRI and IMRI formation in galactic nuclei.

The first goal of the ongoing project presented in Chapter 4 would be to continue an complete the long-term simulations of inclined MBH binaries in circumbinary disks, extending the current runs to larger timescales, allows us to capture the full co-evolution of the binary and its surrounding gas. These extended simulations will allow us to determine whether early misalignment features persist, how warping and disk breaking evolve over time, and what steady-state configurations ultimately emerge. Building upon the current purely hydrodynamical framework, I plan to incorporate magnetic fields to study their role in driving angular momentum transport through the magnetorotational instability and magnetically launched winds, which can substantially modify accretion flows and binary evolution (e.g., Most & Wang, 2024; Wang et al., 2025). Finally, as highlighted in (Lupi, 2023; Fedrigo & Lupi, 2025), adopting a general-relativistic magnetohydrodynamic (GRMHD) framework—whose implementation naturally extends to moving-mesh codes like `AREPO`—will be essential to accurately model the final inspiral stages, capturing strong-field effects, jet formation, and potential electromagnetic counterparts coincident with merger. These developments will bridge the gap between large-scale circumbinary disk dynamics and the relativistic regime, providing a unified picture of SMBH binary evolution that connects theoretical predictions with multi-messenger observations from LISA and pulsar timing arrays.

Appendix A

Dynamically Formed Binaries in Star Clusters

The increased densities during the core collapse phase of star clusters elevates the rate of dynamical encounters, leading to the formation of binaries through three-body interactions. The encounter rate $\bar{C}$ of three initially unbound bodies leading to binary formation in a system of equal mass objects m_* is (Goodman & Hut, 1993; Binney & Tremaine, 2008)

$$\bar{C} \approx \frac{G^5 m_\star^5 n^3}{\sigma^9}, \tag{A.1}$$

where n is the number density and σ the velocity dispersion of the system. Since the above rate refers to equal-mass bodies only, it is however still uncertain how well it predicts the binary formation rates in multi-component environments such as star and globular clusters and/or galactic nuclei. Atallah et al. (2024) found that in such encounters, it is highly unlikely that the two most massive bodies become bound, in contrast to what has mostly been suggested in the literature so far. The large number of single bodies in the system leads to frequent fly-by and exchange interactions with the formed binaries, where one of the member is replaced by a field star. The higher the mass of the incoming body, the higher the probability of it replacing a binary member (Valtonen & Karttunen, 2006). This inevitably results to massive stars becoming members of binaries.

For a system containing stellar-mass BHs the above mechanisms allow the efficient formation of binary BHs (Portegies Zwart & McMillan, 2000; Park et al., 2017; Kremer et al., 2019; Torniamenti et al., 2022; Kritos et al., 2024; Rantala et al., 2024a), potentially leading to their GW-driven coalescence, covering a broad mass-ratio spectrum, detectable with current (Abbott et al., 2016, 2019) and future (Amaro-Seoane et al., 2017) gravitational wave detectors. Additionally, BH-star binaries can be formed through exchange in 3- or 4-body encounters (e.g. Ryu et al., 2023b) in star massive star clusters (e.g. Rastello et al., 2023; Marín Pina et al., 2024; Fantoccoli et al., 2024) potentially explaining the three dormant BHs detected by Gaia (Gaia Collaboration, 2016): Gaia BH1 (El-Badry et al., 2022), BH2 (El-Badry et al., 2023) and BH3 (Gaia Collaboration, 2024).

Bibliography

Aarseth S. J., Heggie D. C., 1976, A&A, 53, 259

Aarseth S. J., Hills J. G., 1972, A&A, 21, 255

Aarseth S. J., Tout C. A., Mardling R. A., 2008, The Cambridge N-Body Lectures. Vol. 760, doi:10.1007/978-1-4020-8431-7,

Abbate F., Possenti A., Ridolfi A., Freire P. C. C., Camilo F., Manchester R. N., D'Amico N., 2018, MNRAS, 481, 627

Abbott B., et al., 2016, Physical Review Letters, 116

Abbott B. P., et al., 2019, The Astrophysical Journal Letters, 882, L24

Abbott R., et al., 2021, Physical Review X, 11

Abbott R., et al., 2023, Physical Review X, 13, 041039

Agarwal M., Milosavljević M., 2011, The Astrophysical Journal, 729, 35

Agazie G., et al., 2023, ApJ, 951, L8

Aharon D., Perets H. B., 2015, The Astrophysical Journal, 799, 185

Aly H., Dehnen W., Nixon C., King A., 2015, MNRAS, 449, 65

Amaro-Seoane P., 2018, Living Reviews in Relativity, 21

Amaro-Seoane P., Freitag M., 2006, The Astrophysical Journal, 653, L53–L56

Amaro-Seoane P., Miller M. C., Freitag M., 2009, The Astrophysical Journal, 692, L50–L53

Amaro-Seoane P., Sesana A., Hoffman L., Benacquista M., Eichhorn C., Makino J., Spurzem R., 2010, Monthly Notices of the Royal Astronomical Society, 402, 2308–2320

Amaro-Seoane P., Sopuerta C. F., Freitag M. D., 2013, MNRAS, 429, 3155

Amaro-Seoane P., et al., 2017, Laser Interferometer Space Antenna (arXiv:1702.00786), https://arxiv.org/abs/1702.00786

Amaro-Seoane P., et al., 2023, Living Reviews in Relativity, 26, 2

Anagnostou O., Trenti M., Melatos A., 2020, Publications of the Astronomical Society of Australia, 37

Anderson J., van der Marel R. P., 2010, The Astrophysical Journal, 710, 1032–1062

Angelo M. S., Santos J. F. C., Maia F. F. S., Corradi W. J. B., 2022, MNRAS, 510, 5695

Antoni A., MacLeod M., Ramirez-Ruiz E., 2019, The Astrophysical Journal, 884, 22

Antoniadis J., et al., 2022, MNRAS, 510, 4873

Antonini F., Merritt D., 2011, The Astrophysical Journal, 745, 83

Antonini F., Barausse E., Silk J., 2015, The Astrophysical Journal, 812, 72

Antonini F., Toonen S., Hamers A. S., 2017, ApJ, 841, 77

Antonov V. A., 1960, Azh, 37, 918

Antonov V. A., 1961, Soviet Ast., 4, 859

Antonov V. A., 1962, Solution of the problem of stability of stellar system Emden's density law and the spherical distribution of velocities. Cambridge University Press

Apostolatos T. A., Cutler C., Sussman G. J., Thorne K. S., 1994, Phys. Rev. D, 49, 6274

Arca-Sedda M., Mastrobuono-Battisti A., 2019, Mergers of globular clusters in the Galactic disc: intermediate mass black hole coalescence and implications for gravitational waves detection (arXiv:1906.05864), https://arxiv.org/abs/1906.05864

Arca-Sedda M., Gualandris A., Do T., Feldmeier-Krause A., Neumayer N., Erkal D., 2020, The Astrophysical Journal, 901, L29

Arca-Sedda M., Rizzuto F. P., Naab T., Ostriker J., Giersz M., Spurzem R., 2021, The Astrophysical Journal, 920, 128

Arca-Sedda M., et al., 2023b

Arca-Sedda M., Kamlah A. W. H., Spurzem R., Rizzuto F. P., Giersz M., Naab T., Berczik P., 2023a

Arca Sedda M., Kamlah A. W. H., Spurzem R., Rizzuto F. P., Naab T., Giersz M., Berczik P., 2023c, MNRAS, 526, 429

Arca-sedda M., Kamlah A. W. H., Spurzem R., Rizzuto F. P., Giersz M., Naab T., Berczik P., 2024, MNRAS, 528, 5140

Armitage P. J., Natarajan P., 2002, ApJ, 567, L9

Aros F. I., Sippel A. C., Mastrobuono-Battisti A., Askar A., Bianchini P., van de Ven G., 2020, Monthly Notices of the Royal Astronomical Society, 499, 4646–4665

Artymowicz P., 1992, PASP, 104, 769

Artymowicz P., Lubow S. H., 1994, ApJ, 421, 651

Artymowicz P., Lubow S. H., 1996, ApJ, 467, L77

Artymowicz P., Clarke C. J., Lubow S. H., Pringle J. E., 1991, ApJ, 370, L35

Askar A., Davies M. B., Church R. P., 2021, Monthly Notices of the Royal Astronomical Society, 502, 2682–2700

Askar A., Baldassare V. F., Mezcua M., 2024, Intermediate-Mass Black Holes in Star Clusters and Dwarf Galaxies (arXiv:2311.12118), https://arxiv.org/abs/2311.12118

Atallah D., Trani A. A., Kremer K., Weatherford N. C., Fragione G., Spera M., Rasio F. A., 2023, Monthly Notices of the Royal Astronomical Society, 523, 4227–4250

Atallah D., Weatherford N. C., Trani A. A., Rasio F., 2024

Babak S., Sesana A., 2012, Phys. Rev. D, 85, 044034

Babak S., et al., 2017, Physical Review D, 95

Bailin J., Steinmetz M., 2005, The Astrophysical Journal, 627, 647–665

Baker J. G., Centrella J., Choi D.-I., Koppitz M., van Meter J., 2006, Physical Review Letters, 96

Banerjee S., Belczynski K., Fryer C. L., Berczik P., Hurley J. R., Spurzem R., Wang L., 2020, Astronomy & Astrophysics, 639, A41

Bansal K., Taylor G. B., Peck A. B., Zavala R. T., Romani R. W., 2017, ApJ, 843, 14

Bar-Or B., Alexander T., 2016, ApJ, 820, 129

Barack L., Cutler C., 2004, Physical Review D, 69

Barausse E., Dvorkin I., Tremmel M., Volonteri M., Bonetti M., 2020, The Astrophysical Journal, 904, 16

Barausse E., Dey K., Crisostomi M., Panayada A., Marsat S., Basak S., 2023, Phys. Rev. D, 108, 103034

Bardeen J. M., Petterson J. A., 1975, ApJ, 195, L65

Barnes J. E., Hernquist L. E., 1991, ApJ, 370, L65

Barnes J. E., Hernquist L., 1992, ARA&A, 30, 705

Barrows R. S., Comerford J. M., Greene J. E., Pooley D., 2017, ApJ, 838, 129

Bastian N., Gieles M., Efremov Y. N., Lamers H. J. G. L. M., 2005, Astronomy & Astrophysics, 443, 79–90

Baumgardt H., 2016, Monthly Notices of the Royal Astronomical Society, 464, 2174–2202

Baumgardt H., Makino J., 2003, Monthly Notices of the Royal Astronomical Society, 340, 227–246

Baumgardt H., Gualandris A., Portegies Zwart S., 2006, Monthly Notices of the Royal Astronomical Society, 372, 174–182

Bañados E., et al., 2014, The Astronomical Journal, 148, 14

Bañados E., et al., 2017, Nature, 553, 473–476

Beckmann R. S., et al., 2025, MNRAS, 536, 1838

Begelman M. C., Blandford R. D., Rees M. J., 1980, Nature, 287, 307

Behroozi P., Wechsler R. H., Hearin A. P., Conroy C., 2019, MNRAS, 488, 3143

Bekenstein J. D., 1973, ApJ, 183, 657

Bellazzini M., Bragaglia A., Carretta E., Gratton R. G., Lucatello S., Catanzaro G., Leone F., 2012, Astronomy & Astrophysics, 538, A18

Bellini A., et al., 2018, The Astrophysical Journal, 853, 86

Bellovary J., Luo Y., Quinn T. R., Munshi F., Tremmel M., Wadsley J., 2025, ApJ, 986, 208

Berczik P., Merritt D., Spurzem R., 2005, The Astrophysical Journal, 633, 680–687

Berti E., 2006, Classical and Quantum Gravity, 23, S785

Berti E., Kesden M., Sperhake U., 2012, Physical Review D, 85

Bhatia R. K., Read M. A., Hatzidimitriou D., Tritton S., 1991, A&AS, 87, 335

Binney J., Tremaine S., 2008, Galactic Dynamics: Second Edition. Princeton University Press, Princeton, NJ USA

Blaauw A., 1961a, Bull. Astron. Inst. Netherlands, 15, 265

Blaauw A., 1961b, Bull. Astron. Inst. Netherlands, 15, 265

Blaauw A., 1993, in Cassinelli J. P., Churchwell E. B., eds, Astronomical Society of the Pacific Conference Series Vol. 35, Massive Stars: Their Lives in the Interstellar Medium. p. 207

Blaes O., Lee M. H., Socrates A., 2002, The Astrophysical Journal, 578, 775–786

Blanchet L., Qusailah M. S. S., Will C. M., 2005, The Astrophysical Journal, 635, 508–515

Blanchet L., Buonanno A., Faye G., 2006, Phys. Rev. D, 74, 104034

Blecha L., Loeb A., 2008, Monthly Notices of the Royal Astronomical Society

Blecha L., Cox T. J., Loeb A., Hernquist L., 2011, MNRAS, 412, 2154

Blecha L., Snyder G. F., Satyapal S., Ellison S. L., 2018, MNRAS, 478, 3056

Bluck A. F. L., Conselice C. J., Bouwens R. J., Daddi E., Dickinson M., Papovich C., Yan H., 2009, MNRAS, 394, L51

Bluck A. F. L., Conselice C. J., Buitrago F., Grützbauch R., Hoyos C., Mortlock A., Bauer A. E., 2012, ApJ, 747, 34

Blumenthal G. R., Faber S. M., Primack J. R., Rees M. J., 1984, Nature, 311, 517

Bogdanović T., Reynolds C. S., Miller M. C., 2007, The Astrophysical Journal, 661, L147–L150

Bollati F., Lupi A., Dotti M., Haardt F., 2024, A&A, 690, A194

Bondi H., 1952, MNRAS, 112, 195

Bondi H., Hoyle F., 1944, MNRAS, 104, 273

Bonetti M., Haardt F., Sesana A., Barausse E., 2016, MNRAS, 461, 4419

Bonetti M., Perego A., Capelo P. R., Dotti M., Miller M. C., 2018, Publications of the Astronomical Society of Australia, 35

Bonetti M., Sesana A., Haardt F., Barausse E., Colpi M., 2019, Monthly Notices of the Royal Astronomical Society, 486, 4044–4060

Bonetti M., et al., 2020, Monthly Notices of the Royal Astronomical Society: Letters, 493, L114–L119

Bonnor W. B., Rotenberg M. A., 1961, Proceedings of the Royal Society of London Series A, 265, 109

Boroson T. A., Lauer T. R., 2009, Nature, 458, 53

Bortolas E., Mapelli M., Spera M., 2017, Monthly Notices of the Royal Astronomical Society, 474, 1054–1064

Bortolas E., Gualandris A., Dotti M., Read J. I., 2018, MNRAS, 477, 2310

Bortolas E., Franchini A., Bonetti M., Sesana A., 2021, The Astrophysical Journal Letters, 918, L15

Boubert D., Erkal D., Evans N. W., Izzard R. G., 2017, Monthly Notices of the Royal Astronomical Society, 469, 2151–2162

Bourne M. A., Fiacconi D., Sijacki D., Piotrowska J. M., Koudmani S., 2024, MNRAS, 534, 3448

Bowen D. B., Campanelli M., Krolik J. H., Mewes V., Noble S. C., 2017, ApJ, 838, 42

Bowen D. B., Mewes V., Campanelli M., Noble S. C., Krolik J. H., Zilhão M., 2018, The Astrophysical Journal Letters, 853, L17

Boylan-Kolchin M., Ma C.-P., Quataert E., 2004, The Astrophysical Journal, 613, L37–L40

Brem P., Amaro-Seoane P., Sopuerta C. F., 2014, MNRAS, 437, 1259

Brenneman L. W., et al., 2011, ApJ, 736, 103

Britzen S., et al., 2018, MNRAS, 478, 3199

Britzen S., et al., 2021, MNRAS, 503, 3145

Broggi L., Bortolas E., Bonetti M., Sesana A., Dotti M., 2022, Monthly Notices of the Royal Astronomical Society, 514, 3270–3284

Bromley B. C., Kenyon S. J., Geller M. J., Barcikowski E., Brown W. R., Kurtz M. J., 2006, The Astrophysical Journal, 653, 1194–1202

Brown W. R., 2015, ARA&A, 53, 15

Brown D. A., Zimmerman P. J., 2010, Physical Review D, 81

Brown W. R., Geller M. J., Kenyon S. J., Kurtz M. J., 2005, The Astrophysical Journal, 622, L33–L36

Brown W. R., Geller M. J., Kenyon S. J., Kurtz M. J., 2006, The Astrophysical Journal, 647, 303–311

Brown W. R., Geller M. J., Kenyon S. J., 2008, The Astrophysical Journal, 690, 1639–1647

Brown W. R., Geller M. J., Kenyon S. J., 2012, The Astrophysical Journal, 751, 55

Brown W. R., Geller M. J., Kenyon S. J., 2014, The Astrophysical Journal, 787, 89

Brügmann B., González J. A., Hannam M., Husa S., Sperhake U., 2008, Physical Review D, 77

Bulirsch R., Stoer J., 1966, Numerische Mathematik, 8, 1

Bustamante S., Springel V., 2019, MNRAS, 490, 4133

Camargo D., 2021, ApJ, 923, 21

Campanelli M., Lousto C. O., Marronetti P., Zlochower Y., 2006, Phys. Rev. Lett., 96, 111101

Campanelli M., Lousto C. O., Zlochower Y., Merritt D., 2007a, Physical Review Letters, 98

Campanelli M., Lousto C., Zlochower Y., Merritt D., 2007b, The Astrophysical Journal, 659, L5–L8

Cappellari M., Copin Y., 2003, Monthly Notices of the Royal Astronomical Society, 342, 345–354

Capuzzo-Dolcetta R., 1993, The Astrophysical Journal, 415, 616

Capuzzo-Dolcetta R., Fragione G., 2015, Monthly Notices of the Royal Astronomical Society, 454, 2677–2690

Capuzzo-Dolcetta R., e Melo I. T., 2017, Monthly Notices of the Royal Astronomical Society, 472, 4013

Cárdenas-Avendaño A., Sopuerta C. F., 2024, arXiv e-prints, p. arXiv:2401.08085

Cardoso V., Gualtieri L., 2016, Classical and Quantum Gravity, 33, 174001

Carretero-Castrillo M., Ribó M., Paredes J. M., 2023, Astronomy & Astrophysics, 679, A109

Casertano S., Hut P., 1985, ApJ, 298, 80

Casetti-Dinescu D. I., Girard T. M., Korchagin V. I., van Altena W. F., López C. E., 2010, The Astronomical Journal, 140, 1282–1293

Cattorini F., Giacomazzo B., 2024, Astroparticle Physics, 154, 102892

Chandrasekhar S., 1942, Principles of stellar dynamics. The University of Chicago press

Chandrasekhar S., 1943, ApJ, 97, 255

Chang P., Strubbe L. E., Menou K., Quataert E., 2010, Monthly Notices of the Royal Astronomical Society, 407, 2007–2016

Chapon D., Mayer L., Teyssier R., 2013, Monthly Notices of the Royal Astronomical Society, 429, 3114–3122

Charisi M., Bartos I., Haiman Z., Price-Whelan A. M., Graham M. J., Bellm E. C., Laher R. R., Márka S., 2016, MNRAS, 463, 2145

Chemerynska I. V., Ishchenko M. V., Sobolenko M. O., Khoperskov S. A., Berczik P. P., 2022, Advances in Astronomy and Space Physics, 12, 18–24

Chen X., Liu F. K., 2013, ApJ, 762, 95

Chen X., Liu F. K., Magorrian J., 2008, ApJ, 676, 54

Chen X., Madau P., Sesana A., Liu F. K., 2009, ApJ, 697, L149

Chen X., Sesana A., Madau P., Liu F. K., 2011, ApJ, 729, 13

Chen S., Middleton H., Sesana A., Del Pozzo W., Vecchio A., 2017, MNRAS, 469, 2455

Chen S., Sesana A., Conselice C. J., 2019, MNRAS, 488, 401

Chen Y.-C., et al., 2020, MNRAS, 499, 2245

Chen Y.-C., Hwang H.-C., Shen Y., Liu X., Zakamska N. L., Yang Q., Li J. I., 2022, ApJ, 925, 162

Chen N., et al., 2023, MNRAS, 522, 1895

Chin S. A., 1997, Physics Letters A, 226, 344

Chin S. A., 2007, arXiv e-prints, p. arXiv:0704.3273

Chin S. A., Chen C. R., 2005, Celestial Mechanics and Dynamical Astronomy, 91, 301

Chomiuk L., Strader J., Maccarone T. J., Miller-Jones J. C. A., Heinke C., Noyola E., Seth A. C., Ransom S., 2013, The Astrophysical Journal, 777, 69

Ciurlo A., et al., 2020, Nature, 577, 337

Civano F., et al., 2012, ApJ, 752, 49

Cocchiararo F., Franchini A., Lupi A., Sesana A., 2024, A&A, 691, A250

Cohn H., 1980, ApJ, 242, 765

Colpi M., 2014, Space Sci. Rev., 183, 189

Colpi M., et al., 2024, arXiv e-prints, p. arXiv:2402.07571

Combi L., Ressler S. M., 2024, arXiv e-prints, p. arXiv:2403.13308

Comerford J. M., Griffith R. L., Gerke B. F., Cooper M. C., Newman J. A., Davis M., Stern D., 2009, ApJ, 702, L82

Comerford T. A. F., Izzard R. G., Booth R. A., Rosotti G., 2019, Monthly Notices of the Royal Astronomical Society, 490, 5196–5209

Conselice C. J., 2003, ApJS, 147, 1

Conselice C. J., 2014, Annual Review of Astronomy and Astrophysics, 52, 291–337

Conselice C. J., Mundy C. J., Ferreira L., Duncan K., 2022, ApJ, 940, 168

Contenta F., et al., 2018, Monthly Notices of the Royal Astronomical Society, 476, 3124–3136

Contigiani O., Rossi E. M., Marchetti T., 2019, Monthly Notices of the Royal Astronomical Society, 487, 4025–4036

Cox T. J., Dutta S. N., Di Matteo T., Hernquist L., Hopkins P. F., Robertson B., Springel V., 2006, The Astrophysical Journal, 650, 791–811

Croce A. D., Pascale R., Giunchi E., Nipoti C., Cignoni M., Dalessandro E., 2023

Csizmadia P., Debreczeni G., Rácz I., Vasúth M., 2012, Classical and Quantum Gravity, 29, 245002

Cuadra J., Armitage P. J., Alexander R. D., Begelman M. C., 2009, MNRAS, 393, 1423

Cutler C., Flanagan E., 1994, Physical Review D, 49, 2658–2697

D'Orazio D. J., Charisi M., 2023, arXiv e-prints, p. arXiv:2310.16896

D'Orazio D. J., Duffell P. C., 2021, ApJ, 914, L21

D'Orazio D. J., Haiman Z., MacFadyen A., 2013, MNRAS, 436, 2997

D'Souza R., Kauffman G., Wang J., Vegetti S., 2014, MNRAS, 443, 1433

Dai Y. S., et al., 2021, ApJ, 923, 156

Damiano A., Borgani S., Valentini M., Murante G., Tornatore L., Strakos P., Jaros M., 2025, arXiv e-prints, p. arXiv:2506.20740

Damour T., Deruelle N., 1985, Annales de L'Institut Henri Poincare Section (A) Physique Theorique, 43, 107

Danby J. M. A., 1988, Fundamentals of Celestial Mechanics, 2nd edn. Willmann-Bell, Inc., Virginia, USA

Dauser T., Garcia J., Parker M. L., Fabian A. C., Wilms J., 2014, MNRAS, 444, L100

Davis M., Efstathiou G., Frenk C. S., White S. D. M., 1985, ApJ, 292, 371

De Lucia G., Blaizot J., 2007, MNRAS, 375, 2

Decarli R., et al., 2020, The Astrophysical Journal, 902, 110

Dehnen W., 1993, MNRAS, 265, 250

Dehnen W., Hernandez D. M., 2017, MNRAS, 465, 1201

Dekel A., Sari R., Ceverino D., 2009, ApJ, 703, 785

Di Cintio A., Tremmel M., Governato F., Pontzen A., Zavala J., Bastidas Fry A., Brooks A., Vogelsberger M., 2017, Monthly Notices of the Royal Astronomical Society, 469, 2845–2854

Di Matteo T., Colberg J., Springel V., Hernquist L., Sijacki D., 2008, ApJ, 676, 33

Dieball A., Müller H., Grebel E. K., 2002, A&A, 391, 547

Do T., Martinez G. D., Kerzendorf W., Feldmeier-Krause A., Sedda M. A., Neumayer N., Gualandris A., 2020, The Astrophysical Journal, 901, L28

Dosopoulou F., Antonini F., 2017, ApJ, 840, 31

Dotti M., Sesana A., Decarli R., 2012, Advances in Astronomy, 2012, 1–14

Doğan S., Nixon C. J., King A. R., Pringle J. E., 2018, MNRAS, 476, 1519

Downing J. M. B., Benacquista M. J., Giersz M., Spurzem R., 2010, Monthly Notices of the Royal Astronomical Society, 407, 1946–1962

Du C., Li H., Yan Y., Newberg H. J., Shi J., Ma J., Chen Y., Wu Z., 2019, The Astrophysical Journal Supplement Series, 244, 4

Duffell P. C., D'Orazio D., Derdzinski A., Haiman Z., MacFadyen A., Rosen A. L., Zrake J., 2020, ApJ, 901, 25

Duffell P. C., et al., 2024, ApJ, 970, 156

Duncan K., et al., 2019, ApJ, 876, 110

Dunhill A. C., Alexander R. D., Nixon C. J., King A. R., 2014, MNRAS, 445, 2285

Dunn G., Holley-Bockelmann K., Bellovary J., 2020, The Astrophysical Journal, 896, 72

D'Orazio D. J., Haiman Z., Duffell P., MacFadyen A., Farris B., 2016, Monthly Notices of the Royal Astronomical Society, 459, 2379–2393

Ebisuzaki T., Makino J., Okumura S. K., 1991, Nature, 354, 212

Eftekharzadeh S., Myers A. D., Hennawi J. F., Djorgovski S. G., Richards G. T., Mahabal A. A., Graham M. J., 2017, MNRAS, 468, 77

Einsel C., Spurzem R., 1997, arXiv e-prints, pp astro–ph/9704284

Einstein A., 1915, Sitzungsberichte der Königlich Preussischen Akademie der Wissenschaften, 47, 831

El-Badry K., et al., 2022, Monthly Notices of the Royal Astronomical Society, 518, 1057–1085

El-Badry K., et al., 2023, Monthly Notices of the Royal Astronomical Society, 521, 4323–4348

Ennoggi L., et al., 2025, Phys. Rev. D, 112, 063009

Eracleous M., Boroson T. A., Halpern J. P., Liu J., 2012, ApJS, 201, 23

Erkal D., Boubert D., Gualandris A., Evans N. W., Antonini F., 2018, Monthly Notices of the Royal Astronomical Society, 483, 2007–2013

Ernst A., Glaschke P., Fiestas J., Just A., Spurzem R., 2007, Monthly Notices of the Royal Astronomical Society, 377, 465–479

Evans F. A., Rasskazov A., Remmelzwaal A., Marchetti T., Castro-Ginard A., Rossi E. M., Bovy J., 2023, Monthly Notices of the Royal Astronomical Society, 525, 561–576

Event Horizon Telescope Collaboration et al., 2022, ApJ, 930, L12

Fabricius M. H., et al., 2014, The Astrophysical Journal, 787, L26

Fakhouri O., Ma C.-P., Boylan-Kolchin M., 2010, Monthly Notices of the Royal Astronomical Society, 406, 2267–2278

Fantoccoli F., Barber J., Dosopoulou F., Chattopadhyay D., Antonini F., 2024

Farrell S. A., Webb N. A., Barret D., Godet O., Rodrigues J. M., 2009, Nature, 460, 73–75

Farris B. D., Liu Y. T., Shapiro S. L., 2010, Physical Review D, 81

Farris B. D., Gold R., Paschalidis V., Etienne Z. B., Shapiro S. L., 2012, Physical Review Letters, 109

Farris B. D., Duffell P., MacFadyen A. I., Haiman Z., 2014, Monthly Notices of the Royal Astronomical Society: Letters, 447, L80–L84

Fastidio F., Bortolas E., Gualandris A., Sesana A., Read J., Dehnen W., 2025, arXiv e-prints, p. arXiv:2506.16539

Fedrigo G., Lupi A., 2025, A&A, 700, A112

Feldmeier A., et al., 2013, Astronomy & Astrophysics, 554, A63

Ferrarese L., Merritt D., 2000, ApJ, 539, L9

Ferrarese L., et al., 2006, The Astrophysical Journal, 644, L21

Ferreira L., Conselice C. J., Duncan K., Cheng T.-Y., Griffiths A., Whitney A., 2020, ApJ, 895, 115

Fiestas J., Spurzem R., 2012, Astrophys. Space Sci. Proc., pp 235–237

Finn L. S., Thorne K. S., 2000, Physical Review D, 62

Fitchett M. J., 1983, MNRAS, 203, 1049

Fontecilla C., Chen X., Cuadra J., 2017, Monthly Notices of the Royal Astronomical Society: Letters, 468, L50–L54

Forastier B. R., Pina D. M., Gieles M., Zwart S. P., Antonini F., 2024, Binary-single interactions with different mass ratios (arXiv:2405.16999), https://arxiv.org/abs/2405.16999

Ford E. B., Kozinsky B., Rasio F. A., 2000, ApJ, 535, 385

Foster R. S., Backer D. C., 1990, ApJ, 361, 300

Fowler W. A., Hoyle F., 1964, ApJS, 9, 201

Fragione G., Capuzzo-Dolcetta R., 2016, Monthly Notices of the Royal Astronomical Society, 458, 2596–2603

Fragione G., Gualandris A., 2019, Monthly Notices of the Royal Astronomical Society, 489, 4543–4556

Fragione G., Capuzzo-Dolcetta R., Kroupa P., 2017, Monthly Notices of the Royal Astronomical Society, p. stx106

Fragione G., Kocsis B., Rasio F. A., Silk J., 2022, The Astrophysical Journal, 927, 231

Fragner M. M., Nelson R. P., 2010, A&A, 511, A77

Franchini A., Sesana A., Dotti M., 2021, MNRAS, 507, 1458

Franchini A., Lupi A., Sesana A., 2022, The Astrophysical Journal Letters, 929, L13

Frank J., King A., Raine D. J., 2002, Accretion Power in Astrophysics: Third Edition

Freire P. C. C., et al., 2017, MNRAS, 471, 857

Freitag M., Rasio F. A., Baumgardt H., 2006a, Monthly Notices of the Royal Astronomical Society, 368, 121–140

Freitag M., Gurkan M. A., Rasio F. A., 2006b, Monthly Notices of the Royal Astronomical Society, 368, 141–161

Fries L. B., et al., 2023, ApJ, 948, 5

Frigo M., Naab T., Rantala A., Johansson P. H., Neureiter B., Thomas J., Rizzuto F., 2021, Monthly Notices of the Royal Astronomical Society, 508, 4610–4624

Fuentes-Carrera I., Jablonka P., Sarajedini A., Bridges T., Djorgovski G., Meylan G., 2008, A&A, 483, 769

Fujii M. S., Wang L., Tanikawa A., Hirai Y., Saitoh T. R., 2024, Science, 384, 1488–1492

Fujimoto S., et al., 2024, Primordial Rotating Disk Composed of ≥15 Dense Star-Forming Clumps at Cosmic Dawn (arXiv:2402.18543), https://arxiv.org/abs/2402.18543

Fumagalli G., Romero-Shaw I., Gerosa D., De Renzis V., Kritos K., Olejak A., 2024, Physical Review D, 110

GRAVITY Collaboration et al., 2020, A&A, 636, L5

Gaia Collaboration 2016, A&A, 595, A2

Gaia Collaboration 2018, A&A, 616, A1

Gaia Collaboration 2023, A&A, 674, A1

Gaia Collaboration 2024, A&A, 686, L2

Gaia Collaboration et al., 2024, A&A, 686, L2

Gair J. R., Glampedakis K., 2006, Phys. Rev. D, 73, 064037

Gammie C. F., 2001, ApJ, 553, 174

García J., et al., 2014, ApJ, 782, 76

Garg M., Tiwari S., Derdzinski A., Baker J. G., Marsat S., Mayer L., 2024, MNRAS, 528, 4176

Gebhardt K., et al., 2000, ApJ, 539, L13

Gebhardt K., Rich R. M., Ho L. C., 2002, ApJ, 578, L41

Generozov A., Stone N. C., Metzger B. D., Ostriker J. P., 2018, Monthly Notices of the Royal Astronomical Society, 478, 4030–4051

Genina A., Springel V., Rantala A., 2024, MNRAS, 534, 957

Gerhard O. E., 1983, MNRAS, 202, 1159

Gerosa D., Berti E., 2019, Physical Review D, 100

Gerosa D., Sesana A., 2014, Monthly Notices of the Royal Astronomical Society, 446, 38–55

Gerosa D., Kesden M., Sperhake U., Berti E., O'Shaughnessy R., 2015, Physical Review D, 92

Gerosa D., Hébert F., Stein L. C., 2018, Physical Review D, 97

Giacomazzo B., Baker J. G., Coleman Miller M., Reynolds C. S., van Meter J. R., 2012, The Astrophysical Journal, 752, L15

Gieles M., Portegies Zwart S. F., 2011, Monthly Notices of the Royal Astronomical Society: Letters, 410, L6–L7

Gieles M., Balbinot E., Yaaqib R. I. S. M., Hénault-Brunet V., Zocchi A., Peuten M., Jonker P. G., 2018, MNRAS, 473, 4832

Giersz M., 1986, Acta Astron., 36, 181

Giersz M., Heggie D. C., 1994, Monthly Notices of the Royal Astronomical Society, 268, 257–275

Giersz M., Heggie D. C., 1997, Monthly Notices of the Royal Astronomical Society, 286, 709

Gies D. R., Bolton C. T., 1986, ApJS, 61, 419

Ginat Y. B., Perets H. B., 2024

Giusti C., et al., 2023, ApJ, 953, 125

Gnedin O. Y., Gould A., Miralda-Escude J., Zentner A. R., 2005, The Astrophysical Journal, 634, 344–350

Goicovic F. G., Cuadra J., Sesana A., Stasyszyn F., Amaro-Seoane P., Tanaka T. L., 2015, Monthly Notices of the Royal Astronomical Society, 455, 1989–2003

Goicovic F. G., Sesana A., Cuadra J., Stasyszyn F., 2017, Monthly Notices of the Royal Astronomical Society, 472, 514–531

Goicovic F. G., Maureira-Fredes C., Sesana A., Amaro-Seoane P., Cuadra J., 2018, Monthly Notices of the Royal Astronomical Society, 479, 3438–3455

Gold R., Brügmann B., 2013, Physical Review D, 88

Gold R., Paschalidis V., Ruiz M., Shapiro S. L., Etienne Z. B., Pfeiffer H. P., 2014, Physical Review D, 90

Goldreich P., Tremaine S., 1980, ApJ, 241, 425

González J. A., Sperhake U., Brügmann B., Hannam M., Husa S., 2007, Physical Review Letters, 98

Goodman J., 2003, Monthly Notices of the Royal Astronomical Society, 339, 937–948

Goodman J., Hut P., 1993, ApJ, 403, 271

Goulding A. D., Pardo K., Greene J. E., Mingarelli C. M. F., Nyland K., Strauss M. A., 2019, ApJ, 879, L21

Governato F., Colpi M., Maraschi L., 1994, Monthly Notices of the Royal Astronomical Society, 271, 317–322

Governato F., et al., 2010, Nature, 463, 203–206

Gragg W. B., 1965, SIAM Journal on Numerical Analysis, 2, 384

Graham A. W., Onken C. A., Athanassoula E., Combes F., 2011, MNRAS, 412, 2211

Graham M. J., et al., 2015, Nature, 518, 74

Grasha K., et al., 2017, The Astrophysical Journal, 840, 113

Greene J. E., Strader J., Ho L. C., 2020, Annual Review of Astronomy and Astrophysics, 58, 257–312

Grindlay J. E., Heinke C., Edmonds P. D., Murray S. S., 2001, Science, 292, 2290

Gualandris A., Portegies Zwart S., 2007, Monthly Notices of the Royal Astronomical Society: Letters, 376, L29–L33

Gualandris A., Read J. I., Dehnen W., Bortolas E., 2017, MNRAS, 464, 2301

Gualandris A., Khan F. M., Bortolas E., Bonetti M., Sesana A., Berczik P., Holley-Bockelmann K., 2022, Monthly Notices of the Royal Astronomical Society, 511, 4753–4765

Guillard N., Emsellem E., Renaud F., 2016, Monthly Notices of the Royal Astronomical Society, 461, 3620

Gültekin K., et al., 2009, ApJ, 698, 198

Haiman Z., 2004, The Astrophysical Journal, 613, 36–40

Haiman Z., Kocsis B., Menou K., 2009, The Astrophysical Journal, 700, 1952–1969

Hamers A. S., 2021, Research Notes of the AAS, 5, 275

Hamers A. S., Thompson T. A., 2019, ApJ, 883, 23

Hamers A. S., Pols O. R., Claeys J. S. W., Nelemans G., 2013, MNRAS, 430, 2262

Hamers A. S., Portegies Zwart S. F., Merritt D., 2014, Monthly Notices of the Royal Astronomical Society, 443, 355–387

Hani M. H., Sparre M., Ellison S. L., Torrey P., Vogelsberger M., 2018, MNRAS, 475, 1160

Hattori K., Valluri M., Bell E. F., Roederer I. U., 2018, The Astrophysical Journal, 866, 121

Hattori K., Valluri M., Castro N., Roederer I. U., Mahler G., Khullar G., 2019, The Astrophysical Journal, 873, 116

Hazboun J., Romano J., Smith T., 2019, The Journal of Open Source Software, 4, 1775

Heath R. M., Nixon C. J., 2020, A&A, 641, A64

Heber U., Edelmann H., Napiwotzki R., Altmann M., Scholz R. D., 2008, A&A, 483, L21

Heggie D. C., 1975, MNRAS, 173, 729

Heggie D. C., 1993, Gravothermal Oscillations (arXiv:astro-ph/9312018), https://arxiv.org/abs/astro-ph/9312018

Heggie D., Hut P., 2003, The Gravitational Million-Body Problem: A Multidisciplinary Approach to Star Cluster Dynamics. Cambridge University Press

Heinämäki P., 2001, A&A, 371, 795

Hellström C., Mikkola S., 2010, Celestial Mechanics and Dynamical Astronomy, 106, 143

Hénault-Brunet V., Gieles M., Strader J., Peuten M., Balbinot E., Douglas K. E. K., 2020, MNRAS, 491, 113

Hennawi J. F., et al., 2006, AJ, 131, 1

Hennawi J. F., Prochaska J. X., Cantalupo S., Arrigoni-Battaia F., 2015, Science, 348, 779–783

Hernquist L., 1990, ApJ, 356, 359

Herwig E., Arrigoni Battaia F., Bañados E., Farina E. P., 2025, A&A, 694, L12

Hills J. G., 1975a, AJ, 80, 809

Hills J. G., 1975b, Nature, 254, 295

Hills J. G., 1988, Nature, 331, 687

Hills J. G., 1991, AJ, 102, 704

Hilz M., Naab T., Ostriker J. P., Thomas J., Burkert A., Jesseit R., 2012, Monthly Notices of the Royal Astronomical Society, 425, 3119–3136

Hirsch H. A., Heber U., O'Toole S. J., Bresolin F., 2005, Astronomy & Astrophysics, 444, L61–L64

Hobbs G., Lorimer D. R., Lyne A. G., Kramer M., 2005, Monthly Notices of the Royal Astronomical Society, 360, 974–992

Hobbs G., et al., 2010, Classical and Quantum Gravity, 27, 084013

Hochart E., Portegies Zwart S., 2024, A&A, 685, A123

Hoffman L., Loeb A., 2007, Monthly Notices of the Royal Astronomical Society, 377, 957–976

Holman M., Touma J., Tremaine S., 1997, Nature, 386, 254

Hoogerwerf R., de Bruijne J. H. J., de Zeeuw P. T., 2001, Astronomy & Astrophysics, 365, 49–77

Hopkins P. F., Hernquist L., Cox T. J., Di Matteo T., Robertson B., Springel V., 2006, ApJS, 163, 1

Hopkins P. F., Hernquist L., Cox T. J., Kereš D., 2008, ApJS, 175, 356

Hopman C., Alexander T., 2006, ApJ, 645, 1152

Horton M. A., Krause M. G. H., Hardcastle M. J., 2023, MNRAS, 521, 2593

Horton M. A., Hardcastle M. J., Miley G. K., Tasse C., Shimwell T., 2025, A&A, 699, A338

Hoyle F., Lyttleton R. A., 1939, Proceedings of the Cambridge Philosophical Society, 35, 405

Huang Y., et al., 2017, The Astrophysical Journal Letters, 847, L9

Huang Y., Li Q., Liu J., Dong X., Zhang H., Lu Y., Du C., 2024

Hughes S. A., 2024, Phys. Rev. D, 109, 064077

Hui L., Ostriker J. P., Tremaine S., Witten E., 2017, Phys. Rev. D, 95, 043541

Hut P., Bahcall J. N., 1983, ApJ, 268, 319

Huško F., Lacey C. G., Baugh C. M., 2022, MNRAS, 509, 5918

Hwang H.-C., Shen Y., Zakamska N., Liu X., 2020, ApJ, 888, 73

Häberle M., et al., 2024, Nature, 631, 285–288

Ibata R., et al., 2009, The Astrophysical Journal, 699, L169–L173

Ishchenko M., Sobolenko M., Berczik P., Panamarev T., 2023, Kinematics and Physics of Celestial Bodies, 39, 33–44

Ishchenko M., et al., 2024, A&A, 686, A225

Ito T., Ohtsuka K., 2019, Monographs on Environment, Earth and Planets, 7, 1

Ivanov P. B., Papaloizou J. C. B., Polnarev A. G., 1999, Monthly Notices of the Royal Astronomical Society, 307, 79–90

Ivezić Ž., et al., 2019, ApJ, 873, 111

Jalali B., Baumgardt H., Kissler-Patig M., Gebhardt K., Noyola E., Lützgendorf N., de Zeeuw P. T., 2012, Astronomy & Astrophysics, 538, A19

Jesseit R., Naab T., Burkert A., 2005, Monthly Notices of the Royal Astronomical Society, 360, 1185–1200

Johansson P. H., Naab T., Burkert A., 2009, ApJ, 690, 802

Ju W., Greene J. E., Rafikov R. R., Bickerton S. J., Badenes C., 2013, ApJ, 777, 44

Justham S., Wolf C., Podsiadlowski P., Han Z., 2008, Astronomy & Astrophysics, 493, 1081–1091

Kamann S., Wisotzki L., Roth M. M., Gerssen J., Husser T. O., Sandin C., Weilbacher P., 2014, A&A, 566, A58

Kamann S., et al., 2016, Astronomy & Astrophysics, 588, A149

Kamlah A. W. H., et al., 2022, Monthly Notices of the Royal Astronomical Society, 516, 3266–3283

Kapil V., Mandel I., Berti E., Müller B., 2023, Monthly Notices of the Royal Astronomical Society, 519, 5893–5901

Katz M. L., Kelley L. Z., Dosopoulou F., Berry S., Blecha L., Larson S. L., 2020, MNRAS, 491, 2301

Kayo I., Oguri M., 2012, MNRAS, 424, 1363

Kelley L. Z., Blecha L., Hernquist L., 2017a, MNRAS, 464, 3131

Kelley L. Z., Blecha L., Hernquist L., Sesana A., Taylor S. R., 2017b, MNRAS, 471, 4508

Kelley L. Z., D'Orazio D. J., Di Stefano R., 2021, MNRAS, 508, 2524

Kelly B. J., Baker J. G., Etienne Z. B., Giacomazzo B., Schnittman J., 2017, Physical Review D, 96

Kenyon S. J., Bromley B. C., Geller M. J., Brown W. R., 2008, The Astrophysical Journal, 680, 312–327

Kesden M., Gerosa D., O'Shaughnessy R., Berti E., Sperhake U., 2015, Physical Review Letters, 114

Khan F. M., Preto M., Berczik P., Berentzen I., Just A., Spurzem R., 2012, The Astrophysical Journal, 749, 147

Khan F. M., Fiacconi D., Mayer L., Berczik P., Just A., 2016, ApJ, 828, 73

Khan A., Paschalidis V., Ruiz M., Shapiro S. L., 2018, Physical Review D, 97

Kharb P., Lal D. V., Merritt D., 2017, Nature Astronomy, 1, 727

Khoperskov S., Mastrobuono-Battisti A., Di Matteo P., Haywood M., 2018, A&A, 620, A154

Kidder L. E., 1995, Phys. Rev. D, 52, 821

King I. R., 1966, AJ, 71, 64

King A., 2008, New Astron. Rev., 52, 253

King A. R., Pringle J. E., 2006, MNRAS, 373, L90

King A. R., Lubow S. H., Ogilvie G. I., Pringle J. E., 2005, MNRAS, 363, 49

Kızıltan B., Baumgardt H., Loeb A., 2017a, Nature, 542, 203

Kızıltan B., Baumgardt H., Loeb A., 2017b, Nature, 545, 510

Klein A., et al., 2016, Physical Review D, 93

Kocevski D. D., et al., 2015, ApJ, 814, 104

Kochanek C. S., 1992, ApJ, 385, 604

Komberg B. V., 1968, Soviet Ast., 11, 727

Komossa S., 2012, Advances in Astronomy, 2012, 1–8

Komossa S., Burwitz V., Hasinger G., Predehl P., Kaastra J. S., Ikebe Y., 2003, ApJ, 582, L15

Königsdörffer C., Gopakumar A., 2006, Phys. Rev. D, 73, 124012

Koposov S. E., et al., 2019, Monthly Notices of the Royal Astronomical Society, 491, 2465–2480

Kormendy J., Ho L. C., 2013, ARA&A, 51, 511

Kormendy J., Richstone D., 1995, ARA&A, 33, 581

Koss M., Mushotzky R., Treister E., Veilleux S., Vasudevan R., Trippe M., 2012, ApJ, 746, L22

Koss M., et al., 2014, Monthly Notices of the Royal Astronomical Society, 445, 515–527

Koss M. J., et al., 2016, ApJ, 824, L4

Koss M. J., et al., 2023, ApJ, 942, L24

Koudmani S., Somerville R. S., Sijacki D., Bourne M. A., Jiang Y.-F., Profit K., 2024, MNRAS, 532, 60

Kozai Y., 1962, AJ, 67, 591

Krause M. G. H., et al., 2019, MNRAS, 482, 240

Kremer K., et al., 2019, Physical Review D, 99

Kreuzer S., Irrgang A., Heber U., 2020, Astronomy & Astrophysics, 637, A53

Kritos K., Strokov V., Baibhav V., Berti E., 2024

Kroupa P., 2001, Monthly Notices of the Royal Astronomical Society, 322, 231

Krumholz M. R., McKee C. F., Bland-Hawthorn J., 2019, Annual Review of Astronomy and Astrophysics, 57, 227–303

Kulkarni G., Loeb A., 2012, Monthly Notices of the Royal Astronomical Society, 422, 1306–1323

Kulkarni S. R., Hut P., McMillan S., 1993, Nature, 364, 421

Küpper A. H. W., Maschberger T., Kroupa P., Baumgardt H., 2011, Monthly Notices of the Royal Astronomical Society, 417, 2300

LIGO Scientific Collaboration et al., 2015, Classical and Quantum Gravity, 32, 074001

Lacey C., Cole S., 1993, MNRAS, 262, 627

Lahén N., Naab T., Johansson P. H., Elmegreen B., Hu C.-Y., Walch S., 2020, The Astrophysical Journal, 904, 71

Lanzoni B., et al., 2013, ApJ, 769, 107

LeVeque R. J., 2002, Finite Volume Methods for Hyperbolic Problems. Cambridge University Press, Cambridge, UK, https://www.cambridge.org/core/books/finite-volume-methods-for-hyperbolic-problems/97D5D1ACB1926DA1D4D52EAD6909E2B9

Leigh N. W. C., Georgiev I. Y., Böker T., Knigge C., den Brok M., 2015, Monthly Notices of the Royal Astronomical Society, 451, 859

Leigh N. W. C., et al., 2017, Monthly Notices of the Royal Astronomical Society, 474, 5672–5683

Lense J., Thirring H., 1918, Physikalische Zeitschrift, 19, 156

Leung G. Y. C., Leaman R., van de Ven G., Battaglia G., 2019, Monthly Notices of the Royal Astronomical Society, 493, 320–336

Levin Y., 2006, The Astrophysical Journal, 653, 1203–1209

Li Y.-B., Luo A., Zhao G., Lu Y., Ren J., Zuo F., 2011, The Astrophysical Journal, 744, L24

Li G., Naoz S., Kocsis B., Loeb A., 2015, MNRAS, 451, 1341

Li K., Bogdanović T., Ballantyne D. R., 2020, The Astrophysical Journal, 896, 113

Li Y.-B., et al., 2021, ApJS, 252, 3

Liao J., Du C., Li H., Ma J., Shi J., 2023, ApJ, 944, L39

Liao S., Irodotou D., Johansson P. H., Naab T., Rizzuto F. P., Hislop J. M., Rawlings A., Wright R. J., 2024, Monthly Notices of the Royal Astronomical Society, 528, 5080–5097

Lidov M. L., 1962, Planet. Space Sci., 9, 719

Lim H., Rodriguez C. L., 2020, Physical Review D, 102

Lin D., et al., 2018, Nature Astronomy, 2, 656–661

Liu B., Lai D., Wang Y.-H., 2019, ApJ, 883, L7

Löckmann U., Baumgardt H., Kroupa P., 2008, ApJ, 683, L151

Lodato G., Nayakshin S., King A. R., Pringle J. E., 2009, MNRAS, 398, 1392

Loose H. H., Kruegel E., Tutukov A., 1982, A&A, 105, 342

Lotz J. M., Jonsson P., Cox T. J., Croton D., Primack J. R., Somerville R. S., Stewart K., 2011, ApJ, 742, 103

Lousto C. O., Healy J., 2019, Physical Review D, 100

Lousto C. O., Zlochower Y., 2008, Physical Review D, 77

Lousto C. O., Zlochower Y., 2011, Physical Review Letters, 107

Lu T.-N., Kong A. K. H., 2011, The Astrophysical Journal, 729, L25

Lubow S. H., 1992, ApJ, 401, 317

Lupi A., 2023, MNRAS, 519, 1115

Lynden-Bell D., 1999, Physica A: Statistical Mechanics and its Applications, 263, 293–304

Lynden-Bell D., Wood R., Royal A., 1968, Mon. Not. Roy. Astron. Soc., 138, 495

Lützgendorf N., Kissler-Patig M., Noyola E., Jalali B., de Zeeuw P. T., Gebhardt K., Baumgardt H., 2011, Astronomy & Astrophysics, 533, A36

Ma L., Hopkins P. F., Kelley L. Z., Faucher-Giguère C.-A., 2023, Monthly Notices of the Royal Astronomical Society, 519, 5543–5553

MacFadyen A. I., Milosavljević M., 2008, The Astrophysical Journal, 672, 83–93

Mackey A. D., Wilkinson M. I., Davies M. B., Gilmore G. F., 2008, Monthly Notices of the Royal Astronomical Society, 386, 65–95

Maggiore M., 2007, Gravitational Waves. Vol. 1: Theory and Experiments. Oxford Master Series in Physics, Oxford University Press

Maggiore M., et al., 2020, Journal of Cosmology and Astroparticle Physics, 2020, 050–050

Makino J., Funato Y., 2004, The Astrophysical Journal, 602, 93–102

Man A. W. S., Zirm A. W., Toft S., 2016, ApJ, 830, 89

Mancieri D., Broggi L., Vinciguerra M., Sesana A., Bonetti M., 2025a, arXiv e-prints, p. arXiv:2509.02394

Mancieri D., Broggi L., Bonetti M., Sesana A., 2025b, Astronomy & Astrophysics, 694, A272

Mangiagli A., Caprini C., Volonteri M., Marsat S., Vergani S., Tamanini N., Inchauspé H., 2022, Phys. Rev. D, 106, 103017

Manikantan V., Paschalidis V., Bozzola G., 2025, Phys. Rev. D, 112, 043004

Mann C. R., et al., 2019, ApJ, 875, 1

Mannerkoski M., Johansson P. H., Pihajoki P., Rantala A., Naab T., 2019, ApJ, 887, 35

Mannerkoski M., Johansson P. H., Rantala A., Naab T., Liao S., 2021, ApJ, 912, L20

Mannerkoski M., Rawlings A., Johansson P. H., Naab T., Rantala A., Springel V., Irodotou D., Liao S., 2023, MNRAS, 524, 4062

Mannucci F., et al., 2022, Nature Astronomy, 6, 1185

Mansbach P., 1970, ApJ, 160, 135

Mantha K. B., et al., 2018, MNRAS, 475, 1549

Mapelli M., Santoliquido F., Bouffanais Y., Arca Sedda M., Artale M. C., Ballone A., 2021, Symmetry, 13, 1678

Marchetti T., Rossi E. M., Kordopatis G., Brown A. G. A., Rimoldi A., Starkenburg E., Youakim K., Ashley R., 2018a, in Recio-Blanco A., de Laverny P., Brown A. G. A., Prusti T., eds, Vol. 330, Astrometry and Astrophysics in the Gaia Sky. pp 181–184, doi:10.1017/S1743921317005671

Marchetti T., Rossi E. M., Brown A. G. A., 2018b, Monthly Notices of the Royal Astronomical Society, 490, 157–171

Marchetti T., Evans F. A., Rossi E. M., 2022, Monthly Notices of the Royal Astronomical Society, 515, 767–774

Mardling R. A., Aarseth S. J., 2001, MNRAS, 321, 398

Marín Pina D., Rastello S., Gieles M., Kremer K., Fitzgerald L., Rando Forastier B., 2024, Astronomy & Astrophysics, 688, L2

Mastrobuono-Battisti A., Khoperskov S., Di Matteo P., Haywood M., 2019, Astronomy & Astrophysics, 622, A86

Matsubayashi T., Makino J., Ebisuzaki T., 2007, ApJ, 656, 879

Matsui H., et al., 2012, ApJ, 746, 26

Matsumoto H., Tsuru T. G., Koyama K., Awaki H., Canizares C. R., Kawai N., Matsushita S., Kawabe R., 2001, The Astrophysical Journal, 547, L25–L28

Maureira-Fredes C., Goicovic F. G., Amaro-Seoane P., Sesana A., 2018, Monthly Notices of the Royal Astronomical Society, 478, 1726–1748

Mayer L., Kazantzidis S., Madau P., Colpi M., Quinn T., Wadsley J., 2007, Science, 316, 1874–1877

Mazzolari G., Bonetti M., Sesana A., Colombo R. M., Dotti M., Lodato G., Izquierdo-Villalba D., 2022, MNRAS, 516, 1959

Memmesheimer R.-M., Gopakumar A., Schäfer G., 2004, Phys. Rev. D, 70, 104011

Menci N., Cavaliere A., Fontana A., Giallongo E., Poli F., Vittorini V., 2004, ApJ, 604, 12

Menon S. H., et al., 2021, Monthly Notices of the Royal Astronomical Society, 507, 5542–5566

Merritt D., 2013, Dynamics and Evolution of Galactic Nuclei. Princeton University Press

Merritt D., Milosavljević M., 2005, Living Reviews in Relativity, 8, 8

Merritt D., Poon M. Y., 2004, ApJ, 606, 788

Merritt D., Vasiliev E., 2010, The Astrophysical Journal, 726, 61

Merritt D., Mikkola S., Szell A., 2007, ApJ, 671, 53

Merritt D., Alexander T., Mikkola S., Will C. M., 2011, Phys. Rev. D, 84, 044024

Mezcua M., 2017, International Journal of Modern Physics D, 26, 1730021

Mezcua M., Roberts T. P., Sutton A. D., Lobanov A. P., 2013, MNRAS, 436, 3128

Mezcua M., Roberts T. P., Lobanov A. P., Sutton A. D., 2015, Monthly Notices of the Royal Astronomical Society, 448, 1893–1899

Middleton H., Sesana A., Chen S., Vecchio A., Del Pozzo W., Rosado P. A., 2023, MNRAS, 525, 1077

Mihos J. C., Hernquist L., 1994, ApJ, 437, L47

Mihos J. C., Hernquist L., 1996, ApJ, 464, 641

Mikkola S., Aarseth S. J., 1993, Celestial Mechanics and Dynamical Astronomy, 57, 439

Mikkola S., Merritt D., 2006, MNRAS, 372, 219

Mikkola S., Merritt D., 2008, AJ, 135, 2398

Mikkola S., Tanikawa K., 1999, MNRAS, 310, 745

Mikkola S., Valtonen M. J., 1990, ApJ, 348, 412

Mikkola S., Valtonen M. J., 1992, MNRAS, 259, 115

Miles M. T., et al., 2025, MNRAS, 536, 1489

Milosavljević M., 2004, The Astrophysical Journal, 605, L13

Milosavljević M., Merritt D., 2003, ApJ, 596, 860

Milosavljević M., Merritt D., 2001, The Astrophysical Journal, 563, 34–62

Miranda R., Muñoz D. J., Lai D., 2017, MNRAS, 466, 1170

Mocz P., Vogelsberger M., Hernquist L., 2014, MNRAS, 442, 43

Moody M. S. L., Shi J.-M., Stone J. M., 2019, ApJ, 875, 66

Moore B., 1994, Nature, 370, 629

Moore C. J., Cole R. H., Berry C. P. L., 2014, Classical and Quantum Gravity, 32, 015014

Mora T., Will C. M., 2004, Phys. Rev. D, 69, 104021

Mora M. D., Puzia T. H., Chanamé J., 2019, A&A, 622, A65

Morscher M., Pattabiraman B., Rodriguez C., Rasio F. A., Umbreit S., 2015, The Astrophysical Journal, 800, 9

Most E. R., Wang H.-Y., 2024, ApJ, 973, L19

Moster B. P., Naab T., White S. D. M., 2013, MNRAS, 428, 3121

Moster B. P., Naab T., White S. D. M., 2018, MNRAS, 477, 1822

Moster B. P., Naab T., White S. D. M., 2020, MNRAS, 499, 4748

Muñoz D. J., Springel V., Marcus R., Vogelsberger M., Hernquist L., 2013, MNRAS, 428, 254

Mundy C. J., Conselice C. J., Duncan K. J., Almaini O., Häußler B., Hartley W. G., 2017, MNRAS, 470, 3507

Muñoz D. J., Miranda R., Lai D., 2019, The Astrophysical Journal, 871, 84

Muñoz D. J., Lai D., Kratter K., Miranda R., 2020, The Astrophysical Journal, 889, 114

Myers A. D., Richards G. T., Brunner R. J., Schneider D. P., Strand N. E., Hall P. B., Blomquist J. A., York D. G., 2008, ApJ, 678, 635

NANOGrav Collaboration et al., 2025, arXiv e-prints, p. arXiv:2508.16534

Naab T., et al., 2014, Monthly Notices of the Royal Astronomical Society, 444, 3357–3387

Naoz S., 2016, ARA&A, 54, 441

Naoz S., Haiman Z., 2023, ApJ, 955, L27

Naoz S., Rose S. C., Michaely E., Melchor D., Ramirez-Ruiz E., Mockler B., Schnittman J. D., 2022, The Astrophysical Journal Letters, 927, L18

Narayan R., 2000, ApJ, 536, 663

Nate Bode J., Wegg C., 2013, arXiv e-prints, p. arXiv:1310.5745

Nayakshin S., Cuadra J., Springel V., 2007, Monthly Notices of the Royal Astronomical Society, 379, 21

Nealon R., Ragusa E., Gerosa D., Rosotti G., Barbieri R., 2022, MNRAS, 509, 5608

Neumayer N., Seth A., Böker T., 2020, The Astronomy and Astrophysics Review, 28

Neunteufel P., 2020, Astronomy & Astrophysics, 641, A52

Nguyen D. D., et al., 2017, ApJ, 836, 237

Nipoti C., 2025, A&A, 697, A74

Nixon C. J., 2012, MNRAS, 423, 2597

Nixon C. J., Cossins P. J., King A. R., Pringle J. E., 2011, MNRAS, 412, 1591

Nixon C., King A., Price D., 2013, MNRAS, 434, 1946

Noble S. C., Mundim B. C., Nakano H., Krolik J. H., Campanelli M., Zlochower Y., Yunes N., 2012, The Astrophysical Journal, 755, 51

Norman C., Silk J., 1983, ApJ, 266, 502

Noyola E., Gebhardt K., Kissler-Patig M., Lützgendorf N., Jalali B., de Zeeuw P. T., Baumgardt H., 2010, The Astrophysical Journal, 719, L60–L64

Ogiya G., Hahn O., Mingarelli C. M. F., Volonteri M., 2020, Monthly Notices of the Royal Astronomical Society, 493, 3676–3689

Oh S.-H., et al., 2015, AJ, 149, 180

Ostriker E. C., 1999, The Astrophysical Journal, 513, 252–258

Ostriker J. P., Hausman M. A., 1977, ApJ, 217, L125

O'Leary R. M., Rasio F. A., Fregeau J. M., Ivanova N., O'Shaughnessy R., 2006, The Astrophysical Journal, 637, 937–951

O'Leary J. A., Moster B. P., Naab T., Somerville R. S., 2020, Monthly Notices of the Royal Astronomical Society

Paduano A., et al., 2024, The Astrophysical Journal, 961, 54

Pakmor R., Springel V., 2013, MNRAS, 432, 176

Pakmor R., Bauer A., Springel V., 2011, MNRAS, 418, 1392

Pakmor R., Kromer M., Taubenberger S., Springel V., 2013, The Astrophysical Journal, 770, L8

Pakmor R., Springel V., Bauer A., Mocz P., Munoz D. J., Ohlmann S. T., Schaal K., Zhu C., 2016, MNRAS, 455, 1134

Pappas G., Sotiriou T. P., 2015, MNRAS, 453, 2862

Park D., Kim C., Lee H. M., Bae Y.-B., Belczynski K., 2017, Monthly Notices of the Royal Astronomical Society, 469, 4665–4674

Partmann C., Naab T., Rantala A., Genina A., Mannerkoski M., Johansson P. H., 2024, MNRAS, 532, 4681

Paschalidis V., Bright J., Ruiz M., Gold R., 2021, The Astrophysical Journal Letters, 910, L26

Pechetti R., et al., 2022, The Astrophysical Journal, 924, 48

Pelupessy F. I., Jänes J., Portegies Zwart S., 2012, New Astron., 17, 711

Peres A., 1962, Phys. Rev., 128, 2471

Perets H. B., Šubr L., 2012, The Astrophysical Journal, 751, 133

Perets H. B., Gualandris A., Kupi G., Merritt D., Alexander T., 2009, The Astrophysical Journal, 702, 884–889

Peters P. C., 1964, Phys. Rev., 136, B1224

Peters P. C., Mathews J., 1963, Physical Review, 131, 435

Petkova M., Springel V., 2011, MNRAS, 415, 3731

Peuten M., Zocchi A., Gieles M., Gualandris A., Hénault-Brunet V., 2016, Monthly Notices of the Royal Astronomical Society, 462, 2333–2342

Pfister H., Lupi A., Capelo P. R., Volonteri M., Bellovary J. M., Dotti M., 2017, Monthly Notices of the Royal Astronomical Society, 471, 3646–3656

Pfister H., Volonteri M., Dubois Y., Dotti M., Colpi M., 2019, Monthly Notices of the Royal Astronomical Society, 486, 101–111

Phukon K. S., Johnson-McDaniel N. K., Singh A., Gupta A., 2025, arXiv e-prints, p. arXiv:2504.20543

Pillepich A., et al., 2018, MNRAS, 473, 4077

Poisson E., Will C. M., 2014, Gravity: Newtonian, Post-Newtonian, Relativistic. Cambridge University Press, Cambridge, UK

Polak B., et al., 2024, A&A, 690, A207

Pooley D., Rappaport S., 2006, ApJ, 644, L45

Portegies Zwart S. F., 2000, The Astrophysical Journal, 544, 437–442

Portegies Zwart S. F., McMillan S. L. W., 2000, The Astrophysical Journal, 528, L17–L20

Portegies Zwart S. F., McMillan S. L. W., 2002, The Astrophysical Journal, 576, 899–907

Portegies Zwart S. F., Makino J., McMillan S. L. W., Hut P., 1999, A&A, 348, 117

Portegies Zwart S. F., Baumgardt H., Hut P., Makino J., McMillan S. L. W., 2004a, Nature, 428, 724

Portegies Zwart S. F., Baumgardt H., Hut P., Makino J., McMillan S. L. W., 2004b, Nature, 428, 724–726

Poveda A., Ruiz J., Allen C., 1967, Boletin de los Observatorios Tonantzintla y Tacubaya, 4, 86

Power C., Navarro J. F., Jenkins A., Frenk C. S., White S. D. M., Springel V., Stadel J., Quinn T., 2003, MNRAS, 338, 14

Pratten G., Klein A., Moore C. J., Middleton H., Steinle N., Schmidt P., Vecchio A., 2023a, Phys. Rev. D, 107, 123026

Pratten G., Schmidt P., Middleton H., Vecchio A., 2023b, Phys. Rev. D, 108, 124045

Press W. H., Teukolsky S. A., 1977, ApJ, 213, 183

Preto M., Berentzen I., Berczik P., Merritt D., Spurzem R., 2009, in Journal of Physics Conference Series. p. 012049 (arXiv:0811.3501), doi:10.1088/1742-6596/154/1/012049

Preto M., Berentzen I., Berczik P., Spurzem R., 2011, The Astrophysical Journal, 732, L26

Pretorius F., 2005, Phys. Rev. Lett., 95, 121101

Price-Whelan A. M., 2017, The Journal of Open Source Software, 2, 388

Prieto E. G., Weatherford N. C., Fragione G., Kremer K., Rasio F. A., 2024

Pringle J. E., 1991, MNRAS, 248, 754

Pringle J. E., 1992, MNRAS, 258, 811

Quinlan G. D., 1996, New Astronomy, 1, 35–56

Qunbar I., Stone N. C., 2024, Phys. Rev. Lett., 133, 141401

Rabago I., Zhu Z., Lubow S., Martin R. G., 2024, MNRAS, 533, 360

Ragusa E., Lodato G., Price D. J., 2016, Monthly Notices of the Royal Astronomical Society, 460, 1243–1253

Rajamuthukumar A. S., Bauer E. B., Justham S., Pakmor R., de Mink S. E., Neunteufel P., 2024

Rantala A., Pihajoki P., Johansson P. H., Naab T., Lahén N., Sawala T., 2017, ApJ, 840, 53

Rantala A., Johansson P. H., Naab T., Thomas J., Frigo M., 2018, ApJ, 864, 113

Rantala A., Johansson P. H., Naab T., Thomas J., Frigo M., 2019, ApJ, 872, L17

Rantala A., Pihajoki P., Mannerkoski M., Johansson P. H., Naab T., 2020, MNRAS, 492, 4131

Rantala A., Naab T., Springel V., 2021, Monthly Notices of the Royal Astronomical Society, 502, 5546

Rantala A., Naab T., Rizzuto F. P., Mannerkoski M., Partmann C., Lautenschütz K., 2023, MNRAS, 522, 5180

Rantala A., Naab T., Lahén N., 2024a

Rantala A., Rawlings A., Naab T., Thomas J., Johansson P. H., 2024b, Monthly Notices of the Royal Astronomical Society, 535, 1202–1227

Rasskazov A., Fragione G., Leigh N. W. C., Tagawa H., Sesana A., Price-Whelan A., Rossi E. M., 2019, The Astrophysical Journal, 878, 17

Rastello S., Iorio G., Mapelli M., Arca-Sedda M., Carlo U. N. D., Escobar G. J., Torniamenti S., Shenar T., 2023

Rauch K. P., Tremaine S., 1996, New Astron., 1, 149

Rawlings A., Mannerkoski M., Johansson P. H., Naab T., 2023

Rawlings A., et al., 2025, MNRAS, 537, 3421

Reardon D. J., et al., 2023, ApJ, 951, L6

Redmount I. H., Rees M. J., 1989, Comments on Astrophysics, 14, 165

Rees M. J., 1988a, Nature, 333, 523

Rees M. J., 1988b, Nature, 333, 523

Ressler S. M., Combi L., Li X., Ripperda B., Yang H., 2024, ApJ, 967, 70

Ressler S. M., Combi L., Ripperda B., Most E. R., 2025, ApJ, 979, L24

Reynolds C. S., 2021, ARA&A, 59, 117

Ricarte A., Natarajan P., Dai L., Coppi P., 2016, MNRAS, 458, 1712

Ricarte A., Conroy N. S., Wielgus M., Palumbo D. C. M., Emami R., Chan C.-K., 2025, ApJ, 987, 152

Ricci C., et al., 2017, MNRAS, 468, 1273

Rizzuto F. P., et al., 2020, Monthly Notices of the Royal Astronomical Society, 501, 5257

Rizzuto F. P., et al., 2021, MNRAS, 501, 5257

Rizzuto F. P., Naab T., Spurzem R., Arca-Sedda M., Giersz M., Ostriker J. P., Banerjee S., 2022a, MNRAS, 512, 884

Rizzuto F. P., Naab T., Spurzem R., Arca-Sedda M., Giersz M., Ostriker J. P., Banerjee S., 2022b, Monthly Notices of the Royal Astronomical Society, 512, 884–898

Rizzuto F. P., Naab T., Rantala A., Johansson P. H., Ostriker J. P., Stone N. C., Liao S., Irodotou D., 2023, Monthly Notices of the Royal Astronomical Society, 521, 2930

Roberts D., Gieles M., Erkal D., Sanders J. L., 2025, MNRAS, 538, 454

Robinson I., Schild A., Schucking E. L., eds, 1965, Quasi-stellar sources and gravitational collapse

Robson T., Cornish N. J., Liu C., 2019, Classical and Quantum Gravity, 36, 105011

Rodriguez-Gomez V., et al., 2016, MNRAS, 458, 2371

Rodriguez C., Taylor G. B., Zavala R. T., Peck A. B., Pollack L. K., Romani R. W., 2006, ApJ, 646, 49

Rodriguez C. L., Morscher M., Pattabiraman B., Chatterjee S., Haster C.-J., Rasio F. A., 2015, Physical Review Letters, 115

Roedig C., Sesana A., 2012, Journal of Physics: Conference Series, 363, 012035

Roedig C., Sesana A., 2014, Monthly Notices of the Royal Astronomical Society, 439, 3476–3489

Roedig C., Dotti M., Sesana A., Cuadra J., Colpi M., 2011, Monthly Notices of the Royal Astronomical Society, 415, 3033–3041

Rom B., Linial I., Kaur K., Sari R., 2024, ApJ, 977, 7

Rosas-Guevara Y. M., Bower R. G., McAlpine S., Bonoli S., Tissera P. B., 2019, MNRAS, 483, 2712

Rui N. Z., Weatherford N. C., Kremer K., Chatterjee S., Fragione G., Rasio F. A., Rodriguez C. L., Ye C. S., 2021, Research Notes of the American Astronomical Society, 5, 47

Ryan F. D., 1995, Phys. Rev. D, 52, 5707

Ryu T., Leigh N. W. C., Perna R., 2017a, Monthly Notices of the Royal Astronomical Society, 470, 2–19

Ryu T., Leigh N. W. C., Perna R., 2017b, Monthly Notices of the Royal Astronomical Society, 470, 3049–3067

Ryu T., Perna R., Haiman Z., Ostriker J. P., Stone N. C., 2017c, Monthly Notices of the Royal Astronomical Society, 473, 3410–3433

Ryu T., Perna R., Wang Y.-H., 2022, Monthly Notices of the Royal Astronomical Society, 516, 2204–2217

Ryu T., Perna R., Pakmor R., Ma J.-Z., Farmer R., de Mink S. E., 2023a, Monthly Notices of the Royal Astronomical Society, 519, 5787–5799

Ryu T., Valli R., Pakmor R., Perna R., de Mink S. E., Springel V., 2023b, Monthly Notices of the Royal Astronomical Society, 525, 5752–5766

Röttgers B., Naab T., Cernetic M., Davé R., Kauffmann G., Borthakur S., Foidl H., 2020, Monthly Notices of the Royal Astronomical Society, 496, 152–168

Sabhahit G. N., Vink J. S., Higgins E. R., Sander A. A. C., 2022, MNRAS, 514, 3736

Sabhahit G. N., Vink J. S., Sander A. A. C., Higgins E. R., 2023, MNRAS, 524, 1529

Sala L., Valentini M., Biffi V., Dolag K., 2024, A&A, 685, A92

Samsing J., Ilan T., 2018, Monthly Notices of the Royal Astronomical Society, 476, 1548–1560

Samsing J., MacLeod M., Ramirez-Ruiz E., 2014, The Astrophysical Journal, 784, 71

Samsing J., MacLeod M., Ramirez-Ruiz E., 2017, The Astrophysical Journal, 846, 36

Samsing J., D'Orazio D. J., Askar A., Giersz M., 2018a, Black Hole Mergers from Globular Clusters Observable by LISA and LIGO: Results from post-Newtonian Binary-Single Scatterings (arXiv:1802.08654), https://arxiv.org/abs/1802.08654

Samsing J., Askar A., Giersz M., 2018b, The Astrophysical Journal, 855, 124

Sandoval B., et al., 2023, arXiv e-prints, p. arXiv:2312.02311

Scheuer P. A. G., Feiler R., 1996, MNRAS, 282, 291

Schmidt M., 1963, Nature, 197, 1040

Schnittman J. D., Buonanno A., 2007, The Astrophysical Journal, 662, L63–L66

Sesana A., 2010, ApJ, 719, 851

Sesana A., 2013, MNRAS, 433, L1

Sesana A., Khan F. M., 2015, Monthly Notices of the Royal Astronomical Society: Letters, 454, L66–L70

Sesana A., Haardt F., Madau P., Volonteri M., 2005, The Astrophysical Journal, 623, 23–30

Sesana A., Haardt F., Madau P., 2006, The Astrophysical Journal, 651, 392–400

Sesana A., Haardt F., Madau P., 2007, Monthly Notices of the Royal Astronomical Society: Letters, 379, L45–L49

Sesana A., Vecchio A., Colacino C. N., 2008a, MNRAS, 390, 192

Sesana A., Haardt F., Madau P., 2008b, The Astrophysical Journal, 686, 432–447

Sesana A., Haardt F., Madau P., 2008c, The Astrophysical Journal, 686, 432–447

Sesana A., Madau P., Haardt F., 2009a, Monthly Notices of the Royal Astronomical Society: Letters, 392, L31–L34

Sesana A., Madau P., Haardt F., 2009b, Monthly Notices of the Royal Astronomical Society: Letters, 392, L31–L34

Sesana A., Vecchio A., Volonteri M., 2009c, MNRAS, 394, 2255

Sesana A., Barausse E., Dotti M., Rossi E. M., 2014, ApJ, 794, 104

Sesana A., Haiman Z., Kocsis B., Kelley L. Z., 2018, ApJ, 856, 42

Shakura N. I., Sunyaev R. A., 1976, MNRAS, 175, 613

Shen K. J., et al., 2018, The Astrophysical Journal, 865, 15

Shen Y., Hwang H.-C., Zakamska N., Liu X., 2019, ApJ, 885, L4

Shen Y., et al., 2021, Nature Astronomy, 5, 569

Shen Y., et al., 2023, arXiv e-prints, p. arXiv:2306.15527

Sherwin B. D., Loeb A., O'Leary R. M., 2008, Monthly Notices of the Royal Astronomical Society, 386, 1179–1191

Shi J.-M., Krolik J. H., 2015, ApJ, 807, 131

Shi J.-M., Krolik J. H., Lubow S. H., Hawley J. F., 2012, ApJ, 749, 118

Shibuya T., Miura N., Iwadate K., Fujimoto S., Harikane Y., Toba Y., Umayahara T., Ito Y., 2022, PASJ, 74, 73

Sigurdsson S., Phinney E. S., 1993, ApJ, 415, 631

Silsbee K., Tremaine S., 2017, ApJ, 836, 39

Silverman J. D., et al., 2020, ApJ, 899, 154

Siwek M., Weinberger R., Muñoz D. J., Hernquist L., 2023a, MNRAS, 518, 5059

Siwek M., Weinberger R., Hernquist L., 2023b, MNRAS, 522, 2707

Sopuerta C. F., Yunes N., 2011, Phys. Rev. D, 84, 124060

Souvaitzis L., Rantala A., Naab T., 2025a, arXiv e-prints, p. arXiv:2510.09743

Souvaitzis L., Rantala A., Naab T., 2025b, MNRAS, 539, 45

Souza Lima R., Mayer L., Capelo P. R., Bortolas E., Quinn T. R., 2020, ApJ, 899, 126

Spitzer Lyman J., 1969, ApJ, 158, L139

Spitzer L., 1987, Dynamical evolution of globular clusters. Princeton University Press

Spitzer Lyman J., Hart M. H., 1971, ApJ, 164, 399

Springel V., 2010, MNRAS, 401, 791

Springel V., Di Matteo T., Hernquist L., 2005, MNRAS, 361, 776

Steinborn L. K., Dolag K., Comerford J. M., Hirschmann M., Remus R.-S., Teklu A. F., 2016, MNRAS, 458, 1013

Steinle N., Gerosa D., 2023, MNRAS, 519, 5031

Stemo A., Comerford J. M., Barrows R. S., Stern D., Assef R. J., Griffith R. L., Schechter A., 2021, ApJ, 923, 36

Stone N. C., Küpper A. H., Ostriker J. P., 2017, Monthly Notices of the Royal Astronomical Society, p. stx097

Strader J., Chomiuk L., Maccarone T. J., Miller-Jones J. C. A., Seth A. C., 2012, Nature, 490, 71–73

Strohmayer T. E., Mushotzky R. F., 2003, ApJ, 586, L61

Sugimoto D., Bettwieser E., 1983, MNRAS, 204, 19P

Tacconi L. J., et al., 2018, The Astrophysical Journal, 853, 179

Tamfal T., Capelo P. R., Kazantzidis S., Mayer L., Potter D., Stadel J., Widrow L. M., 2018, The Astrophysical Journal Letters, 864, L19

Tang Y., MacFadyen A., Haiman Z., 2017, Monthly Notices of the Royal Astronomical Society, 469, 4258–4267

Tang Y., Haiman Z., MacFadyen A., 2018, MNRAS, 476, 2249

Tanikawa A., 2013, Monthly Notices of the Royal Astronomical Society, 435, 1358–1375

Tanikawa A., Umemura M., 2014, MNRAS, 440, 652

Taylor C., Reynolds C. S., 2018, ApJ, 855, 120

Tazzari M., Lodato G., 2015, Monthly Notices of the Royal Astronomical Society, 449, 1118–1128

Teboul O., Perets H. B., 2025, ApJ, 984, 12

The NANOGrav Collaboration 2023, The NANOGrav 15-Year Data Set, doi:10.5281/zenodo.8423265, https://doi.org/10.5281/zenodo.8423265

Thirring H., 1918, Physikalische Zeitschrift, 19, 33

Thompson T. A., 2011, ApJ, 741, 82

Thorne K. S., Braginskii V. B., 1976, ApJ, 204, L1

Thorne K. S., Hartle J. B., 1985, Phys. Rev. D, 31, 1815

Tiede C., D'Orazio D. J., 2024, MNRAS, 527, 6021

Tiede C., Zrake J., MacFadyen A., Haiman Z., 2020, The Astrophysical Journal, 900, 43

Tiwari V., Chan C.-H., Bogdanović T., Jiang Y.-F., Davis S. W., Ferrel S., 2025, ApJ, 986, 158

Toomre A., Toomre J., 1972, ApJ, 178, 623

Toonen S., Perets H. B., Hamers A. S., 2018, A&A, 610, A22

Torniamenti S., Rastello S., Mapelli M., Di Carlo U. N., Ballone A., Pasquato M., 2022, Monthly Notices of the Royal Astronomical Society, 517, 2953–2965

Toro E. F., 2009, Riemann Solvers and Numerical Methods for Fluid Dynamics: A Practical Introduction. Springer Berlin Heidelberg, Berlin, Germany

Trani A. A., Di Cintio P., 2025, arXiv e-prints, p. arXiv:2506.02173

Tremaine S. D., Ostriker J. P., Spitzer L. J., 1975, ApJ, 196, 407

Tremaine S., Richstone D. O., Byun Y.-I., Dressler A., Faber S. M., Grillmair C., Kormendy J., Lauer T. R., 1994, AJ, 107, 634

Tremmel M., Governato F., Volonteri M., Quinn T. R., 2015, MNRAS, 451, 1868

Trenti M., Ardi E., Mineshige S., Hut P., 2007, Monthly Notices of the Royal Astronomical Society, 374, 857–866

Trenti M., Vesperini E., Pasquato M., 2009, The Astrophysical Journal, 708, 1598–1610

Tsatsi A., Mastrobuono-Battisti A., van de Ven G., Perets H. B., Bianchini P., Neumayer N., 2016, Monthly Notices of the Royal Astronomical Society, 464, 3720

Übler H., et al., 2024, MNRAS, 531, 355

Übler H., et al., 2025, arXiv e-prints, p. arXiv:2509.21575

Valtonen M., Karttunen H., 2006, The Three-Body Problem. Cambridge University Press

Valtonen M. J., et al., 2008, Nature, 452, 851

Van Wassenhove S., Capelo P. R., Volonteri M., Dotti M., Bellovary J. M., Mayer L., Governato F., 2014, MNRAS, 439, 474

VandenBerg D. A., Brogaard K., Leaman R., Casagrande L., 2013, The Astrophysical Journal, 775, 134

Varisco L., Bortolas E., Dotti M., Sesana A., 2021, Monthly Notices of the Royal Astronomical Society, 508, 1533–1542

Varma V., Gerosa D., Stein L. C., Hébert F., Zhang H., 2019, Physical Review Letters, 122

Vasiliev E., Antonini F., Merritt D., 2015, The Astrophysical Journal, 810, 49

Vennes S., Nemeth P., Kawka A., Thorstensen J. R., Khalack V., Ferrario L., Alper E. H., 2017, Science, 357, 680–683

Vitral E., Kremer K., Libralato M., Mamon G. A., Bellini A., 2022, MNRAS, 514, 806

Vogelsberger M., Sijacki D., Kereš D., Springel V., Hernquist L., 2012, MNRAS, 425, 3024

Volonteri M., 2007, The Astrophysical Journal, 663, L5–L8

Volonteri M., Madau P., Haardt F., 2003, The Astrophysical Journal, 593, 661–666

Volonteri M., Madau P., Quataert E., Rees M. J., 2005, ApJ, 620, 69

Volonteri M., Habouzit M., Colpi M., 2021, Nature Reviews Physics, 3, 732

Volonteri M., Pfister H., Beckmann R., Dotti M., Dubois Y., Massonneau W., Musoke G., Tremmel M., 2022, MNRAS, 514, 640

Vynatheya P., Hamers A. S., Mardling R. A., Bellinger E. P., 2022, Monthly Notices of the Royal Astronomical Society, 516, 4146–4155

Vázquez-Aceves V., Zwick L., Bortolas E., Capelo P. R., Amaro Seoane P., Mayer L., Chen X., 2021, Monthly Notices of the Royal Astronomical Society, 510, 2379–2390

Wang L., et al., 2016, Monthly Notices of the Royal Astronomical Society, 458, 1450–1465

Wang L., Greene J. E., Ju W., Rafikov R. R., Ruan J. J., Schneider D. P., 2017, ApJ, 834, 129

Wang Y.-H., Leigh N., Sesana A., Perna R., 2018, Monthly Notices of the Royal Astronomical Society, 482, 3206–3218

Wang L., Iwasawa M., Nitadori K., Makino J., 2020, Monthly Notices of the Royal Astronomical Society, 497, 536

Wang H.-Y., Most E. R., Hopkins P. F., 2025, arXiv e-prints, p. arXiv:2508.16855

Ward W. R., 1997, Icarus, 126, 261

Weatherford N. C., Kıroğlu F., Fragione G., Chatterjee S., Kremer K., Rasio F. A., 2023, The Astrophysical Journal, 946, 104

Weinberg S., 1972, Gravitation and Cosmology: Principles and Applications of the General Theory of Relativity. John Wiley & Sons, New York

Wen L., 2003, The Astrophysical Journal, 598, 419–430

Wen S., Jonker P. G., Stone N. C., Zabludoff A. I., 2021, The Astrophysical Journal, 918, 46

White S. D. M., 1980, MNRAS, 191, 1P

Will C. M., 2006, Living Reviews in Relativity, 9, 3

Williams D. J., et al., 2025, ApJ, 989, 107

Woosley S. E., 2017, The Astrophysical Journal, 836, 244

Woosley S. E., Blinnikov S., Heger A., 2007, Nature, 450, 390–392

Wu X.-B., et al., 2015, Nature, 518, 512–515

Wyithe J. S. B., Loeb A., 2003, The Astrophysical Journal, 595, 614–623

Xin C., Haiman Z., 2024, MNRAS, 533, 3164

Xu H., et al., 2023, Research in Astronomy and Astrophysics, 23, 075024

Yoshida H., 1990, Physics Letters A, 150, 262

Yu Q., Madau P., 2007, Monthly Notices of the Royal Astronomical Society, 379, 1293–1301

Yu Q., Tremaine S., 2002, Monthly Notices of the Royal Astronomical Society, 335, 965–976

Yu Q., Tremaine S., 2003, The Astrophysical Journal, 599, 1129–1138

Yue M., Fan X., Yang J., Wang F., 2023, AJ, 165, 191

Yunes N., Miller M. C., Thornburg J., 2011a, Phys. Rev. D, 83, 044030

Yunes N., Kocsis B., Loeb A., Haiman Z., 2011b, Phys. Rev. Lett., 107, 171103

Zevin M., et al., 2021, ApJ, 910, 152

Zhang Q., Fall S. M., Whitmore B. C., 2001, The Astrophysical Journal, 561, 727–750

Zhao G.-Y., et al., 2022, ApJ, 932, 72

Zheng Z., et al., 2014, The Astrophysical Journal, 785, L23

Zhou H., Wang T., Zhang X., Dong X., Li C., 2004, ApJ, 604, L33

Zocchi A., Gieles M., Hénault-Brunet V., 2017, Monthly Notices of the Royal Astronomical Society, 468, 4429–4440

Zocchi A., Gieles M., Hénault-Brunet V., 2018, Monthly Notices of the Royal Astronomical Society, 482, 4713–4725

Zrake J., Tiede C., MacFadyen A., Haiman Z., 2021, ApJ, 909, L13

Zwick L., Capelo P. R., Bortolas E., Mayer L., Amaro-Seoane P., 2020, Monthly Notices of the Royal Astronomical Society, 495, 2321–2331

Zwick L., Capelo P. R., Bortolas E., Vázquez-Aceves V., Mayer L., Amaro-Seoane P., 2021, MNRAS, 506, 1007

Zwicky F., 1957, Morphological astronomy. Springer

de La Fuente Marcos R., de La Fuente Marcos C., 2009, A&A, 500, L13

de Rijcke S., Buyle P., Dejonghe H., 2006, MNRAS, 368, L43

de la Fuente Marcos R., de la Fuente Marcos C., 2010, ApJ, 719, 104

del Valle L., Volonteri M., 2018, Monthly Notices of the Royal Astronomical Society, 480, 439–450

van Dokkum P. G., et al., 2010, ApJ, 709, 1018

van Leer B., 2006, Communications in Computational Physics, 1, 192

van der Marel R. P., Anderson J., 2010, ApJ, 710, 1063

von Zeipel H., 1910, Astronomische Nachrichten, 183, 345

Šubr L., Fragione G., Dabringhausen J., 2019, Monthly Notices of the Royal Astronomical Society, 484, 2974–2986

Acknowledgements

First of all, I would like to thank my supervisor, Thorsten Naab, for his invaluable scientific guidance and for granting me the freedom to pursue my own career goals. His mental and emotional support during difficult times, when I felt lost, was crucial in helping me keep going. I would also like to sincerely thank Antti Rantala for co-supervising my projects, for always being responsive to my numerous/numerical questions, and for encouraging me to find my own ways to tackle such challenges rather than simply providing the (perhaps trivial to an experienced scientist) answer. The combined guidance of both Thorsten and Antti has been instrumental in helping me grow into a more independent researcher.

Furthermore, I am grateful to have met Taeho Ryu, who helped me take my first steps in hydrodynamical simulations by providing examples and mini-tutorials that allowed me to set up one of my first independent projects. I would also like to thank Volker Springel and Rüdiger Pakmor for supporting this idea, granting me access to the developers' version of the AREPO code, and recommending Magdalena Siwek as a collaborator. A big thank-you to Magda, who provided the code on which I built and extended my work, and who essentially supervised the project. Finally, I would like to thank Oliver Zier for showing interest in this project and for his valuable contributions and advice on the technical aspects.

A massive thanks to all my peers at MPA and the long-term Munich friends I made along the way, both inside and outside the institute. Julian and Ana — for the coffee breaks, lunches, and long late-night drinking sessions, often in a "support group" format accompanied with bad-dad jokes; Holly, for being as indecisive as I am and always up for something cool; Joaquin, Jay, Yru, and Simon, with whom I immediately felt a cultural connection (mostly through drinking and going out — but not only that, though mostly that), which brought us closer; Fulvio, for always being enthusiastic about music and persuading me to jam or perform at countless MPA events; and Soumya, for being such a kind and thoughtful person. Thanks also to Raph and Eve, for sharing and appreciating my approach to work–life balance; JM, for reminding me to play more guitar and take breaks, while also offering insightful, confidence-building academic advice; Tom and Louise, for hosting so many dinners and parties and for their genuine support, interest, and sharp thinking when handling stressful situations; Harris for becoming a good friend during his scientific visits and sharing similar struggles and aspirations; Chris and Anna, for the cat-themed dinners and hangouts; Aniket, for being an exemplary office mate, always ready to help or remind me of something I might have forgotten; Miha and Hitesh, for making

sure the common room never ran out of beer; and Sunmyon, for listening to my random Japanese-speaking rants.

Additionally, I would like to express my gratitude to my friend and mentor Padelis, who has supported me since my undergraduate years — attending my DJ sets in Thessaloniki after long evening astronomy courses, offering valuable and uplifting career advice, and sharing countless (sober or less sober) discussions about science, philosophy, history, music, travels and life in general. A heartfelt thanks to my M.Sc. supervisor, George Pappas, for guiding me through my first steps in (astro)physics research, and together with Nick Stergioulas, for teaching me the fundamentals of astrophysics and general relativity. I am also deeply grateful to Paola Andreani and Carlos De Breuck for their mentorship and support during my internship at ESO—undertaken in the challenging times of COVID—which ultimately paved the way for my PhD journey in the Garching area and MPA.

I am also deeply grateful to my parents and family for standing by my side when I decided to begin a Physics degree at the age of 26 — with the goal of becoming an astrophysicist — while working night shifts, and for eventually believing in me and in my conviction that dreams and goals can come true if one truly puts their mind to it. Finally, a supermassive thanks to my partner — and hero behind the scenes — Stavroula, for her endless support and understanding throughout the years, especially during the ups, downs, and mood swings of the PhD journey, always reminding me of what truly matters and never ceasing to encourage me to keep going and pursue my goals.